The Dissertation Committee for Owen Michael Williams Certifies that this is the approved version of the following dissertation:

MOLECULAR AND MATERIAL APPROACHES TO PHOTOELECTROCHEMICAL CELLS FOR CARBON DIOXIDE REDUCTION

Committee:

Michael J. Rose, Supervisor

Alan H. Cowley, Co-Supervisor

Richard A. Jones

Allen J. Bard

John G. Ekerdt

MOLECULAR AND MATERIAL APPROACHES TO PHOTOELECTROCHEMICAL CELLS FOR CARBON DIOXIDE REDUCTION

by

Owen Michael Williams, B.S.

Dissertation

Presented to the Faculty of the Graduate School of

The University of Texas at Austin

in Partial Fulfillment

of the Requirements

for the Degree of

Doctor of Philosophy

The University of Texas at Austin

August, 2016

Dedication

To my family – my grandparents, my mother, father, and step father, but most importantly of all, my brothers.

Acknowledgements

First of all, I need to thank those that provided the guidance to help me through graduate school. To Dr. Cowley I owe a great deal of gratitude not simply due to your scientific guidance, but because you provided me an ideal towards which to strive. To show the amount of enthusiasm and joy I have seen in you is something I can only hope to accomplish. I am proud to be your last graduate student. To Dr. Rose, I cannot thank you enough for taking me on when so much else was on your plate. You have served as a role model to me, showing me how to maintain my work ethic in good times and bad.

Beyond the assistance of my advisors, I had help throughout the department. I want to thank Vince Lynch for sharing XRD expertise. I would be lost without the assistance of Hugo Celio and Shouliang Zhang in XPS and SEM studies. Mike Ronalter and Adam Kennedy, thank you for helping in all the hair-brained glassware ideas. Additionally, I want to thank all the members of my committee for their help and support.

There are far too many people that have made my time in graduate school enjoyable. To the other members of the Lost Class, my ***** Jams compatriot, the Three Musketeers, and the Rose Army: I owe you my thanks and certainly more than one beer. In particular, I want to thank Sarah Swingle, Kate Crawford, Kory Mueller, Dan Evans, and Ryan Pekarek for being there to bring me up in bad times and celebrate the good times.

Finally, those I must acknowledge most – my family. Mom and Randy – thank god you moved to Dallas; your love and advice has been invaluable during these five years. Dad, your encouragement and excitement helps keep me going in the hardest of times. To Greg, Danny, and Graham – I could not have done this without you. I love you all.

MOLECULAR AND MATERIAL APPROACHES TO PHOTOELECTROCHEMICAL CELLS FOR CARBON DIOXIDE REDUCTION

Owen Michael Williams, PhD.

The University of Texas at Austin, 2016

Supervisor: Michael J. Rose

Co-Supervisor: Alan H. Cowley

The development of photoelectrochemcial cells for the direct production of storable fuels is a crucial aspect to the energy portfolio of a world that is increasingly shifting towards renewable energy sources. Development of the base scientific knowledge across all components of these devices – general design, photovoltage generation, material stabilization, and chemical catalysis – is required before engineered products become available on the market. Detailed herein are electronic, structural, and catalytic studies on a homogeneous catalyst (acenaphthene based colbaloxime), development of a new method of gold deposition for heterogeneous catalysis and the design, preparation, characterization, and electrochemistry of a cathodic carbon dioxide reduction device using gallium phosphide.

Table of Contents

List of Tables

List of Figures

List of Schemes

Chapter 1: Solar Fuel Generation by Photoelectrochemical Cells

1.1 The Case For Photoelectrochemical cells

Globally, the generation and storage of sustainable, clean energy is one of the largest challenges facing society today. According to the Energy Information Administration, in 2013 energy consumption in the United States reached 97.1 quadrillion British Thermal Units (quads) annually, with the vast majority of this generated by non-renewable sources (approximately 8 quads are attributable to renewables including wind, solar, hydroelectric, biomass, and solar).[1] In the U.S. this value is expected to reach 105.7 quads annually by 2040. The worldwide outlook paints a more extreme picture, with energy consumption increasing from 538 quads currently to 780 quads by 2040 according to the World Energy Outlook.[2]

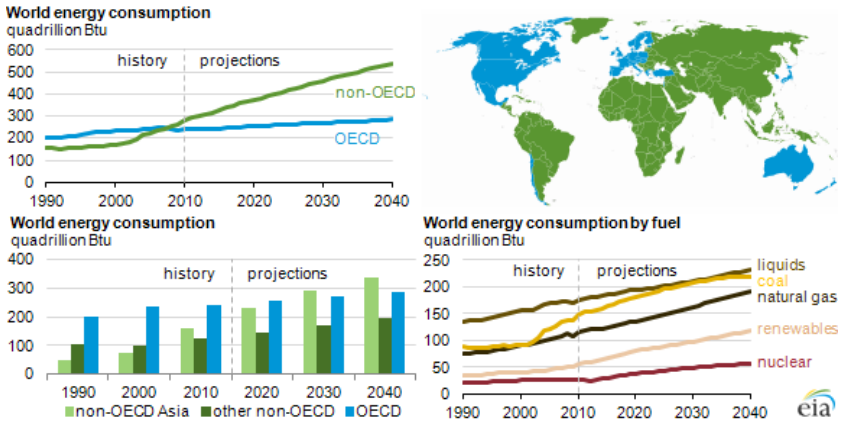

Figure 1. Current world energy consumption has reached ~500 quads annually. Mainly due to growth in non-OECD countries, this value may reach ~800 quads annually by 2040.[3]

This increasing demand for energy – coupled with the ease with which fossil fuels are extracted – suggests that our contribution to global carbon dioxide concentrations will not abate for years to come. According to the Earth System Research Laboratory, the globally averaged CO_2 concentration is 403 ppm.[4] Increasing CO_2 concentrations are widely accepted to cause global warming due to the greenhouse gas effect, although there are many variables in the study of global climate leading to extensive uncertainties in predictions.[5] It has been shown through numerous isotope studies that the current state of warming is an aberration rather than part of a cyclical trend of warming and cooling that occurs outside of anthropomorphic effects.[6–8] The observable consequences of this new age of warming include rising sea levels, unpredictable climates, ecological change, and an increasing occurrence of so-called '100 year events' that prove damaging on a massive scale.[9–13] This last point is so evident that insurance companies have begun factoring global warming risks in their actuarial calculations.[14] Beyond this, however, it is difficult to foresee the consequences of our runaway carbon usage. The consequences of this level of indeterminate warming are somewhat unpredictable, however, it is clear that the development of a strategy to mitigate climate change is necessary. In order to do this, major advances in technology are required to reduce our dependence on non-renewable sources of energy, leading to a more sustainable and predictable future.

Table 1. Energy generation by a variety of sources according to the IEA and the predicted changes that would allow for a more balanced energy portfolio and thereby mitigate the impact of anthropomorphic climate change.[2]

			Current Policies Scenario		New Policies Scenario		450 Scenario	
	2000	2013	2020	2040	2020	2040	2020	2040
Coal	2 343	3 929	4 228	5 618	4 033	4 414	3 752	2 495
Oil	3 669	4 219	4 539	5 348	4 461	4 735	4 356	3 351
Gas	2 067	2 901	3 233	4 610	3 178	4 239	3 112	3 335
Nuclear	676	646	827	1 036	831	1 201	839	1 627
Hydro	225	326	380	507	383	531	384	588
Bioenergy*	1 023	1 376	1 537	1 830	1 541	1 878	1 532	2 331
Other renewables	60	161	296	693	316	937	332	1 470
Total	**10 063**	**13 559**	**15 041**	**19 643**	**14 743**	**17 934**	**14 308**	**15 197**
Fossil-fuel share	*80%*	*81%*	*80%*	*79%*	*79%*	*75%*	*78%*	*60%*
*Non-OECD share***	*46%*	*60%*	*63%*	*70%*	*63%*	*70%*	*63%*	*69%*
CO_2 emissions (Gt)	23.2	31.6	34.2	44.1	33.1	36.7	31.5	18.8

Renewable energy technologies that are currently in production on a wide scale include solar (both photovoltaic and thermal), wind, geothermal, hydroelectric, and biomass. Each of these have their ecological benefits and impacts (i.e. hydroelectric power can supply sustained electricity for a long period of time, but have a large impact on the ecology of river systems). Current large scale energy production typically requires the immediate usage of electricity, causing power plants to operate out of the range of peak efficiency and produces periods of intermittent increased power usage that may produce blackouts or brownouts in developing and developed countries alike. Clearly, the energy portfolio of tomorrow should be built on two pillars: *i)* the generation of large quantities of energy in a reliable, sustainable manner and *ii)* the efficient storage of energy for use in

times of peak consumption. In this way, the energy generated can accommodate what is needed during periods of both high and low usage.

Photoelectrochemical cells (PECs) can solve this problem by generating energy from solar influx and directly storing it in chemical bonds. These energy dense fuels can be used as a storage strategy to generate electricity locally (through fuel cells) when needed or for use in transportation (through combustion). The vast majority of PECs studied to date focus on the complimentary half reactions of proton reduction (hydrogen evolution reaction, HER) and water oxidation (oxygen evolution reaction, OER) at the photocathode and photoanode, respectively. Because these systems mirror the energy cycles performed in plants, using sunlight to convert energy deficient molecules to energy dense molecules, this process is often referred to as 'artificial photosynthesis'. Traditional photosynthesis converts CO_2 and water into energy and oxygen. Artificial photosynthesis, on the other hand, is often used as an umbrella term to describe any process by which solar energy is captured and stored directly in chemical bonds. To date, the reductive part of this process focuses on two widely studied reactions: *i)* proton reduction (collectively this is referred to as water splitting) and *ii)* carbon dioxide reduction.

1.2 PHOTOELECTROCHEMICAL CELL DESIGN

In general, device design must incorporate a stable, electronically efficient semiconductor with catalytically effective molecules or materials. On first pass, a PEC is easily divisible into two parts – one that utilizes photogenerated holes to afford water

oxidation and one that utilizes photogenerated electrons to afford either proton or carbon dioxide reduction. Separating these two processes simplifies the development and testing of novel design constructs, allowing for the investigation and optimization of each side prior to incorporation into a composite device. This work focuses on the development of photocathodic constructs, with a vision to apply lessons learned in the HER arena to the more complicated realm of carbon dioxide reduction. However, a brief overview of general PEC design will be discussed and relevant literature presented. There is a large body of work in this arena with several review articles that explain PECs in depth – only a broad and somewhat simplified overview will be given here.[15–20]

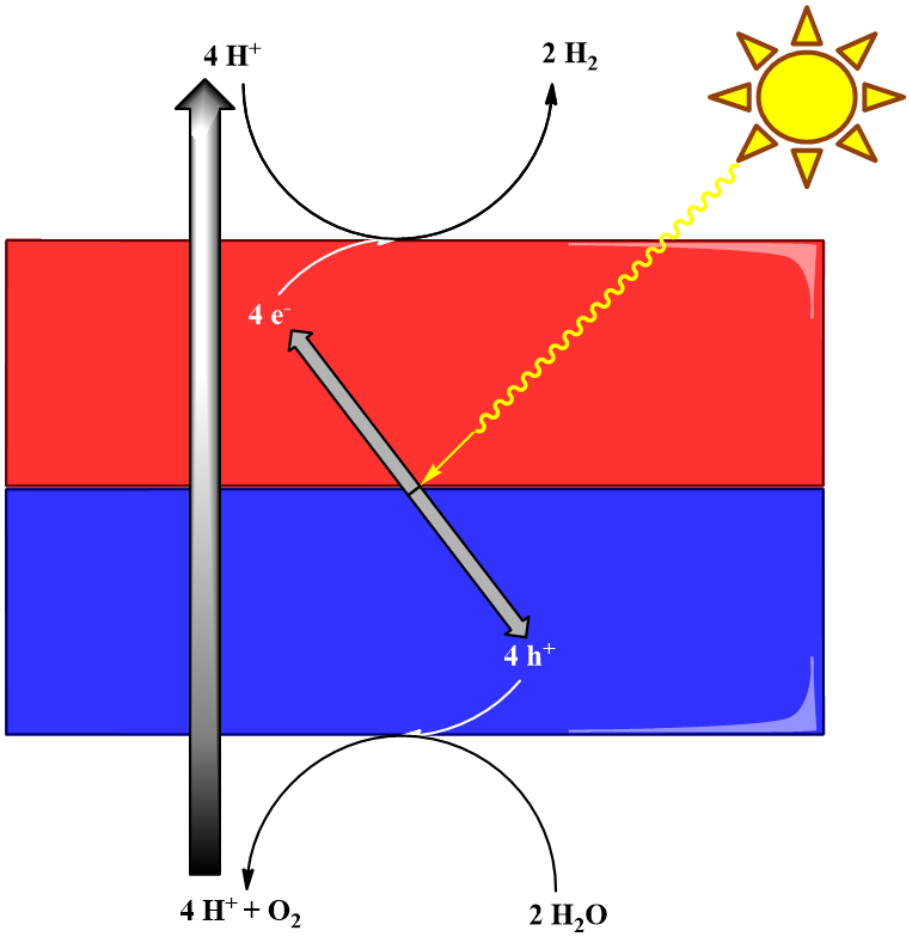

Scheme 1. Basic processes in a photoelectrochemical cell: i) solar photon absorption, ii) charge separation at a p(red)-n(blue) junction, iii) cathodic proton reduction and anodic water oxidation, and iv) proton transfer across the device.

The general mechanism of PECs is outlined in Scheme 1. In these devices, the solar photon flux is used to photoexcite an electron-hole pair in the semiconductor device. These charge carriers can then diffuse to the surface to perform direct chemical transformations when provided with a sufficiently active catalyst. The photoanode combines holes with water to generate oxygen and protons. These protons then pass through the PEC device and

can be utilized at the photocathode. Here, electrons combine with either CO_2 and/or H^+ to generate hydrogen or reduced carbon based species (i.e. CO, HCOOH, CH_3OH, CH_4, *et cetera*). In comparison to traditional photovoltaics, PECs have several restrictions that must be factored into their design. First of all, a large surface area is desirable to allow for a large amount of fuel formation in a relatively small form factor. Secondly, efficient charge utilization requires morphologies that are similar to the length of charge diffusion in semiconductors (on the scale of 1-100 μm). Furthermore, due to the complementary reactions being performed on either side of a device (i.e. cathodic *vs.* anodic), a permeable membrane needs to be incorporated to balance the chemical reactions. The most promising PEC designs on the macro scale recently have been reported by Nate Lewis at Caltech and Peidong Yang at UC-Berkeley.[21,22] A large body of work has allowed for the production of photoelectrodes using photovoltaic nanowires (a design that allows for both large areal densities of catalysts and effective charge transport to the surface) and the combination of these electrodes into a device by the incorporation of a proton permeable membrane.

A schematic of these designs is presented in Figure 2, showing long nanowires affixed to a proton-permeable membrane.[22] This design allows for orthogonal vectors of photon absorption and charge collection to allow for increased utility for semiconductors with short charge carrier diffusion lengths. While the vast majority of research focuses on planar electrodes (due to their simplicity), the methods devised in these studies can equally apply to the more sophisticated cell design outlined below.

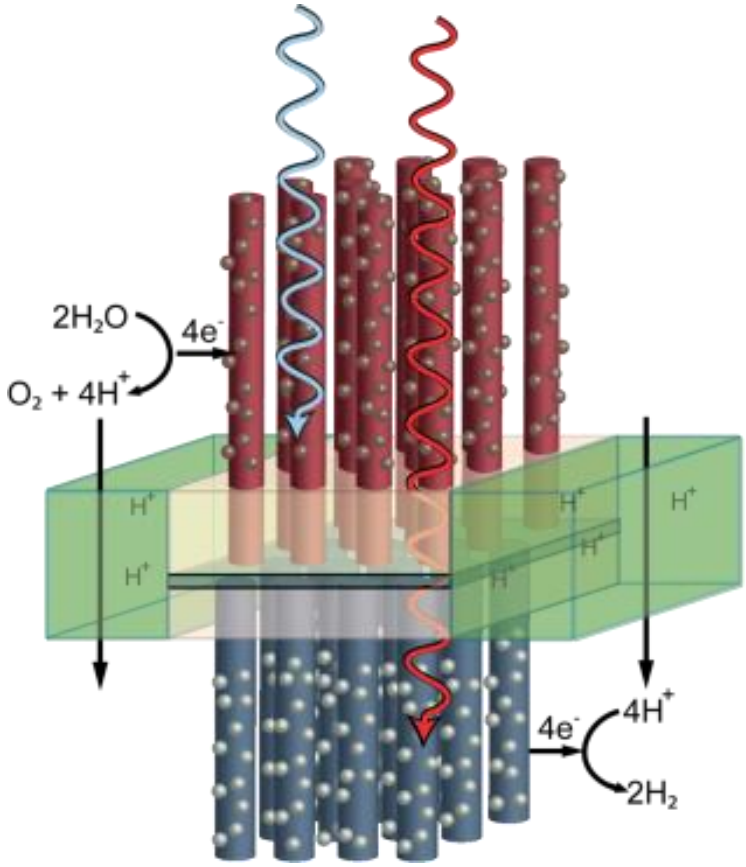

Figure 2. Photoelectrochemical construct that incorporates nanowire photovoltaics into a proton-permeable membrane designed in the lab of Nate Lewis.[22]

The materials that are used on the surface of PECs generally perform one of three important functions: *i)* generation of charge carriers from solar illumination (photovoltaics), *ii)* protection of PVs that are prone to corrosion, or *iii)* use as a catalyst to diminish the overpotential required for thermodynamically uphill reactions (see Scheme 2). Oftentimes, a single material can provide a solution for two or even three of these problems (eg. wide bandgap semiconductor powders). In general, however, most studies

focus on incorporating multiple materials that results in a device with a large photocurrent, long term stability, and catalytic efficiency.

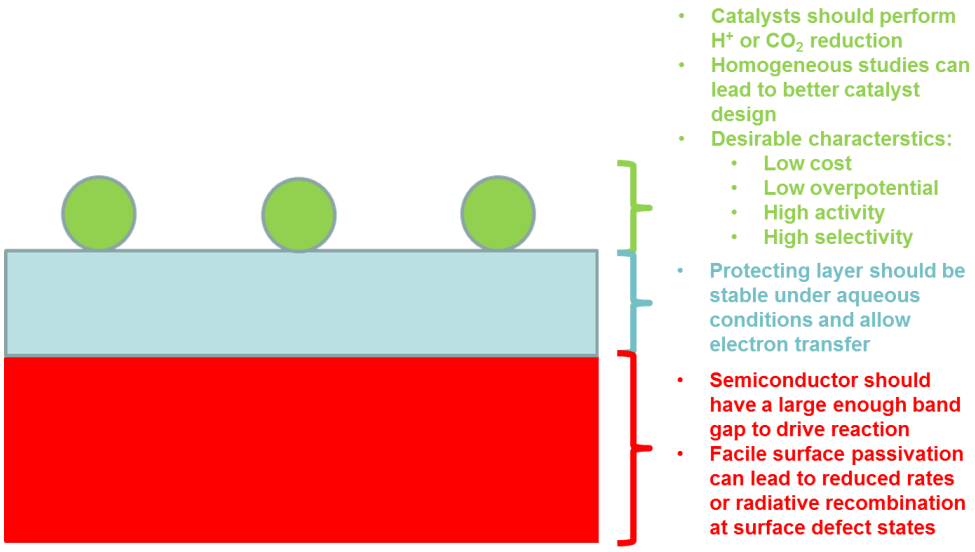

Scheme 2. Basic diagram showing a schematic image of the interface on a semiconductor for photoelectrochemical cell, consisting of three distinct regions: semiconductor (red), protecting layer (blue), and catalyst (green).

1.3 Semiconductors in Photoelectrochemical Cells

For the generation of photovoltages, PECs have relied upon either traditional semiconducting materials such as Si, InP, GaAs (E_g = 1.0 – 3.0) or metal oxides such as TiO_2, WO_3, ZnO, with large band gaps (E_g > 3.0).[17,19,23] Inorganic semiconductors have a number of benefits including high efficiency, utilization of a broad range of solar influx, and high carrier mobility. However, these materials are usually poor intrinsic catalysts, and in general, degrade under aqueous conditions. This corrosion oftentimes leads to surfaces with large quantities of defects. These defect sites then allow for recombination of charge

carriers at surface states which results in the loss of available photocurrent. Metal oxides are relatively more stable than silicon or other binary semiconductors, however, the vast majority of them have a large bandgap which makes inefficient use of the solar spectrum (Figure 3).

Chemically robust materials such as TiO_2 and $SrTiO_3$ have large band gaps (3.0 and 3.2 eV, respectively) and as such are not electronically efficient due to the limited usage of broadband solar photons (less than 20%).[24] Comparatively, silicon and other III-V semiconductors (e.g. GaAs, InP) have reasonably sized band gaps and as such are electronically efficient and can utilize a greater portion of the solar spectrum (~85% for Si).[25] The surfaces of these materials, however, are chemically susceptible under operative conditions, leading to the aforementioned surface defects and correspondingly high rates of electron-hole pair recombination at interfaces.[26] Furthermore, both large band gap metal oxides and non-oxide semiconductors show limited catalytic activity and selectivity compared with traditional heterogeneous (transition metal materials, nanoparticles, etc.)[27,28] and homogeneous catalysts [$P_2N_x(Ni)^{2+}$, cobaloximes, Re(bpy), etc.].[29–31]

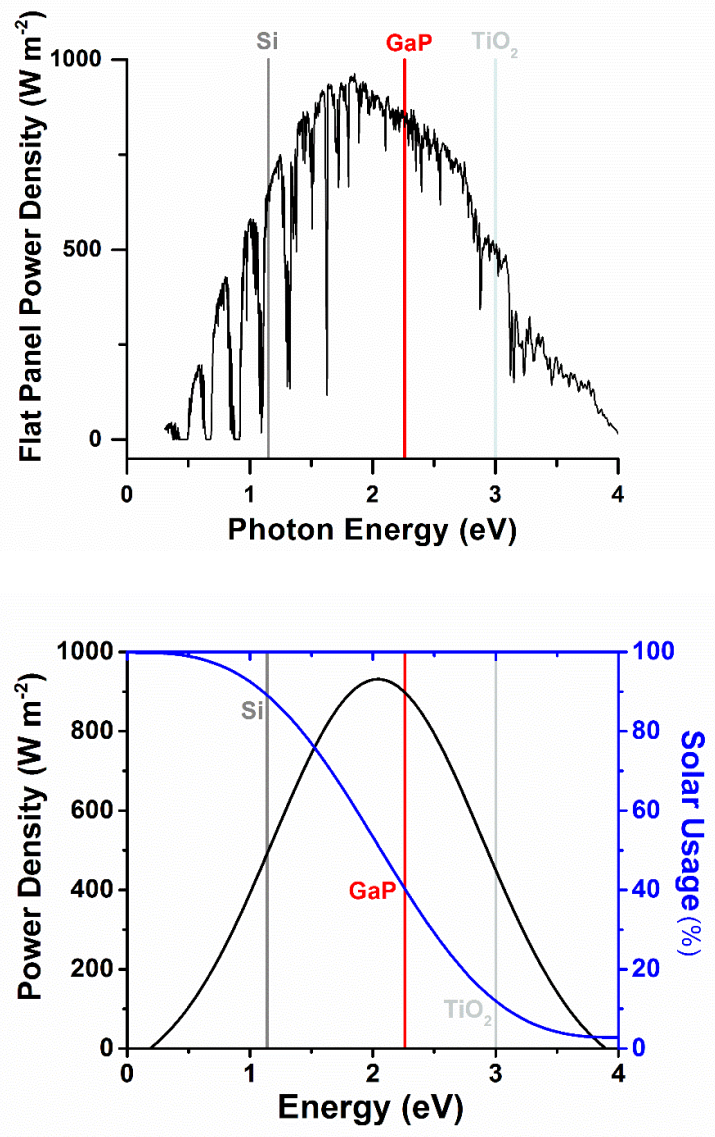

Figure 3. Flat panel power density as a function of the photon energy for measured solar irradiance (top) and a fitted model showing the power density as well as the potential maximum solar power usage based on the band gap of a given material. Si, GaP, and TiO_2 band gaps are incorporated as references.[32]

Importantly, these materials should have band edge positions that 'bracket' (i.e. have the requisite energetics) to perform the corresponding oxidative or reductive reactions

(see Figure 4). The use of a dual band gap PECs can overcome this limitation by combining a low band gap photocathode material with a high band gap photoanode. Furthermore, the surface energetics of the semiconductor are crucial to device performance. For instance, it has been shown that both surficial organics (covalently bound) and metal oxides can facilitate the band bending and thus overall rate of electron transfer across a semiconductor-liquid junction.[33] This is typically accomplished by modification of the surface dipole, either enhancing or diminishing electron transfer across this membrane. Attenuated electron transfer leads to correspondingly higher rates of recombination and compromised device performance.[34]

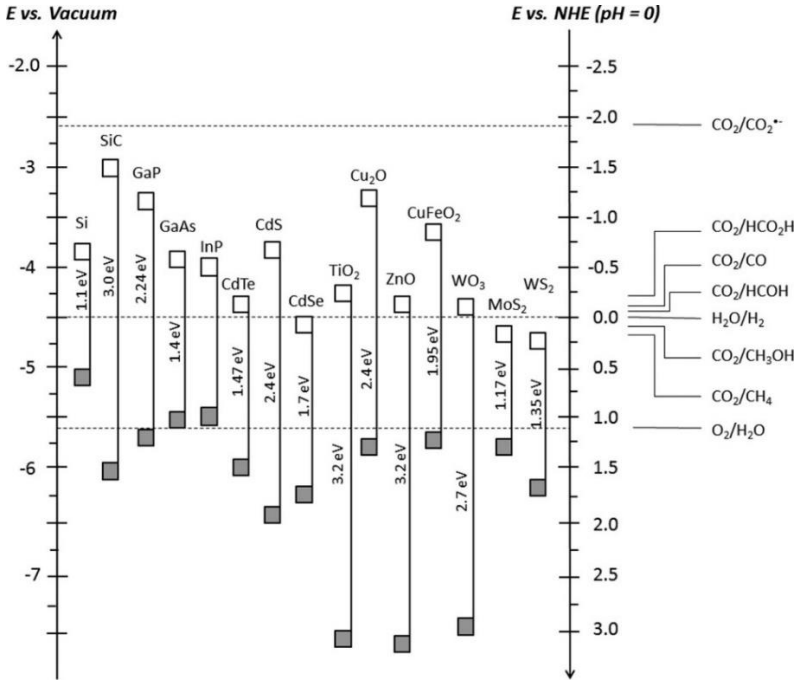

Figure 4. Relative band edge positions of inorganic semiconductors in comparison with the thermodynamic potential of OER, HER and carbon dioxide reduction reactions.[20]

1.4 SEMICONDUCTOR PROTECTION

In order to combat the low corrosion resistance of traditional photovoltaics (primarily silicon, but increasingly more complex III-V semiconductors), researchers have developed several different protective strategies. These include covalent modification of dangling surface bonds, non-covalent layers, and material deposition.[35]

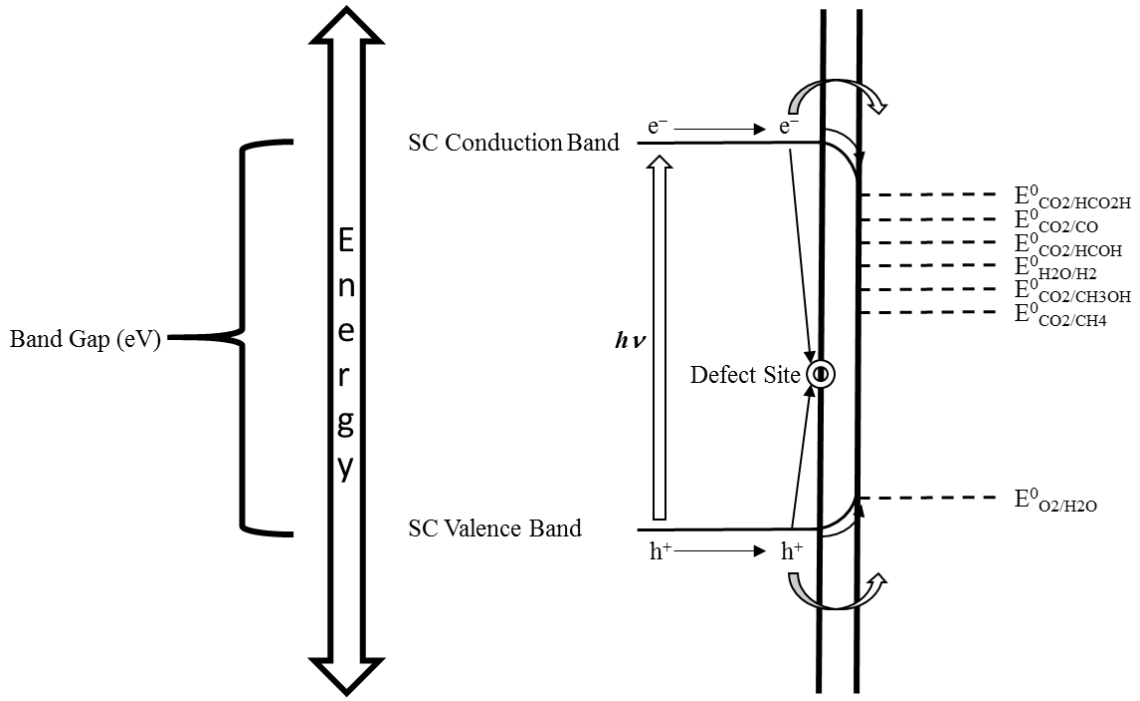

Scheme 3. Energy diagram showing the interface between a traditional semiconductor liquid interface. Note that the cathodic and anodic interfaces are incorporated into the same side of the illustration. Electrons that are photogenerated can recombine at a defect, tunnel through a protecting layer, or conduct through it. The band structure of this interface should allow for oxygen evolution reaction as well as the reduction of CO_2 or protons. Adapted from Walter *et al.*[17]

Many research groups focus on the covalent modification of silicon surfaces – particularly along the (111) crystal facet.[36–41] Previous work has shown that HF etching of this surface allows for generation of atomically flat silicon-hydride terminated surfaces.[42] Further reaction with chlorinating agents (PCl_5) leads to a functional surface that can be modified through traditional Grignard or aryl-lithium based reactions. This well-defined surface greatly reduces the amount of surface state defects and thus increases the device efficiency. This methodology has been used on other binary semiconductors, although the surface chemistry of these materials is much less well developed.[43–45] Group III-V semiconductors have an inherent difficulty in controlling their reactivity due to the bond dipoles present in these materials. Organic protection strategies on 100 surfaces are not as controllable as those for 111 surfaces, primarily due to the more complex surface reactivity, although there are several reported methods for 100 surface functionalization.[46–49]

Furthermore, the surfaces of traditional inorganic semiconductors can be passivated through the deposition of corrosion resistant materials – typically metal oxides. Atomic layer deposition is a preferred method of deposition in semiconductor processing. In this method, alternating pulses of reactive precursors allow for the controlled deposition of metals and metal oxides.[50] For instance, alternating pulses of trimethyl-aluminum and water will deposit a layer of alumina with self-limiting, sequential reactions.[51] In this way, layers with controlled thicknesses at the atomic level can be deposited. Furthermore, the introduction of alternating metal precursors can 'dope' the deposited metal oxide, effecting new electronic characteristics.[52]

In PECs, materials deposition has been applied to a wide variety of systems. Crucially, increased lifetime should be achieved without adversely affecting the efficiency of the overall device. This type of materials-based passivation should allow for sustained protection (i.e. thick enough to be pinhole-free), photon flux (i.e. not highly absorbing at the requisite thicknesses), and be electronically conductive without affecting the energetics of the semiconductor itself. For instance, although aluminum oxide (Al_2O_3) is very stable under aqueous conditions, its band gap disallows electron transfer at thicknesses greater than 3-4 nm and greatly attenuates the potential current at shorter depths. Conversely, zinc oxide (ZnO) and titania (TiO_2) have band edges that align with that of many inorganic semiconductors, but are less stable under extreme pH conditions.

Interestingly, the device characteristics have a strong dependence on the thicknesses of these deposited metal oxide protective layers. Although often thought to result in conformal depositions of metal oxides,[53] recent studies suggest that in the very thin regime (< 2 nm) these materials oftentimes have pinholes that cause an incomplete passivation of the surface and leads to reduced device performance over time.[54] Near the other extreme, at increased thicknesses, these materials may impart their semiconducting properties on the device which may reduce the overall efficiency. For instance, an intrinsically n-type TiO_2 layer deposited caused a decrease in the observable catalytic activity with increasing layer thicknesses on a GaP surface.[55] Furthermore, at very large thicknesses, these layers may become entirely blocking.

It is important to note that the band edge position of these protective layers to ensure that they have the requisite energy for the chemical reaction. Thinner layers may allow for direct conduction of electrons to the liquid interface, but thicker layers of such a material would preclude catalysis. If the band edge position of the protective metal oxide does not exceed the redox potential of the desired reaction (i.e. it is too cathodic for oxidative reactions or too anodic for reductive reactions), thick layers will reduce the capability of the device to perform the desired reaction. Much research has focused on developing new protective material overlayers that allow for efficient electron transfer, increased stability, and enhanced band edge energetics.

1.5 Catalysis in Photoelectrochemical Cells

Electrocatalysts are evaluated based on several factors with large implications in PEC based devices. One of the most important of these characteristics is the inherent overpotential of the electrocatalyst. This represents the additional potential required to affect catalysis beyond the thermodynamic or standard reduction potential of the chemical transformation. The overpotential ultimately represents energy lost in the entire system due to the kinetic limitations of the desired chemical reaction. The best catalysts affect the transformation at the theoretical limit – or standard reduction potential for electrocatalysis. Any additional overpotential required reduces the number of incident photons that are chemically useful.

In the case of proton reduction, platinum metal remains the standard bearer, catalyzing the $2\ H^+ + 2\ e^- \rightarrow H_2$ reaction at 0 V *vs.* NHE.[56] For carbon dioxide reduction and water oxidation (OER), the case is not as simple and no electrocatalysts investigated to date have performed these reactions at the thermodynamic potential. In practical terms, homogeneous cathodic electrocatalysts are required to access a reduced state prior to affecting catalysis and the potential at which this occurs will directly affect the overpotential of the catalysts. Thus, the ability of a complex to stabilize low oxidation states which can then generate metal hydride or metal carboxylate intermediates is crucial in catalytic design for reductive electrocatalysts.

Both heterogeneous and homogeneous catalysts are important in developing photoelectrochemical cells. While in a fully assembled device, homogeneous catalysts are less desirable, they provide an easy method by which a ligand design can be modified to better understand which designs will result in increased activity or selectivity. Ultimately, a strategy for tethering these catalysts to the surface can then be deployed.[31,57] Below is outlined the methods by which homogeneous catalysts are evaluated. Typically, the same metrics hold true for electrode-tethered or heterogeneous catalysts, however the ascension to the requisite reduced state is not the main determinant in heterogeneous metal or metal-oxide catalysts. In this case, the onset potential of catalysis is typically reported and may be affected by the catalyst composition, morphology, and size.[58,59]

The overpotential is typically determined through cyclic voltammetry (CV) studies in which an acid is titrated into an organic solution of the electrocatalyst. If a compound is active for hydrogen evolution, a catalytic wave will appear atop (or cathodic of) a specific redox couple. The overpotential measured and reported in literature has been calculated from various values based on this catalytic CV wave. In some cases, the potential at onset of catalysis is used, while in others, the peak catalytic potential is used. Herein, the first derivative half-wave potential method developed by Fontecave and Artero is used.[60] In this, the calculated theoretical potential based on the equations below is compared with the 'half-wave' potential or the inflection point of the electrocatalytic wave (i.e. the point at which the first derivative is at a maximum).

$$E_{½}^{T} = E_{H^+/H_2}^{0} - \frac{2.303 \times RT}{F} pK_{\alpha} + \varepsilon_D + \frac{RT}{2F} \ln(2K_C^2 C_0 C_{H_2}^0)$$

$$E_{½}^{T} = E_{H^+/H_2}^{0} - \frac{2.303 \times RT}{F} pK_{\alpha} + \varepsilon_D - \frac{RT}{2F} \ln\frac{C_0}{C_{H_2}^0}$$

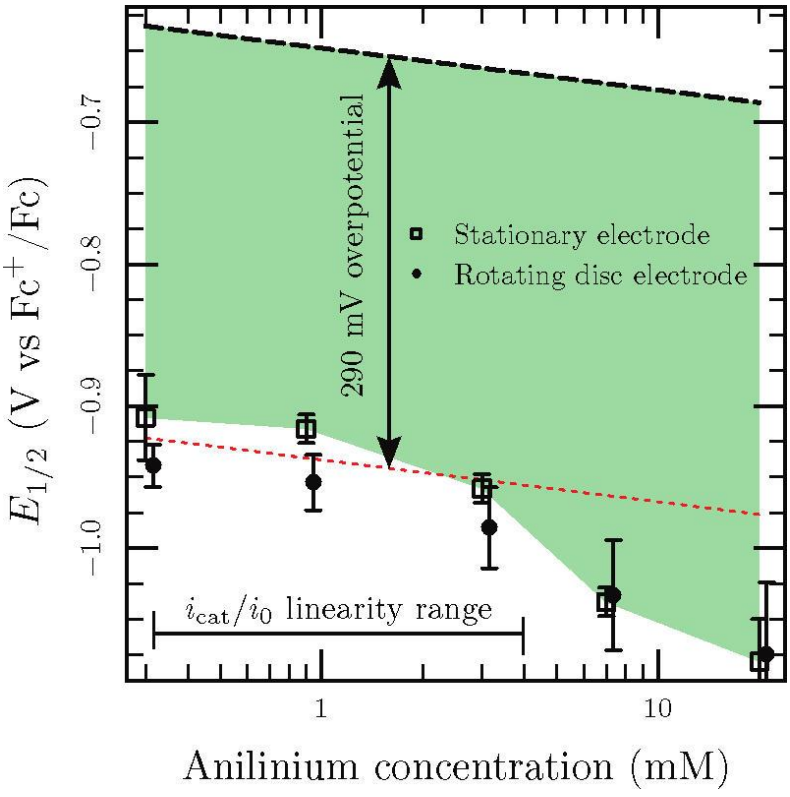

Figure 5. Method for determining the overpotential of a homogeneous electrocatalyst by plotting the half-wave potential versus the acid concentration and comparison of this value to that of the thermodynamic value.[60]

The second most important property of electrocatalysts is the activity, commonly reported in term of the turnover frequency or turnover number. The turnover number is simply a ratio of the moles of hydrogen (or other reductive product) produced over the total number of moles of catalyst in the system (mol H_2/mol cat) and the turnover frequency is this value for a given time period (i.e. mol H_2/mol cat per hour). While the true values for activity require bulk electrolysis, oftentimes the activity of a given complex can be determined or estimated from cyclic voltammetry studies of a complex.

In a common experiment, the catalytic activity is probed through the ratio of the observed current under catalytic conditions to the peak current of the compound itself (i_{cat}/i_p). In acid titration experiments, the observed cyclic voltammetry response can fall into one of several regimes based on the activity of the catalyst and the concentration of substrate (see Figure 6). At lower catalyst activities, the observed profile will typically have an observable anodic wave in the second scan segment. At high catalytic activity and low substrate concentration, all of the substrate is consumed and the profile shows an additional redox peak cathodic of the catalysis. Under higher concentrations, no anodic return wave is observed and the response can be dictated by substrate diffusion (top, middle segment of Figure 6) or by the inherent activity of the catalyst (sigmoidal wave, top right of Figure 6). In these regimes, the catalytic current ratio can be used to determine an estimated observed rate constant (k_{obs}) through the following equation: $\frac{i_{cat}}{i_p} = \frac{n}{0.4463}\sqrt{\frac{RTk_{obs}}{F\,v}}$, where n is the number of electrons involved in turnover (n = 2 for the HER and 2, 4, 6, or 8 for CO_2 reduction), R is the universal gas constant, T is the temperature, F is the Faraday constant, and v is the scan rate.

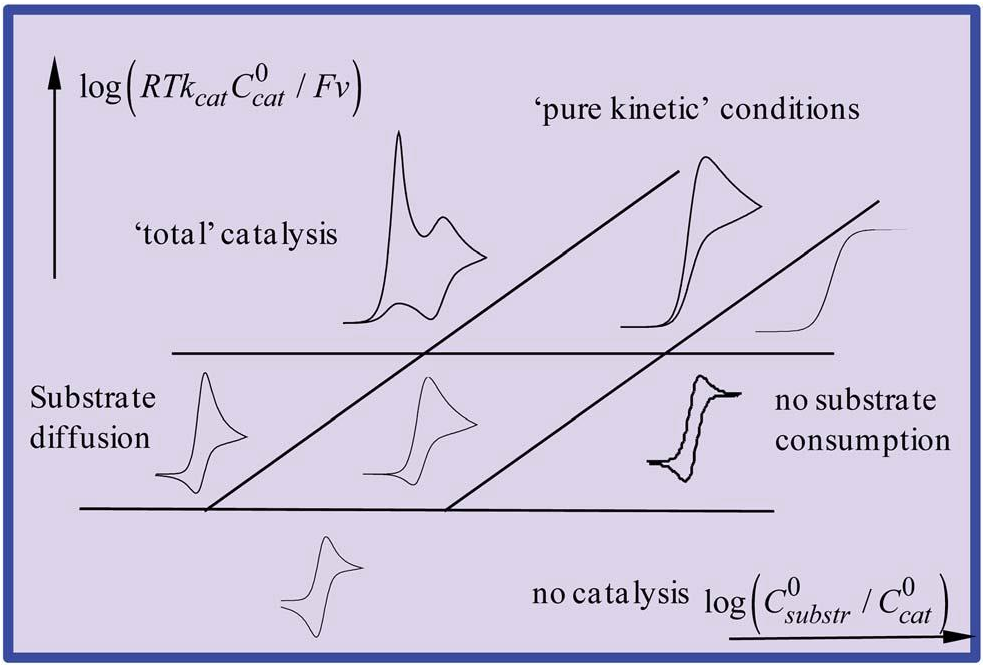

Figure 6. Catalytic regimes showing the potential cyclic voltammetry response based on changing the substrate concentration (increasing left to right) along with changing activity (increasing bottom to top).[61]

Broadly speaking, there are several other desirable characteristics of electrocatalysts. Firstly, with implications specific to CO_2 reduction electrocatalysis, the selectivity of a complex is very important. Indeed, the ability to design selective catalysts represents a major advantage of discrete homogenous electrocatalysts in comparison to their heterogeneous counterparts. Furthermore, the stability of the catalyst is important to determine the practical validity of a homogeneous approach. Several recent reports discuss the dubious nature of homogeneous electrocatalysis in bulk electrolysis – implicating the degradation of catalysts and deposition of heterogeneous materials that act as electrocatalysts themselves.[62–64]

There are a wide variety of electrocatalysts, but the foregoing represents the major metrics by which they are evaluated. Several papers in recent years go into great depth on the electrochemical underpinnings of evaluating electrocatalysts, particularly the work of Artero and Saveant.[61] A brief overview among proton reduction electrocatalysts and carbon dioxide catalysts is given in Chapter 2. Although not comprehensive, several key important features of both proton and carbon dioxide reduction catalysts and their effect on overpotential and activity are outlined and shown in literature examples.

In order to incorporate electrocatalysts into PECs, several criteria must be met. Most importantly, the catalyst needs to show the desired selectivity, an activity that is capable of facilitating the electrical current generated by the underlying photovoltaic, and a transparency that does not adversely affect the flux of solar photons to the surface.[65] For this reason, homogeneous catalysts with high activity that can be incorporated into the surface represent a promising strategy. However, these types of interfaces are typically less stable than their heterogeneous counterparts.

The development and study of a novel electrocatalyst with drastic changes in observed reactivity is discussed in Chapter 2. A new method of depositing heterogeneous electrocatalysts through electrodeposition is discussed in Chapter 3. In Chapter 4, the design and construction of a photovoltaic – catalyst interface is described and used in PEC studies.

Chapter 2: Study of a Naphthalene Appended Cobaloxime*

2.1 Introduction

In the development of robust and effective photoelectrochemical cells (PECs), the development of catalysts is crucial. Catalysts can affect the activity, selectivity, and efficiency of these devices, having a large impact in their practical utility. While heterogeneous catalysts are, in general, much more stable than their homogeneous counterparts, rational ligand design is easily studied in homogeneous systems, allowing for the development of novel design strategies. This rational design can effect selectivity and activity in ways that can later be incorporated into a full device.

The term molecular electrocatalysts broadly defines a category of homogenous catalysts, often organometallic, that require access to a reduced or oxidized state prior to observable catalysis. This type of catalysis is particularly well suited for kinetically difficult transformations for which either reduction or oxidation represents a limiting factor. The hydrogen evolution reaction (HER), oxygen evolution reaction (OER), and carbon dioxide reduction are the most actively studied of these reactions. While both heterogeneous and homogeneous (both organic and inorganic) approaches have been investigated, this introduction will focus on the homogenous approach of metal complexes.

---

*Portions of this chapter have been published elsewhere:
Williams, O. M.; Cowley, A. H.; Rose, M. J. *Dalton Trans.* **2015**, *44* (29), 13017–13029.
OMW Performed the experiments. OMW, AHC, and MJR Designed the experiments and drafted the manuscript.

2.1.1 Homogeneous Proton Reduction Electrocatalysts

In the hydrogen evolution reaction, two protons and two electrons are combined to produce hydrogen. This mechanistically simple reaction can nonetheless follow a variety of pathways in organometallic catalysis. Generally, a metal complex is reduced and then protonated at a vacant coordination site to form a metal hydride species. This species can then release hydrogen through either protonation and release of H_2 gas or through the homolytic cleavage of to the M – H bond in the presence of another metal hydride complex. This basic process is outlined in Scheme 4.

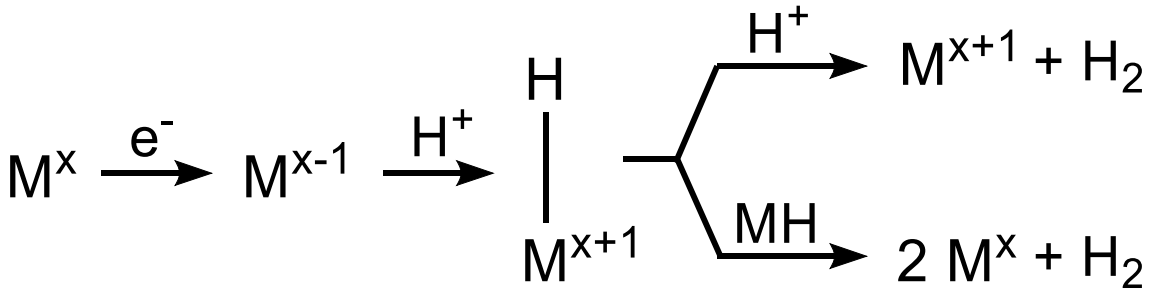

Scheme 4. The generally accepted mechanism for proton reduction involves reduction to a nucleophilic metal species in a low oxidation state, followed by protonation to form a metal hydride species, and release of hydrogen by either protonation and heterolytic cleavage of the metal-hydrogen bond or homolytic cleavage in the presence of another metal hydride complex.

There are a large number of HER electrocatalysts based on transition metal complexes. In favor of lowering cost in comparison to noble metal electrocatalysts, many of these focus on the development of cheaper organometallics of cobalt, nickel, and iron.[66,67] There is a wide body of research on these complexes, with strategies to increase activity, stability in aqueous media, heterogeneous tethering, and incorporation into

photosensitizers. While a full review of these techniques will not be conducted, several important advances and the salient features they utilize will be outlined below, with a heavy emphasis on the study of cobaloximes and other cobalt based complexes.

Both iron and nickel complexes have been used as small molecule electrocatalysts for proton reduction. Iron electrocatalysts have typically mimiced the structure of natural hydrogenase enzymes based on iron-iron, iron-nickel, or mono-iron active sites.[68,69] Recently single metal center iron complexes with strong electron withdrawn pentafluorophenyl groups have been utilized as an HER electrocatalyst.[70] In this case, the fluorinated iron diglyoxime[$Fe(dArFgBF_2)_2(py)_2$], through backbone tuning permitted a remarkable change in the $Fe^{II/I}$ reduction potential, while retaining an analogous catalytic cycle. The strong inductive electronics of the ligand backbone allow for a more readily accessible Fe(I) state which can form the prerequisite metal hydride species. The most impressive of nickel catalysts is the P_2N-Ni(II) complex devised by DuBois and coworkers.[71] In this work, rational ligand design allowed for a large enhancement of catalytic activity with a catalytic rate constant in excess of 100,000 s^{-1}. This shows the validity of the "proton relay" strategy, in which a pendant base is proximal (but not bound) to the metal center. Furthermore, the ability to tune the basicity of the amine through inductive effects was shown in a succession of P_2N_2-Ni(II) catalysts with a variety of aryl substituents.[72]

While nickel and iron are utilized most widely in nature as proton reduction catalytic centers, a large body of work in small molecule electrocatalysis focuses on cobalt based complexes. In early work by Fisher and Eisenberg, cobalt and nickel tetraazomacrocycles were investigated for their electrocatalytic capability for proton and carbon dioxide reduction.[73] However, the most widely studied catalysts are macrocyclic cobalt complexes with imine or oxime based donor ligands.

Cobaloximes herein collectively include those compounds with the following features: *i)* cobalt metal center in the +2 or +3 oxidation state, *ii)* macrocyclic equatorial ligation by oxime or imine based donors, and *iii)* labile axial coordination ligands. The ligating oxime and imine moieties can be linked by hydrogen, aliphatic, or BF_2/BR_2 bridges as seen in Figure 7. The mechanism of HER catalysis by cobaloximes has been investigated by a wide variety of methods, including electrochemistry,[74–77] density functional theory,[78–80] electron paramagnetic spectroscopy,[81] and photophysical techniques.[82,83] Generally, the catalysis can follow one of the two cycles described above – bimolecular heterolytic or unimolecular homolytic cleavage. This cycle is further complicated by the ability to access both a singly reduced and doubly reduced states in several cobaloximes. Thus, either Co^{I} or a nominally Co^{0} compound can undergo protonation to form the Co^{III} or Co^{II} hydride complexes, respectively. Possible proton reduction mechanisms are outlined in Figure 8.

Much of the research among cobaloximes can be traced back to two complexes based on dimethyl and diphenyl glyoxime ligands. Synthesized originally by Schrauzer

and Espenson,[84,85] these complexes attracted attention as electrocatalysts following seminal work concurrently published in 2005 by Peters, and Fontecave and Artero.[74,75] In these early reports, catalysis was found to occur in acidic organic electrolytes after reaching the Co^{I} oxidation state. In 2005, Hu *et al.* reported the electrocatalytic reduction of protons to hydrogen by fluoroborate-bridged cobaloximes $Co(dmgBF_2)_2(MeCN)_2$ and $Co(dpgBF_2)_2(MeCN)_2$.[74] The electron withdrawing nature of the phenyl groups in compound $Co(dpgBF_2)_2(MeCN)_2$ resulted in an anodic shift of the $Co^{II/I}$ redox couple by 250 mV, reducing the overpotential of catalysis. In the same year, Razavet *et al.* reported the electrocatalytic abilities of proton bridged cobaloximes and studied the effects of a variety of para-substituted pyridine axial ligands.[75] Through this, they found that incorporating electron donating groups in the axial ligands can cause a large enhancement in the catalytic rate without drastically affecting the $Co^{II/I}$ reduction potential. Through simulations, it was determined that protonation of a metal hydride and the heterolytic cleavage of the metal hydride bond represented the limiting step in the catalytic mechanism. The electrochemical results of these and other similar cobaloxime complexes are summarized in Table 2.

Later work by Baffert *et al.* showed that $Co(dmgBF_2)_2L_2$ had two redox peaks in the cyclic voltamogram.[77] It was found that with an appropriate choice of acid, catalysis could be affected at either of these redox couples. The second of these was proposed to be a ligand based redox event rather than a formal Co^{0} complex. Further work done by Hu *et al.* investigated cobaloxime complexes with aliphatic linkers highlighting the effect of

sequential additions of electron withdrawing phenyl groups.[76] It was shown that while these groups did shift the $Co^{II/I}$ reduction potential to more positive potentials, this resulted in a concomitant reduction in catalytic activity. Furthermore, in this report a Co^{I} compound was isolated, namely $[Na(12\text{-crown-}4)_2][Co(dpgBF_2)_2(MeCN)]$ showing the five coordinate nature of this catalytic intermediate that provides a site for proton activation. In the cyclic voltammogram, a reversible peak was found after the catalytic peak of $Co(dmgBF_2)_2(MeCN)_2$, which was tentatively assigned as a stable metal hydride species (i.e. Co^{III}-H/Co^{II}-H redox couple).

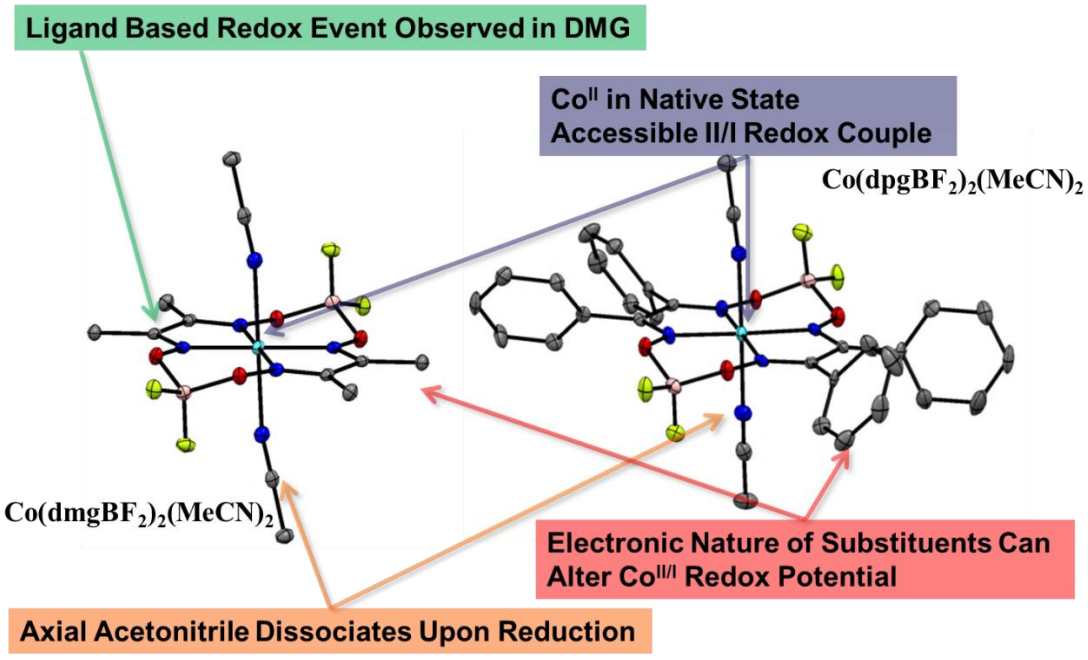

Figure 7. X-ray crystal structures of the common cobaloximes $Co(dmgBF_2)_2(MeCN)_2$ and $Co(dpgBF_2)_2(MeCN)_2$.[76,81]

Many reports have probed the electronic structure of cobaloximes and used density functional theory and photophysical techniques to gain insights into the mechanism of proton reduction. Of crucial importance to the design of more reactive electrocatalysts is an understanding of the predominant catalytic mechanisms, whether they be hemolytic or heterolytic and through which oxidation states they are likely to proceed. The vast majority of these reports have focused on the basic case of $Co(dmgBF_2)_2L_2$ due to its ease of preparation, stability, small relative size, and well known characteristics.

In 2010, Dempsey *et al.* probed the mechanism and kinetics of hydrogen evolution using photophysical techniques.[82,83] In these, a laser flash-quench mechanism, was used to extract rate constants for electron transfer of reduced cobaloxime species. In an experiment of this type, photoexcited $[Ru(bpy)_3]^{2+}$ is quenched by methyl viologen ($MV^{2+} \rightarrow MV^{\bullet -}$) which can then reduce the cobaloxime species, which then re-oxidizes through a variety of pathways. The transient absorption spectra taken between 250 nanoseconds and 50 microseconds after excitation were then fit to obtain electron transfer kinetics data. These data showed that the $Co^{III/II}$ redox rate constant is between 9.5×10^{-8} and 2.6 × 10-5 M^{-1} s^{-1}, while that for the $Co^{II/I}$ redox couple is on the order of 1.2×10^5 M^{-1} s^{-1}, or roughly ten orders of magnitude faster. These data indicate that heterolytic cleavage of Co^{III}-H species to form hydrogen and Co^{III} would be extremely unfavorable in the catalytic cycle due to the slow kinetics of re-reducing the putative Co^{III} species. This would suggest that either reduction of Co^{III}-H to Co^{II}-H or homolytic, bimolecular cleavage of Co^{III}-H species would represent dominant catalytic mechanisms. Further work was done on reduced cobaloxime

species using a photogenerated acid source (bromo-naphthol) to probe the proton transfer processes of the reaction.[83] These studies showed that the reduction of Co^{III}-H complexes to Co^{II}-H complexes is a facile process, with a rate constant of 9.2×10^6 M^{-1} s^{-1}, supporting the assertion that a metal hydride complex is further reduced prior to heterolytic cleavage and release of hydrogen.

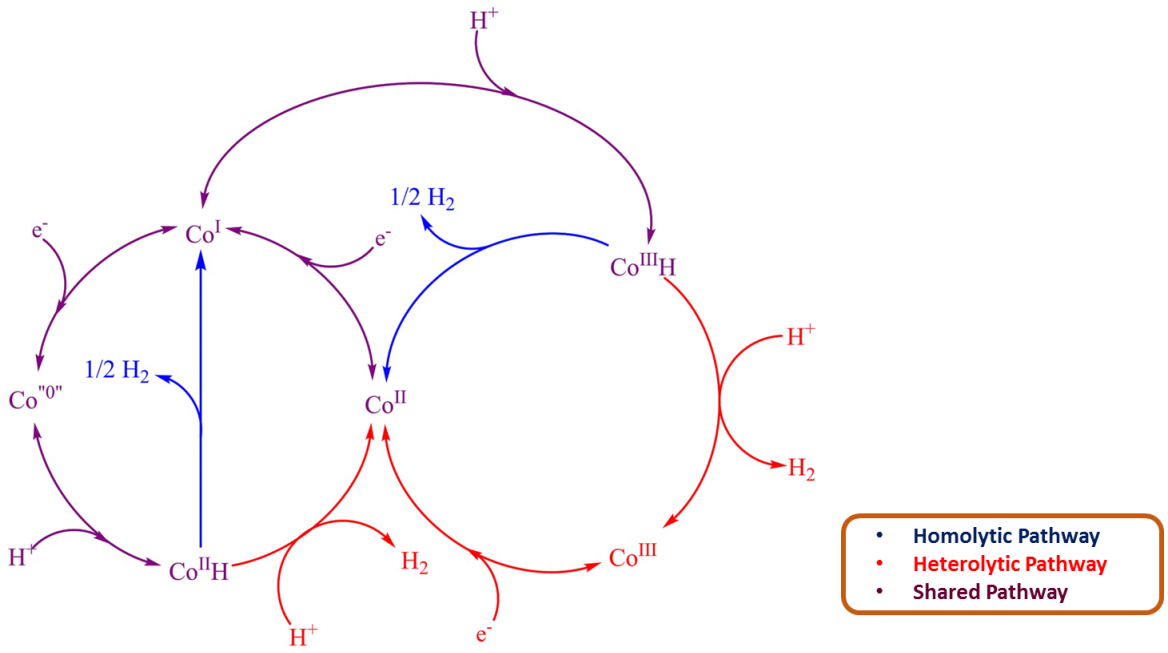

Figure 8. Possible mechanistic cycles for Co^{II} based hydrogen evolution reactions.

In order to understand the possibility of bimolecular hydrogen release mechanisms, several papers have investigated the use of bimetallic cobaloxime complexes in the HER. It was hypothesized that if a bimolecular mechanism is predominant, the close proximity and increased likelihood of collision among tethered molecules should increase the rate constants in these complexes. In work by Valdez *et al.* an ocamethylene linker connected

two cobaloxime based catalytic centers (see Figure 9, left).[86] This activity of this catalyst was compared to mononuclear congeners, showing little enhancement of activity. Other reports on a $[BO_4]^{2-}$ linked electrocatalyst (Figure 9 right) showed an increase in the overpotential of the catalysis, although a direct comparison was difficult due to electron communication between the cobalt metal centers.[87] These results indicate that bimolecular homolytic release of hydrogen is an unlikely reaction mechanism. Thus, the most likely catalytic cycle involves the heterolytic cleavage of a Co^{II}-H complex to release hydrogen.

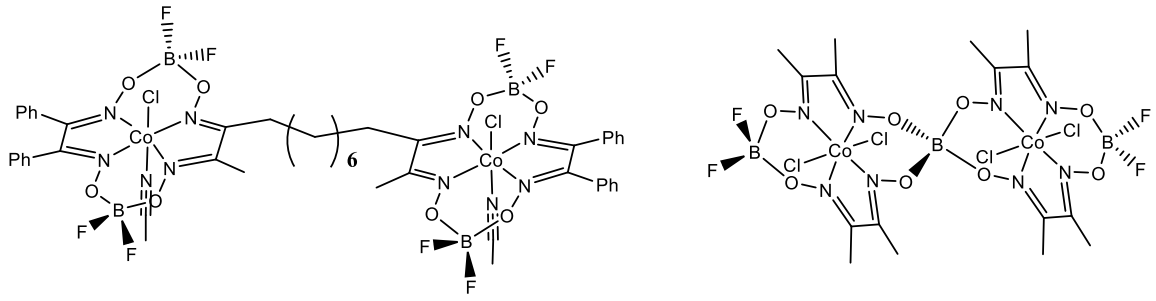

Figure 9. Literature examples of dinuclear cobaloxime based complexes used to test the homolytic cleavage mechanistic pathway in the hydrogen evolution reaction.[86,87]

The ubiquity and robustness of cobaloximes lend to their use in a wide variety of studies. Cobaloximes have also been incorporated into heterogeneous systems such as glassy carbon, nickel oxide, carbon nanotubes, and gallium phosphide substrates.[88–92] Furthermore, cobaloximes have been explored in conjunction with homogeneous photosensitizers, as components in aqueous systems, as a functional catalyst on vesicle membrane surfaces, and used as part of an artificial hydrogenase in a hybrid S*w*Mb system.[93–101] Moreover, increasingly elaborate ligand designs have been devised and

studied. However, only marginal improvements over the most basic complexes have been realized.[102]

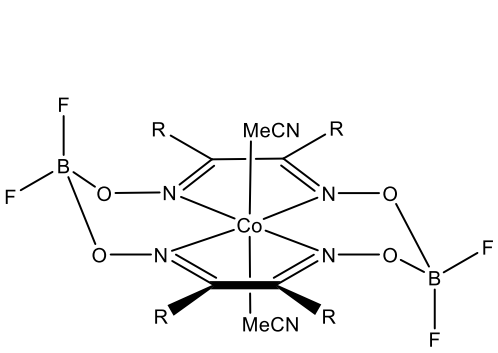

R = Me; Co(dmgBF$_2$)$_2$(MeCN)$_2$
R = Ph; Co(dpgBF$_2$)$_2$(MeCN)$_2$

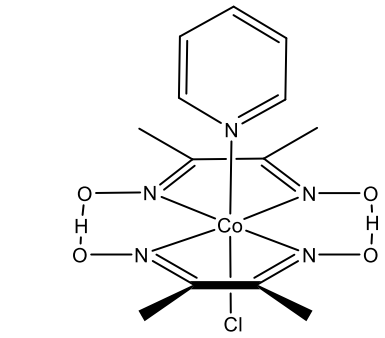

Co(dmgH)$_2$(py)Cl

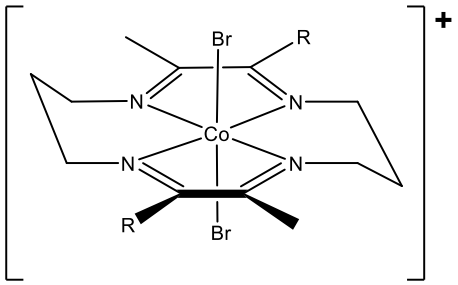

R = Me; [Co(Tim^{Me})$_2$Br$_2$]
R = Ph; [Co(Tim^{Me,Ph})$_2$Br$_2$]

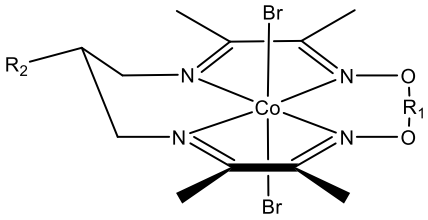

R$_1$ = H, R$_2$ = H; Co(DO)(DOH)pnBr$_2$
R$_1$ = H, R$_2$ = OH; Co(DO)(DOH)OH-pnBr$_2$
R$_1$ = BF$_2$, R$_2$ = H; Co((DO)$_2$BF$_2$)pnBr$_2$

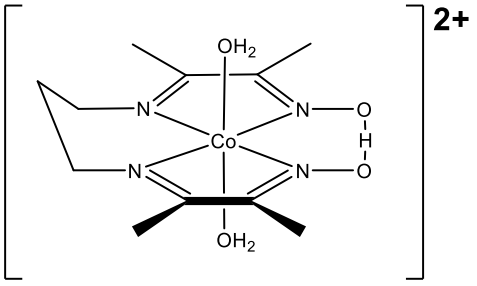

[Co((DO)(DOH)pn(OH$_2$)$_2$]

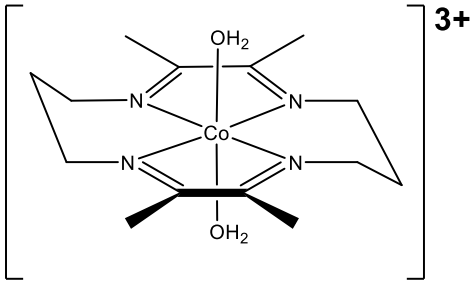

[Co(Tim^{Me})$_2$(OH$_2$)$_2$]

Figure 10. A selection of cobaloxime based complexes studied in the literature.

Table 2. Representative results from bulk electrolysis experiments of various homogeneous transition metal carbon dioxide reduction electrocatalysts. Note: All potentials are reported versus the standard calomel electrode with the following corrections being applied when necessary: $E_{Fc/Fc+} = E_{SCE} - 0.5$; $E_{NHE} = E_{SCE} + 0.25$; $E_{Ag/AgCl} = E_{SCE} + 0.05$.

Catalyst	Potential	TOF(N)	FY		Experimental Conditions	Reference
$Co(dmgBF_2)_2(MeCN)_2$		-0.72	20	~100%	0.5 mM Catalyst; 45 mM TFA; MeCN	Peters[74]
$Co(dpgBF_2)_2(MeCN)_2$		-0.37	11	90%	0.38 mM Catalyst; 7.5 mM HCl; MeCN	Peters[74]
$Co(dmgH)_2(py)Cl$		-0.85	40	85-100%	1.0 mM Catalyst; 200 mM $Et_3NH(BF_4)$; DCE	Fontecave[75]
$[Co(Tim^{Me})_2Br_2]Br$		-0.58	10	90%	0.9 mM Catalyst; 21 mM TsOH; MeCN	Peters[76]
$[Co(Tim^{Me,Ph})_2Br_2]Br$		-0.48	<2	20%	0.9 mM Catalyst; 20 mM HBF_4; MeCN	Peters[76]
$Co(DO)(DOH)pnBr_2$		-0.28	13	92%	0.5 mM Catalyst; 50 mM *p*-$CN(C_6H_4)NH_3(BF_4)$; MeCN	Fontecave[103]
$Co((DO)_2BF_2)pnBr_2$		-0.32	6.6	100%	0.5 mM Catalyst; 50 mM *p*-$CN(C_6H_4)NH_3(BF_4)$; MeCN	Fontecave[103]
$[Co((DO)(DOH)pn(OH_2)_2][ClO4]_2$		-0.93	12	81%	0.3 mM Catalyst; 0.1 M phosphate buffer (pH = 2.2) in water	Peters[98]
$Co(DO)(DOH)OH\text{-}pnBr_2$		-0.93	9	80%	0.3 mM Catalyst; 0.1 M phosphate buffer (pH = 2.2) in water	Peters[98]
$[Co(Tim^{Me})_2(OH_2)_2][ClO_4]_3$		-0.93	1	30%	0.3 mM Catalyst; 0.1 M phosphate buffer (pH = 2.2) in water	Peters[98]

2.1.2 Cobalt Based CO_2 Reduction Electrocatalysts

Carbon dioxide reduction is a much more complex catalytic process than that of the hydrogen evolution reaction. Due to the close values for the thermodynamic potential of many C1 products (see Table 3), the selectivity of the transformation is important. Indeed, it has been shown on heterogeneous catalysts (specifically copper), that a wide variety of higher order (C2 – C4) products can be produced under electrolysis. Typically, homogeneous catalysts focus on the selective reduction of CO_2 to CO (and sometimes formate), with the exception of pyridinium, which has been implicated in catalyzing the $CO_2 \rightarrow CH_3OH$ reaction.[104] As electrolysis is greatly enhanced in the presence of protons, in addition to competing CO_2 reduction products, a desirable catalyst will need to be selective for the activation of CO_2 over that of H^+.

Table 3. Thermodynamic reduction potentials for two, four, six, and eight electron carbon dioxide reduction reactions for C1 products. The standard reduction potential for a single electron reduction of CO_2 is given as a reference to indicate the high kinetic barrier for these reactions.

Carbon Dioxide Reduction Reaction	Standard Potential (V *vs.* NHE)
$CO_2 + 2H^+ + 2e^- \rightarrow CO + H_2O$	$E^0 = -0.53$ V
$CO_2 + 2H^+ + 2e^- \rightarrow HCO_2H$	$E^0 = -0.61$ V
$CO_2 + 4H^+ + 4e^- \rightarrow H_2CO + H_2O$	$E^0 = -0.48$ V
$CO_2 + 6H^+ + 6e^- \rightarrow CH_3OH + H_2O$	$E^0 = -0.38$ V
$CO_2 + 8H^+ + 8e^- \rightarrow CH_4 + 2H_2O$	$E^0 = -0.24$ V
$CO_2 + e^- \rightarrow CO_2^{\bullet -}$	$E^0 = -1.90$ V

In molecular transition metal systems, there are selected reports of carbon dioxide reduction using cobalt and nickel tetraazomacrocycles, iron porphyrins, low-valent bipyridine complexes and polydentate phosphine complexes of precious metals (such as

palladium).[73,105–115] While these catalysts represent remarkable advances in homogeneous carbon dioxide reduction, as a whole, they suffer from the following drawbacks: high overpotential (η), low turnover frequency (TOF), or the use of expensive rare metals (see Table 4). For example, $[Pd(etpC)PPh_3]^+$ has been shown to have high activity (TON = 154), at low overpotentials (-0.75 V *vs.* SCE), albeit with incorporation of a rare metal.[113] Alternatively, the iron-porphyrin complex [(TPP)Fe(Cl)] utilizes the most earth abundant transition metal, but exhibits a more negative operating potential (-1.7 V vs. SCE) and only moderate activity (TOF ≈ 35 hr^{-1}).[116]

Another major issue is establishing selectivity for proton-assisted CO_2 reduction versus parasitic H_2 generation. The primary obstacle involves avoidance of the premature conversion of a low-valent transition metal ($M^{I/0}$) into the corresponding metal hydrides ($M^{II/III}$–H), which demonstrate a strong preference for H_2 generation pathways. One of the preferred routes involves the direct attack of CO_2 by a low-valent metal, thus forming a $M^{II/III}$–CO_2 intermediate that can disproportionate in the presence of protons to generate formic acid (HCO_2H) or a water/gas mixture ($CO + H_2O$). However, the lack of an overall design strategy specific to CO_2 reduction is a major limitation in improving issues facing these catalytic systems.

A widely investigated carbon dioxide reduction electrocatalyst is that of the Re(bipy) system. Initially reported by Lehn *et al.* in 1983, the complex consists of a rhenium(II) catalytic metal center supported by a bipyridine (bpy) ligand, with a halide and

three carbonyl ligands completing the octahedral coordination environment.[117] In these initial studies, $Re(bipy)(CO)_3Cl$ was found to catalyze the reduction of CO_2 to CO at -1.25 V *vs.* NHE with a Faradaic efficiency of 90 – 98% and no parasitic hydrogen production.[110] Crucially, in this system, the bipyridine moiety has been implicated as reductive site in the overall two electron reduction.[118,119] From this, we can infer that the presence of a proximal electron sink is a crucial part of making a catalyst more selective for CO_2 over H^+ activation. Further work on bipyridine systems showed the importance of preventing dimerization as a deactivation pathway as well as the introduction of more cost efficient metals, primarily manganese.[112]

Conversely, little recent work has focused on cobalt based complexes that are implicated in CO_2 reduction. One of the first CO_2 electrocatalysts to be discovered, however, were those of cobalt tetraazomacrocycles, first reported by Fisher and Eisenberg in 1980.[73] These studies found that cobalt tetraazamacrocycles (*ca.* -1.5 V vs. SCE) showed moderate activity (7.8 – 9 turnovers per hour) at high overpotentials (electrolysis at -1.5 V *vs.* SCE) resulting in roughly equal amounts of H_2 and CO production and Faradaic yields of greater than 90 percent for this mixture of products.

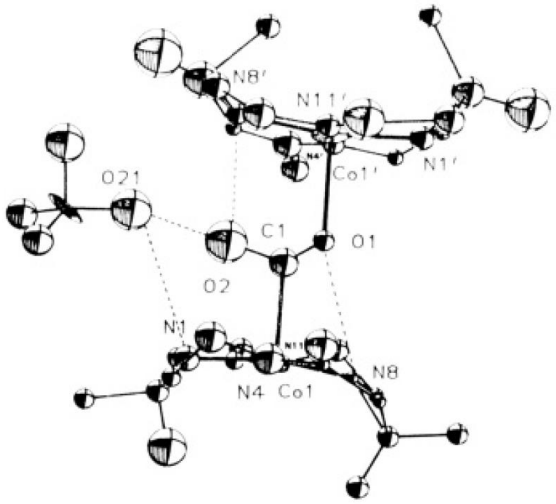

Figure 11. X-ray crystal structure showing the CO_2 bound cobalt tetraazamacrocycle complex.[120]

Further work conducted in the late 1980's and 1990's, primarily by Fujita and Creutz examined the mechanism of this reduction.[121–124] Prior to the spectroscopic work investigating reaction mechanisms, however, Gangi and Durand reported the reversible binding of CO_2 to cobalt metal centers upon electrochemical reduction to the Co^I state, similar to protonation commonly observed in the HER.[125] This work was later confirmed by chemical reductions in which spectroscopic and crystallographic characterization showed a transfer of charge from the Co^I nucleophile to CO_2.[120] Furthermore, in the crystal structure (Figure 11), it was shown that a second cobalt macrocycle coordinates to the oxygen atom of the carboxylate adduct, stabilizing the intermediate. This Lewis acid stabilization was corroborated by Schmidt et al. wherein lithium based electrolytes increased the binding affinity between cobalt and carbon dioxide.[126]

From these works, a reasonable catalytic cycle can be drawn that is analogous to that of proton reduction (Figure 12). In this cycle, an electrochemically reduced cobalt center can reversibly bind CO_2. This Co-carboxylate adduct can then undergo protonation to release water and CO, regenerating a Co^{III} species that can undergo further reductions to continue the catalytic cycle. In aprotic solvents, this cycle favors reaction with another equivalent of CO_2, releasing CO and CO_3^{2-} in the cycle.[127,128] Several other cobalt based complexes have been used for CO_2 reduction, including those supported by Salen, poly-pyridine, and pincer ligands.[129–132] Similarly to the case of bipyridine based catalysts, in work by Lacy *et al.* the redox non-innocence of the ligand was implicated in achieving selectivity for CO_2 reduction without parasitic hydrogen generation.[131] Because of this and and other work that implicates redox non-innocence in CO_2 selective electrocatalysts, we were interested in appending a redox active ligand to the framework of a common hydrogen evolution reaction electrocatalysts in an attempt to control reactivity and selectively favor CO_2 over H^+ reduction.

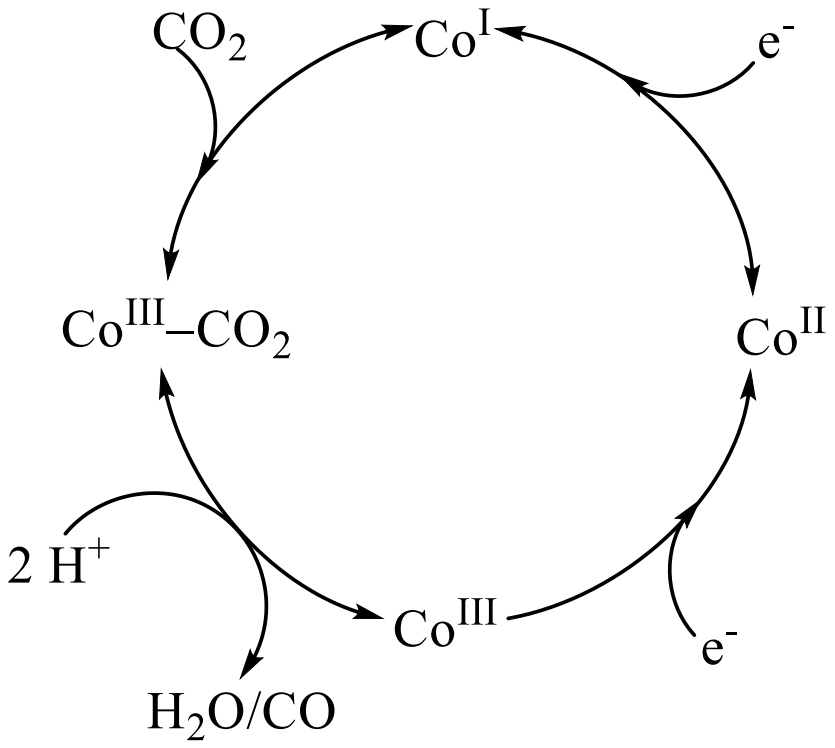

Figure 12. Proposed catalytic cycle for the Co^{II} mediated reduction of CO_2 to CO. Following a one electron reduction, the Co^{I} metal center acts as a nucleophile and can therefore reduce CO_2. This carboxylate adduct can then be protonated to release both water and CO, thus generating a Co^{III} species that can be re-reduced to the active compound.

Table 4. Representative results from bulk electrolysis experiments of various homogeneous transition metal carbon dioxide reduction electrocatalysts. Note: All potentials are reported versus the standard calomel electrode with the following corrections being applied when necessary: $E_{Fc/Fc+} = E_{SCE} - 0.5$; $E_{NHE} = E_{SCE} + 0.25$; $E_{Ag/AgCl} = E_{SCE} + 0.05$. Appropriate experimental conditions are presented (GC = glassy carbon, VC = vitreous carbon). Turnover numbers (TON) rather than turnover frequencies (TOF) are reported when the TOF was not calculated. *This species was found to be an adsorbed active catalyst. Increasing concentrations of the catalyst resulted in the same rate, thus indicating saturation of the electrode surface.[73,105–115]

Catalyst	**Potential**	**TOF(N)**	**FY**	**Exp. Cond.**
Co/Ni Tetraazamacrocycles	-1.3 → -1.6	1 → 4.5	44 → 98	H_2O/MeCN; Hg WE
Ni^{II}(cyclam)	-1.25	1,000*	95+	H_2O; Hg WE
Ni^{II}(cyclam)	-1.45	1.1	~90	H_2O/MeCN; GC WE
TPPFeCl	-1.7	18	80 → 100	DMF/24 mM Mg^{2+}; Hg WE
TPPFeCl	-1.7	30-40	>96	DMF/0.55 M CF_3CH_2OH; Hg WE
$Re(bipy)(CO)_3Cl$	-1.5	21	98	DMF/H_2O; GC WE
$[Ru(bipy)_2(CO)_2]^{2+}$	-1.5	(44)	Variable	DMF/H_2O; Hg WE
Cis-$[Os(bipy)_2(CO)H]^+$	-1.4 → -1.6	(10)	90	MeCN/Trace H_2O; Pt Mesh WE
$Mn(bipy)(CO)_3Br$	-1.7	3.25	~100	MeCN/H_2O; VC WE
$[Pd(triphos)(PR_3)]^+$	-0.8 → -1.1	(3→130)	9 → 85	DMF/HBF_4; VC WE
$[Cu_2(\mu\text{-}PPh_2bipy)_2(MeCN)_2]^{2+}$	-1.65	2	~100	MeCN; Pt WE
$[HFe_4N(CO)_{12}]^-$	-1.25	Not reported	Not reported	MeCN/PhCOOH; VC,GC WE

2.1.3 Bis(imino)acenaphthene

Bis(imino)acenaphthene (BIAN) ligands have proved to be useful for a variety of catalytic systems, that range from C–C bond coupling to polymerization.[133] In particular, the naphthanlene backbone of this ligand facilitates a rich redox chemistry.[134] Moreover, the bis(diisopropyl)phenylimino ligand (dpp-BIAN) is capable of undergoing four successive one electron reductions. In these chemical reductions, it was found that the N-C-C-N fragment of the BIAN ligand can accept two electrons while a further two can be incorporated in the naphthalene appendage. The use of BIAN in metal complexes has shown that genuine redox isomerism can occur between the metal and ligand support.[135,136] Because of this, we were interested in incorporating such a ligand into a electrocatalytic complex (see Figure 13) in order to provide a proximal electron sink.

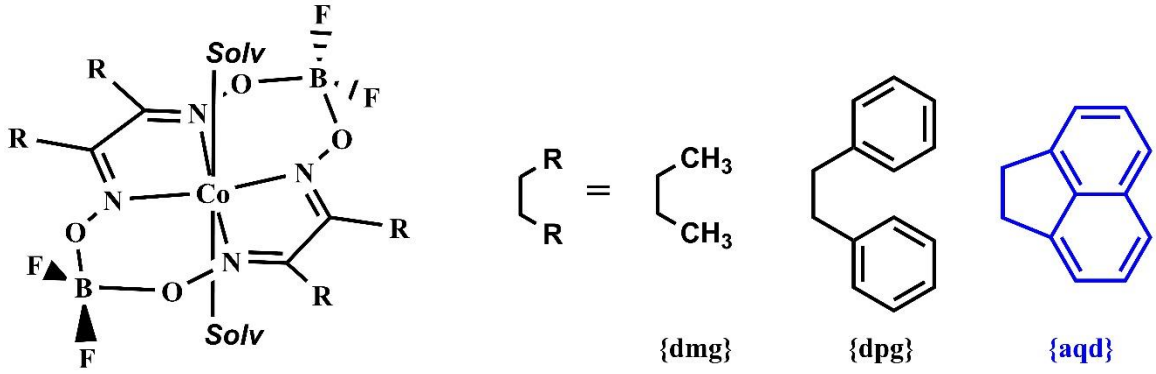

Figure 13. Molecular structures of commonly studied dimethyl and diphenyl cobaloximes in comparison with the naphthalene appended cobaloxime studied herein ($Co(aqdBF_2)_2L_2$, **1**).

2.2 Results and Discussion

2.2.1 Electrochemistry

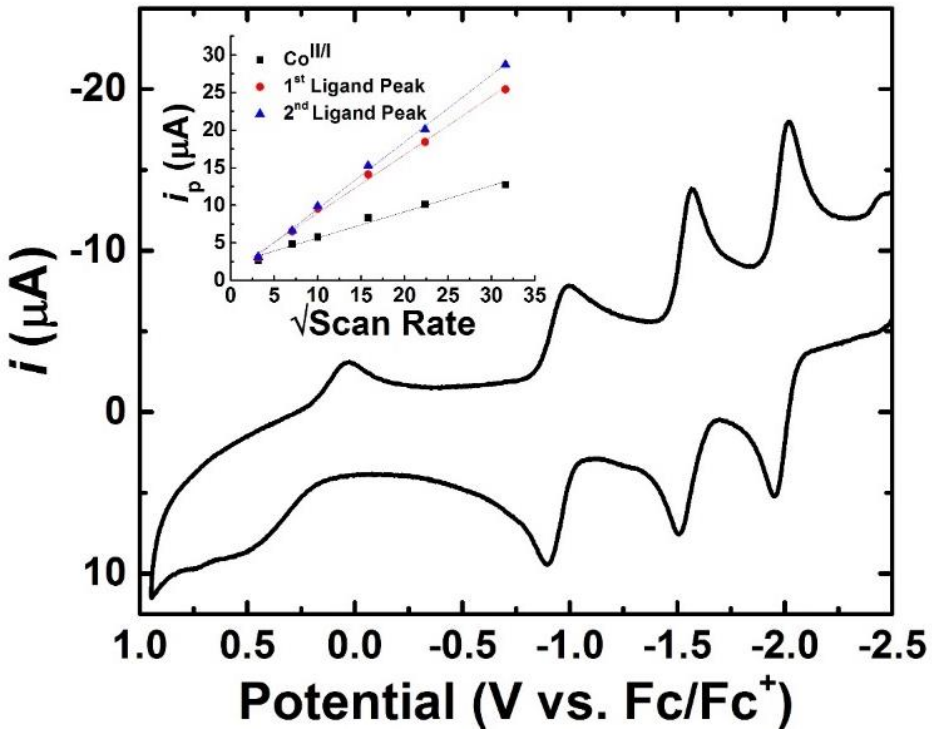

Figure 14. Cyclic voltammetry of $Co(aqdBF_2)_2$ in nitrogen saturated 0.1 M $[NBu_4][PF_6]$ in DMF solution. Experimental conditions: 100 mV s^{-1}; WE: GC, RE: Ag QRE (standardized to an external ferrocene standard), CE: Pt. Inset: scan rate dependence for each cathodic feature, indicating homogeneous processes in each case.

The cyclic voltammogram for the compound $Co(aqdBF_2)_2L_2$ (**1**) in DMF solution is displayed in Figure 14. This complex exhibits a reversible feature at -0.95 V *vs.* Fc/Fc^+ ($\Delta E_p \approx 100$ mV), thereby generating $[Co(aqdBF_2)_2(DMF)]^-$. This response is almost identical to that of the $Co^{II/I}$ reduction potential that was reported for $[Co(dmgBF_2)_2(DMF)_2]$ ($E_{1/2} \approx -1.0$ V *vs.* Fc/Fc^+).[137] The ensuing cathodic sweep revealed two additional reversible features at -1.56 and -2.00 V *vs.* Fc/Fc^+ ($\Delta E_p = 60$ mV in both

cases). Each feature exhibits a linear increase in current with respect to √scan rate (Figure 14, inset; see Figure 15 for full CV traces), thus confirming the occurrence of homogeneous processes in each case.

As a consequence, the reduced species are formulated as $[Co(aqdBF_2)_2(DMF)]^{-}$, $[Co(aqdBF_2)_2]^{2-}$, and $[Co(aqdBF_2)_2]^{3-}$, (the reducing equivalents in the latter two complexes are absorbed by the ligand framework). Furthermore, there is an anodic, quasireversible peak that is assigned to the $Co^{III/II}$ redox couple. Due to the rich redox chemistry of this compound in comparison to its more widely studied analogs, it was possible to isolate these reduced compounds and study their structures, spectroscopy, and potential in electrocatalysis.

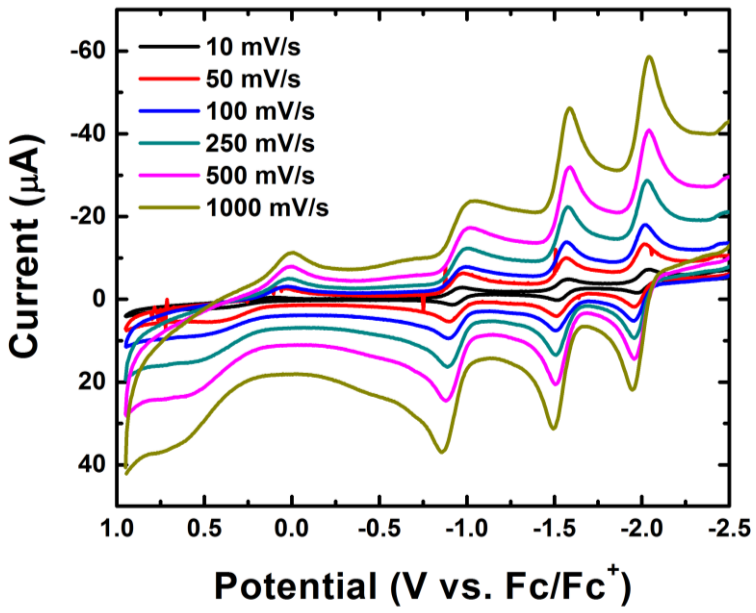

Figure 15. Independent CVs of $Co(aqdBF_2)_2$ in a DMF electrolyte at various scan rates.

2.2.2 Synthesis of Compounds

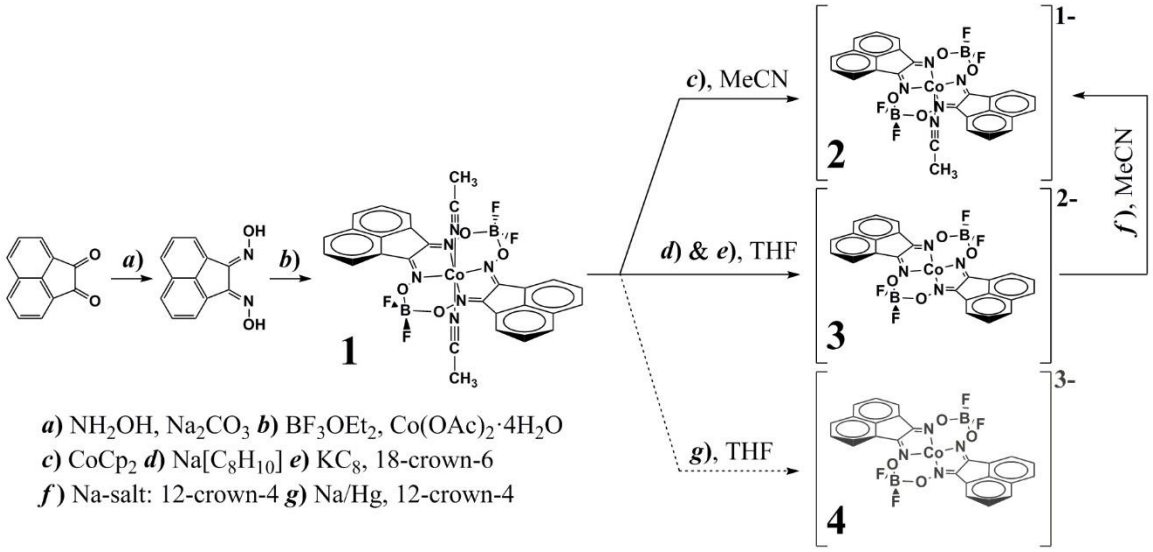

Scheme 5. Synthetic routes for the ligand $aqdH_2$, the complex $Co(aqdBF_2)_2(MeCN)_2$, and the 1, 2, and 3-electron reduced species.

To help probe this rich redox chemistry, a series of chemical reductions were performed with the objective of accessing the putative complexes that had been detected in the cathodic cyclic voltammogram. The stable, one electron reduced species was produced via the reaction of the parent cobaloxime with a near stoichiometric quantity of sodium naphthalide (1.2 equivalents, E ≈ –3.10 V *vs.* Fc/Fc^+)[138] in THF, thus yielding a stable blue-violet solution. Re-dissolution of the solid product in an MeCN solution containing excess 12-crown-4 afforded a violet colored solution. The crystalline product was isolated by vapor diffusion of Et_2O into an MeCN solution to afford the five-coordinate, square pyramidal product $[Na(12\text{-crown-}4)_2][Co(aqdBF_2)_2(MeCN)]$ (**2**). Further details are provided in the X-ray crystallographic section. The difficulties that were encountered in obtaining pure **2** in significant yields prompted a search for an alternative

method of generating the singly reduced species. Regardless of stoichiometry, cobaltocene reduction (E ≈ –1.3 V *vs.* Fc/Fc^+)[138] resulted in the generation of a purple solution in acetonitrile, which is indicative of a one electron reduction. The foregoing assignment was corroborated on the basis of single crystal XRD (Figure 25) and ^1H NMR spectroscopy (Figure 24).

The two-electron reduced species was isolated by treatment of a solution of the parent cobaloxime **1** with an excess potassium graphite (> 3 equivalents, E = –2.90 V *vs.* Fc/Fc^+)[138] in THF, thus forming a dark navy blue solution that was markedly different from the violet colored solution that had been observed for the corresponding one-electron reduced complex. Extraction of the product into a MeCN solution containing dibenzo-18-crown-6 afforded $[K(dibenzo\text{-}18\text{-}crown\text{-}6)]_2[Co(aqdBF_2)_2]$ (**3**), which features the presence of a cobalt center in a square planar geometry (*vide infra*, X-ray Crystallography Section). A similar procedure was found to be effective for the isolation of the alkyl crown congener **3** of formula $[K(18\text{-}crown\text{-}6)]_2[Co(aqdBF_2)_2]$ (**3'**). Finally, the preparation of the three-electron reduced compound (**4**) was carried out by the treatment of **1** with an excess of Na/Hg (E ≈ –2.4 V *vs.* Fc/Fc^+)[138] in a THF solution in the presence of an excess of 12-crown-4. It is important to note that the green solution is not observed in the absence of a supporting crown ether.

Overall, an evaluation of the reduction potentials and stoichiometries of the reductants that were employed failed to reveal a coherent trend regarding the isolated products (among $NaC_{10}H_8$, KC_8, Na/Hg, all of which have a reduction potential cathodic

of –2.0 V *vs.* Fc/Fc^+).[138] The $CoCp_2$ reduction clearly shows a dependence on potential since it only leads to the singly reduced product regardless of stoichiometry. Inspection of the X-ray crystal structures (*vide infra*) revealed the presence of secondary effects due to the interaction of the alkali metals with the complex that represent a determining factor in terms of the identity of the final product. For example, reduction of the parent complex with $NaC_{10}H_8$, KC_8, or Na/Hg in neat THF each generate blue solutions that are indicative of the formation of the 2-electron reduced species. However, subsequent extractions of the various alkali salts into MeCN/crown ether mixtures (to aid solubility and crystallization) produced different results. For example, dissolution of the Na salt of the 2-electron reduced blue species in an MeCN/12-crown-4 mixture caused an immediate color change from blue to violet, (which is indicative of an auto-oxidation process) and resulted in the formation of the 1-electron reduced species **2**.

By contrast, extraction of the K salt of the 2-electron reduced blue species into a MeCN solution that contained 18-crown-6 derivative retained the blue color, which subsequently proceeded to generate the authentic crystalline samples of the 2-electron reduced species **3**. Interestingly, a distinct reductive behavior was evident in THF solution that depended on the presence or absence of a crown ether. In contrast to the blue solutions that were apparent in the absence of the crown ether, the reduction of **1** with Na/Hg in a THF solution that contained 12-crown-4 resulted in the formation of a green solution, which was indicative of the presence of the 3-electron reduced species **4**. Overall, the X-ray crystal structure data revealed the presence or absence of site-specific interactions

between the crowned Na^+ or K^+ ions with the oxime-N/O or BF_2 moieties. Evidently, it is this counterion cooperativity that represents a critical factor in terms of stabilizing the reduced states during isolation. Furthermore, it is clear that careful attention must be paid to the presence (or absence) and identity of the supporting alkali-crown species.

2.2.3 Molecular Structures of Compounds Used

Ligand ($aqdH_2$).

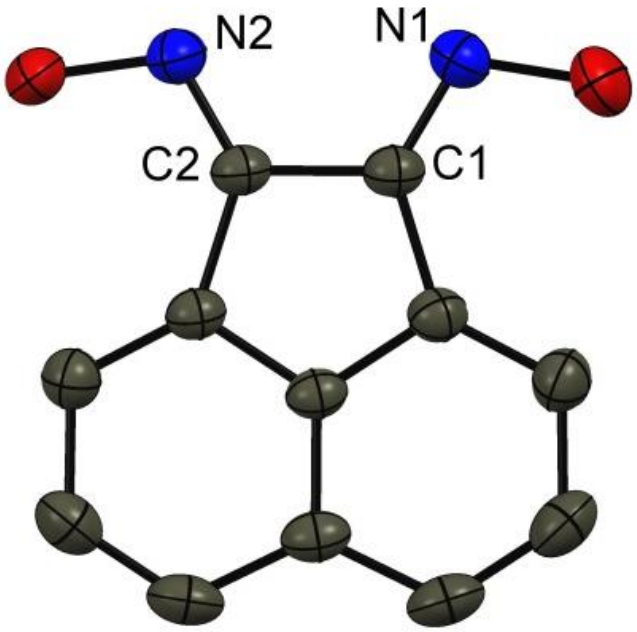

Figure 16. Thermal ellipsoid plot (50% probability) from the X-ray crystal structure of the ligand acenaphthenequinone dioxime.

The X-ray crystal structure of the parent ligand, acenaphthenequinone dioxime ($aqdH_2$, Figure 16) exhibited structural parameters that are consistent with those of other BIAN-Schiff base ligands. Moreover, the C=N bond lengths of 1.285(2) and 1.286(2) Å are consistent with the presence of double bond character and the C–C bond length of

1.502(3) Å is in agreement with the value expected for a single bond. The N1–C1–C2–N2 torsion angle of 6.6(2)° is most likely due to the constrained five membered ring of the acenaphthene framework. All other bond distances fall within the expected ranges for aromatic systems.

[Co(aqdBF$_2$)$_2$(MeCN)$_2$] (1).

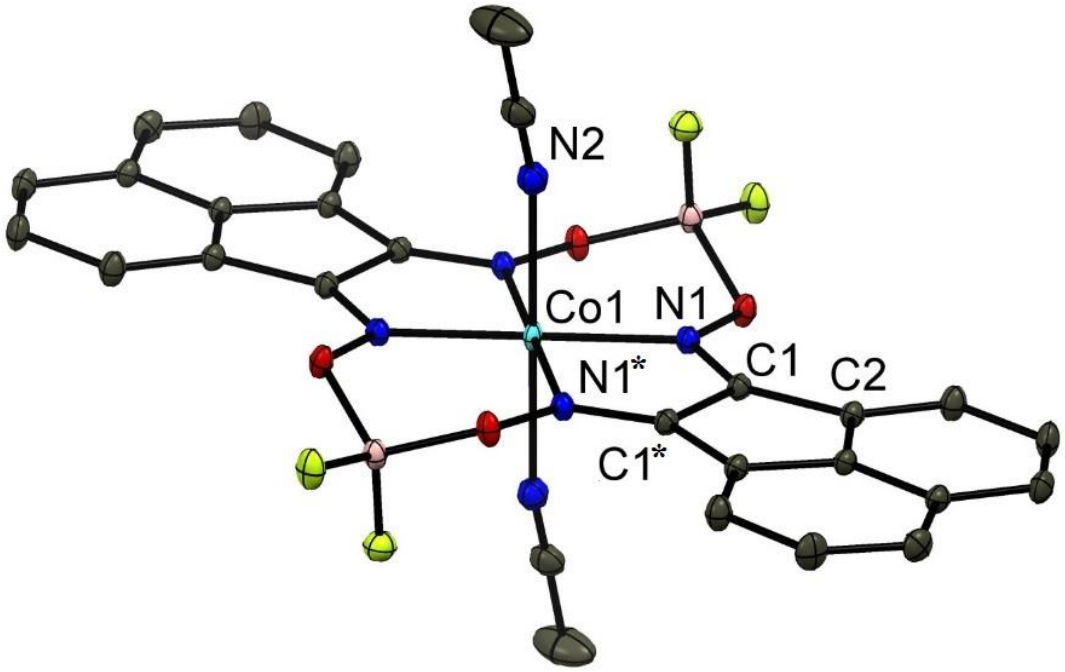

Figure 17. Thermal ellipsoid plot (50% probability) of the parent complex [Co(aqdBF$_2$)$_2$(MeCN)$_2$] (**1**). All hydrogen atoms have been omitted for clarity. Selected bond lengths (Å) and angles (°): N1–Co1, 1.8961(9); N2–Co1, 2.271(2); C1–N1, 1.293(1); C1–C1*, 1.488(2); N1–Co1–N1*, 4.66(4).

The X-ray structure of **1** (Figure 17) revealed the presence of a Co^{II} ion in a pseudo-octahedral geometry. This outcome was anticipated for a cobaloxime of this type that has been crystallized from a coordinating solvent (MeCN). Furthermore, the axial MeCN

ligands are tilted away from a linear orientation by 14.8°, and each MeCN molecule is flanked by a BF_2 bridge that is tilted up or down out of the plane of the macrocycle in order to avoid the axial ligand. The structure of the aqdBF_2 ligand of **1** is essentially planar, as evidenced by the torsion angle of 1.4(1)° for the C2–C1–N1–Co1 chain. The Co–N_{ox} bond distances of 1.896(1) Å for 1 (fourfold crystallographic symmetry) are slightly longer than those found for closely related cobaloximes [Co(dmgBF_2)$_2$(MeCN)$_2$] (1.878(1), 1.881(2) Å)[81] and [Co(dpgBF_2)$_2$(MeCN)$_2$] (1.881(3), 1.889(3) Å).[76] The foregoing results are likely to be a consequence of the expanded N=C–C=N bite angle in the fused naphthalene ring system, which results in N–Co–N angles of 84.66(4)° for aqd, versus 81.70(7)° for dmg or 81.8(1)° for dpg. The axial Co–NMeCN distances of 2.2712(2) Å are also longer than those found in the dmgBF_2 and dpgBF_2 congeners (2.253(2), 2.241(3) Å). However, the C=N and C–C bonds in the macrocycle (1.293(1) and 1.488(2) Å) are commensurate with those of the neutral ligand (1.286(2), 1.285(2) and 1.502(2) Å). Furthermore, the acene C–C bond distance in 1 (1.488(2) Å) is very close to that observed for the free ligand (1.502(2) Å), thus indicating that no electronic change or significant delocalization of charge from the cobalt(II) center to the ligand framework is observable by X-ray diffraction.

[Na(12-crown-4)$_2$][Co(aqdBF$_2$)$_2$(MeCN)] (2).

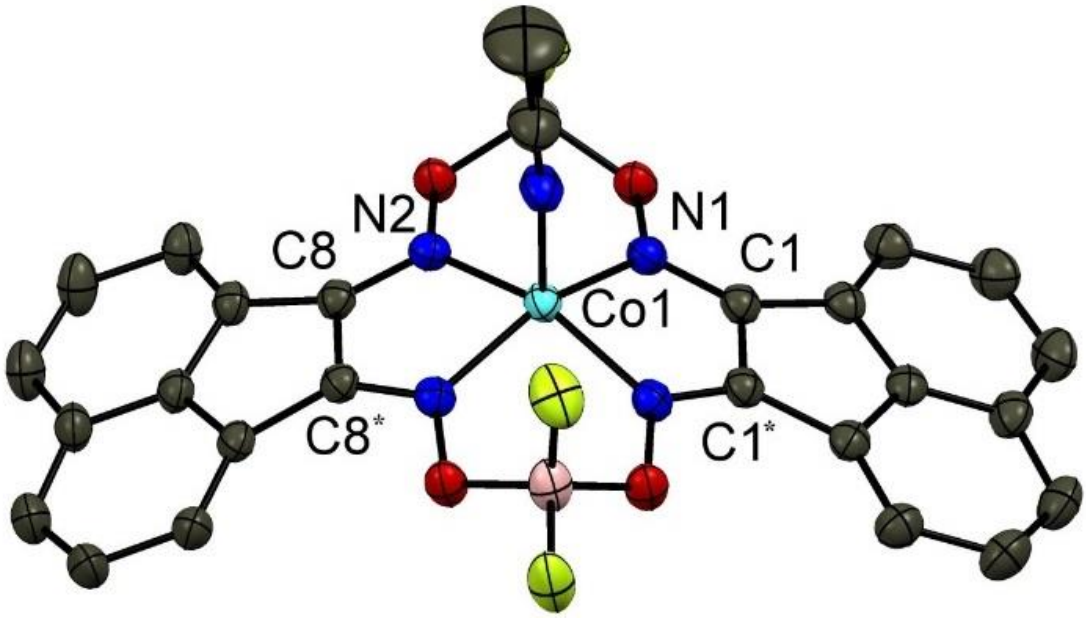

Figure 18. X-ray crystal structures of the anion $[Co^{I}(aqdBF_2)_2(MeCN)]^-$ (50% probability thermal ellipsoids). Hydrogen atoms, counterions, and solvent molecules have been omitted for clarity. Selected bond lengths (Å) and angles (°), with symmetry generated atoms are designated by an asterix (*): N1–Co1, 1.879(2); N2–Co1, 1.887(2); C1–N1, 1.311(2); C8–N2, 1.308(2); C1–C1*, 1.439(3); C8–C8*, 1.445(3).

The cobalt center in **2** adopts a square based-pyramidal structure, which effects a 0.415 Å displacement of the cobalt ion out of the equatorial plane and a significant contraction of the single axial Co–N_{MeCN} bond to 2.007(3) Å, as compared with the two axial Co–N_{MeCN} bonds (2.2714(16) Å) that were observed in the case of the parent complex. A comparison of the structural parameters of **2** with those of the reduced diphenyl (dpg) cobaloxime analog [Na(12-crown-4)$_2$][Co(aqdBF$_2$)$_2$(MeCN)] reveals that the bond lengths are very similar (N–Co_{avg} 1.851 Å ; C=N_{avg} 1.321 Å ; C–C_{avg} 1.457 Å).[76] However, within the ligand framework there is a slight contraction of the N–Co bond length (~0.016 Å), an

elongation of the N–C bond length (~0.017 Å), and a contraction of the C–C bond length (~0.040 Å) in comparison with that of **1**. The slight differences in the C–N and C–C bond distances between **1** and **2** may indicate partial delocalization of the reducing electron onto the N–C–C–N fragment. The bond lengths, however, show altered parameters when compared with that of a model one-electron reduced BIAN, namely the sodium complex of diisopropylphenyl-BIAN (dpp-BIAN). In comparison with Na-dpp-BIAN, complex **2** exhibits slightly shorter C=N (~1.310 *cf.* 1.328 Å) and slightly longer C–C (~1.448 *cf.* 1.446 Å) bond distances.[139] However, due to the significant change in the coordination environments of **1**, **2**, and [Na][dpp-BIAN] it is difficult to assign formal ligand charges and/or metal oxidation states based solely on structural data.

[K(dibenzo-18-crown-6)]$_2$[Co(aqdBF$_2$)$_2$] (3).

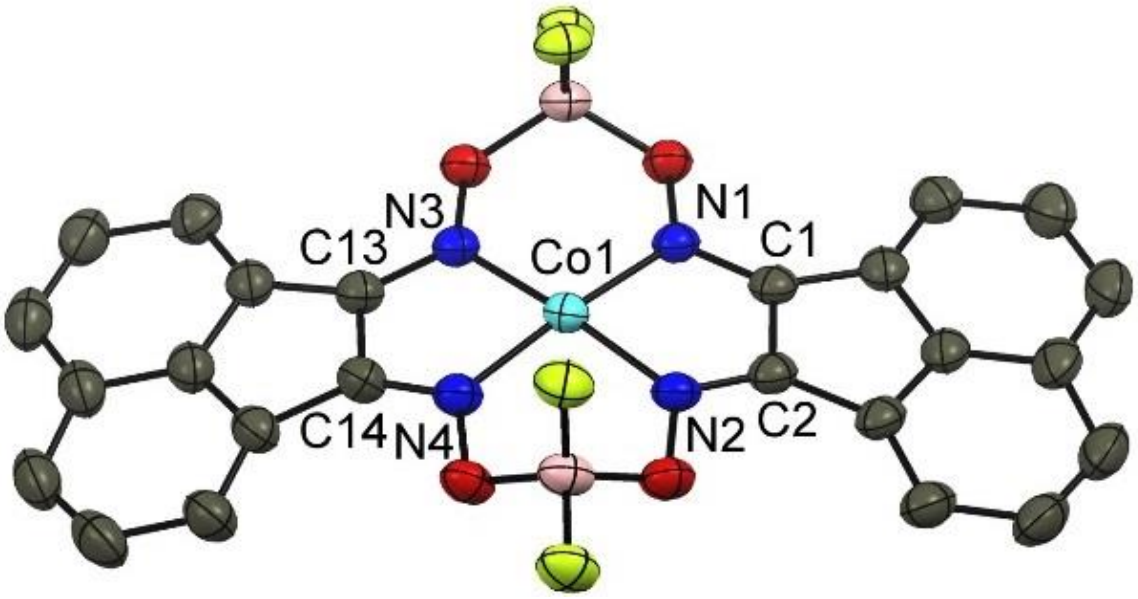

Figure 19. X-ray crystal structures of the anion $[Co^{I}(aqdBF_2)_2^{\bullet-}]^{2-}$ (dibenzo-18-crown-6 K salt), (50% probability thermal ellipsoids). Hydrogen atoms, counterions and solvent molecules have been omitted for clarity. Selected bond lengths (Å) and angles (°): N1–Co1, 1.863(2); N2–Co1, 1.862(2); N3–Co1, 1.859(2); N4–Co1, 1.854(2); C1–N1, 1.339(3); C2–N2, 1.333(4); C13–N3, 1.344(3); C14–N4, 1.335(4); C1–C2, 1.460(4); C13–C14, 1.455(4).

The structure of the doubly reduced complex, **3** (Figure 19) revealed an increase of the planarity of the entire macrocycle in comparison with that of the singly reduced (Na salt) structure (24.01 *cf.* 47.52 degrees for the mean plane angle between the naphthalene backbone units). This outcome is a consequence of the orbital overlap required for effective delocalization of the additional electron. The cobalt center in this compound adopts a square planar structure, and is accompanied by a further contraction of the N–Co bond length (~ 0.024 Å), an elongation of the N–C bond length (~ 0.030 Å), and a lengthening of the C–C bond (~ 0.012 Å) in comparison with those of the singly reduced species. Of particular note are the short contacts between the two chelated potassium cations and the

fluorine atoms (K – F = 2.621(2), 2.655(2) Å) on the BF_2 moieties (Figure 22, left). The open-face chelation of the K^+ ion by dibenzo-18-crown-6 provides coordination sites for the direct interaction of the alkali metal with the electronegative moieties on the cobalt macrocycle. In contrast, the bis-chelated nature of the sodium counterion [Na(12-crown-4)$_2$] found in **2** precluded any direct interaction between the alkali metal and the cobaloxime. As noted in the above, it can be inferred that such a direct contact with the K^+ ion in **3** (and **3'**, see below) stabilizes the reduction state of the complex thereby preventing auto-oxidation (see Figure 22).

[K(18-crown-6)]$_2$[Co(aqdBF$_2$)$_2$] (3').

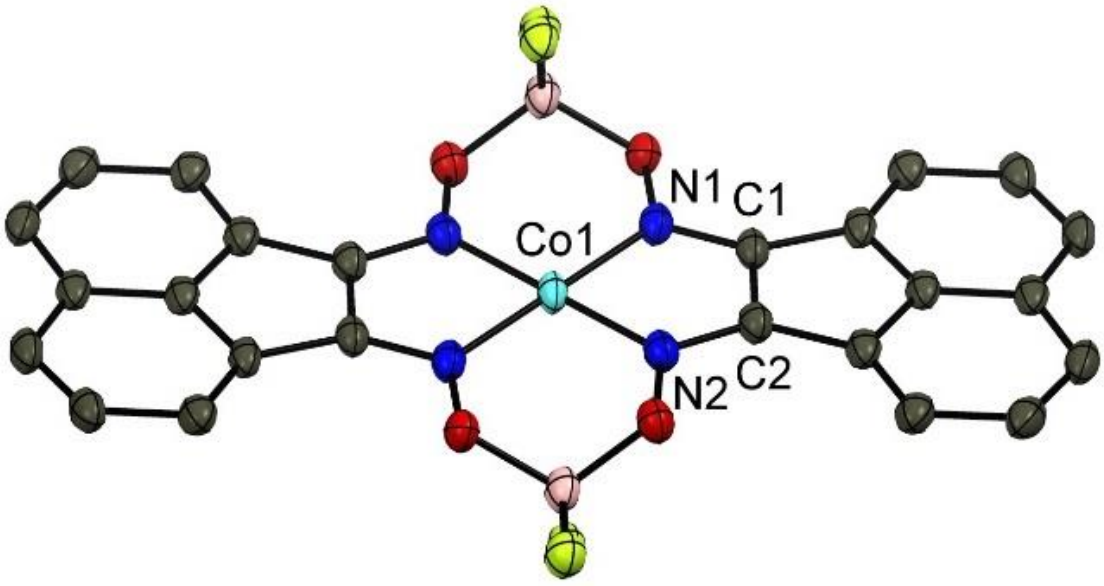

Figure 20. X-ray crystal structures of the anion $[Co^{I}(aqdBF_2)_2^{\bullet-}]^{2-}$ (18-crown-6 K salt), (50% probability thermal ellipsoids). All hydrogen atoms, counterions and solvent molecules have been omitted for clarity. Selected bond lengths (Å) and angles (°): N1–Co1, 1.847(2); N2–Co1, 1.834(2); C1–N1, 1.328(3); C2–N2, 1.326(3); C1–C2, 1.326(3).

In a similar fashion to **3**, the 18-crown-6 ligated K^+ salt, **3'** displayed the same square planar geometry at the cobalt center, with close contact between the crown-stabilized cation and the cobaloxime (Figures 20 and 22). Examination of the structure of **3'** revealed that the potassium cations interact with the macrocycle in a different manner, such that each $[K(18\text{-crown-6})]^+$ unit adopts close contacts with a lateral set of two N – O fragments (an η4 arrangement) on the macrocycle (K – O = 2.896(2), 3.121(2) Å ; K – N = 3.160(2), 3.400(2) Å). The overall closer approach of the entire $[K(18\text{-crown-6})]^+$ fragment to the cobaloxime that was observed in **3'** is a consequence of the less bulky, alkyl framework of the crown in **3'** compared with that of the dibenzo-crown framework

in **3**. Furthermore, the planarity of **3'** was found to have increased in comparison with that of its congener (N–Co–N ~ 180° *cf.* 173°). Interestingly, the increased planarity of **3'** occurs in conjunction with an 'anti' or 'du' orientation of the BF_2 groups, whereas the BF_2 linkers in **3** adopt a 'syn' or 'uu' conformation. The relevant metrical parameters for this complex are comparable to those that were found for **3**, albeit with slightly decreased N – Co bond lengths (~ 0.018 Å), shorter C=N bonds (~ 0.016 Å), and acenphthalene C – C bonds (~ 0.015 Å). The foregoing discrepancies are attributable to the planar orientation of the ligating moieties.

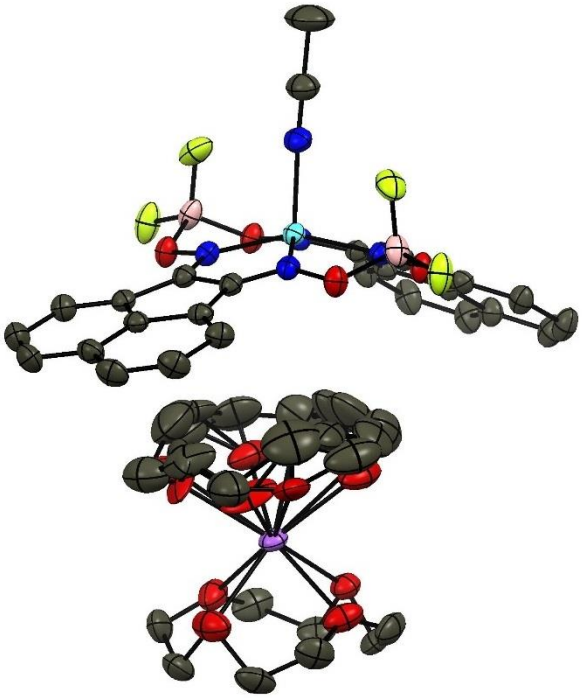

Figure 21. Thermal ellipsoid plot at the 50% probability level for the salt [Na(12-crown-4)$_2$][(Co(aqdBF$_2$)$_2$(MeCN)].

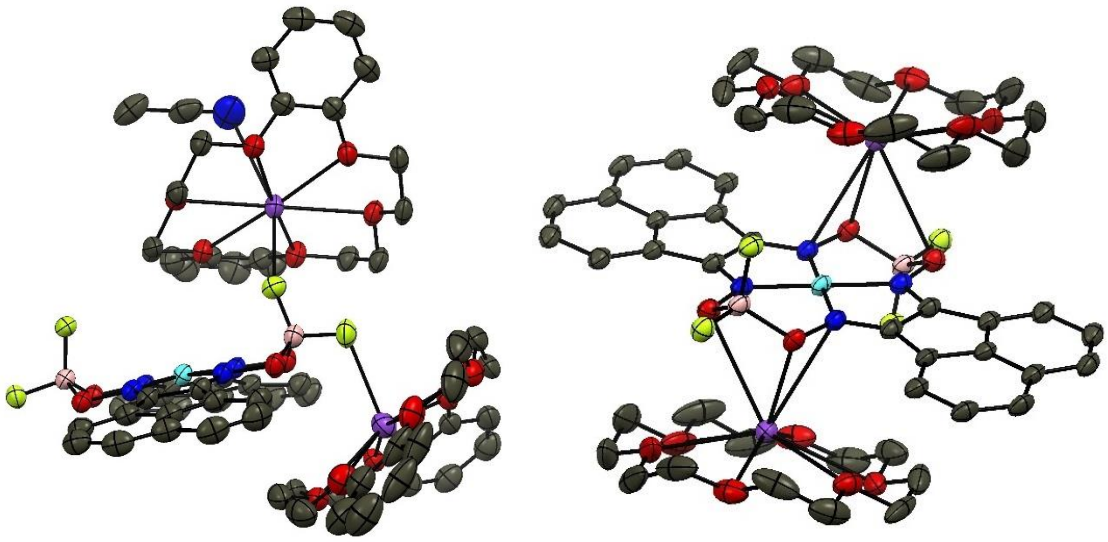

Figure 22. Thermal ellipsoid plot at the 50% probability levels for the salts [K(dibenzo-18-crown-6)]$_2$[(Co(aqdBF$_2$)$_2$] and [K(18-crown-6)]$_2$[(Co(aqdBF$_2$)$_2$].

2.2.4 Electronic Structures of Compounds Used

EPR of [Co(aqdBF$_2$)$_2$(MeCN)$_2$] (1).

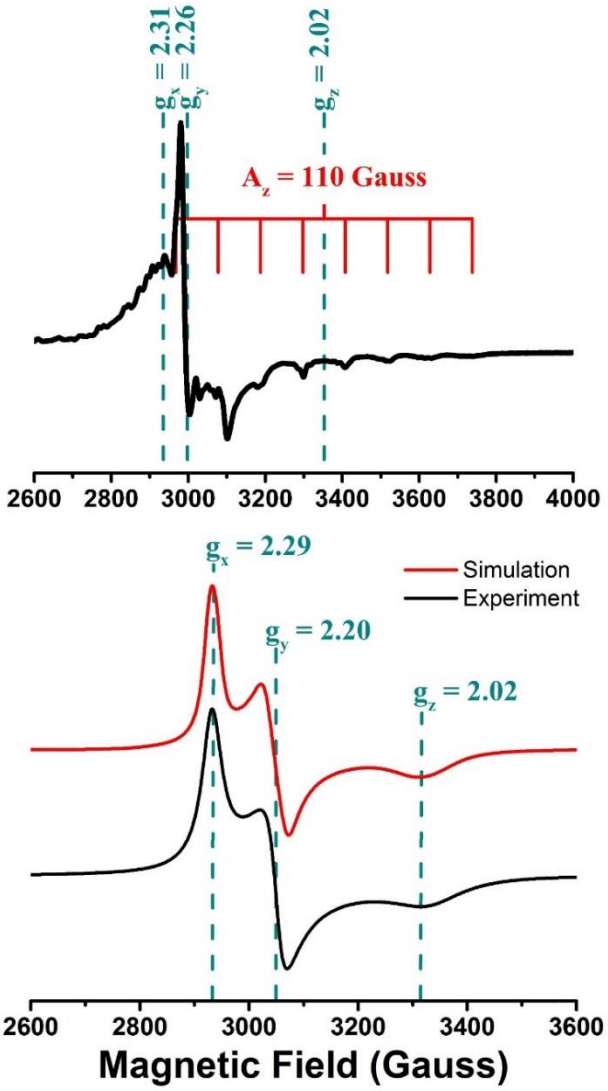

Figure 23. X-band EPR studies of [Co(aqdBF$_2$)$_2$] (**1**). Top panel: X-band EPR spectrum of compound **1** in a frozen glass of 10% MeCN–THF (v/v). Bottom Panel: (Black line) powder EPR spectrum of a solid sample of **1** at 85 K; (red line) along with a simulated EPR spectrum with the following simulation parameters: $g_x = 2.29$, $g_y = 2.20$, $g_z = 2.02$. The instrument parameters for the powder spectrum were as follows: frequency, 9.40 GHz; modulation, 100 kHz; power, 0.2 mW; field modulation, 2 G. The instrument parameters used for the solution spectrum had a frequency of 9.44 GHz, the modulation was 100 kHz along with a power of 25 mW and a field modulation of 10 G.

The EPR spectrum of crystalline **1** was obtained by means of a solid state powder measurement at 85 K, the overall result of which is displayed in the bottom panel of Figure 23. This spectrum is indicative of the presence of a low-spin, axial system as expected for the d^7 Co^{II} ion in **1** supported by the planar $(aqdBF_2)_2$ macrocycle, and coordinated by the two axial MeCN ligands. The simulated EPR signal aligned well with that of the experimental spectrum, thus corroborating the features that were apparent in the range of $g \approx 2\text{-}2.3$ ($g_x = 2.29$, $g_y = 2.20$, $g_z = 2.02$). Furthermore, the result is also consistent with the solid state magnetic susceptibility measurement that was performed on a crystalline sample of 1 ($\mu_{eff} = 1.71\ \mu_B$, 298 K; predicted $\mu_{S.O.} = 1.73\ \mu_B$). Overall, the EPR spectrum of **1** is very similar to those reported for $[Co(dmgBF_2)_2]$ in similar environments ($g_x = 2.26$, $g_y = 2.17$, $g_z = 2.01$ $A_z = 338$ MHz).[81] However, the anticipated ^{59}Co (I = 7/2) hyperfine pattern was not evident in the solid state measurement. This outcome is most likely due to the close proximity of the paramagnetic centers in the crystalline state. However, in a frozen solution of MeCN/THF (10% v/v) at 85 K, complex **1** exhibited a significantly more resolved spectrum (Figure 23, top panel) with primary features at $g_x = 2.31$, $g_y = 2.26$, $g_z = 2.02$. The latter outcome is also indicative of the presence of a low-spin d^7 ion in solution; no features near $g \approx 4.3$ were observed. Furthermore, the solution phase EPR spectrum of **1** exhibited the anticipated eight-line pattern for the I = 7/2 ^{59}Co nucleus, with a coupling constant of $A_z = 110$ G (~310 MHz). The correlation of the hyperfine splitting pattern with the $g_z = 2.02$ feature is consistent with the primary orientation of the unpaired spin being aligned along the z axis, as expected for the singly occupied d_z^2 orbital. This interpretation

is also consistent with the long Co – N_{MeCN} bond distances (2.2714(16) Å) that were evident in the crystal structure of **1**.

^{1}H NMR of [$CoCp_2$][$Co(aqdBF_2)_2(MeCN)$] (2').

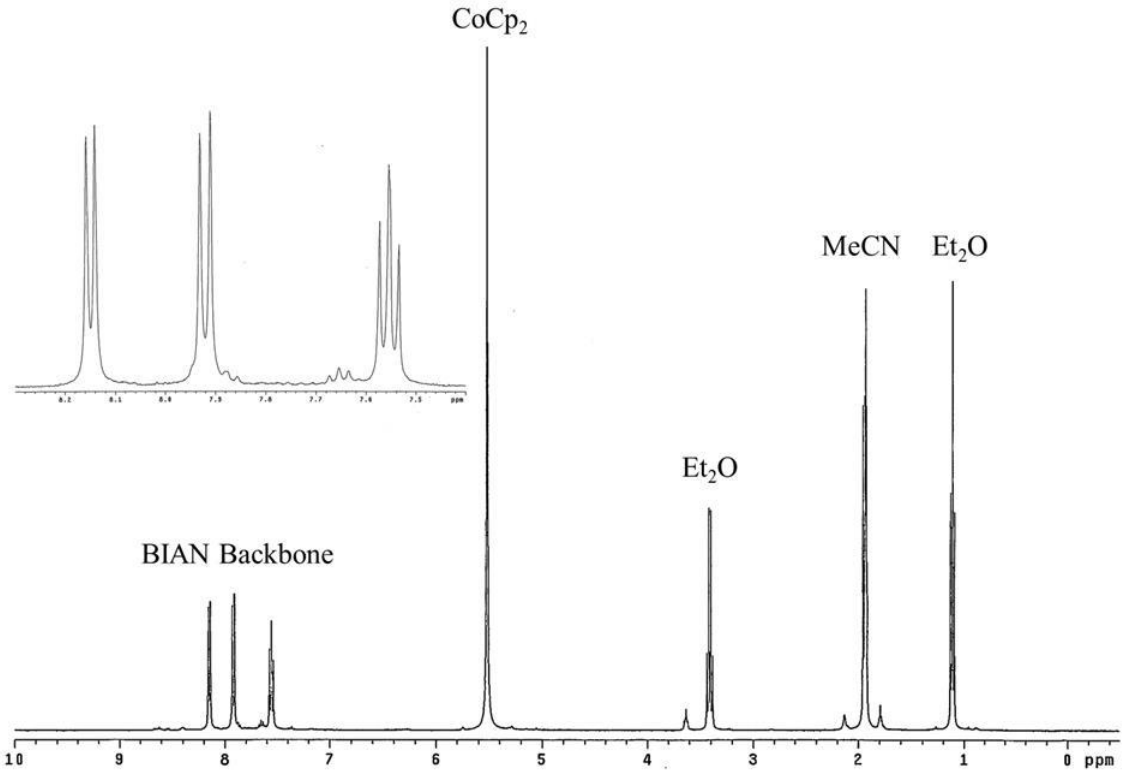

Figure 24. The ^{1}H NMR spectrum of [$CoCp_2$][$Co(aqdBF_2)_2(MeCN)$] (2') in CD_3CN at 298 K (400 MHz). The resulting complex was prepared from cobaltocene and structurally characterized as the cobaltocenium salt.

Following the isolation as the Na-crown salt, the re-dissolution of **2** in CD_3CN resulted in slow bleaching of the solution. This outcome is possibly due to interaction of the residual moisture from the CD_3CN solvent with the reduced species, which, in turn could result in hydrolysis of the complex. The decomposition of the complex in CD_3CN is not due to an inherent instability or reactivity of the complex since **2** was easily extracted

into and crystallized from CH_3CN during the isolation process. In order to circumvent this limitation, an analogous reduction was performed with cobaltocene, which afforded the cobaltocenium salt, **2'**. The prevalent signals observed emanate from the one electron reduced salt, and feature resonances that correspond to those of the cobaloxime anion and the cobaltocenium cation. Identification of the anion as the desired product was confirmed by means of a single crystal X-ray diffraction study (Figure 25).

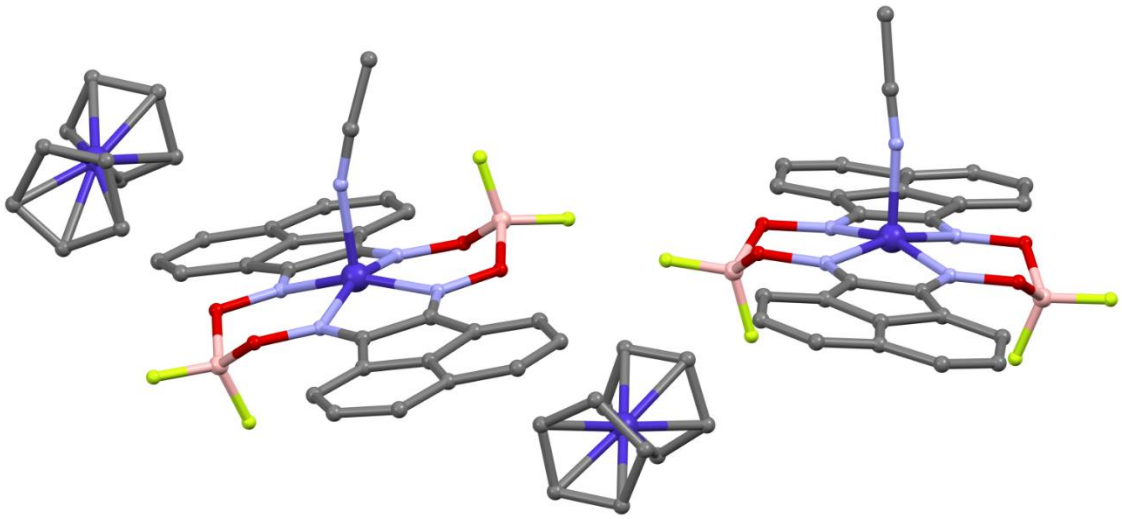

Figure 25. Connectivity structure showing the asymmetric unit of the cobaltocene salt, $[CoCp_2][Co(aqdBF_2)_2(MeCN)]$, **2'**. Incomplete data precluded the generation of a suitable thermal model for this particular crystal.

The anion that resulted from this one-electron reduction afforded a stable CD_3CN solution of the desired complex (Figure 24). The ^1H NMR spectrum of this cobaltocenium salt revealed the presence of a diamagnetic species that exhibited two doublets (δ = 8.15 ppm, J = 6.8 Hz; δ = 7.92 ppm; J = 8.0 Hz) along with a doublet of doublets (δ = 7.56 ppm, J = 6.8, 8.0 Hz) in the aromatic region, thus confirming the presence of the naphthalene

backbone. In comparison with the ^{1}H NMR spectrum of the free aqdH_2 ligand (δ = 12.36 ppm, singlet; δ = 8.35 ppm, doublet, J = 6.6 Hz; d = 8.01 ppm, doublet, J = 7.8 Hz; δ = 7.70 ppm, doublet of doublets, J = 6.8, 8.0 Hz), these resonances only show a slight shift in the aromatic region, signifying that little to no change had taken place in the electronic environment of the naphthalene rings.

EPR of [K(dibenzo-18-crown-6)]$_2$[Co(aqdBF$_2$)$_2$] (3).

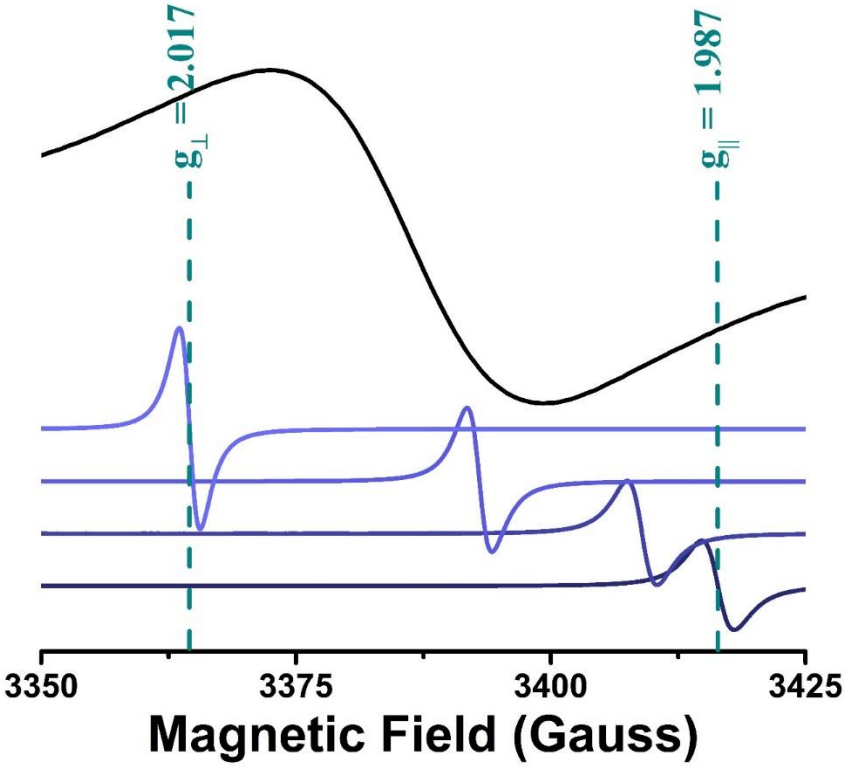

Figure 26. EPR studies of [K(dibenzo-18-crown-6)]$_2$[Co(aqdBF$_2$)$_2$] (**3**): (top) solution EPR spectrum was obtained in frozen MeCN at 85 K; (bottom) single crystal EPR spectrum of **3** was obtained at 85 K during a 90° rotation using a controlled angle goniometer. The instrument parameters for the solution spectrum featured a frequency of 9.44 GHz, a modulation of 100 kHz a power of 20 mW and a field modulation of 0.1 G. The instrument parameters for single crystal spectra had similar parameters with a reduced power of 10 mW.

Solution phase EPR measurements of **3** in either frozen MeCN or MeCN/toluene glass (85 K) revealed a relatively broad feature (~100 G linewidth) centered near g ≈ 2.0 (Figure 26, top). In contrast, the single crystal EPR spectrum of **3** at 85 K (Figure 26, bottom) featured an extremely sharp peak (linewidth < 10 G) with a *g*-value that systematically ranged between 1.987 and 2.017 depending on the orientation of the crystal. The intensity of this feature increased as the resonance shifted to lower magnetic fields upon rotation of the sample tube. Furthermore, the intensity increased approximately two-fold, thus supporting the assignments of $g_{\perp}$ = 2.017 and $g_{\parallel}$ = 1.987 and indicating the presence of an axially anisotropic radical. The proximity of this single feature to the free electron value (g = 2.023), along with the extremely narrow linewidth, strongly suggested the presence of a primarily organic radical. The discrepancy between the line widths of the single crystal and frozen-solution measurements can be accounted for by assuming random orientations (and an average of the signals) in the case of the frozen solution. This is further corroborated by a polycrystalline measurement, which showed a complex spectrum, with no discernible pattern upon rotation (see Figure 27). The assignment of the additional electron as an organic based radical was supported by DFT calculations that were carried out on complex **3**.

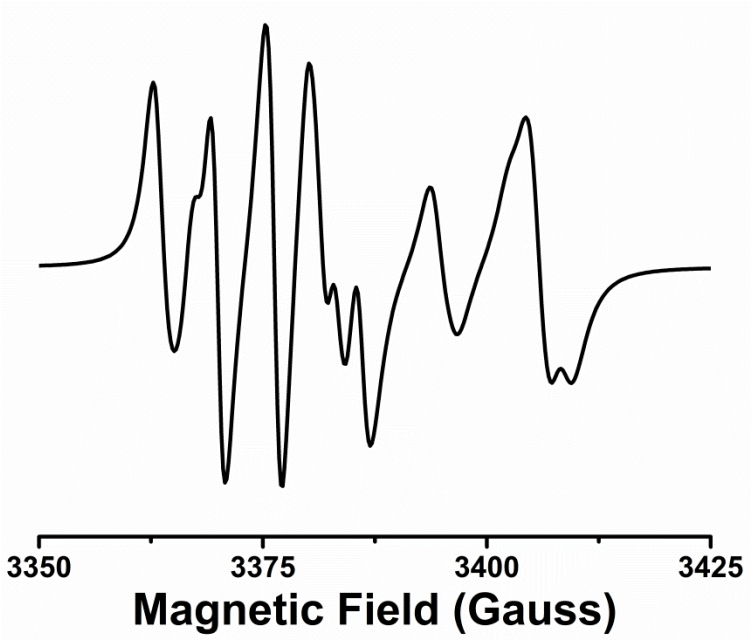

Figure 27. A poly-crystalline EPR spectrum of $[K(dibenzo\text{-}18\text{-}crown\text{-}6)]_2[Co(aqdBF_2)_2]$ (**3**) was obtained at 85 K. The pertinent parameters featured a frequency of 9.45 GHz, modulation of 100 kHz, power of 10 mW and a field modulation of 0.1 G.

^{1}H NMR Spectrum of $[Co(aqdBF_2)_2]3^-$ (4).

The three-electron reduced compound **4** was characterized on the basis of ^{1}H NMR spectroscopy. This complex was generated in situ in d_8-THF solution by reduction with Na/Hg in the presence of 12-crown-4. This reaction resulted in the formation of a green solution that could be analyzed (298 K) by ^{1}H NMR. The diamagnetism of **4** was confirmed by the presence of sharp peaks in the aromatic region. As expected for the acenenaphthalene framework, a pattern of two doublets (δ = 8.21 ppm, J = 7.6 Hz; δ = 7.61 ppm, J = 8.4 Hz) and one triplet (δ = 7.44 ppm, J = 8.0 Hz) was observed. Overall, these

resonances are quite similar to those of the one-electron reduced species **2'**, which exhibits such features at δ = 8.15, 7.92 and 7.56 ppm.

2.2.5 Density Functional Theory Calculations

Density functional theory calculations were performed with the view of confirming the electronic structures that had been proposed for the reduced cobaloxime complexes based on spectroscopic and structural data. The geometry optimizations were performed using the X-ray structure coordinates of **1**, **2**, and **3**. Relevant bond metrics are compared in Table 5. The optimized structure of **1** (S = 1/2) closely mimics that of the crystal structure, albeit with a slight reorientation of the axial acetonitrile solvent. The frontier orbital (SOMO) of this particular compound showed evidence of the presence of an unpaired spin located in the d_z^2 orbital of the metal center. Accordingly, this result confirmed the assignment that had been made based on the EPR results that were discussed earlier.

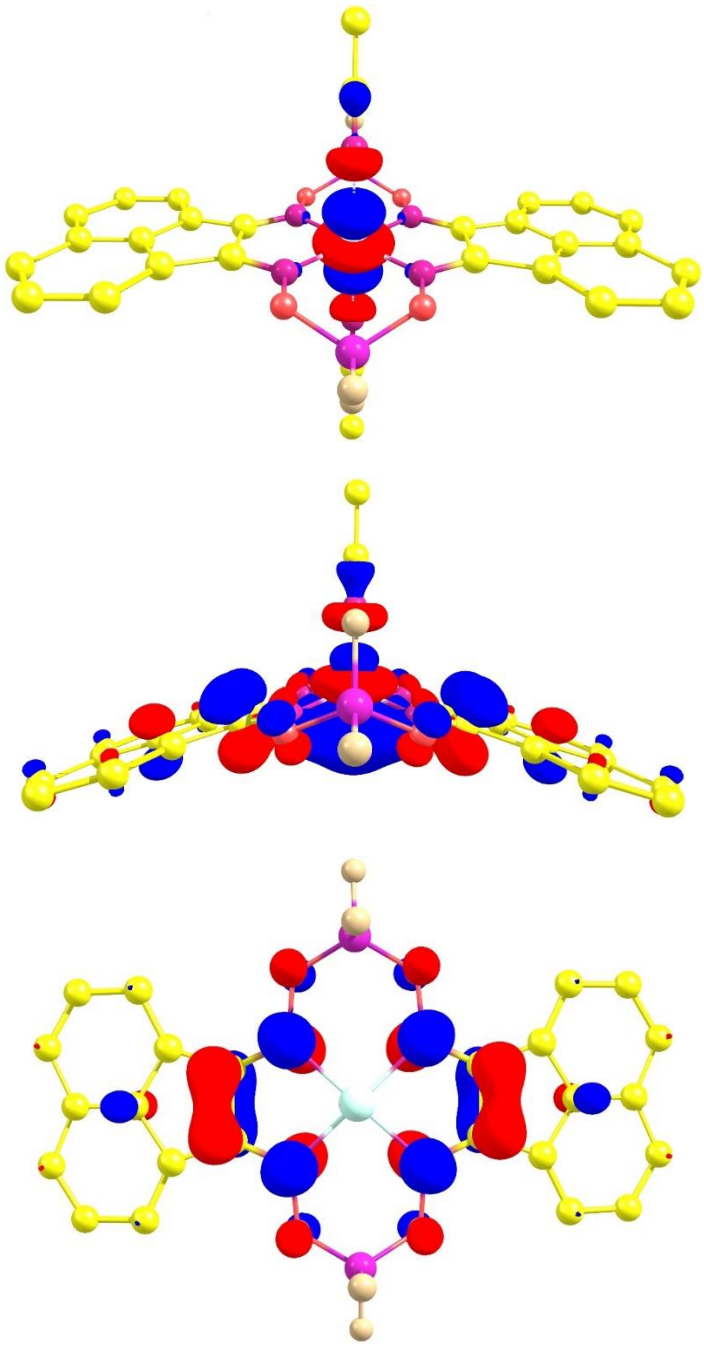

Figure 28. DFT calculated frontier orbitals for **1**–**3** (top to bottom) using the B3P86 functional in conjunction with a Wachters/TZVP hybrid basis set. The geometry optimizations were performed using a smaller basis set (6-31G(d,p)). The surfaces are displayed at the 0.05 isosurface value.

The frontier orbital (HOMO) of **2** shows a pairing of the electrons in the d_z^2 orbital. This in turn accounted for the diamagnetism observed for the one electron reduced complex. There is clear evidence for overlap between this orbital and the p_z orbitals located on the nitrogen atoms. This overlap may account for the changes in bond distances that were detected in the X-ray crystal structure. Furthermore, the location of the additional electron confirms that only a small change had taken place in the electronic environment of the acenaphthene backbone.

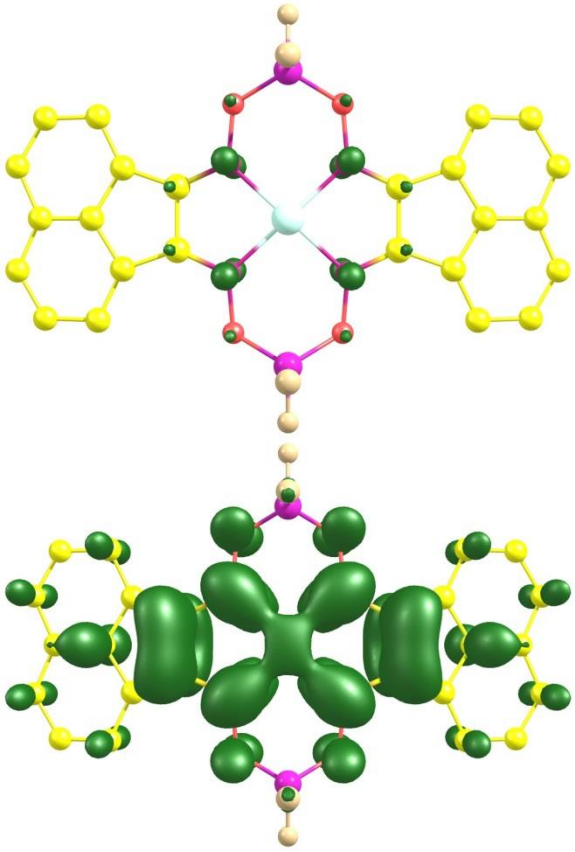

Figure 29. The DFT calculated spin density plot for the anion of $[K(\text{dibenzo-18-crown-6})]_2[Co(aqdBF_2)_2]$ (**3**). The spin density surfaces from the same calculation are displayed here at isosurface values of 0.01 (top) and 0.001 (bottom).

Table 5. Comparative bond lengths for compounds **2**,**3**,**3'** and DFT calculated structures for **1**, **2**, and **3**.

Complex	**aqdH$_2$** ligand	**1** neutral	**2** 1e$^-$ reduced	**3** 2e$^-$ reduced	**3′** 2e$^-$ reduced	**1 (DFT)** neutral	**2 (DFT)** 1 e$^-$ reduced	**3 (DFT)** 2e$^-$ reduced
Co–N$_{ox}$	–	1.8961(10)	1.8795(17)	1.863(2)	1.835(2)	1.897	1.876	1.840
Co–N$_{ox}$	–	–	1.8870(17)	1.861(2)	1.847(2)	–	–	1.843
Co–N$_{ox}$	–	–	–	1.859(2)	–	–	–	1.839
Co–N$_{ox}$	–	–	–	1.854(2)	–	–	–	1.842
Co–N$_{MeCN}$	–	2.2714(16)	2.007(3)	–	–	2.216	1.891	–
C=N$_{ox}$	1.285(2)	1.2932(15)	1.310(3)	1.339(3)	1.328(3)	1.297	1.314	1.330
C=N$_{ox}$	1.286(2)	–	1.308(3)	1.333(4)	1.326(3)	–	–	1.329
C=N$_{ox}$	–	–	–	1.344(3)	–	–	–	1.327
C=N$_{ox}$	–	–	–	1.355(4)	–	–	–	1.327
C–C$_{ac\text{-}napth}$	1.502(2)	1.488(2)	1.445(4)	1.460(4)	1.443(4)	1.482	1.445	1.444
C–C$_{ac\text{-}napth}$	–	–	–	1.455(4)	–	–	–	1.444
N–Co–N *trans*	–	180	154.54(8)	172.93(9)	180.0(1)	180	153.66	172.04
N–Co–N *trans*	–	–	–	172.73(9)	–	–	153.67	172.34

The frontier orbital (SOMO) and spin desity plots (Figures 28 and 29) that were obtained for **3** indicate that the unpaired spin is located in an orbital that spans the metal center and is primarily delocalized across the two N–C–C–N fragments (S = 1/2). Interestingly, the spin density also extended slightly onto the glyoximato oxygen. An extended view of the spin density revealed that the spin density encapsulates the central cobalt ion, but is only slightly localized on the metal center. By contrast, at this isosurface value the ligand framework is replete with spin density. Unrestricted DFT calculations showed a similar alpha spin density plot, albeit accompanied by significant spin contamination (S^2_{calc} = 1.00; S^2_{exp} = 0.75). This may indicate that contributions from both $Co^{I}L^{\bullet-}$ and $Co^{II}L^{2-}$ are feasible for this particular compound.

2.2.6 Electrocatalysis

The proclivity of the title complex for proton reduction was determined electrochemically. For this purpose, CV titrations were performed with additions of two commonly used proton sources, namely *p*-toluenesulfonic acid [TsOH is dissociated, the functional acid is DMF-H^+] and benzoic acid ($PhCO_2H$). The overpotentials for H^+ reduction were determined by the first derivative method described by Fontecave and Artero.[140] Interestingly, the addition of TsOH failed to result in any increase in current at the $Co^{II/I}$ redox couple, a process that is otherwise observed for the majority of cobaloximes. Alternatively, low concentrations of TsOH (2.5 mM) effect a significant increase in current at the third redox event (i_{max}/i_p = 5.77), which is one full volt cathodic of the $Co^{II/I}$ redox potential. At further cathodic potentials (–2.5 V), a related hydritic cobalt

intermediate (tentatively assigned) also displayed a reversible peak. At higher concentrations of TsOH (up to 25 mM), the catalyzed $2H^+ \rightarrow H_2$ transformation was evidenced by a significant increase in current (i_{max}/i_p = 43.3, 25 mM, Figure 30) at –2.3 V *vs.* Fc/Fc^+, which corresponds to a rather high overpotential (η_{TsOH} = 1.5 V, Figure 33). By contrast, when $[Co(dmgBF_2)_2(DMF)_2]$ was monitored with a similarly strong acid (HBF_4) in DMF a low overpotential of η = 0.4 V was determined.[76]

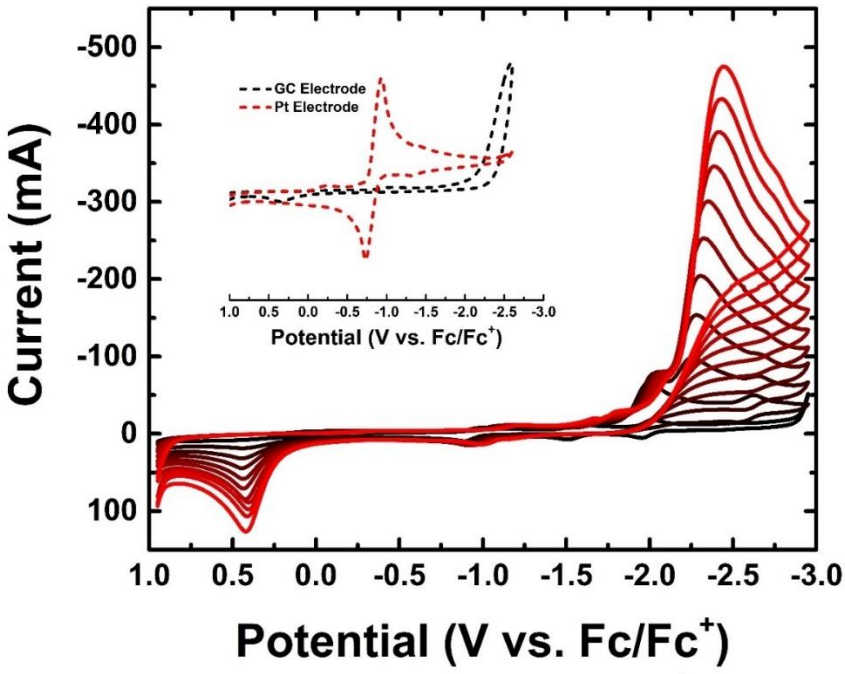

Figure 30. The CV studies of $Co(aqdBF_2)_2$ in the presence of tosic acid ranged from 2.5 to 25 equivalents. The inset shows the I-V response in the presence of 25 mM of TsOH using a glassy carbon (black dashed line) or platinum (red dashed) working electrode.

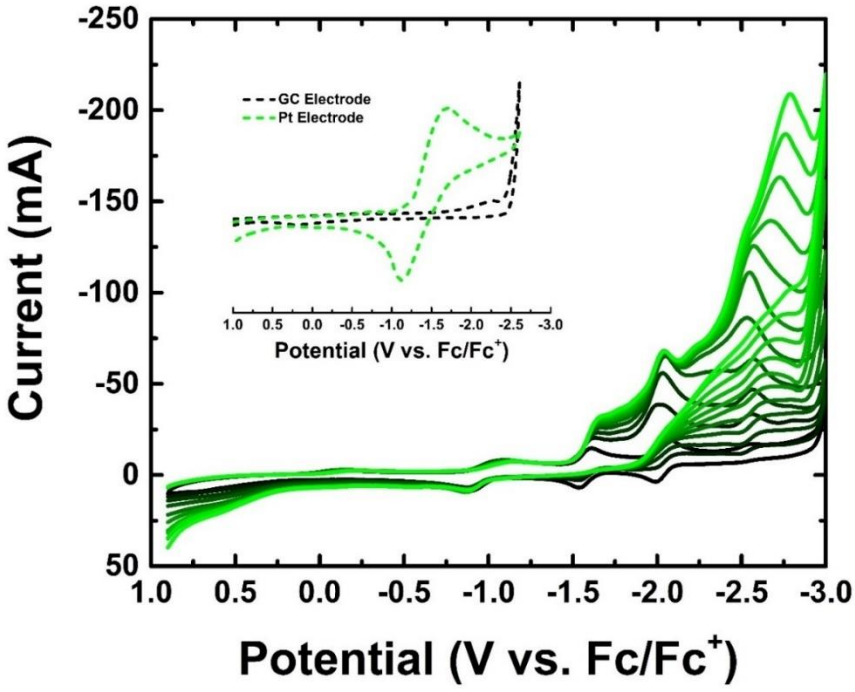

Figure 31. The CV studies of $Co(aqdBF_2)_2$ in the presence of benzoic acid ranged from 2.5 to 25 equivalents. The inset shows the I-V response in the presence of 25 mM of $PhCO_2H$ using a glassy carbon (black dashed line) or platinum (red dashed) working electrode.

An analogous set of experiments with the weaker acid $PhCO_2H$ (10 mM) revealed a surprisingly similar increase in current at the third redox event (i_{max}/i_p = 6.06). However, a catalytic wave was not observed until –2.5 V *vs.* Fc/Fc^+ (i_{max}/i_p = 20.0, Figure 31). The acid concentration dependence for $PhCO_2H$ is indicative of homoconjugation (Figure 33), η_{PhCO2H} = 1.1 V) as expected for the presence of a carboxylic acid in an organic solvent. The linear dependence of the √scan rate versus peak current for the CVs that were carried out in the presence of $PhCO_2H$ suggests that these processes are homogeneous (Figure 32). Variation of the scan rate permitted a determination of the rate constant (k = 13,630 M^{-2} s^{-1}) for the $2H^+ \rightarrow H2$ conversion in the presence of benzoic acid.

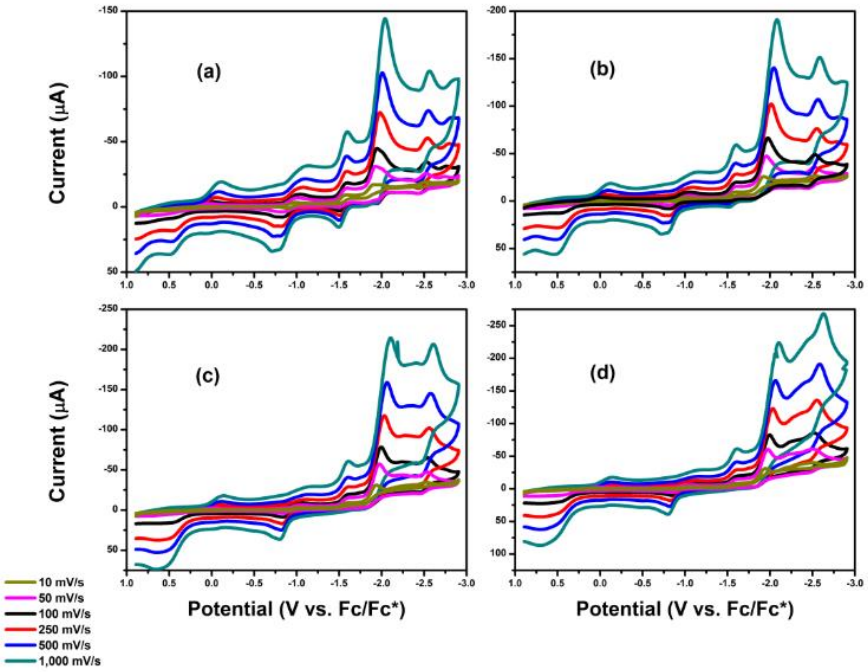

Figure 32. The scan rate dependences of 2.5, 5.0, 7.5, and 10 equivalents of $PhCO_2H$ titrated into a DMF electrolyte (0.1 M $TBAPF_6$) containing 1 mM $Co(aqdBF_2)_2$.

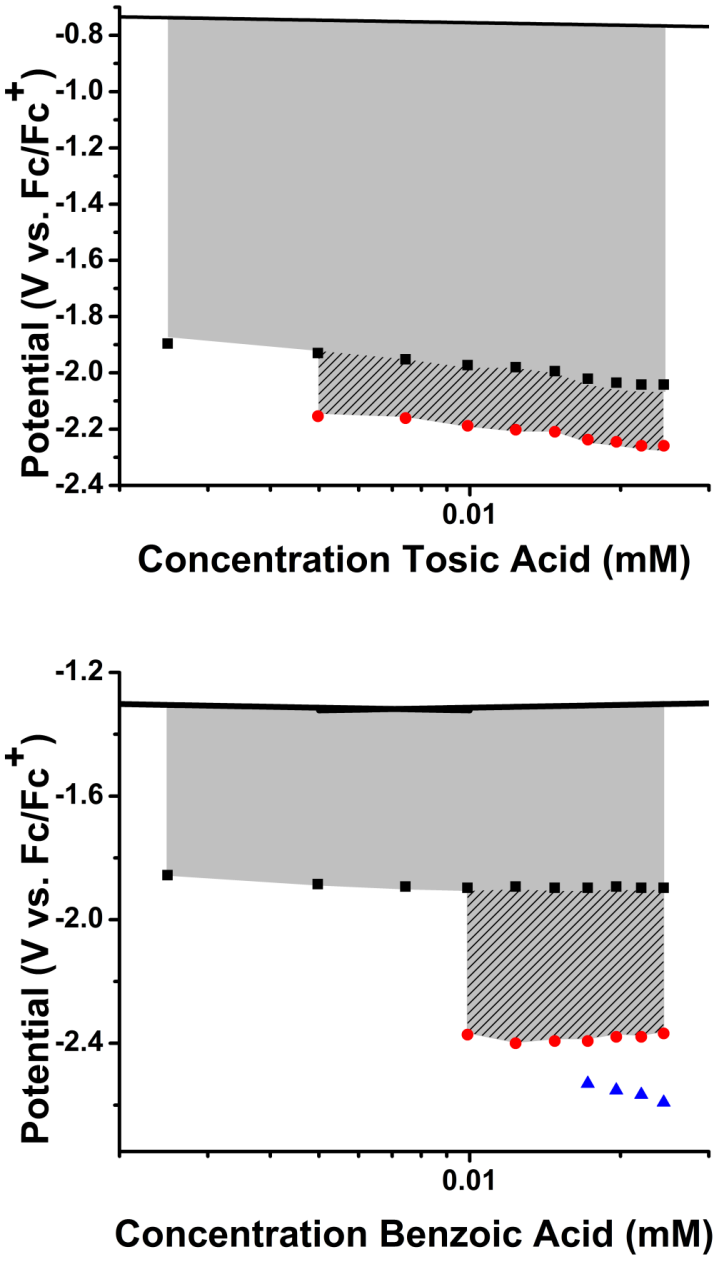

Figure 33. The catalytic reduction "half-wave" potential was determined by the derivative technique and plotted vs. ln[TsOH] (top) and ln[$PhCO_2H$] (bottom). The overpotentials were determined by comparison with the theoretical half-wave potentials that were defined in Chapter 1 (black line).

In order to evaluate the reactivity of the reduced species of **1** with CO_2, CV experiments were performed in the presence of CO_2, the results of which are displayed in Figure 34. Titration of CO_2 (2.5 to 41 mM, followed by complete saturation of CO_2 in DMF (0.204 M)[141] during the CVs of 1•$(DMF)_2$ resulted in a significant increase in current ($i_{max}/i_p \approx 6$) that coincides with the third redox event at –2.0 V *vs.* Fc/Fc^+. A concomitant loss of the corresponding anodic wave is also observed. At more cathodic potentials, a new feature exhibiting a larger increase in current ($i_{max}/i_p \approx 12$) event is apparent near –2.5 V *vs.* Fc/Fc^+.

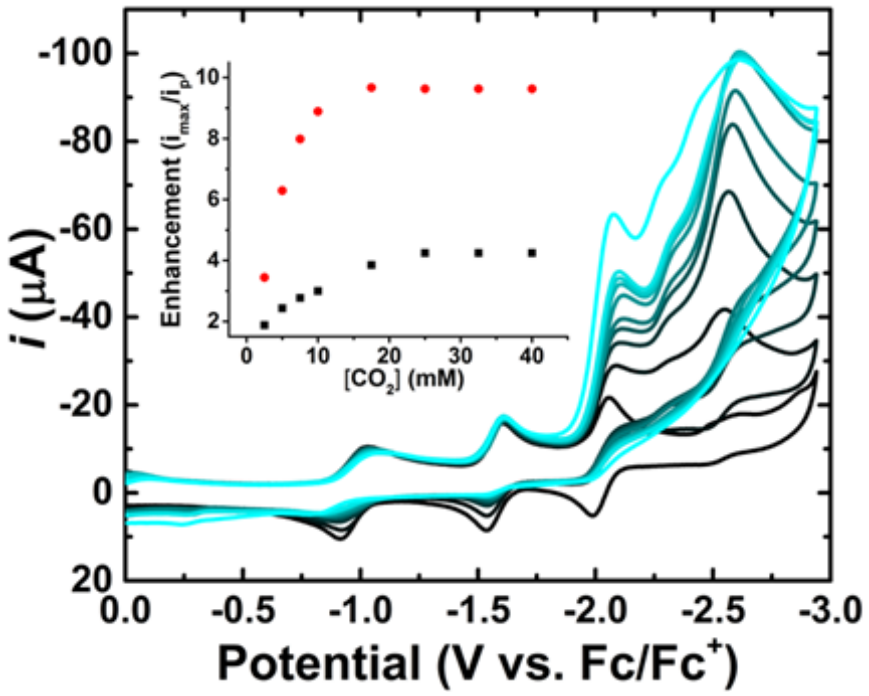

Figure 34. Carbon dioxide titrations into 1 mM $Co(aqdBF_2)_2$ in a DMF electrolyte (0.1 M $TBAPF_6$) showing the increase in current atop the third redox event and at more cathodic potentials. The inset shows the ratio of the maximum current over the peak, one electron current.

Importantly, both peaks can be abolished and re-established by repeated N_2/CO_2 purge cycles as seen in Figure 35. Both of the peaks in the presence of CO_2 exhibit a scan rate dependence that is consistent with homogeneous processes (linear with √scan rate, Figure 36). In control experiments without a catalyst (Figure 37), the CV scans in the presence of CO_2 generated minimal current at -2.0 V (< 3 μA; 6% of catalyst + CO_2 current) and -2.5 V *vs*. Fc/Fc^+ (< 7 μA, 7% catalyst + CO_2 current). On the basis of the above data, it is concluded that a reduced species of $1•(DMF)_2$ participates in the activation of CO_2 in a homogeneous process that is not proton dependent.

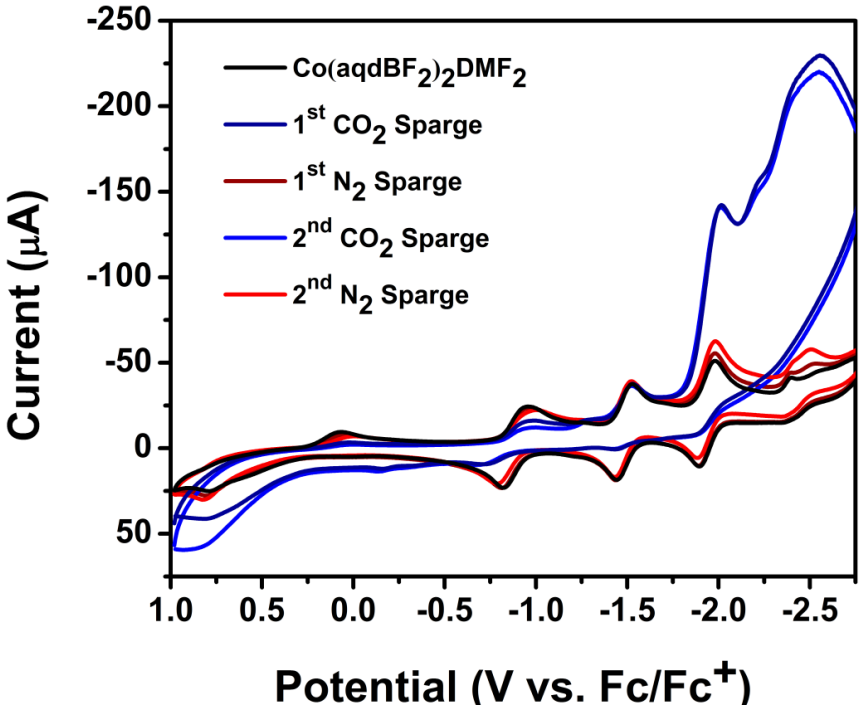

Figure 35. The cyclic voltammograms were recorded during the cycling of N_2/CO_2 into a 1.0 mM solution of $Co(aqdBF_2)_2(DMF)_2$.

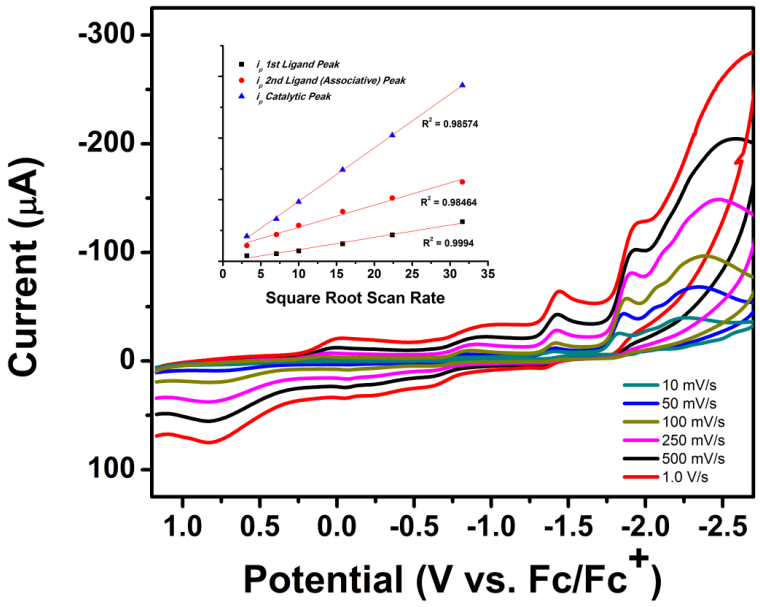

Figure 36. Variation of scan rate (10 - 1,000 mV/s) of $Co(aqdBF_2)_2(DMF)_2$ under CO_2 saturated conditions.

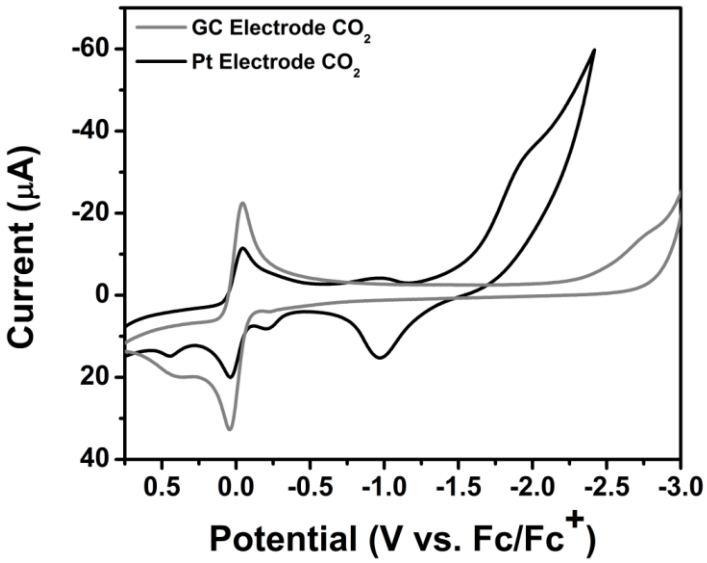

Figure 37. Cyclic voltammograms under CO_2 saturated conditions of a DMF electrolyte at both Pt and GC button electrodes.

The important issue of CO_2/H_2 selectivity was probed by taking CVs of **1**•$(DMF)_2$ in the presence of two different proton sources (Figure 38). The enhancement that is evident on top of the third reduction peak is nearly invariant of substrate, which is indicative of an isopotentionstatic reduction after reaction with the substrate. It would seem that this step is not 'catalytic', but indicates the formation of a modified complex that requires further action (with protons or electrons) to complete dissociation/turnover. In the case of TsOH, the acidity of the protons represents a sufficient driving force for catalysis at more anodic potentials. Conversely, an additional electron transfer (as evidenced by reversibility under low concentrations) is required to effect H_2 evolution with benzoic acid as well as CO_2 reduction. Only at these potentials is it possible to detect the true catalytic onset, including product dissociation and re-entry of the active cobalt species into the catalytic cycle.

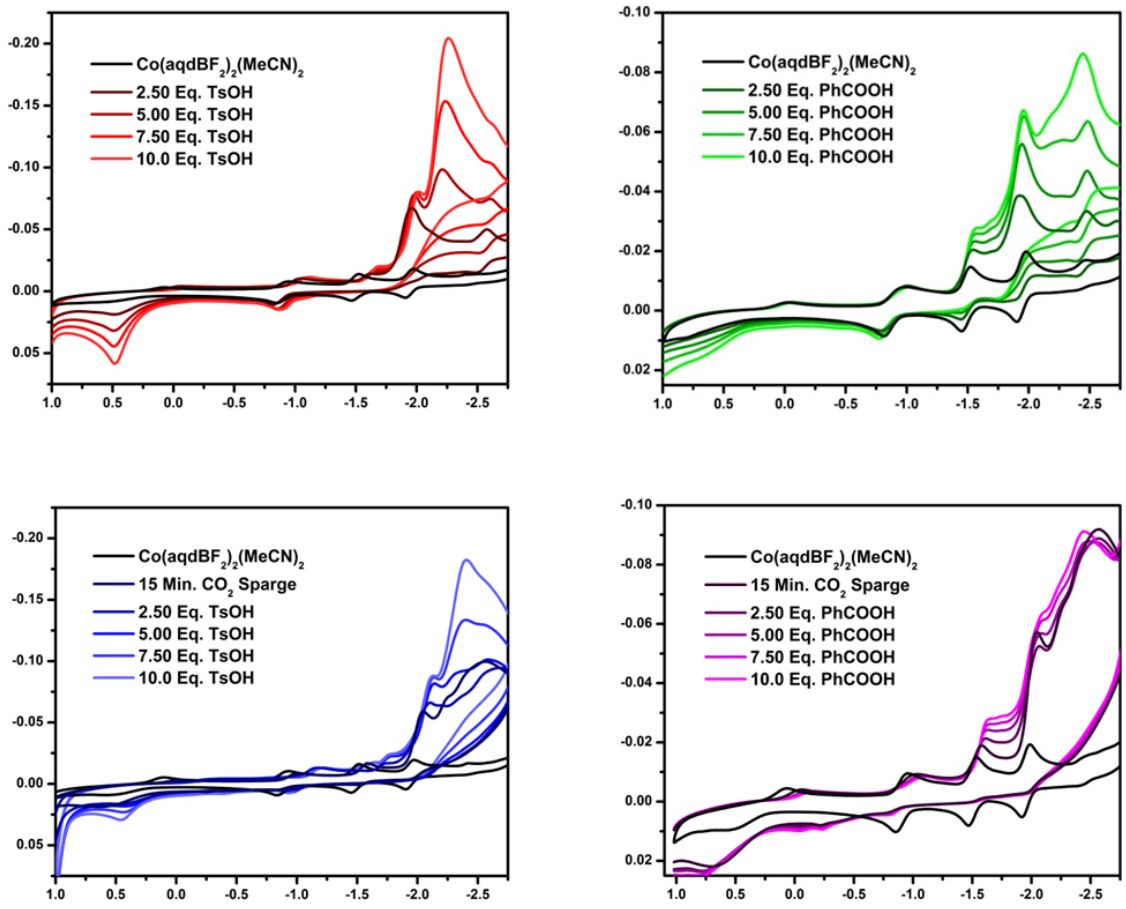

Figure 38. Comparison of acid titrations (0 – 10 mM) of tosic acid (left two graphs) and benzoic acid (right two graphs) under either N_2 (top two graphs) or CO_2 saturation (bottom two graphs).

In the presence of tosic acid, the reduction of CO_2 is obscured by efficient proton reduction catalysis that occurs at low acid concentrations, thus indicating the existence of competing reactions. At higher acid concentrations, however, a proton reductive peak clearly overtakes the catalytic response. The catalytic peak of proton reduction (TsOH) closely mirrors the results obtained under a nitrogen atmosphere, albeit at slightly more cathodic potentials (E_p = -2.35 V *vs.* Fc/Fc^+; 25 mM TsOH). Given the foregoing observations, it can be inferred that the predominant catalysis

that is taking place involves the formation of H_2, along with minimal amounts of carbon dioxide reduction. Because of the decreasing thermodynamic driving force associated with the reduction of benzoic acid protons to H_2 it was deemed more appropriate to attempt the proton coupled reduction of CO_2. In sharp contrast to TsOH, the reduction of protons to H_2 in this case does not appear to be a strongly competing catalytic mechanism within the range of predominantly CO_2 electrocatalysis. A small peak that was detected at -2.4 V indicated that very small increases in current take place upon increasing the acid concentration. The reduction of protons in this environment does not appear to occur until more cathodic potentials (E_{cat} < -2.5 V). Thus, based on the thermodynamic driving force for proton reduction (i.e. the acidity, pK_a, of a particular acid), one can choose an acid that is appropriate to assist in CO_2 reduction without generating a large amount of parasitic hydrogen evolution.

Initial bulk electrolysis (BE) experiments were attempted in a custom H-cell to determine the activity for the hydrogen evolution reaction without CO_2. In any given experiment, a large amount of current was found to pass during the electrolysis of a benzoic acid solution, and hydrogen production was detected by GC. The subsequent rinse tests, however show a similar efficiency for the reaction. This similarity of currents can be attributed to native electrode surface reactions, catalyst degradation, metal deposition, and/or solvent degradation. Such processes are more prevalent over the extended time periods associated with bulk electrolysis. The extreme potentials required to observe (by

CV) a catalytic response render the analysis of catalytic capability difficult. While no comprehensive study of acids has been performed in DMF as in the case of MeCN,[142] it is likely that these experiments are being performed near or beyond the edge of the useful potential window ($E_{BE} < E_{inf}$) for each acid. In comparison with the literature cobaloximes, the limitations regarding the operating potential for proton reduction in this particular case are evident. Furthermore, the stabilities of some of the complexes that have been used in bulk electrolysis experiments have been called into question recently.[62,143]

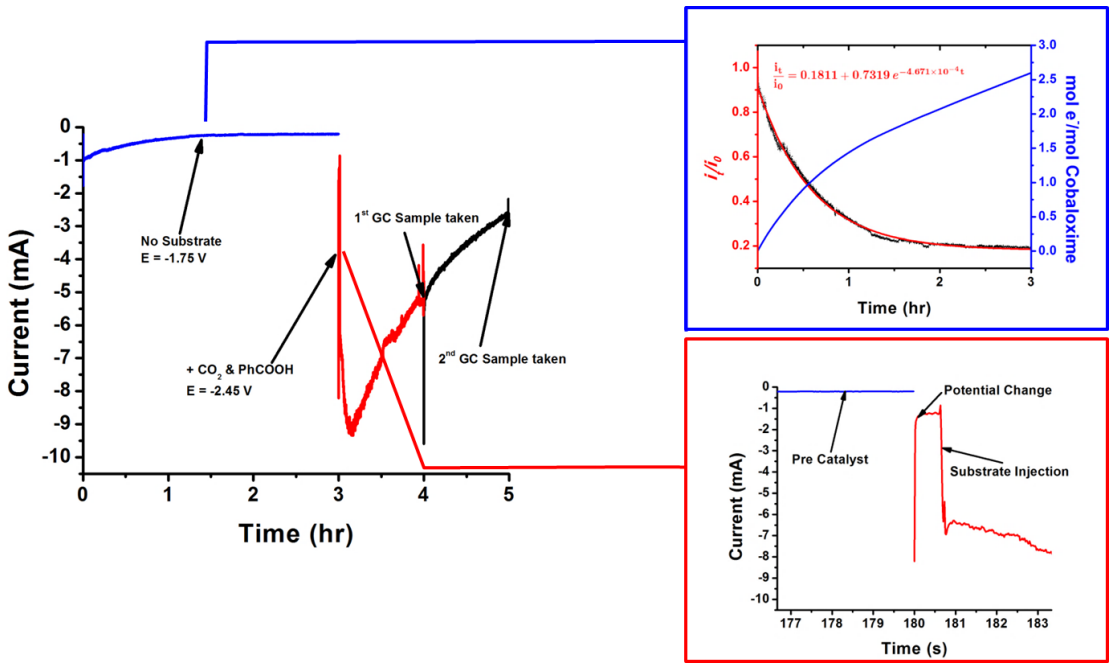

Figure 39. Typical bulk electrolysis experiments involve a pre-charge period of three hours in which the potential was held cathodic of the second redox peak, thereby generating the putative $[Co(aqdBF_2)_2]^{2-}$ species. Following this period, the potential was shifted further cathodic (to -2.45 V *vs.* Fc/Fc^+) and the substrates $PhCO_2H$ and CO_2 injected. The GC samples were taken one and two hours after injection of the substrate.

To support the findings of the CO_2 cyclic voltammetry experiments bulk electrolysis was pursued with **1**•$(DMF)_2$ in the presence of benzoic acid and CO_2 (see Figure 39). In order to obtain the highest rate of catalysis, the potential was held just cathodic of the observed catalytic peaks at -2.45 V *vs.* Fc/Fc^+ in DMF. During an initial pre-electrolysis, the two electron reduced species was generated, integration of the period of electrolysis gives 2.5 electrons passed per catalyst without background subtraction, indicating complete generation of the doubly reduced precatalyst. Following this period, the potential was shifted to a more cathodic potential, resulting in an increased current, indicative of the addition of an additional electron into the system. Approximately one second later, a second solution containing substrate (CO_2 and $PhCO_2H$) was injected, which resulted in a large increase in current (~7 mA). This potential was held and headspace gas samples taken after one and two hours to determine the product profile. Interestingly, although 38 Coulombs of charge had passed (corresponding to a TOF $\approx$ 6.5 hr^{-1}), the Faradaic yield of hydrogen only reached 5-10% while that for CO showed a 1-5% yield.

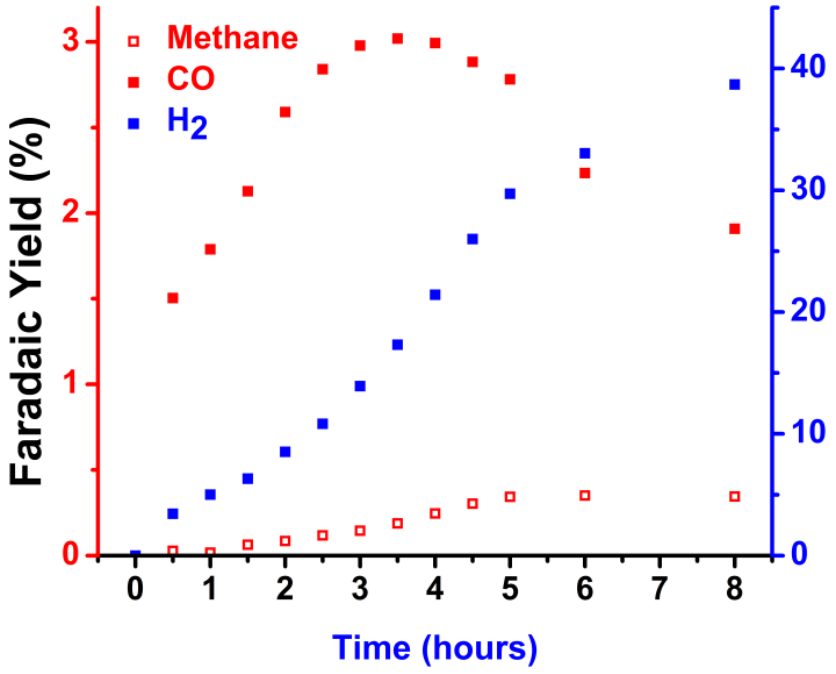

Figure 40. Long term bulk electrolysis experiments for the electrocatalytic reduction of CO_2 over a period of eight hours. An initial period of CO generation is superseded by predominant hydrogen generation at periods greater than 3 hours.

Longer term bulk electrolysis experiments (Figure 40) showed that while there is an initial increase in the generation of CO, over long time periods, CO ceases to be generated while H_2 production overtakes the catalytic response. This result would seem to indicate that over the long time periods associated with bulk electrolysis, degradation of the catalyst precludes observation of the efficiency and selectivity through product profiles.

2.3 CONCLUSIONS

The fusing of a naphthalene ring to a traditional cobaloxime electrocatalyst greatly affects due to the ability to affectively withdraw electron density from the metal center. Reductive studies on the parent cobaloxime complex show a large degree of delocalization of electron density across the naphthalene backbone. Spectroscopic and density functional theory studies indicate that reduction follows a paramagnetic – diamagnetic – paramagnetc – diamagnetic sequence, with tentative assignments of the reduced species as follows: $Co^{II}(aqdBF_2)_2L_2 \rightarrow Co^{I}(aqdBF_2)_2L \rightarrow Co^{I}(aqdBF_2)_2^{\bullet -} \rightarrow Co^{I}(aqdBF_2)_2^{2-}$. Electrocatalytic studies on this complex revealed a large overpotential in the case of proton reduction, wherein catalysis does not occur until cathodic of the third redox peak. Similar redox activity is seen in the presence of CO_2, however the relative pK_a of the acids allow for a competitive reactivity in the presence of CO_2 and a proton source. These studies could not be confirmed via bulk electrolysis experiments due to the degradation of the electrocatalyst over extended time periods under reductive conditions and in the presence of substrate.

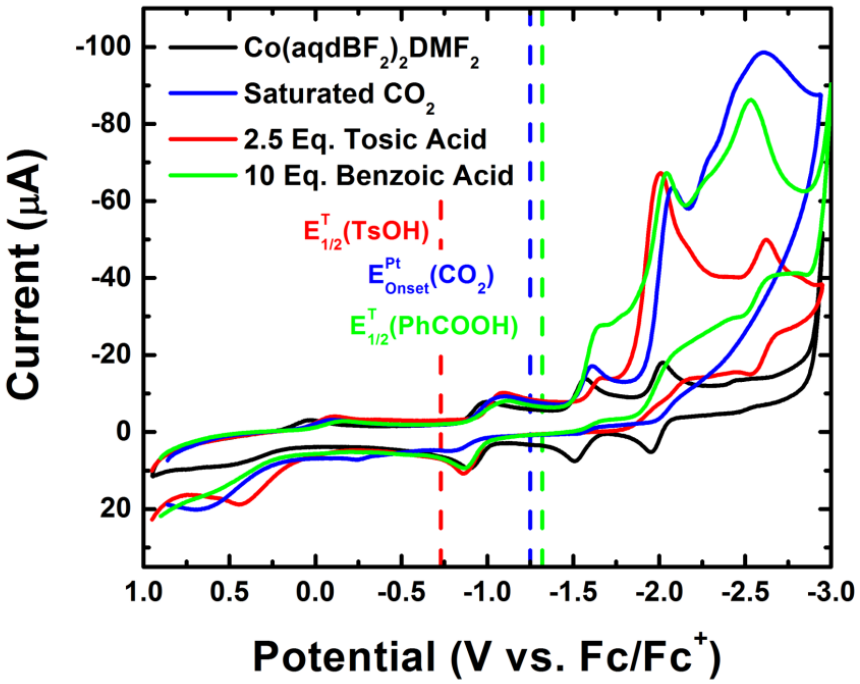

Figure 41. CVs of the title compound $Co(aqdBF_2)_2L_2$ in the presence of a variety of substrates – CO_2, TsOH, $PhCO_2H$ – showing the lack of reactivity that is otherwise observed in cobaloxime systems.

2.4 Experimental

2.4.1 Reagents and Procedures

Cobalt(II) acetate, potassium graphite, sodium metal, mercury, and cobaltocene were purchased from Strem Chemicals. Acenaphthenequinone, hydroxylamine hydrochloride, boron trifluoride etherate, naphthalene, dibenzo-18-crown-6, 18-crown-6 and 12-crown-4 were purchased from Acros Organics and used as received. The ligand $aqdH_2$ was synthesized according to the published procedure of Satake et al.[144] All solvents used in the syntheses were purchased from Fisher Scientific, and dry solvents were obtained using a Pure Process Technology solvent purification system. Anhydrous DMF

was purchased from Acros Organics and used without further purification for all the electrochemical studies.

2.4.2 Syntheses of Metal Complexes

[Co(aqdBF$_2$)$_2$(MeCN)$_2$] (1).

Complex **1** was prepared by using a method that is similar to the one described by Bakac and Espenson.[85] A 50 mL Schlenk flask was charged with (0.50 g, 2.8 mmol) of acenaphthenequinonedioxime and (0.30 g; 1.2 mmol) of Co(OAc)$_2$●4H$_2$O, and placed under vacuum for 20 min. Dry Et$_2$O (30 mL) was added, thereby generating a light brown slurry. Next, 1.5 mL of BF$_3$●Et$_2$O was added via syringe. After stirring the reaction mixture for 12 hours, the resulting dark brown precipitate was collected by subsequent filtration. The brown/red powder that had formed was stirred in 20 mL of MeCN for one hour. Subsequent filtration resulted in the isolation of a bright red powder of [Co(aqdBF$_2$)$_2$(MeCN)$_2$]: 0.249 g; 0.378 mmol; 31.5%. IR (cm^{-1}): 3603 (m), 3530 (m), 1623 (m) 1484 (w) 1416 (w), 1134 (s), 987 (s), 965 (s), 911 (s), 826 (s), 775 (s), 539 (m), 508 (m). UV/Vis in THF, λ_{max} (nm): 505, 340, 280 μ_{eff} = 1.71 μ_B. EPR: g_x = 2.29, g_y = 2.20, g_z = 2.02, 85 K, solid powder. Elem. Analys. for $C_{28}H_{18}B_2CoF_4N_6O_4$ (%) calculated: C 51.03, H 2.75, N 12.75; found: C 50.98, H 2.63 N 12.37. HR-MS for [1-2MeCN$^+$Na]$^+$: calculated, 600.02130; found, 600.02090.

[Na(12-crown-4)$_2$][Co(aqdBF$_2$)$_2$(MeCN)] (2).

Complex **2** was isolated by dissolving 20.7 mg of the parent compound (0.0314 mmol) in 8 mL of THF. Following this, 1.29 equivalents of Na[$C_{10}H_8$] was added to the

reaction mixture from a standard solution (0.3 mL, 0.135 M Na[$C_{10}H_8$] in THF). The latter solution was allowed to stir for thirty minutes ultimately generating a purple-blue solution. The solvent was removed under reduced pressure and the resulting powder dissolved in acetonitrile, affording a violet solution with a brown precipitate, which was removed by filtration. Vapor diffusion of Et_2O into the latter solution in the presence of excess (100 mg, 0.568 mmol) 12-crown-4 yielded X-ray quality crystals of compound **2**. Yield: 10.5 mg; 0.011 mmol; 34%. IR (cm^{-1}): 2868 (w), 1609 (w), 1519 (w), 1484 (w) 1443 (w), 1411 (w), 1363 (w), 1304 (w), 1244 (w), 1143 (m), 1093 (s), 983 (s), 912 (s), 849 (m), 827 (m), 789 (m). UV/Vis in THF/MeCN (10:1), λ_{max} (nm): 560, 770. This complex was unstable upon re-dissolution in CD_3CN. An alternative salt (below) was prepared to obtain a ^1H NMR spectrum of the singly reduced anion.

[Co(Cp)$_2$][Co(aqdBF$_2$)$_2$(MeCN)] (2').

The parent cobaloxime (23.7 mg, 0.036 mmol) was dispersed in MeCN solution. The subsequent addition of 21.3 mg of cobaltocene (0.126 mol) resulted in the generation of a non-turbid violet solution. The latter solution was allowed to stir for thirty minutes, following which, most of the MeCN solvent was removed under reduced pressure. The solution was then subjected to the addition of Et_2O, generating a purple precipitate of **2'**. The resulting filtrate was dissolved in CD_3CN in order to obtain a satisfactory ^1H NMR spectrum. Yield: 25 mg; 0.031 mmol; 86%. Crystallization of this compound was effected by vapor diffusion of Et_2O into the above mentioned solution to afford X-ray quality crystals. NMR: δ = 8.15 ppm, d; J = 6.8 Hz; δ = 7.92 ppm, d; J = 8.0 Hz, δ = 7.56 ppm,

dd; J = 6.8, 8.0 Hz; δ = 5.52 ppm, singlet. Elem. Analys. for $C_{36}H_{25}B_2Co_2F_4N_5O_4$ (%) calculated: C 53.57, H 3.12, N 8.68; found: C 53.69, H 3.08 N 8.62.

[K(dibenzo-18-crown-6)]$_2$[Co(aqdBF$_2$)$_2$] (3).

Complex **3** was synthesized by dissolving 22.4 mg of the parent compound (0.034 mmol) in 8 mL of THF. After the addition of 3.2 equivalents of KC_8 (15 mg; 0.111 mmol) the resulting solution was allowed to stir for thirty minutes and filtered to remove any remaining traces of the reductant. To this solution 3.7 equivalents of dibenzo-18-crown-6 (45 mg; 0.125 mmol) were added, resulting in a slight color shift from deep navy blue to a dark blue-green. The solvent was then removed under reduced pressure and the resulting powder was dissolved in acetonitrile, which retained the blue-green hue observed in THF solution. Vapor diffusion of Et_2O into the latter solution afforded a crop of X-ray quality crystals of the desired compound. Crystalline Yield: 21 mg; 0.015 mmol; 45%. IR (cm^{-1}): 2929 (w), 1587 (m), 1504 (s), 1452 (m) 1248 (s), 1213 (s), 1124 (s), 993 (s), 942 (s), 813 (m), 766 (m), 743 (s). UV/Vis in THF, λ_{max} (nm): 605 (broad), 770 (broad). This complex proved too unstable for extended times in the solid state to obtain satisfactory elemental analysis.

[K(18 -crown-6)]$_2$[Co(aqdBF$_2$)$_2$] (3').

The complex **3'** was synthesized by a similar procedure as for 3, with 21.6 mg of 1 (0.033 mmol) and 3.1 equivalents of KC_8 (13.7 mg; 0.102 mmol). Following filtration to remove the reducing equivalents, excess 18-crown-6 was added to the solution (34.9 mg; 0.132 mmol). Crystallization of this compound was achieved directly from the above THF

solution at reduced temperatures (–20 °C) in an argon atmosphere. Crystalline Yield: 16 mg; 0.014 mmol; 41%. IR (cm^{-1}): 2882 (m), 1601 (m), 1520 (m), 1473 (w) 1410 (w), 1352 (m), 1250 (w), 1109 (s), 1060 (m), 1008 (s), 825 (m), 778 (s). This complex proved too unstable for extended times in the solid state to obtain satisfactory elemental analysis.

2.4.3 Electrochemistry

Cyclic voltammograms and bulk electrolysis experiments were carried out using a Pine Wavenow potentiostat. All CV experiments were performed in a 0.1 M *n*-tetrabutylammonium hexafluorophosphate (NBu_4PF_6)/N,N-dimethylformamide electrolyte solution equipped with a glassy carbon button working, a platinum wire counterelectrode, and a silver wire quasi-reference electrode. The resulting potentials are reported with respect to the ferrocene/ferrocenium redox couple (these values can be calculated with respect to SCE by the addition of 0.5 V). The bulk electrolysis measurements were carried out in a custom H-cell with two frits separating the working and counter electrode compartments (V ~ 50 mL) or a larger bulk electrolysis cell with a custom fritted glass insert for the counter electrode. Each cell was equipped with a glassy carbon rod (Tokai Carbon) as the working electrode and counter electrode. The silver wire reference electrode was connected to the potentiostat by means of a copper wire. In the H-cell experiments, a pre-charge period of approximately three hours was employed by holding the potentiostat to a potential just cathodic of the second redox peak, thus generating an intense blue solution of the pre-catalyst.

2.4.4 X-ray Crystallography

Structures were solved, refined, and analyzed using standard procedures.[145–149] Definitions used for calculating $R(F)$, $wR(F^2)$ and the goodness of fit, S, are given below. All figures were generated using Mercury.[150] Details regarding the data collection and solution parameters for $aqdH_2$ and the cobalt complexes are summarized in Appendix B.

$$R(F) = \sqrt{\frac{\sum w(|F_o|^2 - |F_c|^2)^2}{\sum w(|F_o|)^4}}$$

$$R(F) = \frac{\sum(|F_o| - |F_c|)}{\sum|F_o|}$$

$$S = \frac{\sum w(|F_o|^2 - |F_c|^2)^2}{(n-p)}$$

$aqdH_2$

Crystals were grown by slow evaporation of a solution of $aqdH_2$ in Et_2O/Hexanes. A single, light yellow crystal was used for data collection, with approximate dimensions 0.114 × 0.106 × 0.094 mm. The data were collected at 25 °C on a Rigaku SCX-Mini diffractometer using a graphite monochromator with MoKα radiation (λ = 0.71073 Å). A total of 920 frames of data were collected using ω and ϕ-scans with a scan range of 1.0° and a counting time of 60.0 seconds per frame. Data reduction was performed using Rigaku Americas Corporations Crystal Clear version 1.40. Details of crystal data, data collection and structure refinement are listed in Tables B1 – B3. The oxime bound protons were

observed in the electron difference map and modeled by a freely rotating riding model on the oxime oxygens. They were refined isotropically without restraints.

[Co(aqdBF$_2$)$_2$(MeCN)$_2$]MeCN (1).

Crystals of **1** were grown by layering acetonitrile over a saturated solution of the compound in THF. A whole parallelpiped crystal was used for data collection, with approximate dimensions 0.401 × 0.164 × 0.126 mm. The data were collected at –120 °C on a Nonius Kappa CCD diffractometer using a Bruker AXS Apex II detector and a graphite monochromator with MoKα radiation (λ = 0.71073 Å). Reduced temperatures were maintained by use of an Oxford Cryosystems 600 low-temperature device. A total of 1,048 frames of data were collected using ω and ϕ-scans with a scan range of 0.8° and a counting time of 46.24 seconds per frame. Data reduction was performed using SAINT V8.27B. Details of crystal data, data collection and structure refinement are listed in Tables B4 – B6. The hydrogen atoms on C8 were observed in a ΔF map and refined with isotropic displacement parameters, with the hydrogen sitting on the mirror plane assigned a site occupancy factor of 0.5. All other hydrogen atoms were affixed to the carbons with an appropriate riding model.

[Na(12-crown-4)$_2$][Co(aqdBF$_2$)$_2$(MeCN)] (2).

Crystals of **2** were grown by vapor diffusion of Et_2O into a saturated solution of the above complex in MeCN. A dark purple fragment was broken away from a large crystal and used for data collection, with approximate dimensions 0.371 × 0.224 × 0.170 mm. The data were collected at –123 °C on an Agilent Technologies SuperNova diffractometer using

an Atlas S2 Detector and CuKα radiation (λ = 1.54184 Å). Reduced temperatures were maintained by use of an Oxford Cryosystems 700 low-temperature device. A total of 1,053 frames of data were collected using ω-scans with a scan range of 1.0° and a counting time of 1.0 - 4.5 seconds per frame. Data reduction was performed using CrysAlisPro. Details of crystal data collection and structure refinement are listed in Tables B7 – B9. One of the crown-ether molecules was refined without bonds to symmetry generated atoms via a PART -1 instruction card. The alternate crown was modelled with positional disorder in the ethylene bridging units. All non-hydrogen atoms were refined anisotropically, solvent molecules and disordered crown ether atoms were refined with UDP, but not positional restraint.

[K(dibenzo-18-crown-6)]$_2$[Co(aqdBF$_2$)$_2$] (3).

Crystals of **3** were grown by vapor diffusion of Et_2O into a saturated solution of the above complex in MeCN. A dark blue shard was used for data collection, with approximate dimensions 0.435 × 0.374 × 0.275 mm. The data were collected at –123 °C on a Agilent Technologies SuperNova diffractometer using an Atlas S2 Detector and CuKα radiation (λ = 1.54184 Å). Reduced temperatures were maintained by use of an Oxford Cryosystems 700 low-temperature device. A total of 1,031 frames of data were collected using ω-scans with a scan range of 1.0° and a counting time of 1.0 - 20 seconds per frame. Data reduction was performed using CrysAlisPro. Details of crystal data, data collection and structure refinement are listed in Tables B10 – B12. All non-hydrogen atoms were refined

anisotropically and without restraint with the exception of a rigid bond (RIGU) restraint on the solvent ether molecule.

[K(18-crown-6)]$_2$[Co(aqdBF$_2$)$_2$] (3').

Crystals of **3'** were grown at reduced temperature (–20 °C) from a saturated THF solution. A blue shard was used for data collection, with approximate dimensions 0.383 × 0.263 × 0.191 mm. The data were collected at 133 K on a Agilent Technologies SuperNova diffractometer using an Atlas S2 Detector and CuKα radiation (λ = 1.54184 Å). Reduced temperatures were maintained by use of an Oxford Cryosystems 700 low-temperature device. A total of 682 frames of data were collected using ω-scans with a scan range of 1.0° and a counting time of 1.0 - 15 seconds per frame. Data reduction was performed using CrysAlisPro. Details of crystal data, data collection and structure refinement are listed in Tables B13 – B15. All non-hydrogen atoms were refined anisotropically and without restraint.

2.4.5 Physical Measurements

EPR spectra were obtained on a Bruker Biospin EMXplus 114 X-band spectrometer with a liquid nitrogen variable temperature cryostat. Infrared spectra were recorded using a Bruker Alpha spectrometer equipped with a diamond ATR crystal. ^{1}H NMR spectra were collected on a Varian DirecDrive 400 MHz spectrometer. UV/Vis absorption spectra were obtained at 298 K using an Ocean Optics fiber optic system equipped with a low intensity PX-2 pulsed xenon lamp and a USB2000-XR1- ES detector; samples were prepared as 0.1

mM solutions of the complexes in THF in 1 cm quartz cuvettes. Solid state magnetic susceptibilities were measured at 298 K with a Johnson Matthey Mark I instrument.

2.4.6 Gas Chromatography Product Analysis

Gas samples (5 mL) were drawn from the bulk electrolysis cell by means of a Vici gas tight syringe (Cat # 050055). The samples were injected into a Shimadzu GC-2014 Fuel Cell Analyzer gas chromatograph, with an argon gas mobile phase. The products were analyzed on a dual sensor system equipped with a thermal conductivity detector and a flame ionization detector.

2.4.7 DFT Calculations

Geometry optimizations were performed on **1**, **2**, and **3** using the coordinates obtained from the crystal structure as starting point. A Hessian calculation that was performed on the optimized structures showed no imaginary frequencies. The Firefly software package was utilized in conjunction with the B3P86 functional and the 6-31G(d,p) basis set with diffuse functions on heteroatoms and the cobalt center.[151] A larger basis set was used to run energy calculations, consisting of the Wachters basis set for the cobalt center and the TZVP basis set of Barbieri et al. for the remaining atoms.[152,153] Orbitals and spin density plots were visualized and rendered using Chemcraft.[154] Initially, spin density calculations on the doubly reduced species 3 were performed with no restrictions, however, this lead to spin contamination (S^2 = 1.038). Thus, the results displayed are those of a restricted open shell calculation.

Chapter 3: Controlled Electrodeposition of Gold for CO_2 Catalysis

3.1 Introduction

Heterogeneous catalysis is a widely studied field in photoelectrochemical cell design with distinct approaches for proton reduction, water oxidation, and carbon dioxide reduction. The most kinetically simple of these cases, the hydrogen evolution reaction (HER), has been dominated by the catalytic efficiency of platinum. The reason for this is clear – using the hydrogen binding energy with a metal surface as a barometer for catalytic activity, one finds that Pt has a near optimal (i.e. close to zero, $|\Delta G_{0,M\text{-}H}| \approx 0$) binding affinity for protons. For metals that form strong M-H bonds, (i.e. $|\Delta G_{0,M\text{-}H}| << 0$) the release of hydrogen gas is disfavored and proton binding effectively poisons the metal surface. For metals that have little affinity for proton binding (i.e. $|\Delta G_{0,M\text{-}H}| >> 0$), the rate of activation is low, thus lowering the catalysis. If one plots experimental reactivity *versus* the calculated M-H bond energy, a volcano plot is obtained (see Figure 42).[155] Very few catalysts have been able to increase the catalytic activity for the HER over that obtained by platinum. In one case, Greeley and coworkers found through computational screening that a PtBi surface alloy showed a lower value for $|\Delta G_{0,M\text{-}H}|$ and showed, through subsequent experimentation, that it did indeed show an increased catalytic activity.[155]

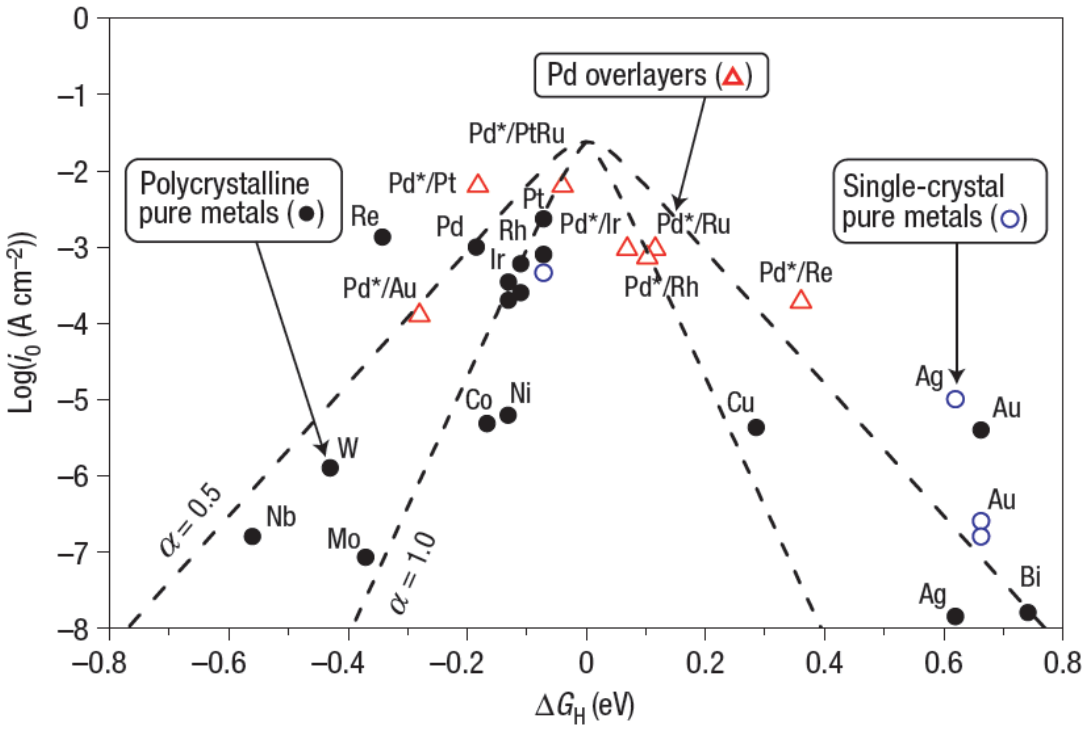

Figure 42. Energy diagram for the metal hydride adsorption. A traditional volcano plot was obtained in which the metals with binding energies close to zero show the highest catalytic activities.[155]

Although platinum remains the standard bearer for activity, the search continues for more cost-conscious materials for the HER. The most widely studied of the non-platinum materials used for this purpose is molybdenum sulfide (MoS_2). This catalyst shows a H-bonding free energy close to zero and shows onset potentials ranging from –0.1 to –0.2 V *vs.* RHE.[156] It has been shown that the catalytic activity of this electrocatalyst comes from edge sites rather than crystalline faces.[157] Further work is being performed in transition metal sulfides, nitrides, carbides, sulfides, phosphides, and selenides – particularly those of iron, cobalt, and nickel.[27]

The case of water oxidation is more complex than that of hydrogen reduction due to the multiple steps required in the reaction. The reaction is formally a four electron, four proton oxidation, resulting in dioxygen. Arguably, the most critical step in this process is O–O bond formation.[158] Heterogeneous catalysts for this transformation typically center on metal oxides, sulfides, and phosphides of 3*d* transition metals that would be prone to oxygen bond formation. Some of the most active catalysts tested to date include $NiFeO_x$, $CoFeO_x$, and IrO_x.[159]

In comparison to both proton reduction and water oxidation, carbon dioxide reduction represents a more difficult challenge. There are a wide variety of factors that result in a complex and difficult transformation. The activation of carbon dioxide is much more difficult than that for protons, due to the activation energy required in CO_2 reduction. For instance, the standard potential for the $CO_2 \rightarrow CO_2^{\bullet -}$ transformation is *ca.* -1.9 V *vs.* SCE. There are a large number of intermediates to consider from carboxylates to carbenes, or extended carbonates.[160,161] A wide variety of potential CO_2 reduction products (5 C-1 products, as well as higher order products) makes the selectivity of the transformation difficult to control.[162] The vast majority of past research has focused on metal oxides – particularly TiO_2.[163,164] Currently, however, there has been much research focusing on metals and metallic nanoparticles with varying composition, size, and morphology.

3.1.1 Heterogeneous CO_2 Reduction on Metal Electrodes

Many metals have been probed for their activity specifically in relation to product selectivity. In 2008, Hori published a large review of carbon dioxide reduction at metal

electrodes, showing their relative selectivity and activities.[165] These compounds are summarized in Table 6. In potassium bicarbonate buffer, at a constant current density of 5.0 mA cm^{-2}, it was shown that gold electrodes had the highest selectivity specifically for the $CO_2 \rightarrow CO$ transformation, while copper electrodes had a higher affinity for further reduced products as well as higher order C-2, C-3 products. Indeed, Jaramillo *et al.* discovered 16 total products are produced at copper metal electrodes under electrolytic conditions.[166] Importantly, copper surfaces are capable of stabilizing intermediate stages in the CO_2 reduction cycle, allowing access for further reduction and coupling of surface-adsorbed intermediates, specifically CO.[162] Furthermore, incorporation of copper into platinum based catalysts greatly increased their selectivity for CO_2 reduction over hydrogen generation.[167]

Table 6. The product distributions of a variety of metal electrodes run at constant current in 0.1 M $KHCO_3$ that were adapted from Hori *et al*.[165]

Electrode	Potential (V *vs.* SHE)	Current Density (mA cm^{-2})	Faradaic Efficiency (%)				
			CH_4	CO	$HCOO^-$	H_2	Total
Pb	-1.63	5.0	0	0	97.4	5.0	102.4
Hg	-1.51	0.5	0	0	99.5	0	99.5
In	-1.55	5.0	0	2.1	94.9	3.3	100.3
Sn	-1.48	5.0	0	7.1	88.4	4.6	100.1
Cd	-1.63	5.0	1.3	13.9	78.4	9.4	103.0
Au	-1.14	5.0	0	87.1	87.1	10.2	98.0
Ag	-1.37	5.0	0	81.5	81.5	12.4	94.6
Zn	-1.54	5.0	0	79.4	79.4	9.9	95.4
Pd	-1.20	5.0	2.9	28.3	28.3	26.2	60.2
Cu	-1.44	5.0	33.3	1.3	9.4	20.5	103.5
Ni	-1.48	5.0	1.8	0	1.4	88.9	92.4
Fe	-0.91	5.0	0	0	0	94.8	94.8
Pt	-1.07	5.0	0	0	0.1	95.7	95.8

3.1.2 Mechanism of CO_2 Reduction on Gold

While planar gold electrodes have shown higher selectivity for the $CO_2 \rightarrow CO$ transformation when compared to other metal electrodes, the activity is low. Between 2012 and 2014, several reports investigating the use of gold nanostructures (clusters, nanoparticles, wires, oxides, etc.) show the highly specific and active production of CO.[168–174] The mechanistic insights provided by these studies can help guide towards increased performance of homogeneous gold based electrocatalysts.

Early work by Kauffman *et al.* probed the electrochemical activity of Au_{25} nanoclusters in aqueous electrochemical measurements (Figure 43).[168] In this study, they found that there is a weak interaction between precise Au_{25} nanoclusters and CO_2 in solution that results in spectral features that evidence an oxidized cluster. It was also found that the activity of Au_{25} nanoclusters outperformed those of larger nanoparticles (2 and 5 nm AuNPs) with an onset potential of –0.2 V *vs.* RHE and an activity of ~10 mmol cm^{-2}_{Au} hr^{-1} (at –0.9 V *vs.* SHE). At low overpotentials, the Faradaic efficiency for the $CO_2 \rightarrow CO$ reaction is close to unity, although at more cathodic potentials, the activity of CO formation increases in conjunction with parasitic H_2 production. This is explained by the increased proton capture at these potentials, which has the dual effect of increasing the rate of the CO_2 catalytic cycle and allowing for release of hydrogen.

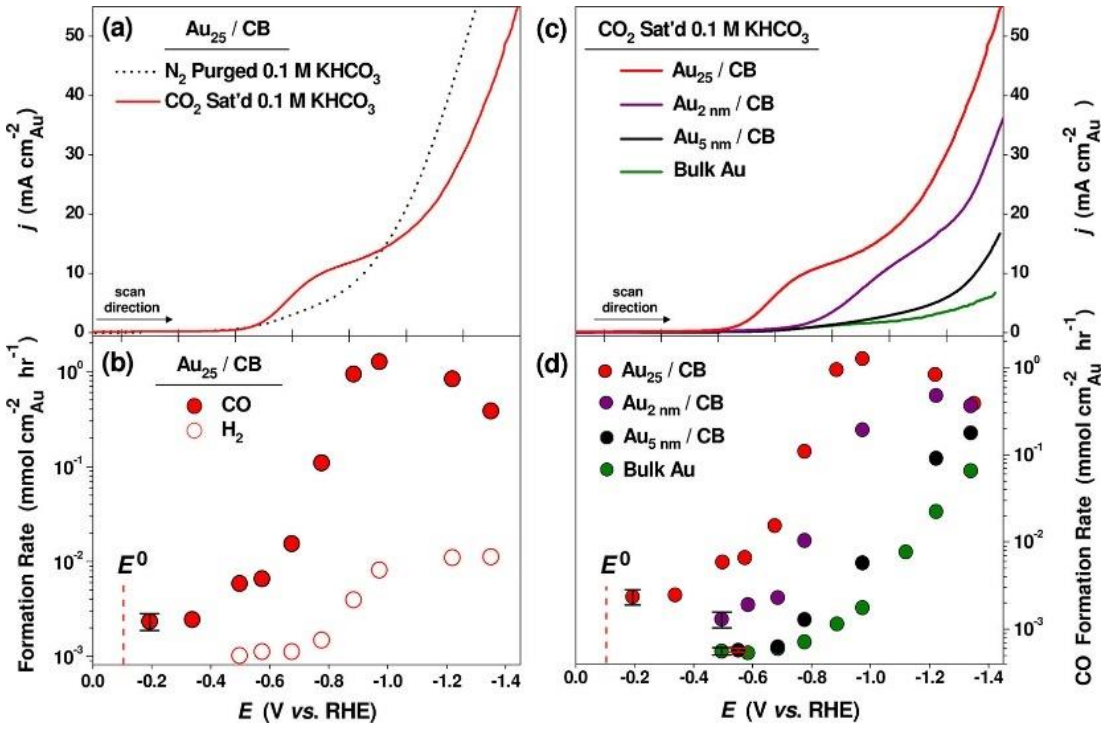

Figure 43. Catalytic responses observed on Au_{25} nanoclusters in comparison to those of AuNPs (2 and 5 nm) as well as bulk gold.[168]

Work by Zhu *et al.* in 2013 used larger sized nanoparticles to determine the catalytic capability and mechanism of non-discreet AuNPs (Figure 44).[170] In this comparative study, 4, 6, 8, and 10 nm gold nanoparticles were tested for their activity for the $CO_2 \rightarrow CO$ transformation. It was found that nanoparticles that are 8 nm in diameter were the most selective catalysts for CO over H_2 generation. This phenomenon is explained by comparing the relative rates of reactivity for face *vs.* edge *vs.* corner sites on nanoparticles. Through DFT calculations, it was shown that edge atoms of the nanoparticle produce the bulk of catalytic activity for CO_2 reduction, with 8 nm AuNPs having an optimal number of edge sites.

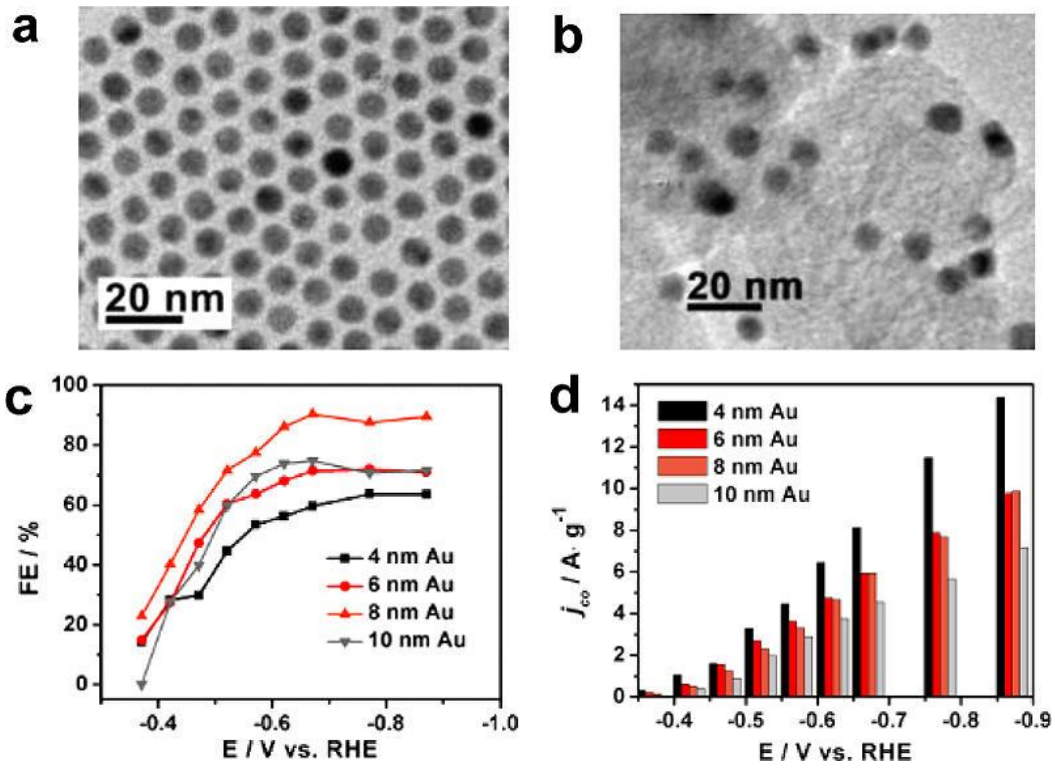

Figure 44. TEM images and catalytic activities for the AuNP derived catalytic reduction of CO_2 to CO.[170]

Using this insight, gold nanowires – a morphology that will greatly increase the percentage of active edge sites – were tested for their activity in the selective $CO_2 \rightarrow CO$ reaction (Figure 45).[174] This study showed larger activity occurred with increasing length of the nanowires as well as a reduction in overpotential and greater Faradaic efficiency, supporting the claim of active edge sites in the heterogeneous electrocatalyst.

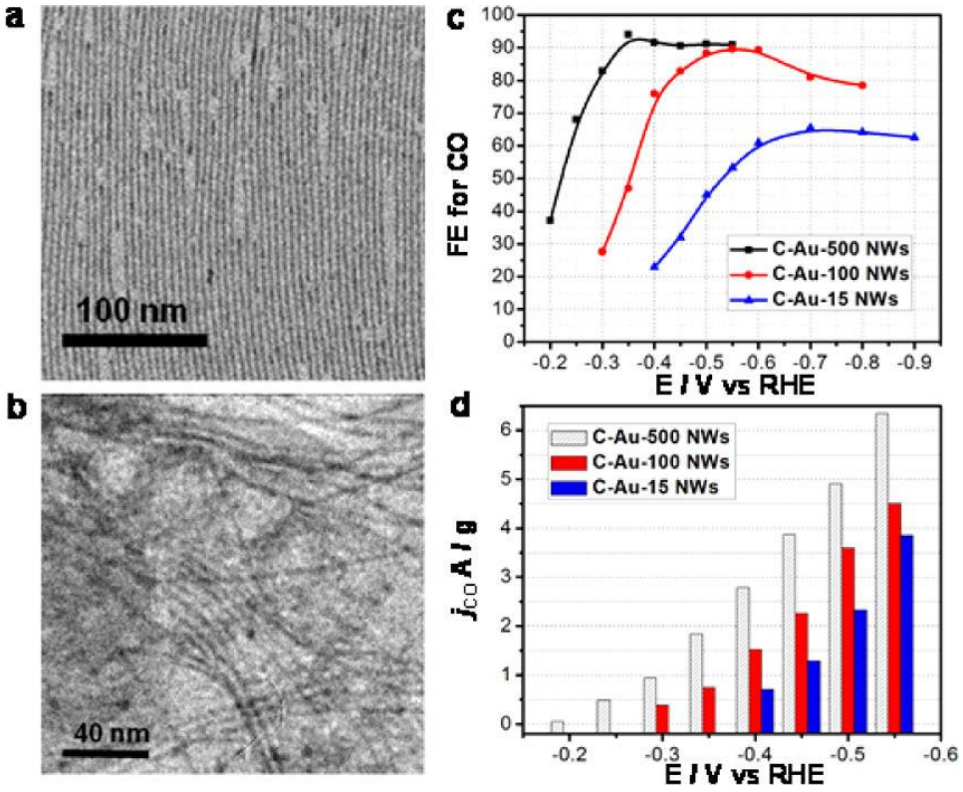

Figure 45. TEM images and catalytic activities for the gold nanowires showing the increased activity and selectivity with longer lengths.[174]

Work on larger sized nanoparticles (18.3 ± 4.4 nm) by Feng *et al.* showed a large dependence on grain boundary concentration (Figure 46).[175] Initial depositions resulted in polycrystalline nanoparticles that had up to four grain boundaries per nanoparticle. Through annealing at different temperatures, these samples increased in nanoparticle size while systematically decreasing the density of surficial grain boundaries. Through these experiments, a clear correlation between decreased grain boundary density and decreased $CO_2 \rightarrow CO$ selectivity was found, suggesting that these boundaries are the catalytically active species.

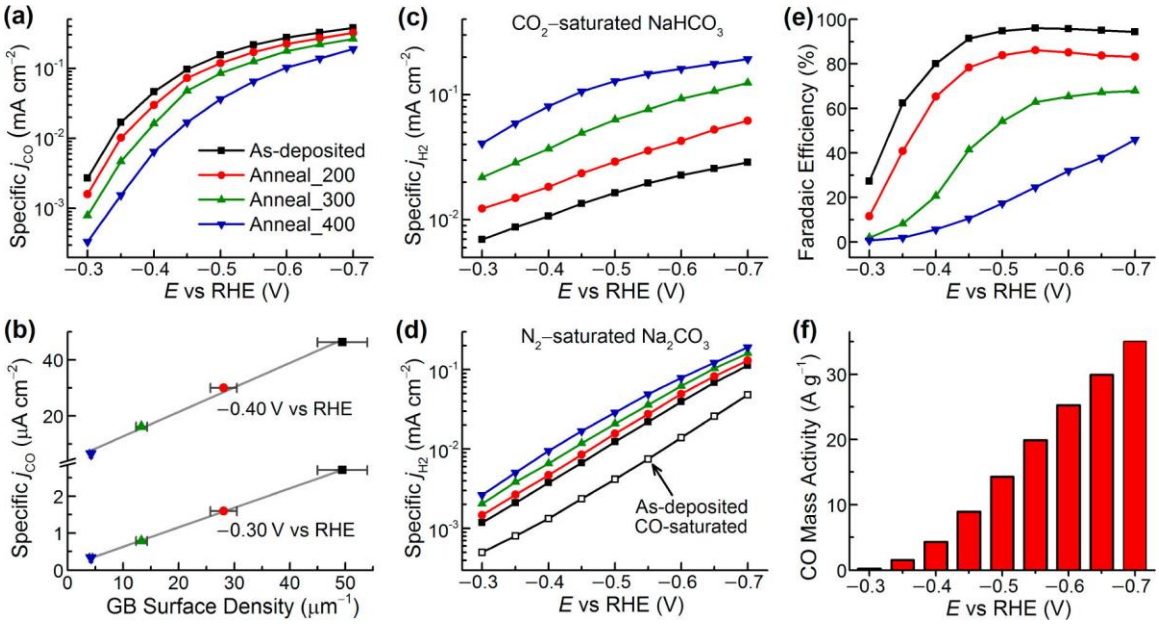

Figure 46. Catalytic responses for carbon dioxide reduction on large gold nanoparticles (~20 nm) and as a function of their grain boundary concentration.[175]

Gold nanoparticles have previously been deposited on glassy carbon (GC) supports and tested electrochemically.[172] In these studies, gold nanoparticles approximately 4 nm in diameter were capped with dodecane thiol and spin coated onto GC electrodes with an approximate surface coverage of 3,000 AuNPs μm^{-2} and tested for catalytic activity. Under these conditions, a roughly equal amount of CO and H_2 were produced, similarly to bulk Au. Scanning electron microscopy analysis of these surfaces showed that surface migration of the AuNPs lead to dendritic assembly on the electrode surface under reducing conditions – a phenomenon that may account for the reduced selectivity under these conditions (Figure 47). Further reports have investigated the catalytic activity of bimetallic gold-silver and

gold-copper nanoparticles, indicating increased performance over their monometallic analogs.[171,173]

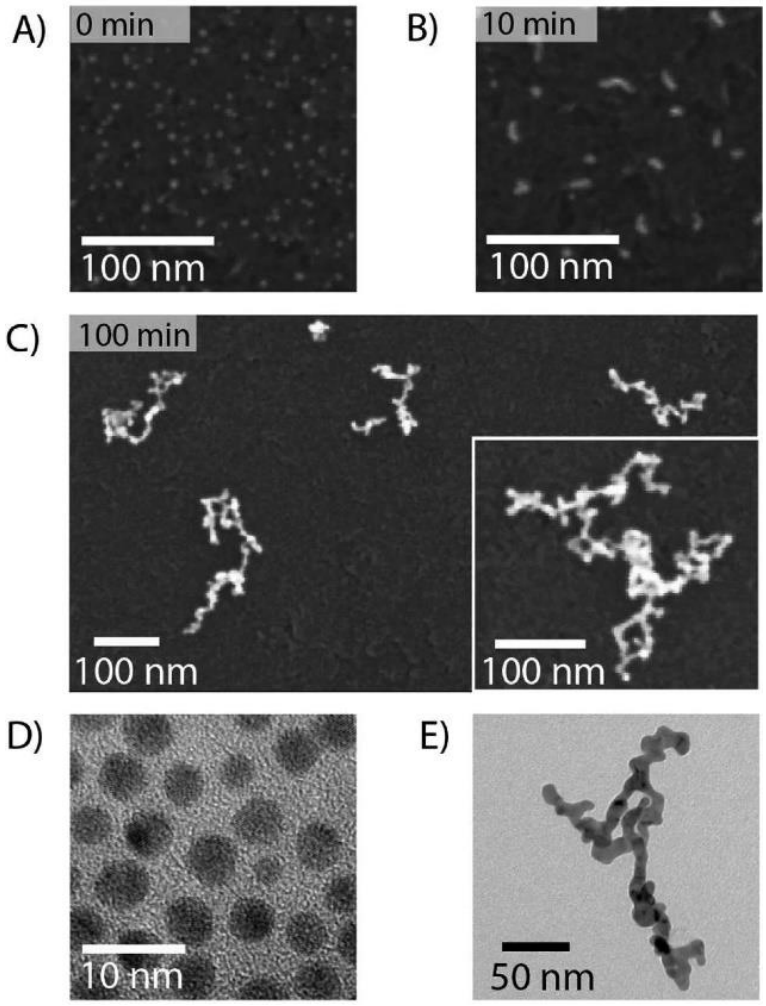

Figure 47. Scanning and tunnelling electron microscopy of glassy carbon electrodes decorated with gold nanoparticles prior to and after electrolysis showing agglomeration on the electrode surface.[172]

Interestingly, a recent DFT calculation performed on gold and silver clusters implicate AuNP corner sites as the most active and selective for CO_2 reduction to CO.[176] In this study, the binding energies of adsorbed COOH, CO, H, and OH were compared

(hereafter, adsorbed species are labelled with an asterisk). The stability of *COOH was used as a metric for the activity of the AuNP for CO production with stronger binding leading to increased activity. The strong binding of *H and *OH could potentially poison catalysis by occupying active sites while the binding energy of *CO should be somewhat weak to allow for its release. The results of these DFT calculations show the strongest *COOH binding and weakest *H binding for corner sites, suggesting it as the most active and selective site (see Table 7). For the calculations on silver nanoparticles, edge sites were implicated as the most active indicating AgNPs could show similar or enhanced characteristics for the catalytic reduction of CO_2 to CO when compared to AuNPs.

Table 7. Calculated binding energies for *H and *COOH on silver and gold as proxies for the activities of carbon dioxide reduction and proton reduction (lower values indicate a higher activity for the reaction).[176]

(eV)	Ag			Au		
	facet (111)	Edge (211)	Corner ($Ag_{309}NP$)	facet (111)	edge (211)	corner ($Au_{309}NP$)
G(*COOH)	1.25	0.79	0.95	1.21	0.70	0.62
G(*H)	0.62	0.45	0.71	0.54	0.21	0.58

3.1.3 Emulsion Deposition and Collision Experiments

Collisions of a wide variety of small particles has been detected on ultramicroelectrodes in emulsion systems, with metal nanoparticles, polymer particles, and large biological molecules and viruses.[177–182] In terms of collisions, there are three descriptive analytical techniques – electrolysis experiments in which a redox active molecule is reduced or oxidized in an emulsion; blocking experiments in which a non-conductive particle blocks the current of an otherwise active redox couple in solution; and catalytic experiments in which a catalytically active nanoparticle 'turns on' catalysis of a substrate in solution.[182,183] All of these phenomena can be observed in potentiostatic experiments through observation of the current at an ultramicroelectrode (UME). To date, no report has shown the successful collision of reverse phase emulsions that result in the electrolysis of an aqueous species. We wished to develop this method in order to controllably deposit metal structures on the surface of an electrode through electrolysis of emulsion droplets in solution.

3.2 Results and Discussion

We report the synthesis of gold nanodeposits on carbon electrodes using an emulsion system. A water-in-oil emulsion, where the oil phase was comprised of dichloroethane (DCE) and tetrabutylammonium hexafluorophosphate, and the aqueous phase was made up of water and a gold salt precursor, was synthesized using sodium dodecyl sulfate as the surfactant. When a droplet collides with a carbon macroelectrode biased at a potential where aurate reduction to gold metal is favorable, a nanodeposit is

formed. The size of these nanodeposits correlated with the initial concentration of the aurate salt, indicating that size-selection of these nanodeposits is possible by tuning the concentration. By studying the collision of these droplets on a carbon fiber ultramicroelectrode (CF-UME), a size distribution of droplets and nanodeposits was calculated from Faraday's Law. The frequency of nanodroplet collision on the CFUME agreed well with calculated values. We further show that this method can be applied to the study of nanodeposit catalysis of the CO_2 reduction reaction.

3.2.1 Deposition Experiments on UMEs

Experiments conducted on CF-UMEs showed a clear collision response when the working electrode was poised at a potential of -0.5 V *vs.* Ag/Ag^+ (approximately -0.8 V *vs.* Fc/Fc^+). In this experiment, a large concentration of aqueous emulsion droplets was used in a continuous dichloroethane phase to allow for observation of droplet electrolysis. By integrating the area under a collision event, the charge passed can be determined. By using the known initial concentration of gold, an average gold droplet size can be determined simply by division of the known number of electrons passed (in mol) by the molarity of the solution. From these experiments, it was determined that water-in-DCE emulsions using sodium dodecyl sulfate as a surfactant (300 mM) produced droplets that had an average radius of 650 nm.

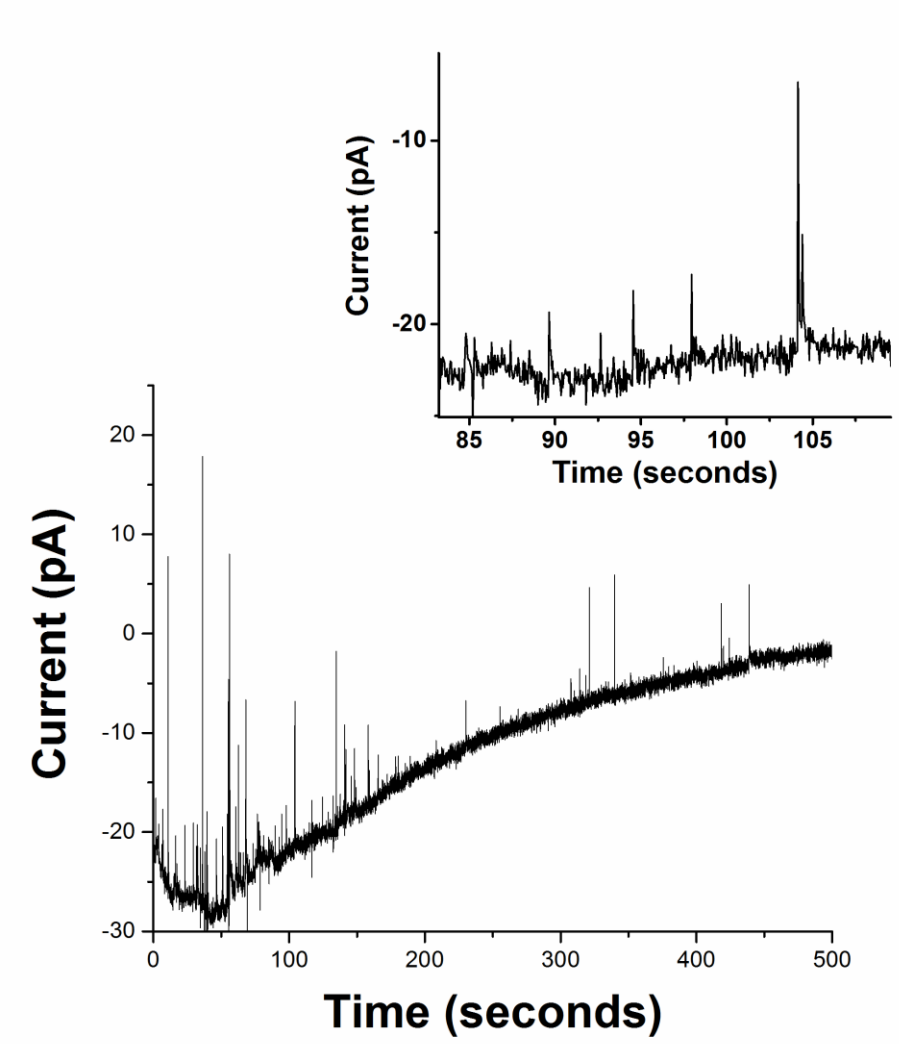

Figure 48. A typical electrolysis experiment was performed on a glassy carbon ultra-micro electrode poised at -0.5 V vs. Ag/Ag^+ showing collision events in a water-in-DCE emulsion.

3.2.2 Macro Experiments – Control of Size

The size dependence of the emulsion system was investigated on carbon foil electrodes using emulsions consisting of 20 μL of aqueous solution with SDS surfactant (300 mM) in 20 mL of DCE electrolyte (0.1 M $TBAPF_6$). This dilute emulsion ([droplet] ~ 1.44 picomolar) proved sufficiently concentrated to give reasonably dense coverage (>

10 nanodeposits per square micrometer) on the electrode after five minutes of electrolysis. Although the standard reduction potential of gold is very positive at +1.5 V, no deposition was observed at 0 V *vs.* Ag/Ag^+, however a negatively poised electrode (-0.5 V *vs.* Ag/Ag^+) showed moderate coverages.

From X-ray photoelectron spectroscopy, one can determine the surficial coverage of gold (by integration of the Au 4*f* signal), which shows a linear relationship with the initial gold concentration. The XPS signals were normalized to the peak for carbon at a binding energy of 284.6 eV. From these spectra, gold signals were observed at 84 and 87.5 eV, consistent with Au(0). Peaks that would correspond to oxidized Au(I) or Au(III) were not observed.

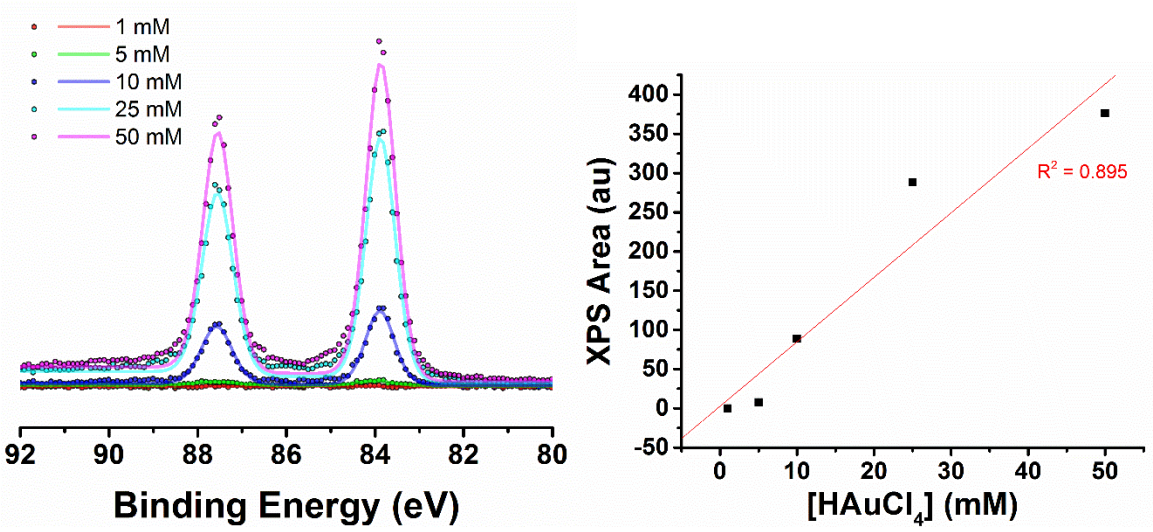

Figure 49. Correlation between the integrated XPS area for the Au 4*f* region spectra as a function of the initial gold concentration in the emulsion droplets.

From scanning electron microscopy (SEM), it is clear that the changing concentration of gold directly affects the size of the nanodeposits (Figures 50 to 54). The standard deviation of nanoparticle size scales with the concentration of gold, likely correlated with the polydispersity of emulsion droplets. Growth of the nanodeposits is irregular and does not result in typical cuboctahedron geometries seen in most AuNPs. This can be seen at high magnification under SEM where even 5 mM Au solutions produce non-uniform deposits.

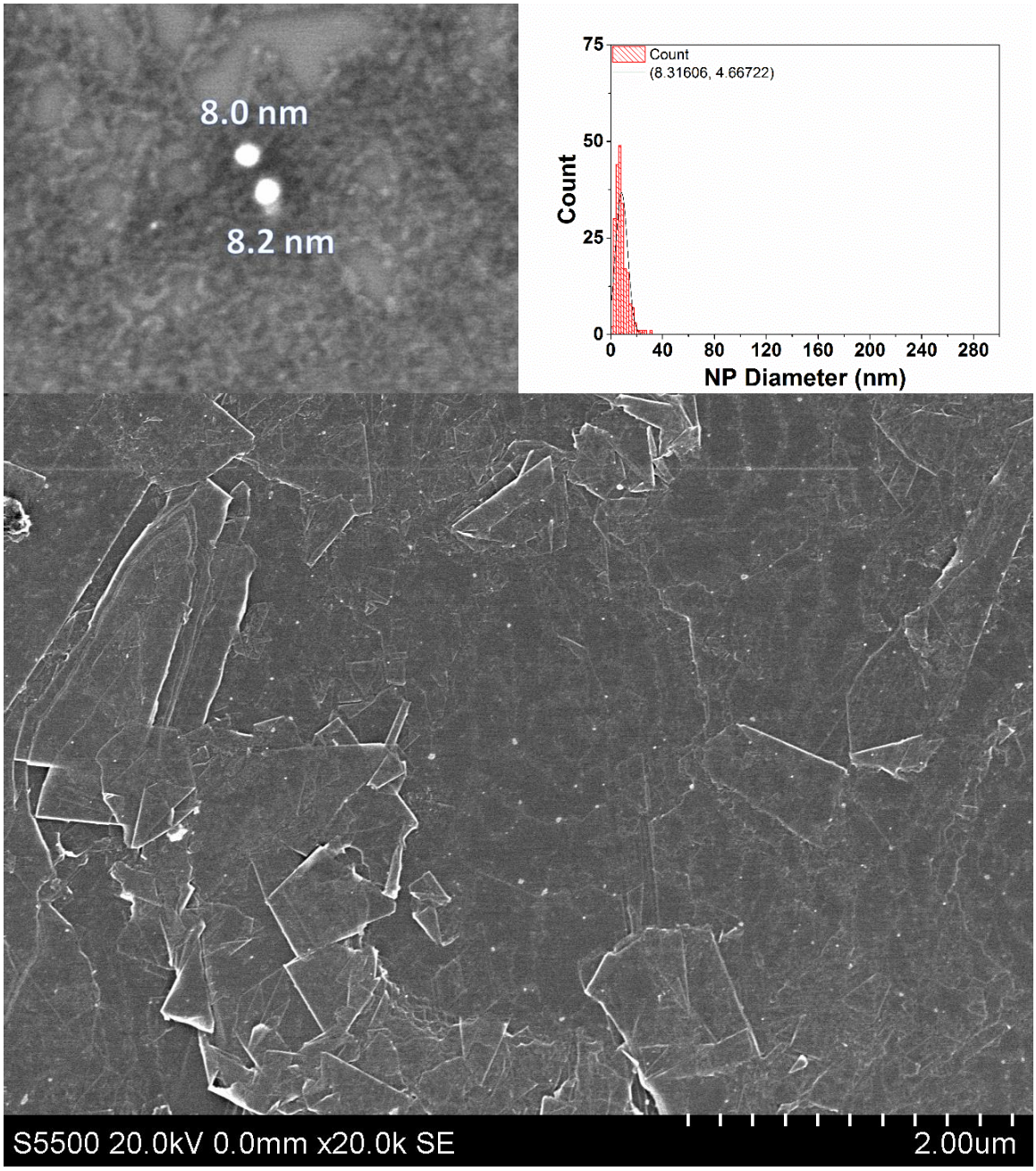

Figure 50. Representative SEM images obtained by electrolysis of 1 mM Au emulsion solutions on a carbon foil electrode. Top left: high magnification image showing the morphology of deposits, top right: distribution of the nanodeposit diameters, bottom: low magnification (20k ×) SEM mage.

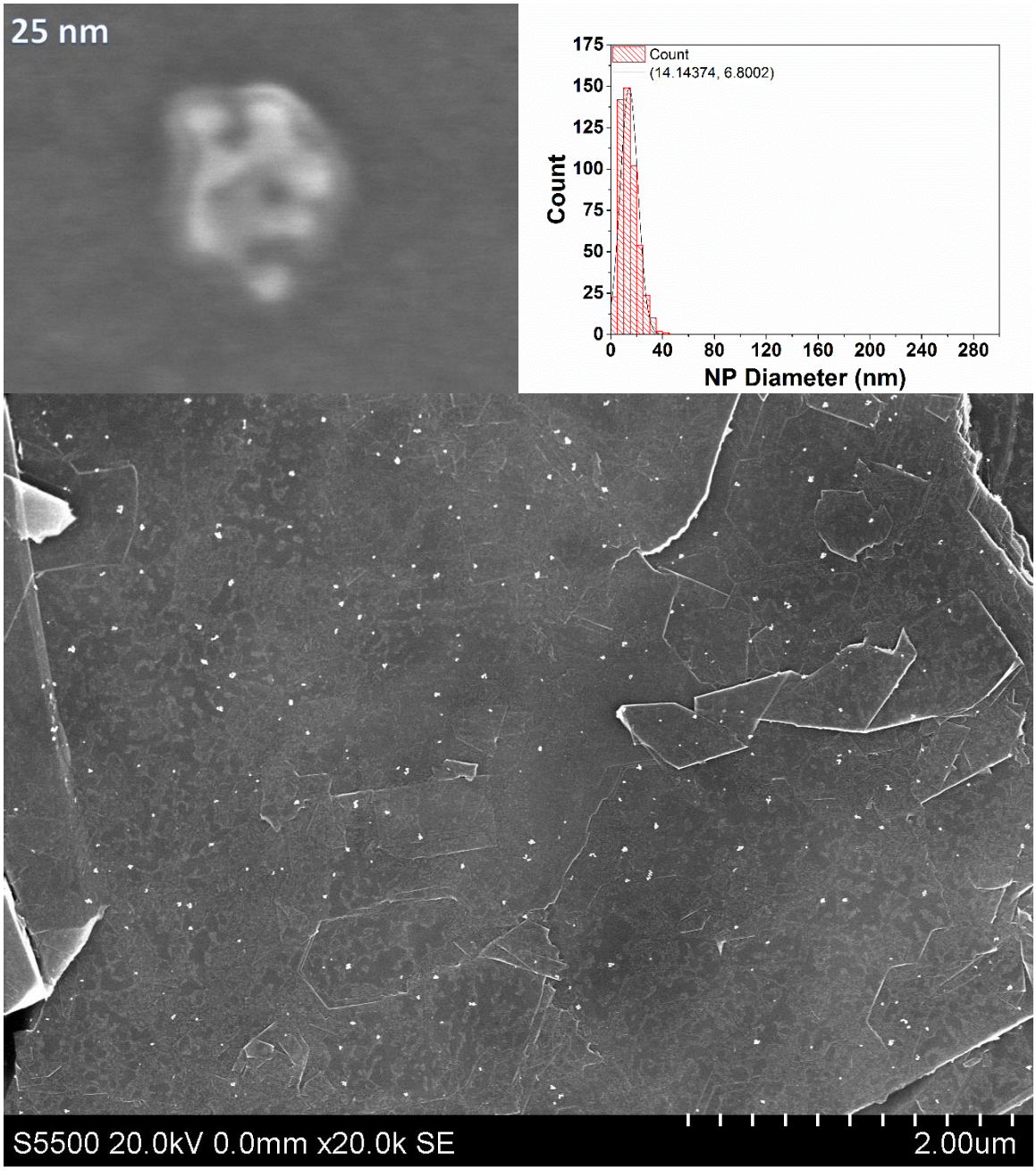

Figure 51. Representative SEM images obtained by electrolysis of 5 mM Au emulsion solutions on a carbon foil electrode. Top left: high magnification image showing the morphology of deposits, top right: distribution of the nanodeposit diameters, bottom: low magnification (20k ×) SEM mage.

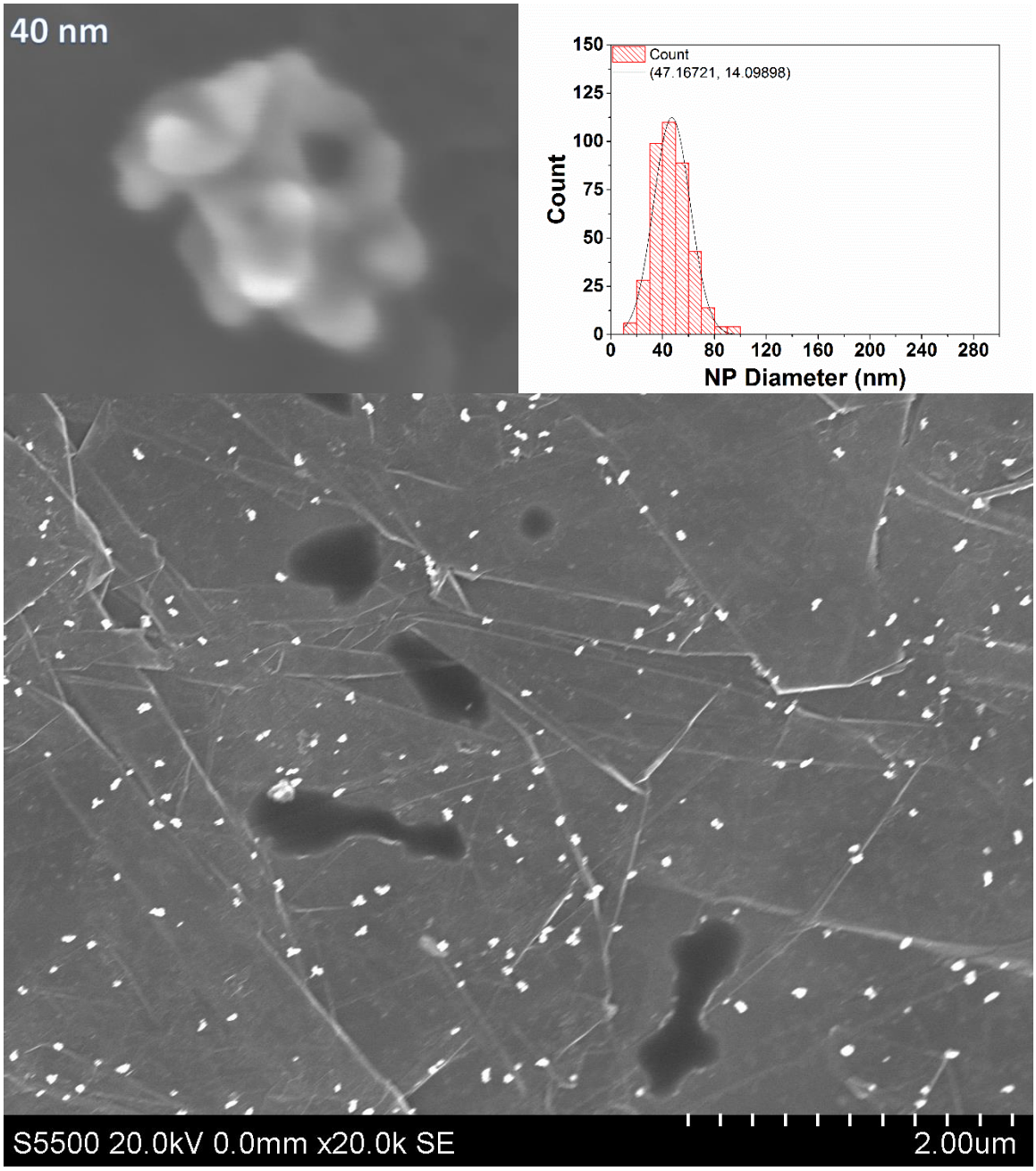

Figure 52. Representative SEM images obtained by electrolysis of 10 mM Au emulsion solutions on a carbon foil electrode. Top left: high magnification image showing the morphology of deposits, top right: distribution of the nanodeposit diameters, bottom: low magnification (20k ×) SEM mage.

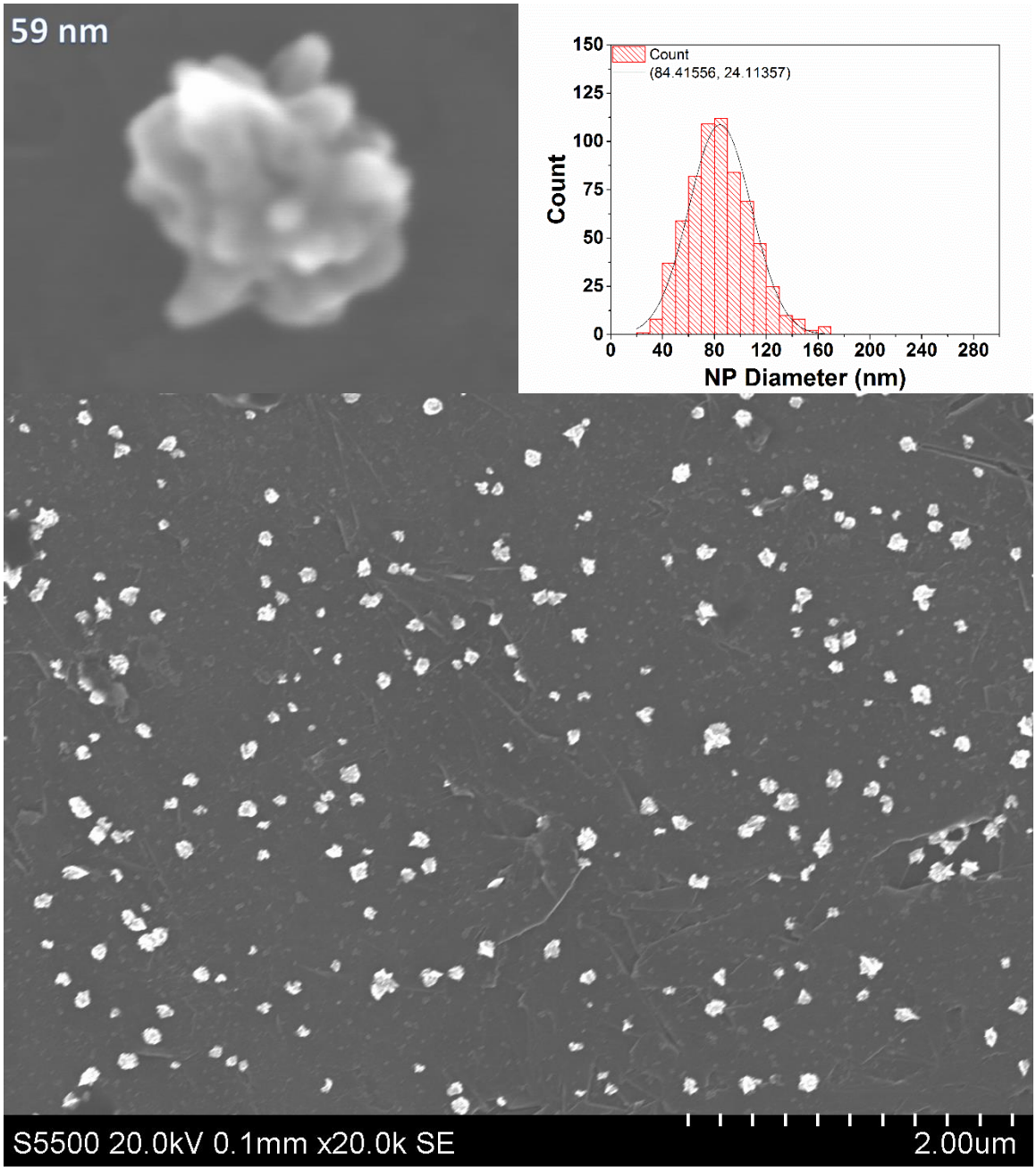

Figure 53. Representative SEM images obtained by electrolysis of 25 mM Au emulsion solutions on a carbon foil electrode. Top left: high magnification image showing the morphology of deposits, top right: distribution of the nanodeposit diameters, bottom: low magnification (20k ×) SEM mage.

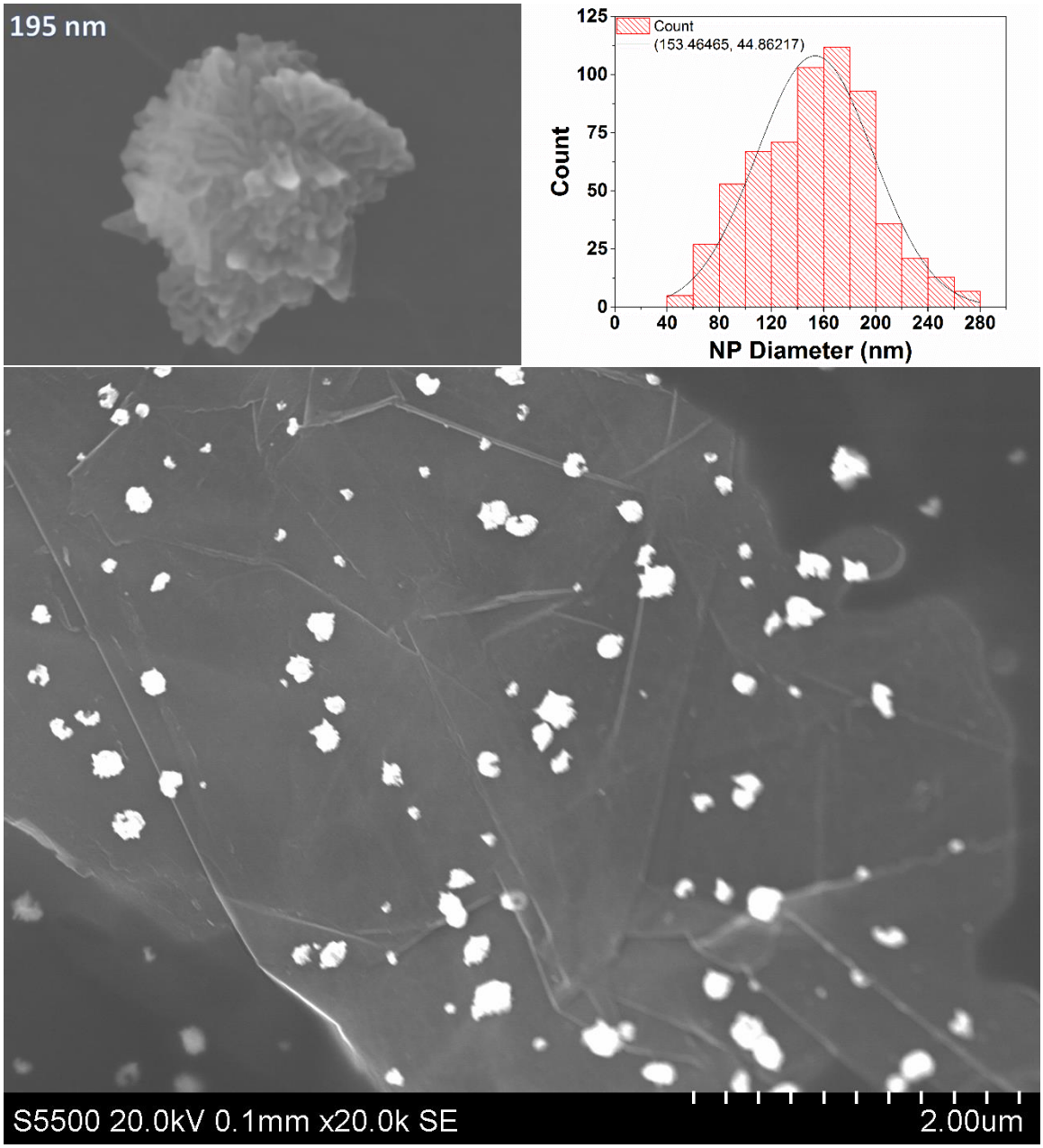

Figure 54. Representative SEM images obtained by electrolysis of 50 mM Au emulsion solutions on a carbon foil electrode. Top left: high magnification image showing the morphology of deposits, top right: distribution of the nanodeposit diameters, bottom: low magnification (20k ×) SEM mage.

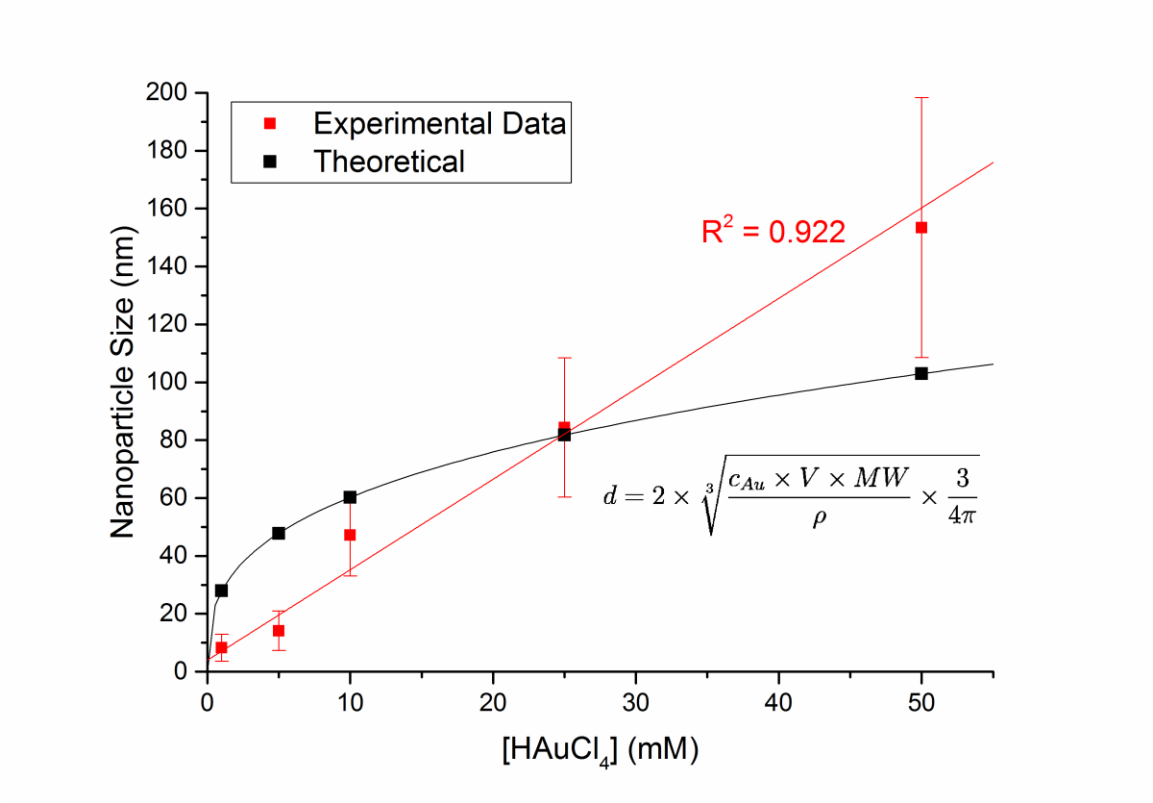

Figure 55. Comparison of the theoretical (expected for spherical growth) and experimental diameter of gold nanodeposits as a function of initial gold precurson concentration.

Interestingly, if the average size is plotted with respect to initial gold concentration, a linear relationship is shown rather than the expected cubic relationship for uniform nanoparticles (Figure 55). This shows that the growth mechanism of nanodeposits is not uniform, creating shapes that are not consistent with typical cuboidal AuNPs. This is clear upon close inspection of nanodeposits. After annealing the samples at 400 °C, the size observed by SEM drops markedly. In the case of 50 mM [Au] solutions, the size reduced to between 80 and 120 nm, in line with the expected diameter. Unfortunately, due to surface migration, the smaller nanodeposits coalesced on the surface to NPs approximately 20-30

nm in diameter, disallowing a comparison between size and gold concentration after annealing. The foregoing results support the conclusion of non-uniform deposition shape, rather than changing droplet size, as predicted from the initial SEM images.

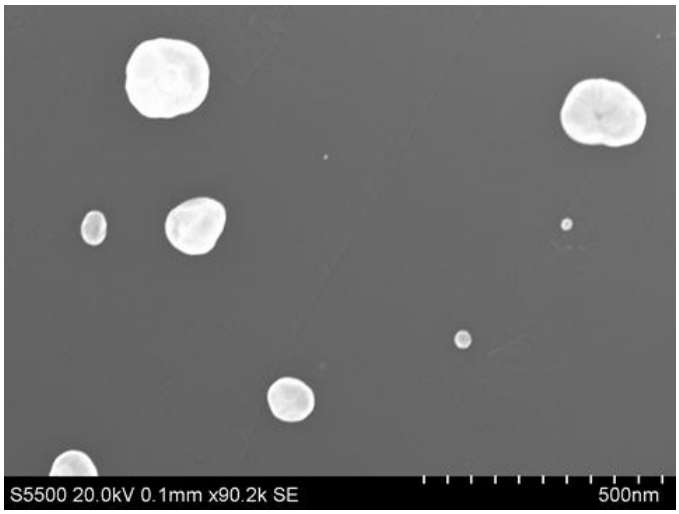

Figure 56. SEM image from an annealed electrode onto which gold was deposited from a 50 mM emulsion in DCE.

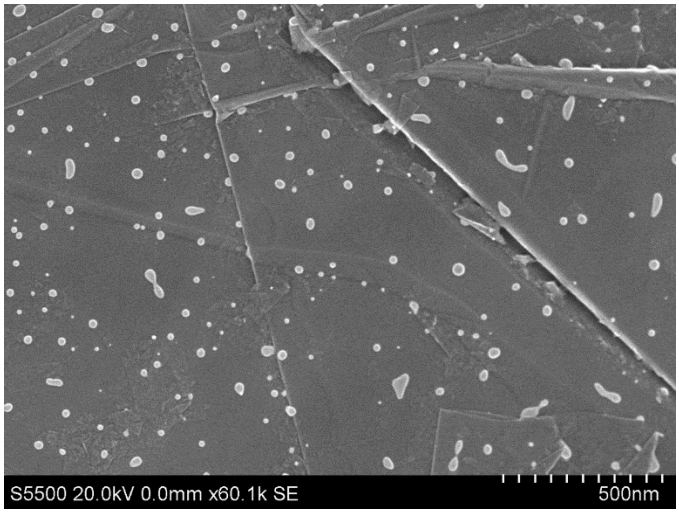

Figure 57. SEM image from an annealed electrode onto which gold was deposited from a 1 mM emulsion in DCE showing surface migration and agglomeration into larger deposits.

This method has been attempted with several other metal precursors, with limited success. Most depositions with platinic acid or copper sulfate resulted in no observable depositions or very sparse deposits. Even though their redox potential is positive, a large negative applied potential was necessary (-1.0 V *vs.* Ag/Ag^+) to observe any depositions at all. The use of $AgNO_3$ as a metal precursor, however, resulted in reproducible depositions at -0.5 V *vs.* Ag/Ag^+. The EDX spectra of both Au and Ag deposits confirm their elemental composition (Figure 58). In comparison to the gold deposits, however, these were smaller and did not have a roughened morphology and showed a much larger degree of aggregation (Figure 59). Attempts were made to make a mixed precursor system, however, the corresponding solubility of Au and Ag salts precluded the generation of a stable solution with both metal precursors.

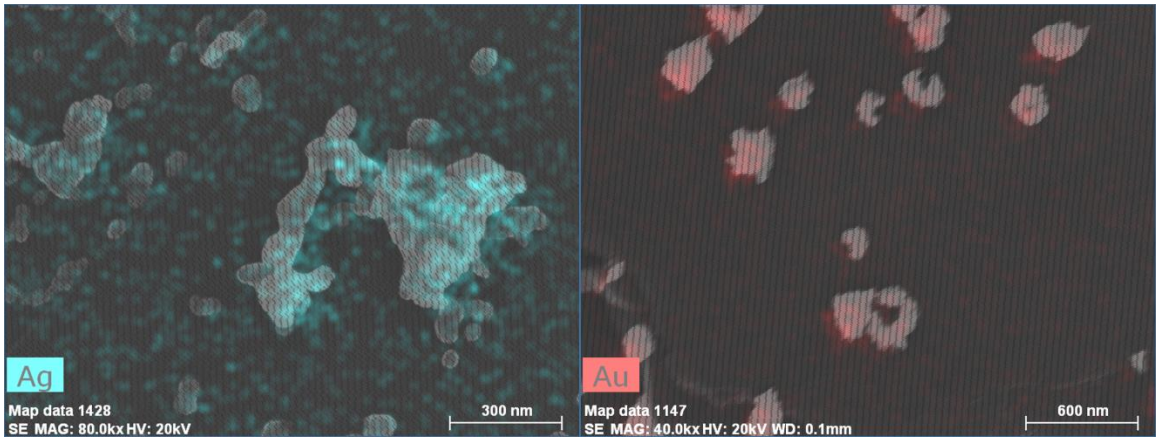

Figure 58. Energy dispersive X-ray mapping images confirming the deposition of metallic gold and silver nanostructures.

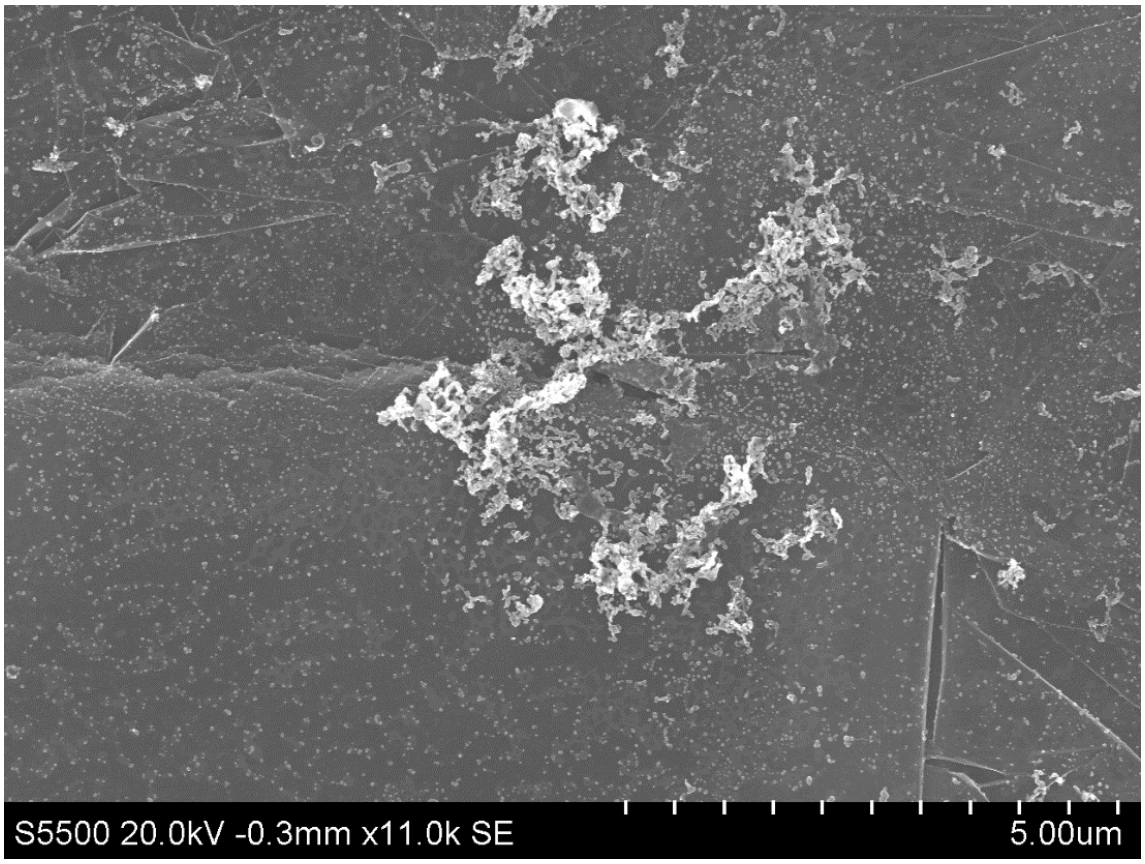

Figure 59. Scanning electron micrograph of a silver ($AgNO_3$) emulsion deposition showing a large degree of aggregation in addition to those of individual deposits.

3.2.3 Macro Experiments – Control of Coverage

Modifications of this method were attempted in order to gain control of the overall coverage of nanodeposits on the electrode surface. This requires increasing the overall number of surface collisions through either increasing the droplet concentration or performing electrolysis for an extended period of time. Using 1 mM emulsion droplets, electrolysis was performed over extended time periods of 5, 10, 30, and 60 minutes. Rather than increase the coverage of uniform 8 nm deposits, the extended time periods increased

the average size of nanodeposits as seen in SEM. This result indicates the successive deposition of gold from droplets preferentially occurs at previously deposited sites.

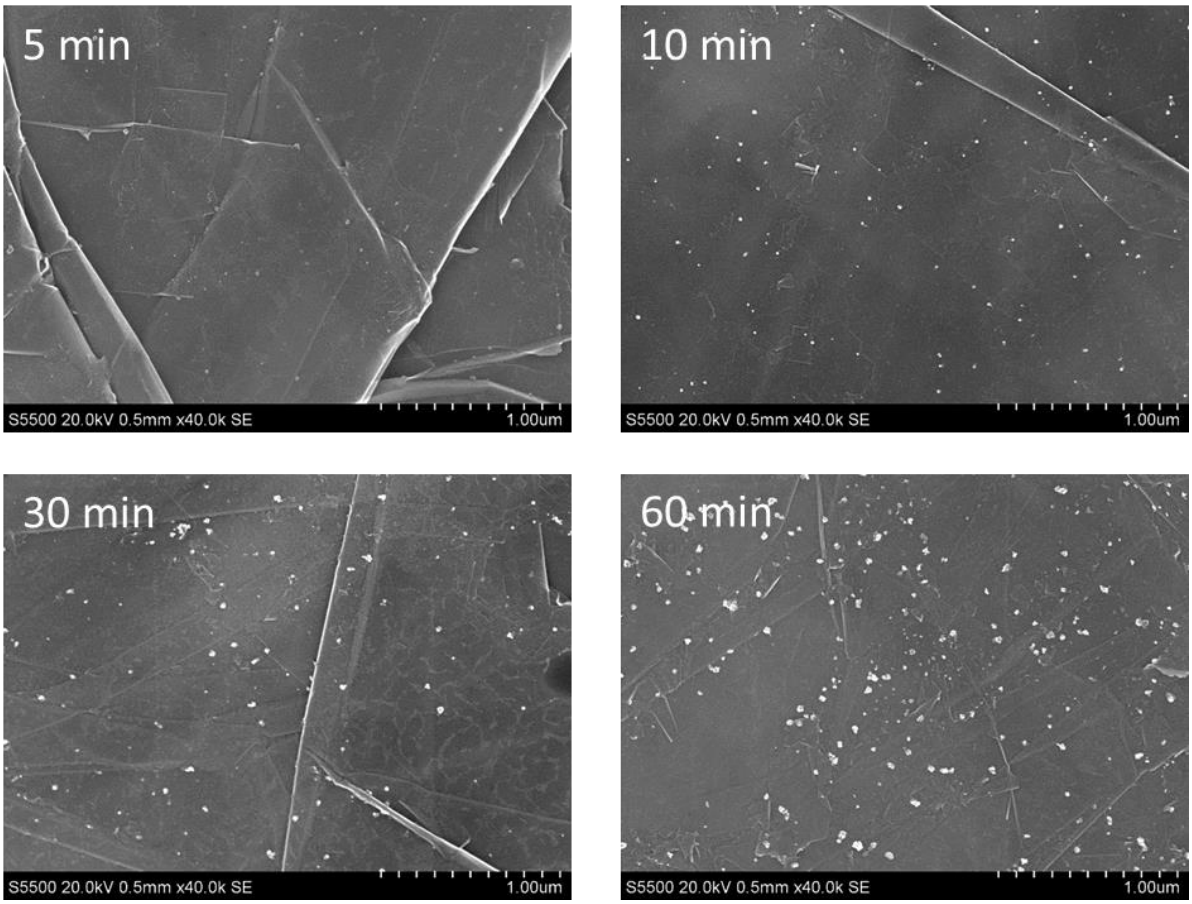

Figure 60. SEM images taken after 5, 10, 30, and 60 minute electrolyses using a 1 mM gold precursor in a water/DCE emulsion.

Another method was attempted to control coverage by variation of the concentration of the emulsion droplet in the system. This was achieved by adding increasing amounts of the water solution into the DCE organic phase (20, 40, 60, 80, 100 μL) and running the electrolysis for five minutes in each case. Because, in each case, the concentration of SDS would remain the same, the emulsion droplet size is expected to

remain constant. Thus, the effect of increasing the organic phase would be simply to increase the droplet concentration. However, at much larger concentrations, the aggregation of emulsion droplets has been observed. Similar to the time dependent experiments, these studies showed an increasing deposit size rather than increasing coverage.

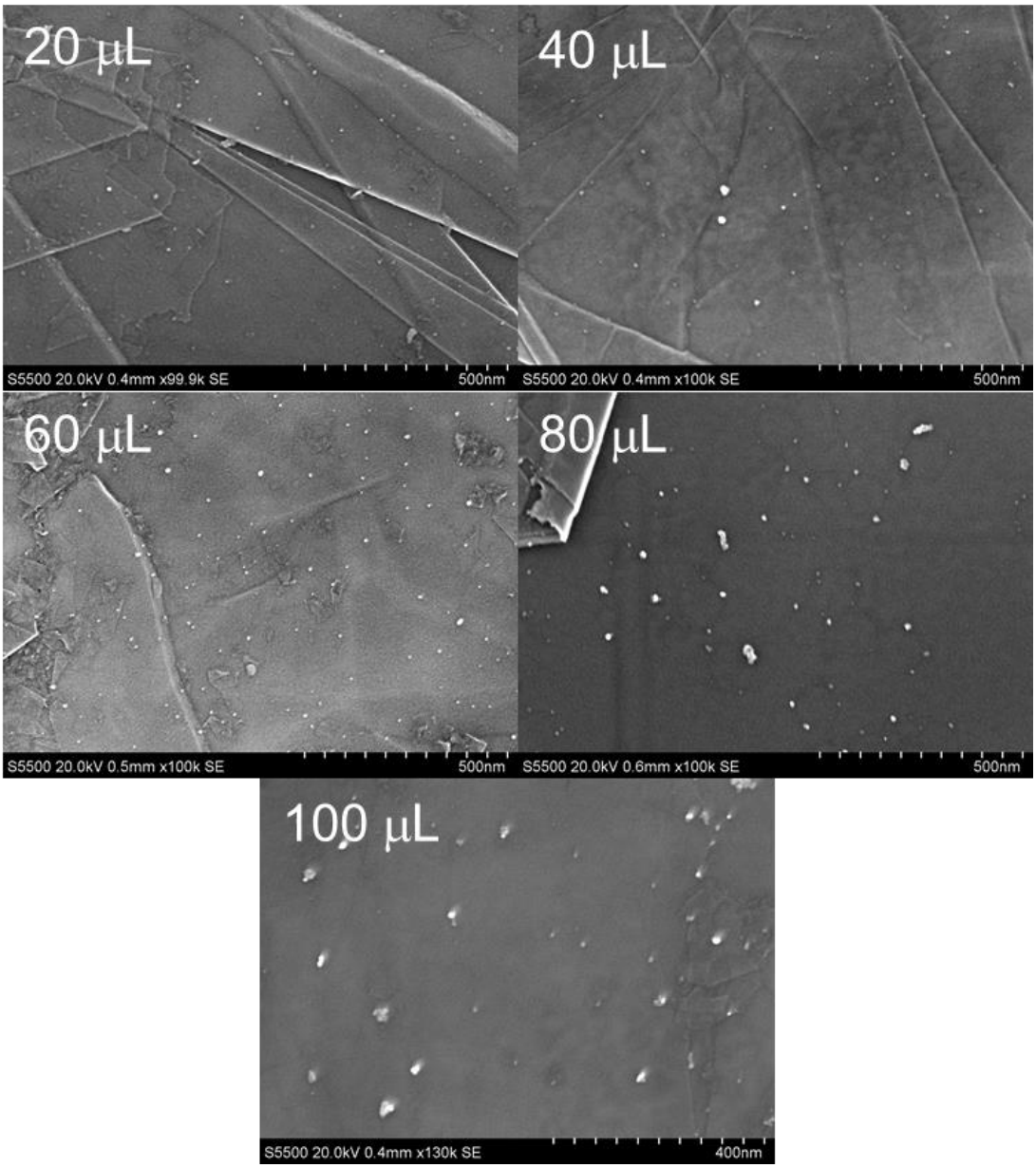

Figure 61. SEM images taken from gold emulsion depositions with varying droplet concentrations.

This phenomenon may have several explanations as outlined in Scheme 6. Firstly, migration along the electrode surface of small, metastable gold clusters to an already-established deposition site during the collision would increase deposit sizes with increased

collisions. Secondly, while it has been shown that the electroactive area of colliding droplets is on the scale of one nanometer, the area of close contact between the droplet and the electrode may be much larger than this area. Based on this overlap, deposition may preferentially occur at a previously deposited nanocluster site in close proximity to the boundary of the emulsion.

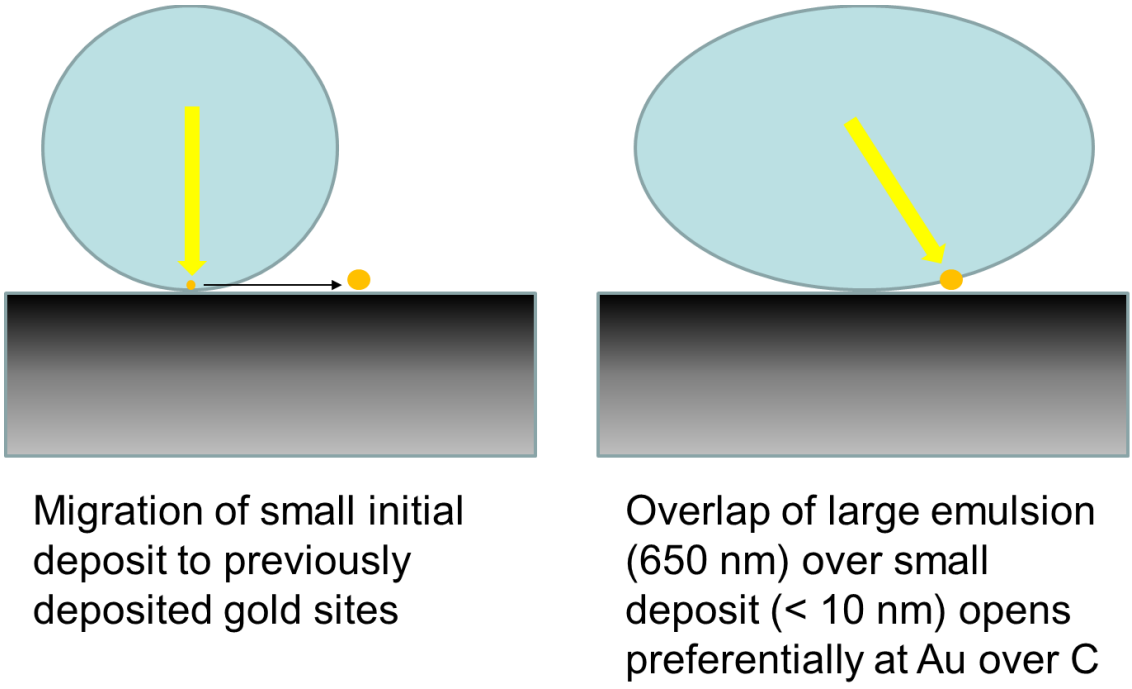

Scheme 6. Potential deposition mechanisms that feature a high number of individual collisions showing preferential growth at previously established deposition sites.

3.2.4 Electrocatalysis of Deposited Gold Nanocrystallites

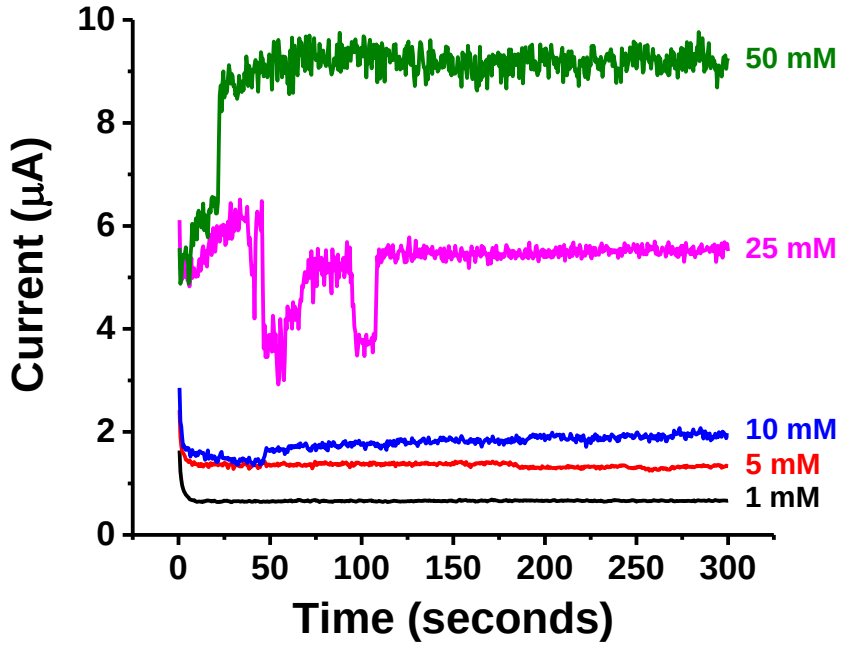

Figure 62. Current profiles for gold depositions on glassy carbon button electrodes with varying initial gold precursor concentrations.

Electrocatalytic experiments were performed on glassy carbon button electrodes (*d* = 3 mm) following the same deposition mechanism as those performed on larger form carbon foil electrodes. The depositions were performed in a three electrode cell at a constant potential for five minutes. Integration of the electrolysis curve allows for a determination of the total current passed and ultimate determination of the quantity of gold deposited. The total amount of gold deposited ranged from 0.14 μg to 1.82 μg, although there was not a clear linear trend to the deposited gold calculated (1 mM, 0.14 μg; 5 mM, 0.28 μg; 10 mM, 0.36 μg; 25 mM, 1.08 μg; 50 mM, 1.82 μg). It was also evident that the convection in the stirred solution has a large impact on current passed, suggesting that the

removal of droplets from the surface after deposition requires additional force from a stirred solution.

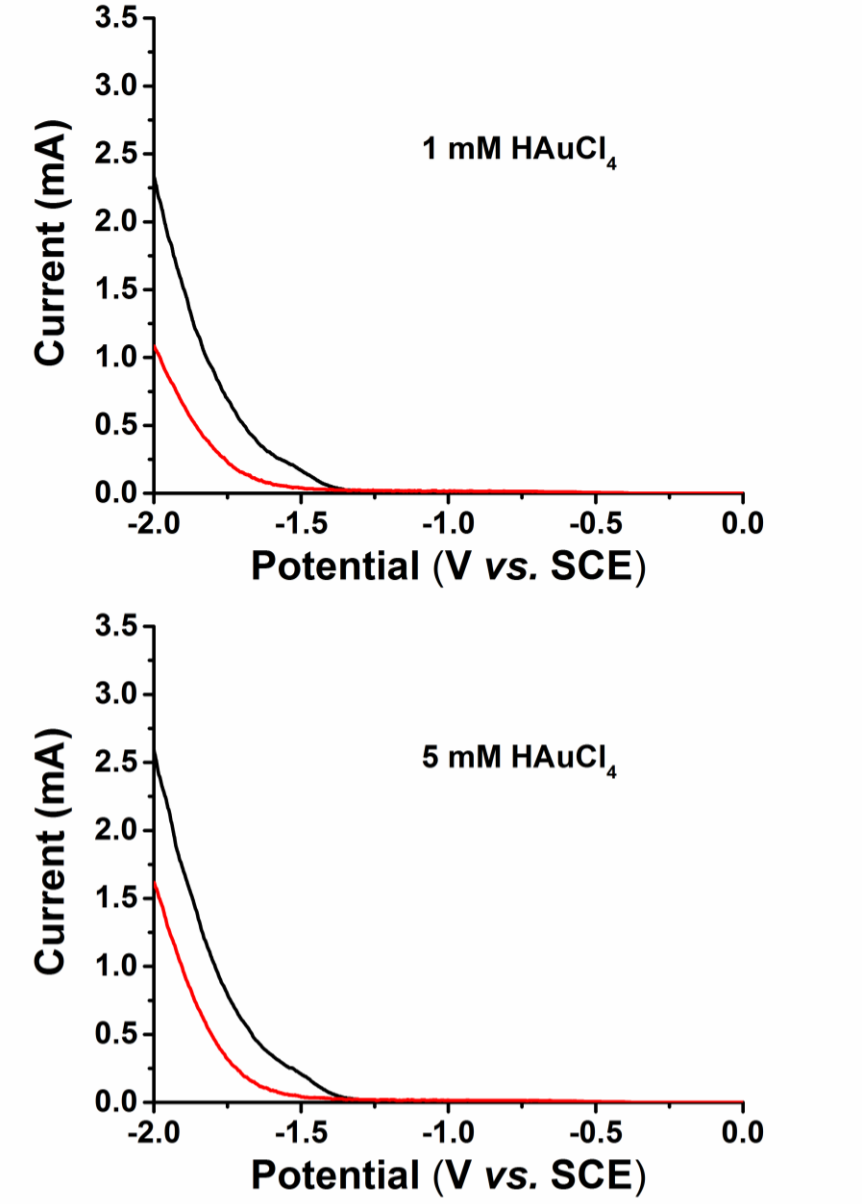

Figure 63. Linear sweep voltammograms in N_2 (red) or CO_2 (black) saturated 0.1 M $NaHCO_3$(aq) on glassy carbon button electrodes onto which gold from 1 mM (top) and 5 mM (bottom) [Au]-emulsion solutions had been deposited.

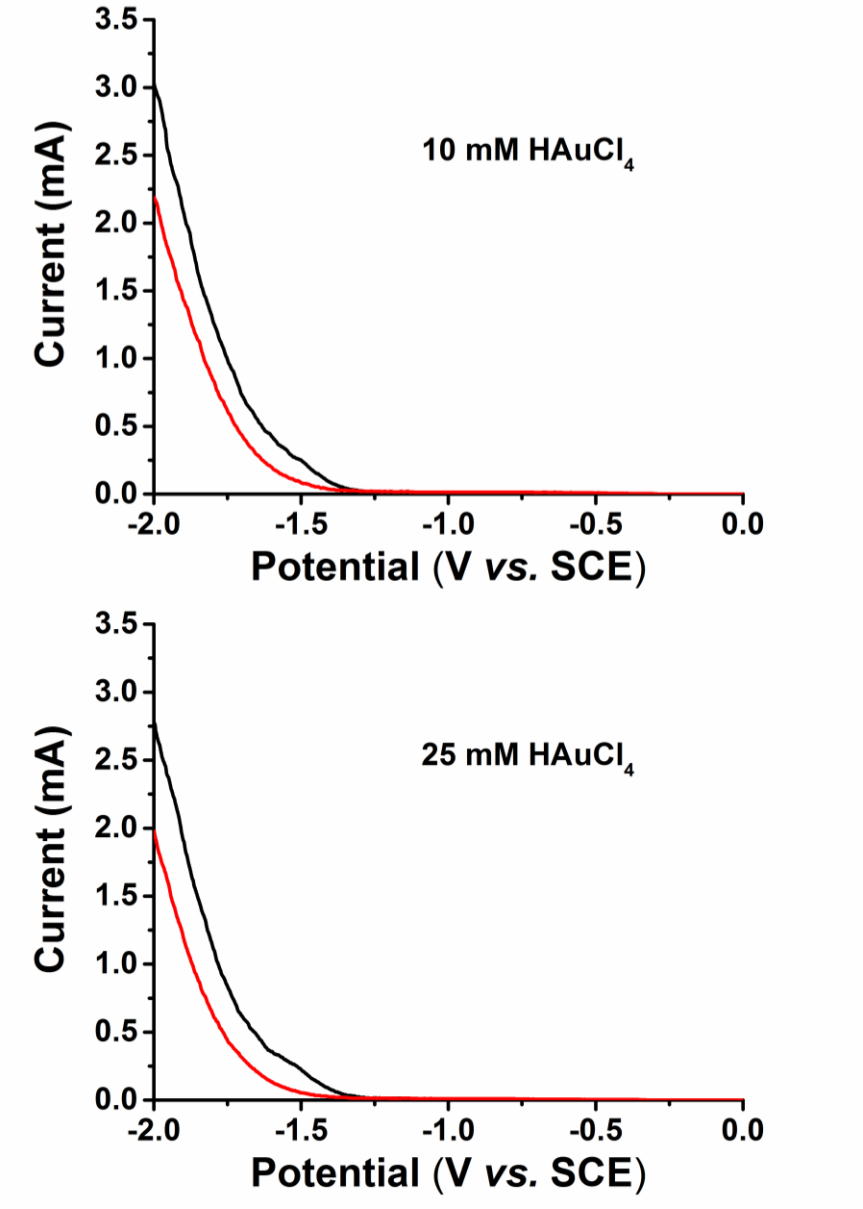

Figure 64. Linear sweep voltammograms in N_2 (red) or CO_2 (black) saturated 0.1 M $NaHCO_3$(aq) on glassy carbon button electrodes onto which gold from 10 mM (top) and 25 mM (bottom) [Au]-emulsion solutions had been deposited.

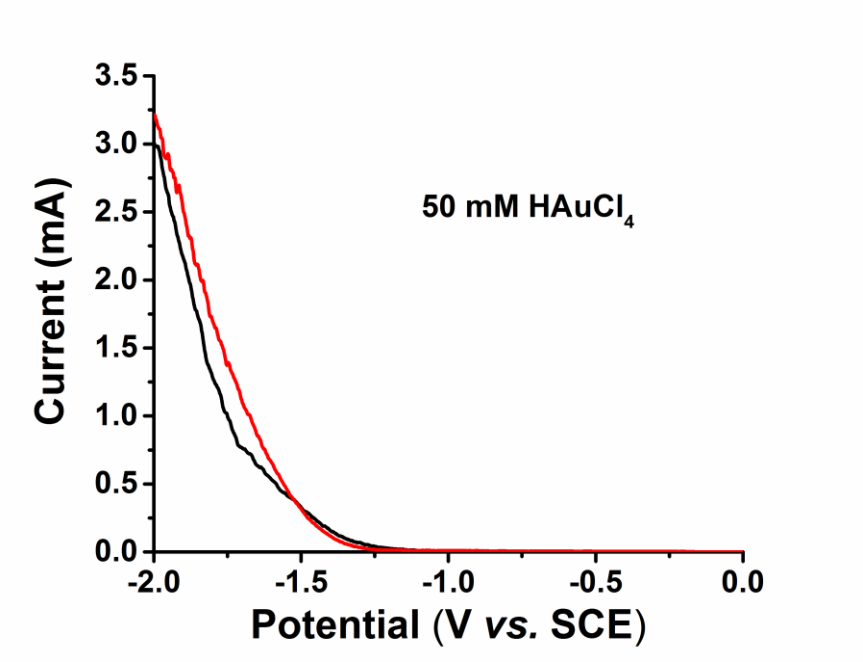

Figure 65. Linear sweep voltammograms in N_2 (red) or CO_2 (black) saturated 0.1 M $NaHCO_3$(aq) on glassy carbon button electrodes onto which gold from a 50 mM [Au]-emulsion solution had been deposited.

Each sample was tested in 0.5 M $NaHCO_3$ to determine the catalytic properties under either N_2 or CO_2 saturation. Under all deposition parameters a large increase in current was observed in comparison to the background current of a glassy carbon button (Figures 63 - 65, see Figure 66 for control LSVs). However, in each case an onset of current is seen between -1.25 V and -1.4 V *vs.* SCE, corresponding to an overpotential of 500 mV for the $CO_2 \rightarrow CO$ transformation and 1.5 V for the $2\ H^+ \rightarrow H_2$ transformation. Although the onset current is relatively negative, in each case a clear shoulder could be observed at -1.5 V *vs.* SCE that may result from catalysis occurring at the nanodeposit surface. This potential is only ~200 mV anodic of the onset observed prior to deposition, which may be due to the very small amount of gold deposited.

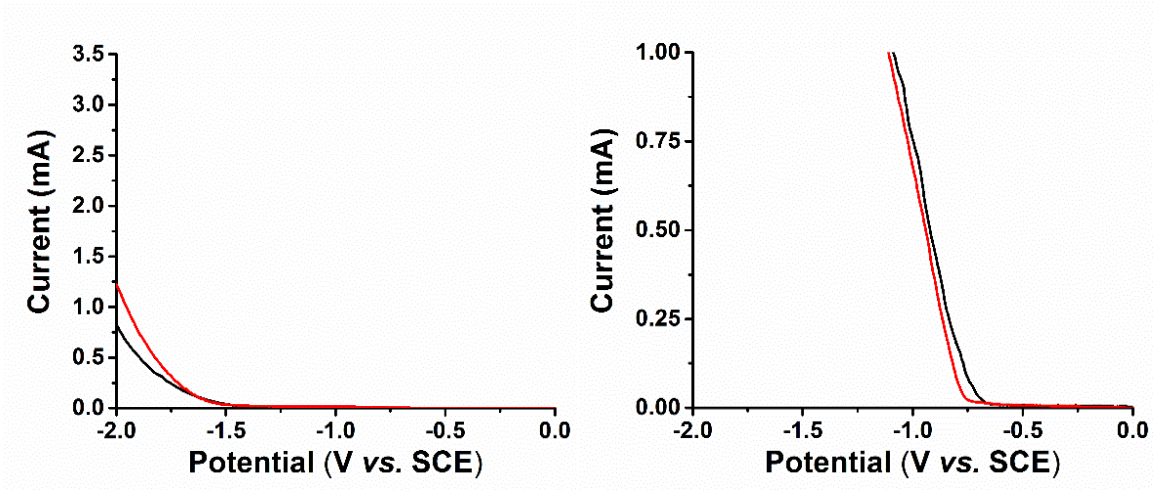

Figure 66. Linear sweep voltammograms in N_2 (red) or CO_2 (black) saturated 0.1 M $NaHCO_3$(aq) deposited on glassy carbon (left) and platinum (right) button electrodes.

While a clear catalytic activity cannot be determined with these data due to the observation of increased current on a bare electrode at -1.5 V *vs.* SCE, several trends are evident. In looking at each deposition sequentially, the current density increases with an increase in the amount of gold deposited, although this trend does not hold across all concentrations. Specifically, at concentrations higher than 10 mM, only minimal additional increases in current at -2.0 V *vs.* SCE are observed. However, in comparing the ratio of current obtained under CO_2 saturation with that obtained under N_2 saturation a size dependence emerges, with smaller nanocrystallites showing preference for CO_2 reduction. This result is in accordance with literature reports in which smaller nanoparticles – with an increased percentage of corner and edge sites as a proportion of the total amount of Au – were implicated in CO_2 catalysis. The deposition resulting from 50 mM solutions shows no clear increase upon CO_2 saturation, while the 1 mM has the largest ratio of current obtained under CO_2 when compared to N_2 saturated electrolyte (~ 2.25:1).

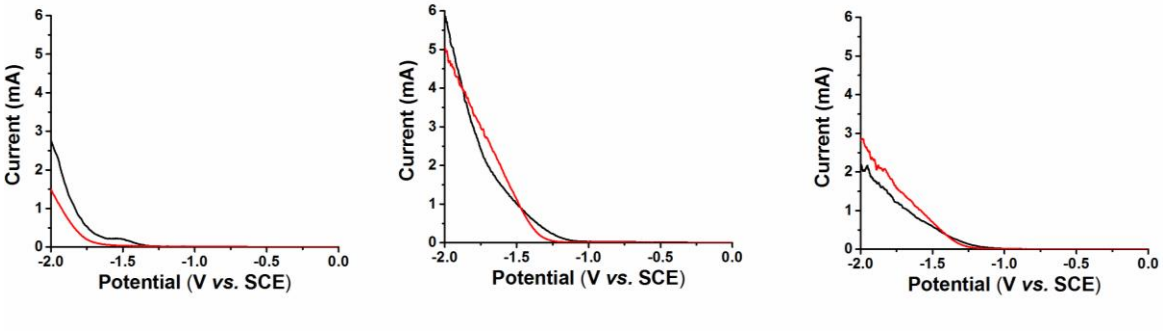

Figure 67. Comparison of catalysis (in N_2 (red) or CO_2 (black) saturated 0.5 M $NaHCO_3$(aq)) obtained from a 1 mM [Au] deposition experiment on glassy carbon along with a 45-minute deposition of a 20 μL : 20 mL solution (left), a 10-minute deposition of a 100 μL : 20 mL solution (center), and the results obtained using an Au button electrode (right).

In order to gain a better understanding of the catalysis that is capable with this deposition mechanism, longer term electrolyses were carried out, the results of which are shown in Figure 67. Initially, a 45-minute electrolysis was performed with a 20 μL:20 mL 1.0 mM [Au] emulsion. This showed a similar selectivity for CO_2 activity and increased current. Importantly, the shoulder centered at -1.5 V vs. SCE was much more prominent in this case. In another experiment, a 100 μL:20 mL 1.0 mM [Au] emulsion was deposited for ten minutes. In this case, observable onset was seen near -1.1 V *vs.* SCE under CO_2 saturated conditions. This onset mimics the value obtained on a gold button electrode indicating a loss of size-dependent catalytic properties. Indeed, in comparison to N_2 saturation, this deposition did not show as much selectivity at more cathodic potentials.

3.3 CONCLUSIONS

Reverse emulsions can effectively be used to deposit metallic crystallites from organic solutions using a suitable surfactant. This type of deposition mechanism allows for a degree of control over deposit size simply by changing the concentration of gold precursors. These depositions resulted in growths that were irregular and that showed unique surface morphologies. Attempts to control the coverage of uniform deposits resulted in increasing deposit size, indicating that preferential deposition occurs at previously established metallic sites. Testing in CO_2 reduction experiments showed that these nano-deposits can be effectively used to directly attach a heterogeneous electrocatalyst to an electrode surface and show some preference for the reduction of CO_2 in aqueous media.

3.4 EXPERIMENTAL

3.4.1 Preparation of Solutions

The following reagents were obtained from Sigma Aldrich: tetrabutylammonium hexafluorophosphate ($TBAPF_6$), sodium dodecyl sulfate (SDS), and tetrachloroauric(III) acid. Ultrapure MilliQ water was obtained from a filtration system. Dichloroethane (DCE) and methanol solvents were obtained from Fisher.

Various solutions were prepared following the same general procedure. First a 300 mM SDS solution was prepared by dissolving 1.73 g of SDS in 20 mL of ultrapure water. Sonication in a water bath aided in complete dissolution of the SDS. Gold solutions for electrodeposition were prepared by dissolving 20 mg of tetrachloroauric(III) acid (50% Au

by weight) in the SDS solution, resulting in 1 mL of 50 mM gold. By serial dilutions of this solution, gold solutions of 25, 10, 5 and 1 mM were prepared using 300 mM SDS solution as the diluent. To form the emulsion, 20 uL of each of the solutions from the serial dilutions was mixed with 20 mL of 0.1 M $TBAPF_6$ in DCE. Prior to electrolysis, these solutions were sonicated in an ultrasonicator for 1.5 minutes to aide in forming emulsions droplets of more uniform size. Additional solutions were made with increasing ratios of aqueous solutions using 40, 60, 80, and 100 mL of the 1 mM gold solution.

3.4.2 Deposition Experiments

A three electrode cell was set-up was used as described in the electrochemistry section. Constant mixing of the solution was applied by a magnetic stir bar. Nitrogen was bubbled into the solution for 5 minutes before performing chronoamperometry and allowed to continue throughout the process. A typical chronoamperometry experiment held the potential at -0.5 V *vs*. Ag/Ag^+ for 300 seconds. For coverage experiments, the length of electrolysis was extended to 600, 1800, and 3600 seconds for the 20 uL of 1 mM gold emulsion solution. After electrodeposition, the electrodes were washed by soaking them in three successive vials of DCE to remove any remaining electrolyte. These were then rinsed with methanol and drying under vacuum overnight.

3.4.3 Scanning Electron Microscopy and X-Ray Photoelectron Spectroscopy

X-ray photoelectron spectra were measured using a Kratos Axis Ultra XPS equipped with an Al-Kα X-ray source monochromated to 1486.5 eV. The photoelectron take-off angle was 0° and the pressure in the acquisition chamber was on the order of 10^{-9}

torr for all samples analyzed. All quantification was performed in CasaXPS software using the Kratos Relative Sensitivity Factor (RSF) library. Survey scans were obtained under the following conditions: pass energy of 80, 1.000 eV step size, and 300 ms dwell time. The Au signals show the expected 4*f* 7/2 and 4*f* 5/2 signals and the total signal area was used. The surface composition and morphology of the wafer pieces were investigated by SEM on a Hitachi S5500 SEM system with a cold probe at a current of 20 mA and voltage of 20 kV.

3.4.4 Electrochemistry

The electrochemical measurements were taken using a Gamry Interface 1000E potentiostat containing a three-electrode cell. A Sonics Vibra-Cell VC 750 sonicator was deployed for forming emulsion droplets. A silver wire electrode served as the quasi reference electrode, a platinum wire functioned as the counter electrode, and carbon foils, glassy carbon buttons, or carbon fiber ultramicroelectrodes were used as the working electrode. Electrocatalytic experiments were performed on a CH Instruments 600E potentiostat with Pt wire counter and Ag reference electrodes.

Chapter 4: Gallium Phosphide in Photoelectrochemical Cells*

4.1 Introduction

4.1.1 Synthesis, Structure and Properties of Gallium Phosphide

While the vast majority of research on PECs focuses on silicon photoelectrodes, there are many reports on other semiconductors, specifically III-V semiconductors (InP, GaAs, GaP, etc). Compound semiconductors have several advantages over silicon, the main one of which is extended band gaps and band edge positions that are well aligned with desired photoelectrochemical reactions. These semiconductors come with a high manufacturing cost and less developed chemistries.

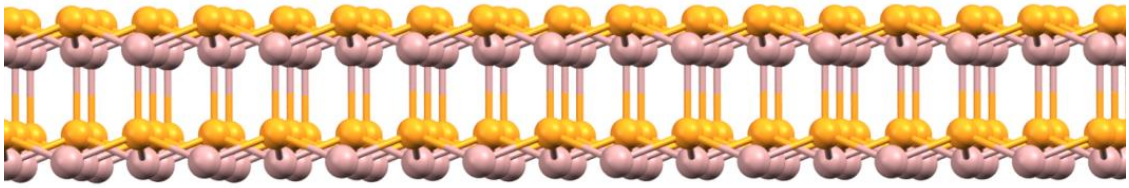

Scheme 7. Zinc blende structure of gallium phosphide featuring surfaces with atop phosphorus (purple) along with gallium (orange) atoms. These surfaces are denoted GaP(111)B and GaP(111)A, respectively. Furthermore, wafers can be cut along a GaP(100) facet that contains both gallium and phosphorus on the surface.

---

*Portions of this chapter have been published elsewhere:
Williams, O. M.; Shi, J. W.; Rose, M. J. *Chem. Commun.* **2016**.
OMW and JWS performed the experiments. OMWand MJR designed the experiments and drafted the manuscript.

Gallium phosphide is produced by a modified Czrolkowski method in which a boron oxide layer prevents the escape of volatile phosphorous. This method produces GaP with a zinc blende structure consisting of stoichiometric amounts of gallium and phosphorus. An ingot produced by this method can then be sliced and polished to leave specific faces exposed, the most common of which are GaP(100), GaP(111)A, and GaP(111)B. GaP(100), similar to silicon, has a Ga–P bond exposed, while GaP(111)A has gallium atop sites and GaP(111)B has phosphorus atop sites (see Scheme 7).

4.1.2 GaP Surface Chemistry and Protection

Both materials[55,184,185] and molecular[43,186–188] approaches have been used to manipulate the GaP surface resulting in enhanced passivation and performance. The development of this field, however, has not progressed as far as silicon passivation strategies due to the high cost of III-V semiconductors, no known methods to produce atomically flat surfaces, and the more complex reactivity that results from polarized bonds in a binary material.

Organic Protection Strategies

While there have been several major advances in the organic modification of group III-V semiconductors, the field has lagged far behind the development of silicon surface protection. In the case of silicon, a general method allows for the generation of an atomically flat Si(111) hydride surface.[189] This surface can easily be chlorinated and functionalized with a variety of nucleophiles, typically *in situ* generated aryl lithium reagents.[36,190] Furthermore, the functionalization of Si(100) surfaces is also well

developed, typically following attachment through cyclization of unsaturated organic moieties.[46–48] While this process can be ported to binary systems, the field is again less developed than that of silicon.[49]

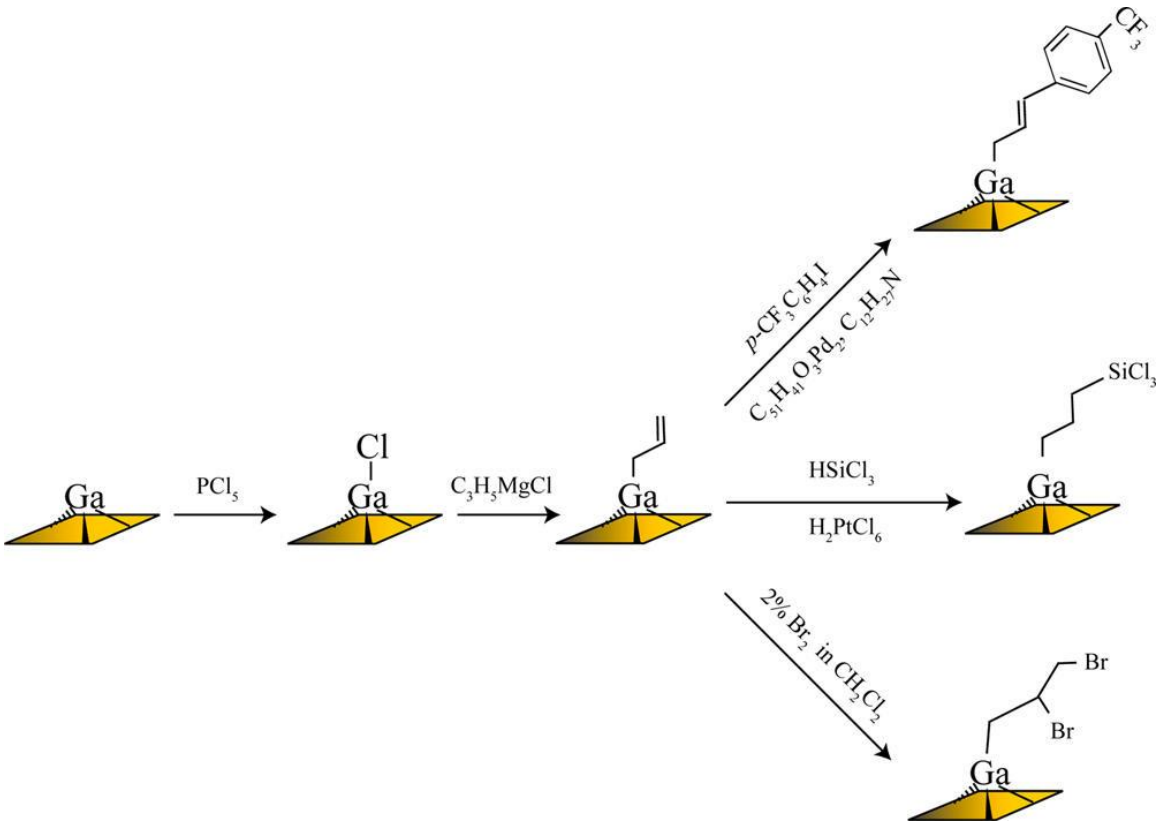

Figure 68. Chemical functionalization of a GaP(111)A surface reported by Peczonczyk *et al.* following chlorination, Grignard nucleophilic, and secondary functionalization steps.[187]

Work in the Maldonado lab in particular has focused on finding chemical methods to attach organic moieties to the surface of GaP. Original studies focused on developing methods analogous to the silicon chlorination strategy.[43] In one work, they showed that a general chlorination – Grignard reaction sequence was able to covalently attach alkyl

chains to a GaP(111)A (Ga atop) surface.[191] Interestingly, the same sequence with an exposed GaP(111)B surface (P atop) did not result in clean modification due to reactivity between PCl_5 reagent and the surficial phosphorous: $PCl_5 \leftrightarrow PCl_3 + Cl_2$. In later work Peczonczyk *et al.* extended this strategy to couple allyl functional groups which could undergo further coupling reactions, hydrosilylations, and electrophilic addition of bromine (see Figure 68).[187] Work on GaP(111)A methylated surfaces showed an enhanced stability under photoelectrochemical conditions when compared with freshly etched surfaces.[186] Specifically, the chemical modification disallowed the cathodic degradation of GaP(111)A surfaces leading to a non-Fermi level pinned surface, an indication of low surface state defect densities.[186]

While the modification of GaP(111)B surfaces have proven much more difficult than GaP(111)A surfaces, methods have been developed to allow for covalent modification. Work by Brown *et al.* used a Williamson ether type reaction to chemically attach molecules to the surface.[188] In this sequence, H_2SO_4 etched GaP(111)B surfaces produce dangling P–OH moieties that can attack a suitable electrophile ($C_{18}H_{37}Br$, $C_{14}H_{29}Br$, $C_{10}H_{21}Br$, *p*-$CF_3C_6H_4CH_2Br$, *o*-$CF_3C_6H_4CH_2SO_2Cl$, and Coomassie Blue).

Comparatively less work has been performed on GaP(100) surfaces. Several reports, however have shown the validity of azide and alkyne functionalization to passivate the wafers.[49] One of the more promising studies focus on the polymerization of polyvinylpyridine onto the surface and post modification with a cobaloxime catalyst. The PEC performance of this construct is discussed in a later section.[91]

Materials Protection Strategies

Materials based protection strategies have also been investigated on GaP semiconductor surfaces. Primarily, work by Cronin studies the utility of a titania coating in the protection of GaP in PECs.[55,192] In long term electrolysis experiments (5 hours), it was found that bare GaP surfaces had a largely roughened surface (± 143 nm) in comparison to TiO_2 passivated surfaces (± 1 nm). This degradation occurs with a corresponding drop in photocurrent, indicating the increase in surface recombination upon degradation of a bare surface. This type of passivation has also been applied in photoanodic systems in which surface protection is more important due to the potential for oxidative corrosion. Conductivity and stability is achieved by using amorphous TiO_2 with accessible defect states acting as hopping sites.[193]

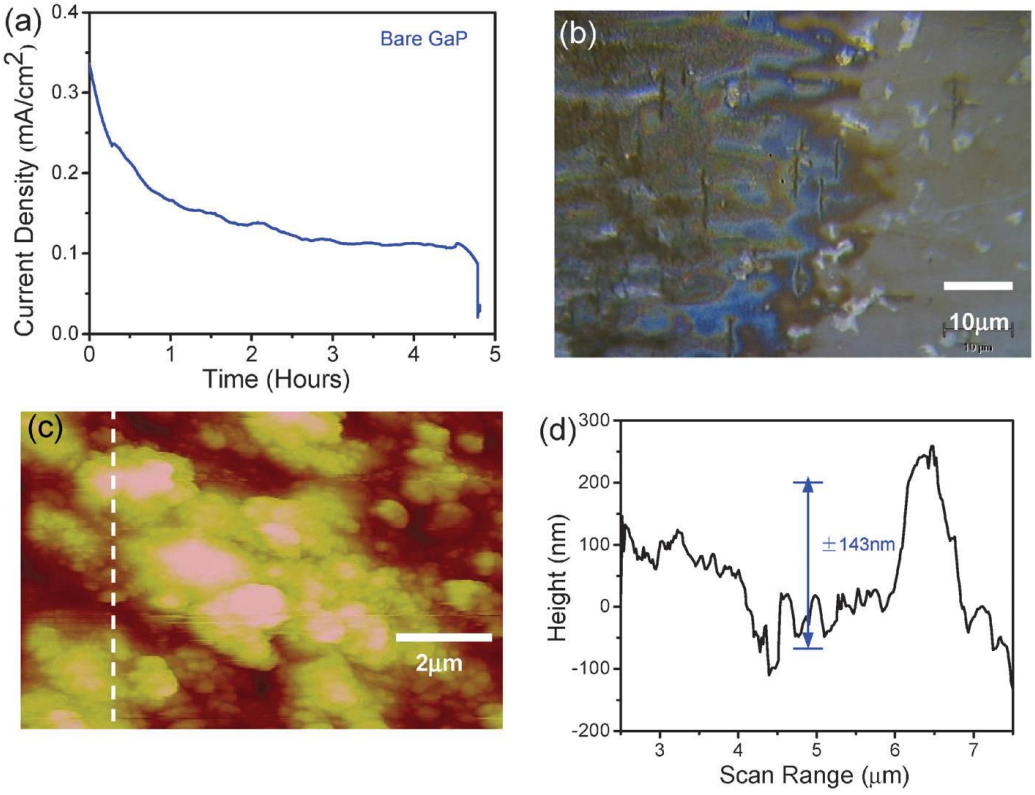

Figure 69. Photocurrent density, optical microscopy, and atomic force microscopy showing the roughened surface of GaP after extended periods of electrolysis.[55]

4.1.3 GaP Based PEC Devices

Gallium phosphide based PECs have been used in PECs to afford water oxidation,[193] proton reduction,[91,92,194–196] and – of particular promise – CO_2 reduction.[184,197,198] Table 8 shows a summary of photocathodic constructs incorporating GaP. The vast majority of these studies focus on the reduction of protons to hydrogen or the reduction of CO_2 – and of most importance its direct reduction to methanol.

Initial reports from Halmann in 1978 studied the photoelectrochemical reduction of CO_2 on a planar *p*-type GaP electrode.[199] In this study, formic acid, formaldehyde, and

methanol were produced. After sixteen hours of illumination, degradation of the semiconductor resulted in the necessity for an increased potential, however methanol was measured in 60% current yield. This work was corroborated by Honda and Fujishima in 1979, where similar results were obtained on GaP planar electrodes as well as semiconductor powders.[200]

There is little literature available between the reports of Halmann and Honda in the late 1970's and more recent GaP studies. In 2008, Bocarsly reported the reduction of CO_2 to methanol on GaP electrodes with near unity current yield using pyridinium as a catalyst (see Figure 70).[201] These studies report a faradaic efficiency of 96% under 365 nm illumination for the $CO_2 \rightarrow CH_3OH$ transformation at a 270 mV underpotential. They propose that pyridinium acts as an electron shuttle, allowing for multiple reduction events to occur.[104] This idea was expanded on in the work of Cronin, wherein TiO_2 passivated GaP electrodes were used for both CO_2 and proton reduction. Although a pyridinium catalyst was used, the Faradaic yield in these studies was only 55%, a value that remained similar with and without the catalyst. In proton reduction experiments, it was found that gold deposited on a GaP|TiO_2 substrate enhanced catalysis through plasmon resonance coupling to the semiconductor surface resulting in a reduction of the onset potential.

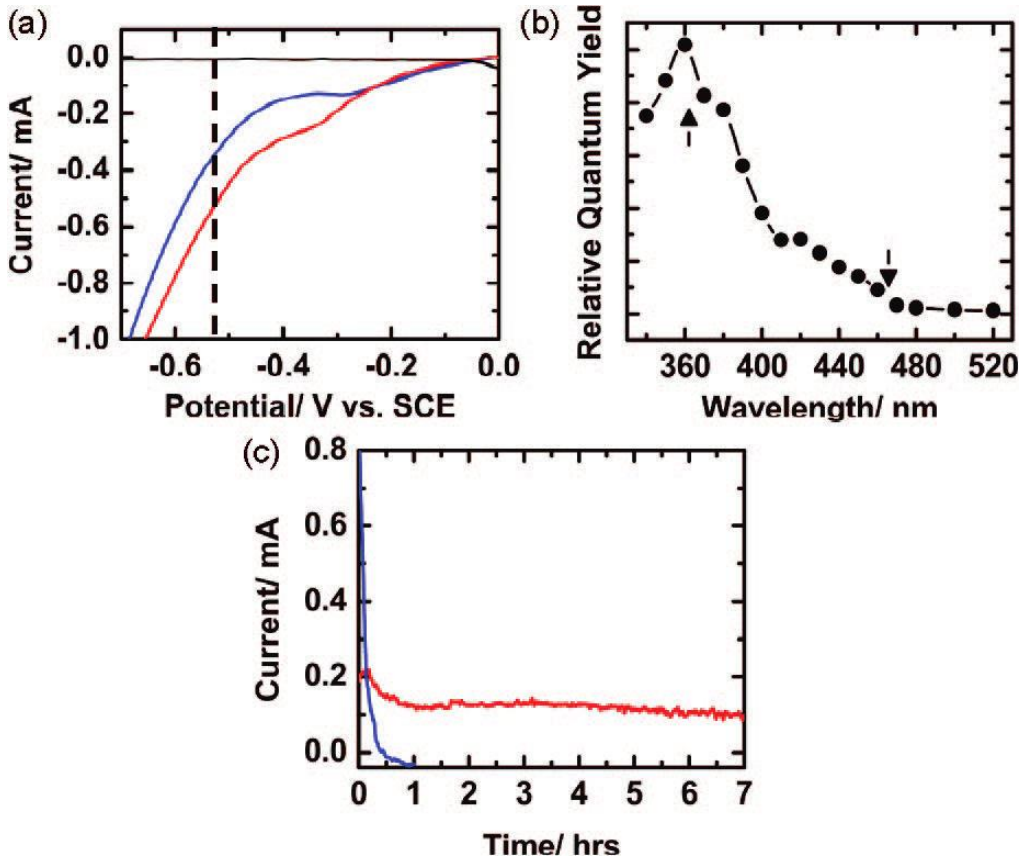

Figure 70. Electrochemical results reported by Bocarsly showing an enhanced photocurrent under CO_2 saturation conditions. The bottom graph shows the response under electrolysis conditions with (red) and without (blue) pyridinium in the solution.[201]

Several other groups have incorporated gallium phosphide into proton reduction PECs.[91,92,194–196,202] Nearly all these reports utilize AM1.5G illumination and generate hydrogen at underpotentials of 200 – 400 mV. Work conducted in the lab of Gary Moore focuses on the incorporation of surface bound discrete cobaloxime electrocatalysts through the grafting of polymers containing N-donor moieties.[91,92,202] In initial reports, a construct consisting of GaP(100) surfaces with polymerized 4-vinylpyridine bound to cobaloxime catalysts showed enhanced photocatalysis over a catalyst free control. This construct

showed a faradaic efficiency of 88% for hydrogen during a 30-minute illuminated electrolysis at +0.17 V *vs.* RHE. Later work showed a similar process could lead to surface bound cobaloxime catalysts on GaP(111) surfaces.[202]

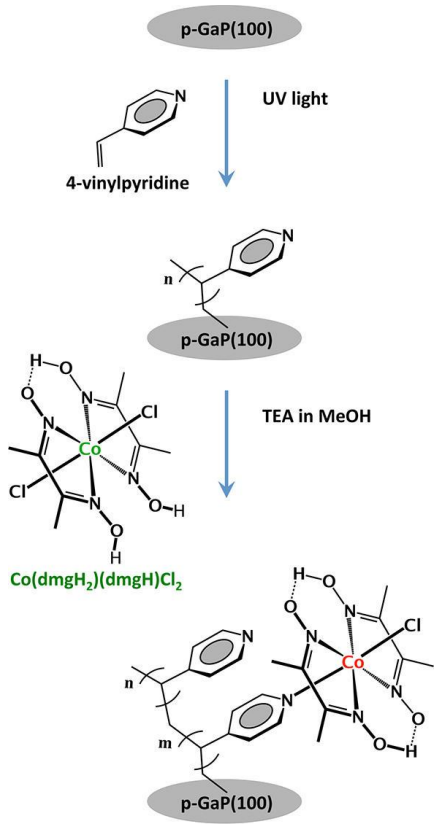

Figure 71. GaP surface developed by Moore *et al.* by interfacing a cobaloxime catalyst with a GaP surface.[91]

Related work by Yang and Bakkers used GaP nanowires to construct photoelectrochemical cathodes.[194–196] This type of geometry allows for much higher surface area while retaining the light absorbing properties of planar GaP. Solution synthesized GaP nanowires were constructed with surficial platinum nanoparticles and showed Faradaic yields of 80% at potentials and currents comparable to planar GaP, with

much less GaP used. Another study investigated the utility of wurzite GaP nanowires grown on a GaP(111)B substrate.[194] This paper reports the highest values obtained for the open circuit potential and short circuit current of any GaP device reported to date, with a Faradaic yield of hydrogen at 97% with a platinum surface catalyst. Furthermore, the use of etching procendures may provide an effective and cost efficient way to increase the surface area and charge carrier collection abilities of GaP.[185,203]

While this is a well-developed field, a complete understanding of the nature of the catalysis of these devices, and the interface between photocurrent generator and catalyst has yet to be developed. Reports for CO_2 reduction on gallium phosphide produce methanol at reasonable yields, although the mechanism of reduction is not well understood. Furthermore, GaP PECs for hydrogen production typically utilize expensive platinum based catalysts, with the exception of reported cobaloxime surface catalysts, which show leeching into solution under extended electrolysis. Here, we attempt to develop a construct that incorporates a known selective electrocatalyst in order to produce a device with specific catalytic product profiles.

Table 8. Previously reported bulk electrolysis studies on the photoelectrochemical reduction of protons and carbon dioxide on gallium phosphide. (a) potentials are reported in V *vs.* SCE, (b) wurzite gallium phosphide nanowires were used, (c) the potential in this case gradually increased to -1.4 V due to degradation, (d) Faradaic yield of methanol is reported, (e) Faradaic yield of hydrogen is reported.

Construct	Reference	Illumination	Potential[a]	FY (%)
p-GaP	Halmann[197]	Hg lamp	-0.86[c]	60[d]
p-GaP pyridinium	Bocarsly[198]	465 nm	-0.4	83[d]
			-0.3	90[d]
		365 nm	-0.4	89[d]
			-0.3	92[d]
p-GaP|TiO_2 pyridinium	Cronin[184]	532 nm	-0.74	55[d]
p-GaP (WZ)[b] platinum	Bakkers[194]	AM1.5	+0.24	97[e]
p-GaP|PVP cobaloxime	Moore[91,92]	AM1.5	+0.44	88[e]
p-GaP NW	Yang[195,196]	AM1.5	+0.34	79[e]

4.2 Results and Discussion

In previous work, we determined that deposition of Al_2O_3 by atomic layer deposition (ALD) on methylated silicon(111) substrates results in a film free of pinholes after approximately 30 cycles (~30 Å).[204] The slow rate of electron transfer – caused by the insulating nature of these films – was enhanced by the ALD-based deposition of platinum nanoparticles on the surface which proved effective for light-driven $H^+ \rightarrow H_2$ conversion (solar $\rightarrow H_2$, $\eta = 1\%$).[40,204] In this chapter an analogous construct for PEC $CO_2 \rightarrow$ CO conversion on *p*-GaP using AuNPs is reported. Compared with methylated Si(111), the GaP case proved more complex – due to the greater surface roughness of GaP(100),

diminished electron transfer at the GaP|metal-oxide interface, and challenges adsorbing various sources of AuNPs to substrates. Ultimately, a device incorporating a gallium phosphide semiconductor, metal oxide protecting layer, and catalytic gold nanoparticles was successfully constructed and tested in photoelectrochemical conditions.

4.2.1 Wafer Fabrication

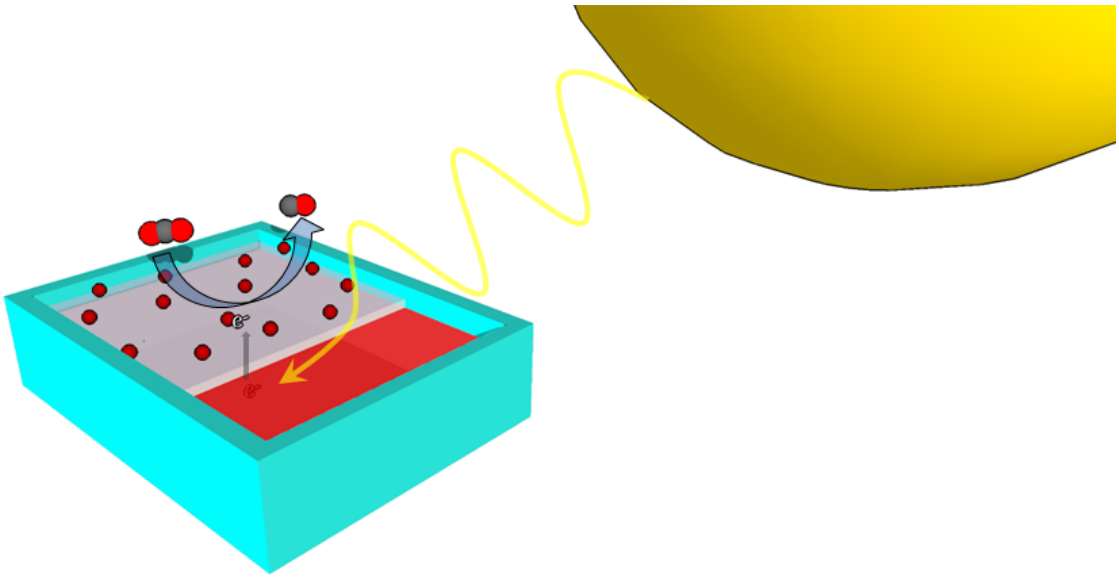

Scheme 8. Schematic of a proposed wafer device with a gallium phosphide substrate, metal oxide protecting layer, and surficial nanoparticle catalysts for carbond dioxide reduction.

Atomic Layer Deposition

The substrate functionalization is summarized in Scheme 9. In order to provide a clean surface for atomic layer deposition (ALD), the wafers were degreased by subsequent sonication in acetone, methanol, DCM, and water. A basic (NH_4OH) etching procedure was used to remove the native oxide, although there was likely rapid regrowth of a small amount of oxide following the etching procedure. Only two other reported methods of etching the GaP(100) surface have been reported and are shown to have removed less oxide

than a basic etch.[205,206] Thermally grown layers of $GaPO_x$ showed that this oxide layer is predominantly $GaPO_4$ by X-ray diffraction. X-ray photoelectron spectroscopy of this surface indicated a thick oxide was grown under high temperatures and ambient atmosphere.

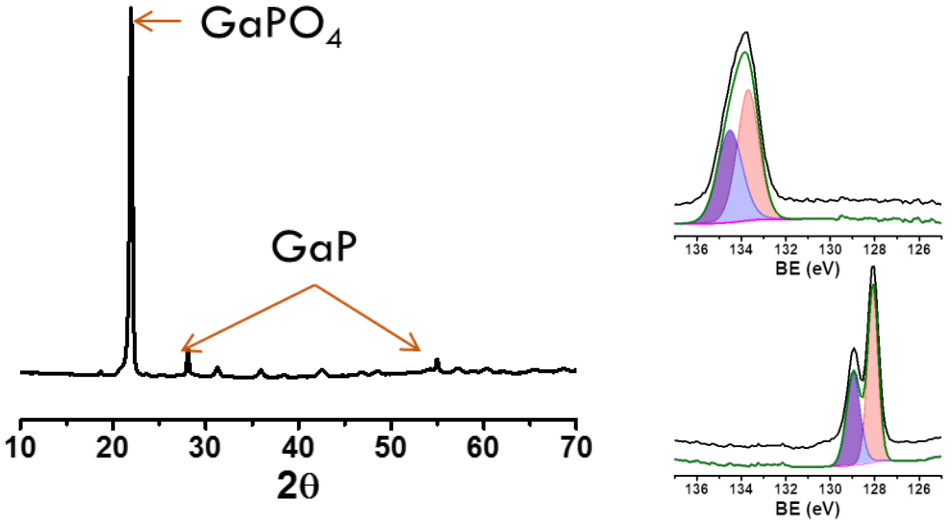

Figure 72. X-ray diffraction of a thermally grown oxide surface on top of a GaP(111) substrate showing peaks for $GaPO_4$. XPS results (left: bottom – fresh etch, top – thermal oxide) corroborated by the presence of predominantly P(V) signals on the surface following oxidation.

Following the etching procedure, the wafers were immediately introduced into the atomic layer deposition chamber. Metal oxides were deposited by ALD of Al_2O_3 using trimethyl aluminum (TMA), or ZnO using diethyl zinc (DEZ). The composition of the resulting device was investigated by XPS. It is important to note the lack of an oxidized P(V) signal both before and after ALD, which would be evident at a binding energy of 133 eV. Using the attenuated gallium phosphide P 2*p* signal (Figure 73, as compared with an etched-only substrate), the nominal thickness of the ALD Al_2O_3 layer (30 cycles) was determined to be ~15 Å. The discrepancy between the determined value and the expected

thickness (30 Å, based on the reported growth rate, 1.04 Å/cycle) could be a result of the surface roughness of base-etched GaP(100) (not atomically flat), estimated to be ~10-15 Å.[207] The zinc oxide deposition was performed using 16 cycles of zinc oxide, plus four cycles of alumina deposition (for aqueous stability) to afford an analogous layer thickness (ZnO = 1.7 Å/cycle, Al_2O_3 = 1.04 Å/cycle).

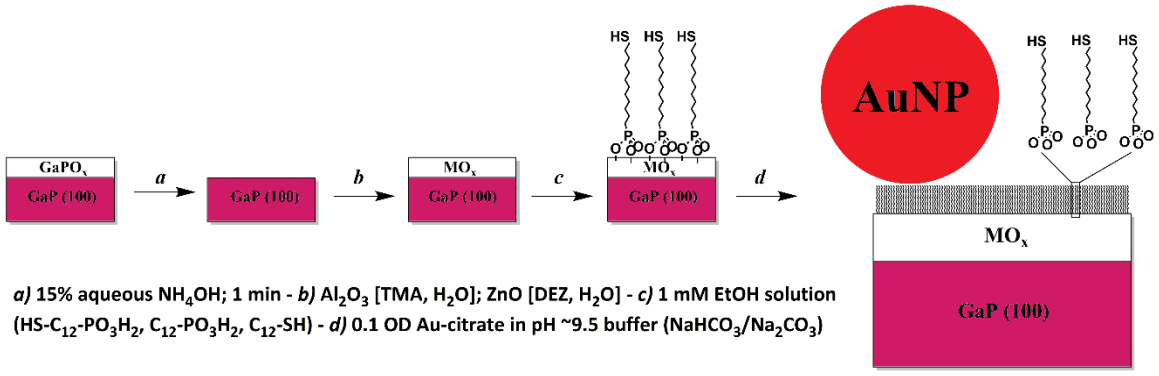

Scheme 9. Process for electrode wafer fabrication including *i)* etching, *ii)* atomic layer deposition, *c)* self-assembled monolayer formation, and *d)* gold nanoparticle deposition.

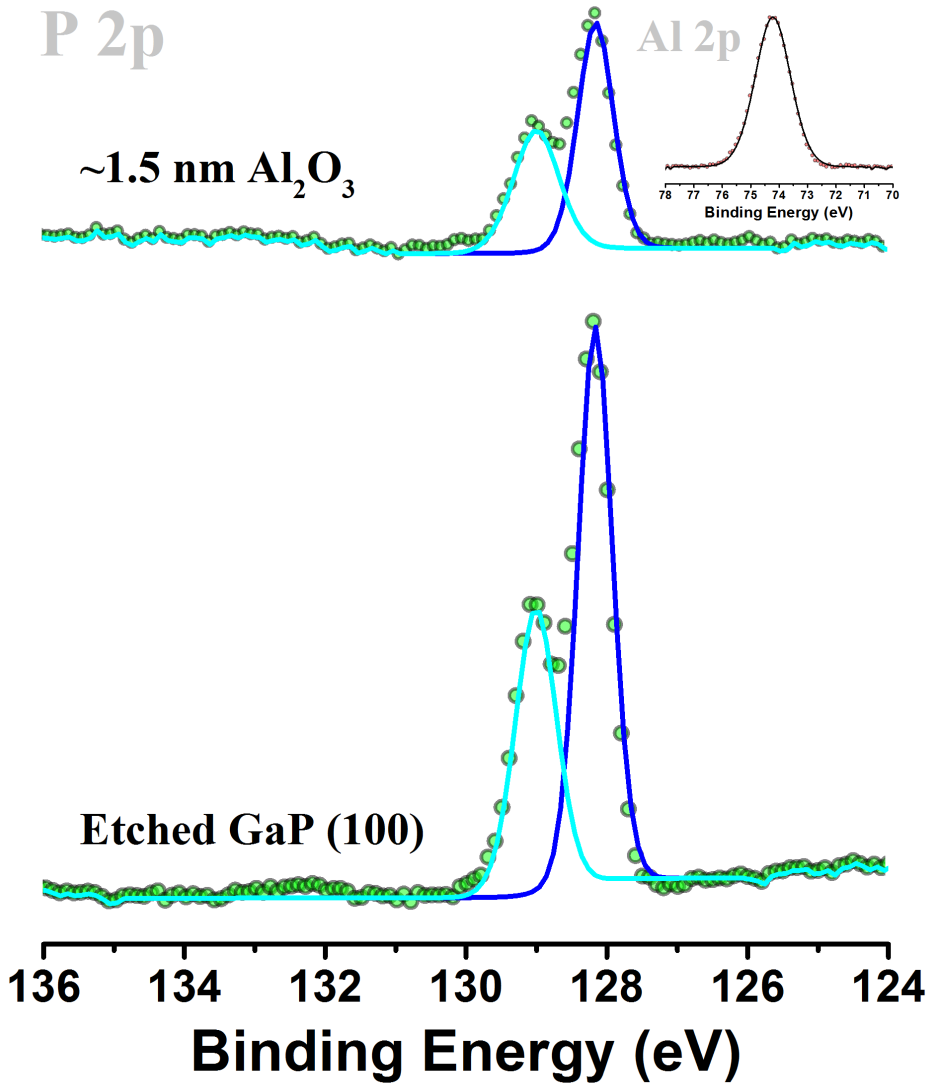

Figure 73. X-ray photoelectron spectra for the P 2*p* and Al 2*p* regions prior to (bottom) and after (top) the atomic layer deposition of aluminum oxide.

Self-Assembled Monolayer Deposition

In order to provide a chemical link between the metal oxide protecting layer and the nanoparticle catalyst, a Janus type linker was used with terminal phosphonate and thiol end groups. To allow for self-assembled monolayer (SAM) formation, the wafer samples

were soaked in an ethanolic solution of the monomer overnight (14-20 hours). Following incubation of GaP|metal-oxide with the thioalkylphosphonate, the appearance of a phosporous(V) feature (Figure 74a) at a binding energy of 132 eV was evident (in contrast to the gallium phosphide P(III) feature at 127 eV). Additionally, a distinct S 2*p* peak at 162 eV was observed.

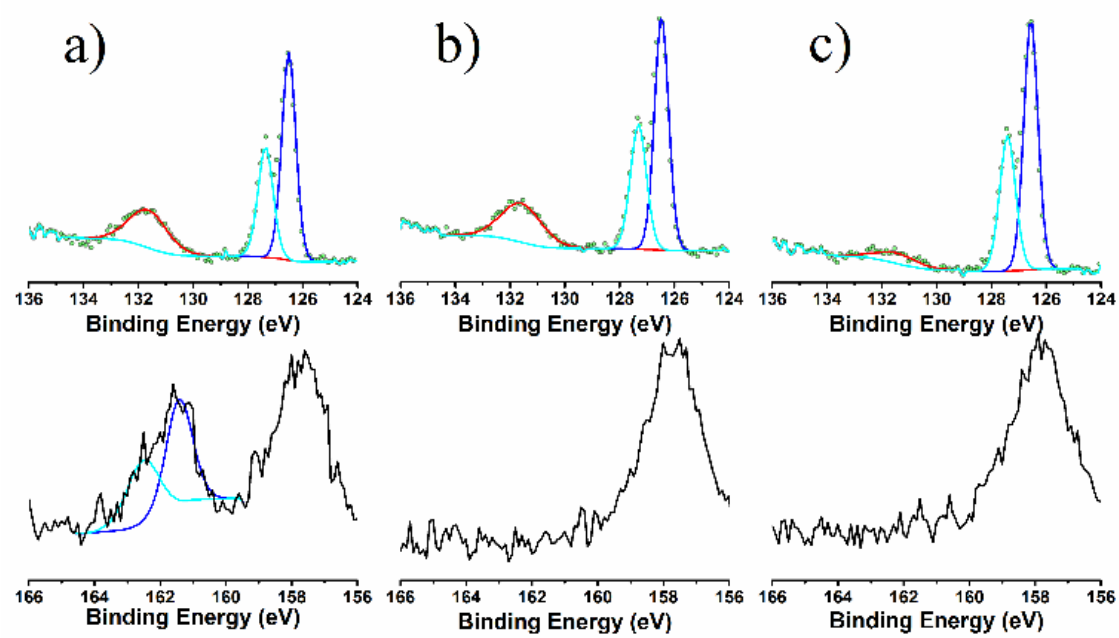

Figure 74. X-ray photoelectron spectra for the P 2*p* and S 2*p* regions after soaking in *a)* 12-mercaptododecyl phosphonic acid, *b)* dodecylphosphonic acid, and *c)* dodecanethiol. S 2*p* signals were detected between 160 and 164 eV, while the feature at 158 eV corresponds to that of Ga 3*s* photoelectrons.

To evaluate the postulated binding mode of the thioalkylphosphonate, control experiments were performed using the analogous reagent without each capping group. Treatment of the substrate with dodecylphosphonic acid (no thiol) resulted in the phosphorous(V) feature, but no sulfur 2*p* signal (Figure 74b). The complementary experiment using dodecanethiol resulted in neither the phosphonate signal nor the sulfur

signal (Figure 74c). These results clearly indicate the preferential binding of the phosphonate tail to the Al_2O_3 surface. As such, the thiol moiety is ideally oriented for the binding of AuNPs.

Gold Nanoparticle Attachment to SAM

Attempts at different strategies for attachment found that solution-based depositions of AuNPs (bare, PVP-coated, and citrate coated) on the GaP|metal-oxide substrate proved ineffective or irreproducible. Subsequently, adsorption of AuNPs was achieved by exposure of the GaP|metal-oxide|$O_3PC_{12}SH$ construct to a pH ~9.5 carbonate buffer solution (to facilitate thiol deprotonation) containing a 0.1 OD concentration of 10 nm, citrate-stabilized AuNPs. It was determined in experiments on Si|MOx|SAM constructs (Figure 75) and has been reported in the literature[208–210] that more basic pH solutions results in degradation of the SAM. XPS region spectra for these fully constructed wafers showed all the appropriate signals for the devices as per Scheme 9 and are included in the experimental section of this chapter.

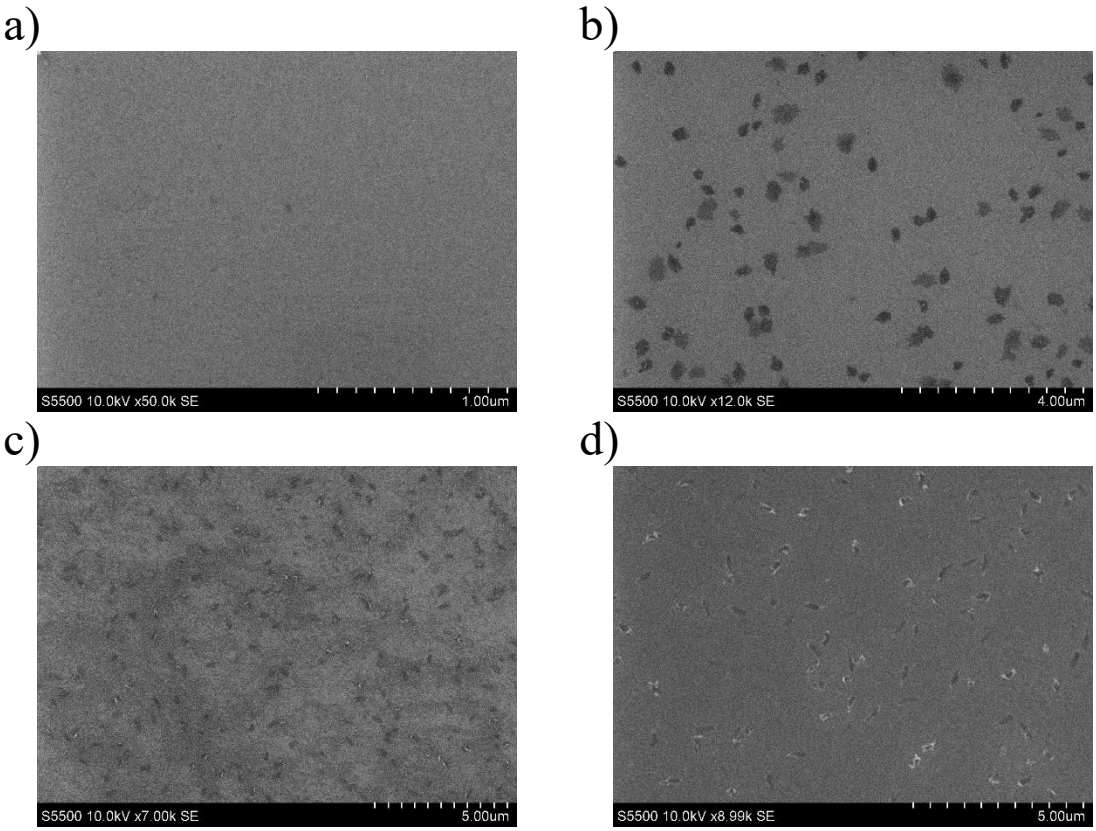

Figure 75. Scanning electron micrograph of Si|Al_2O_3|$PO_3H_2C_{12}$ surfaces after soaking in *(a)* pH = 9.5, *(b)* pH = 10.0, *(c)* pH = 10.5, and *(d)* pH = 11.0 carbonate/bicarbonate aqueous buffers.

Following treatment of the GaP|metal-oxide|SAM substrate with AuNPs, the coverage of the particles was assessed by SEM imaging. The images of the wafer (Figure 76) indicated a surface coverage of ~100 nanoparticles per square micron. The AuNP deposition occurred similarly for both Al_2O_3 and ZnO constructs. Attempted deposition on a bare *p*-GaP(100)|Al_2O_3 surface resulted in lower coverages and irregular, irreproducible deposition. It also is notable that increased incubation times (> 12 - 18 h) did not result in larger nanoparticle surface coverages, indicating a self-limiting deposition mechanism.

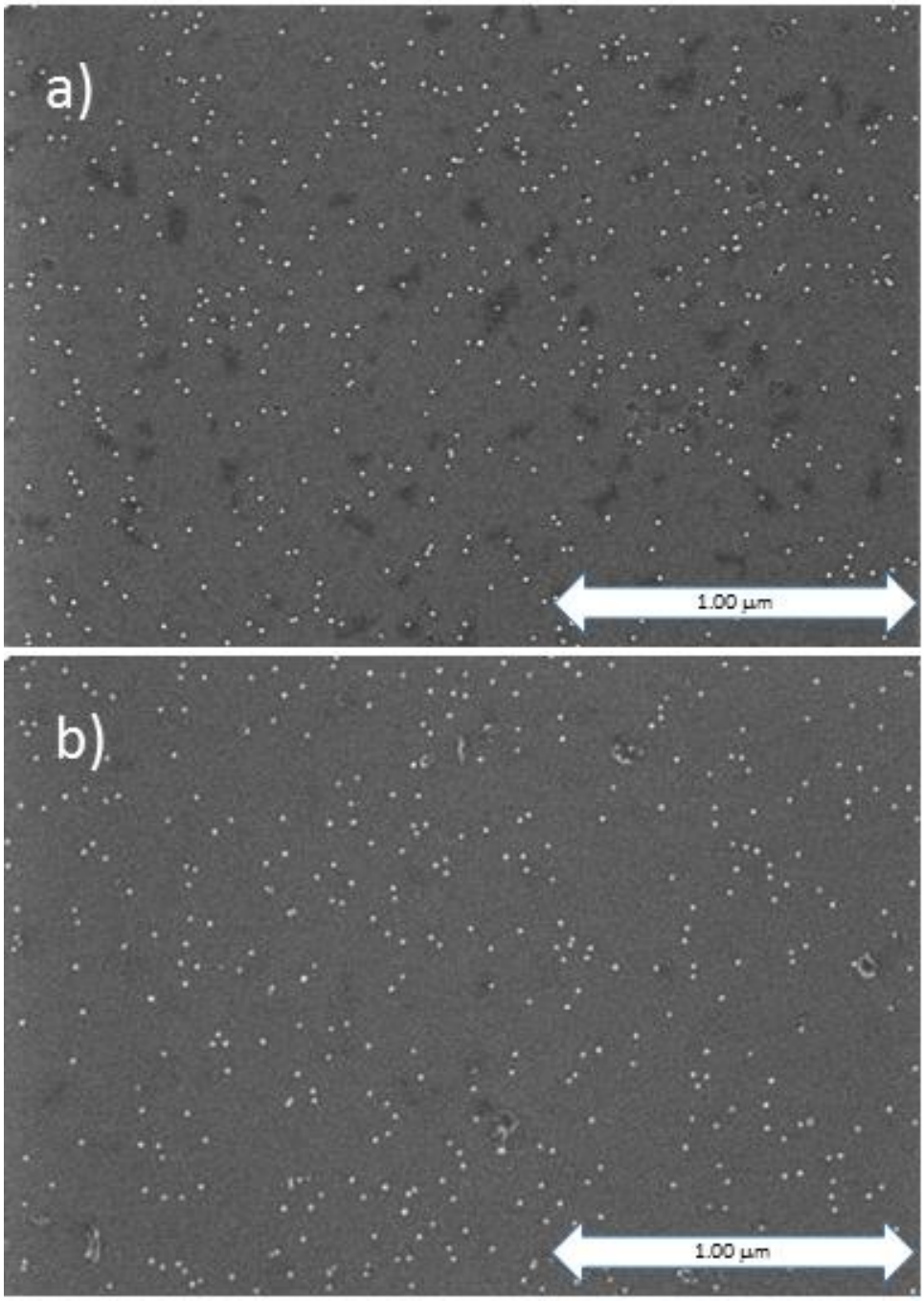

Figure 76. Scanning electron micrographs of GaP|Al_2O_3|SAM|$AuNP_{10nm}$ (top) and GaP|ZnO(16)Al_2O_3(4)|SAM|$AuNP_{10nm}$ (bottom).

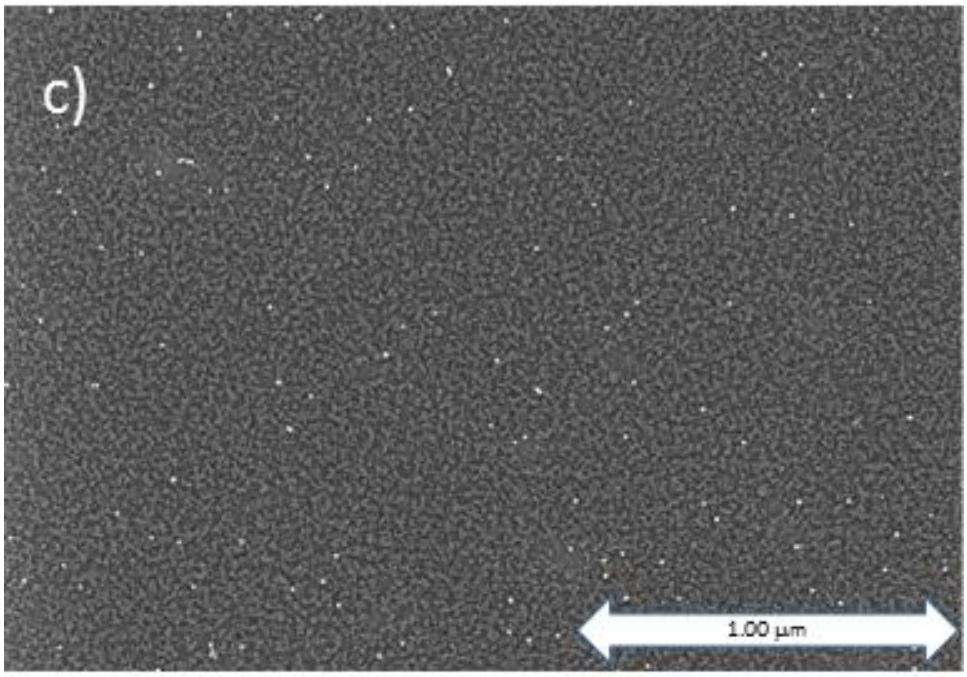

Figure 77. Scanning electron micrographs of GaP|Al_2O_3|$AuNP_{10nm}$ showing reduced coverage without the self-assembled monolayer.

Further depositions were attempted with both 5 nm AuNPs and 20 nm AuNPs. Interestingly, while the 5 nm nanoparticles showed similar coverage to the 10 nm depositions, a very low coverage was observed for 20 nm nanoparticles. This is likely due to the size of the nanoparticle in comparison to the amount of available attachment sites on the SAM surface. Depositions attempted without the use of a pH 9.5 carbonate/bicarbonate buffer showed no nanoparticle coverage.

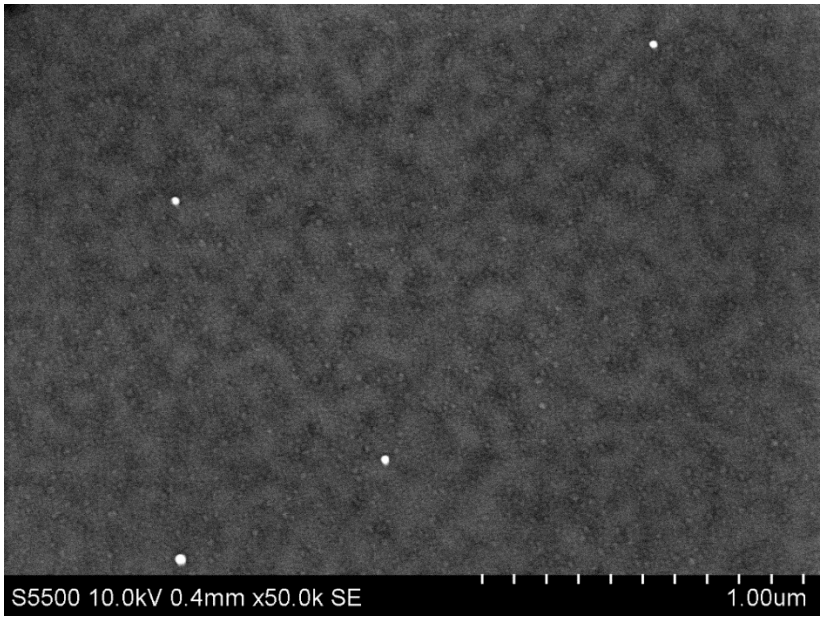

Figure 78. SEM image of GaP|ZnO(16)Al_2O_3(4)|SAM|$AuNP_{20nm}$ at 50k × maginification.

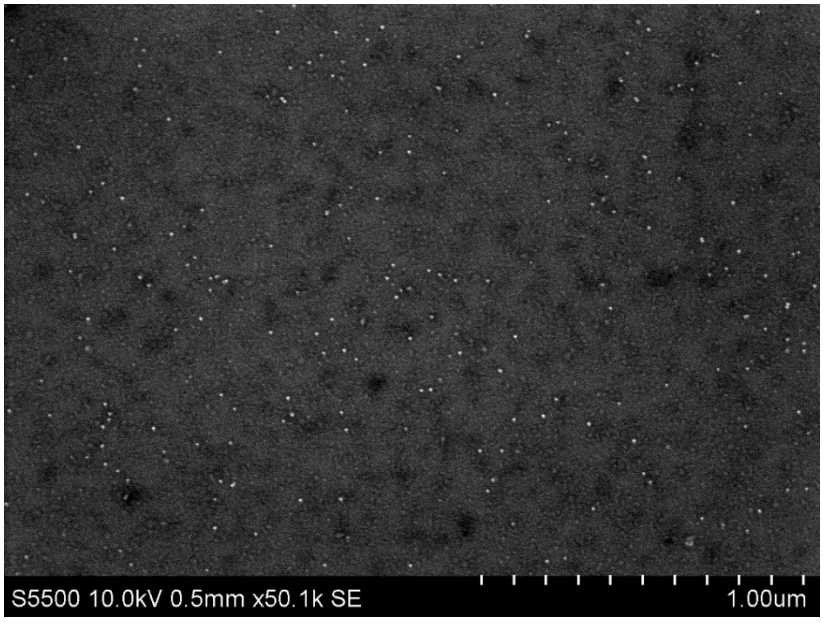

Figure 79. SEM image of GaP|ZnO(16)Al_2O_3(4)|SAM|$AuNP_{5nm}$ at 50k × maginification.

4.2.2 Electrochemistry of Wafers

Organic Electrochemistry

Prior to undertaking H^+ or CO_2 reduction studies, it was desirable to establish the electron transfer (ET) properties of the system. The direct tunneling distance through a blocking layer (Al_2O_3) for an electron is observable at thicknesses less than 40 Å under ideal conditions.[211] The non-aqueous photo electrochemistry (Figures 80 and 81) of the substrate was thus pursued using an MeCN solution of ethyl viologen (EtV^{2+}). While the NH_4OH etched substrate exhibited 184 μA/cm^2, the deposition of the ultrathin alumina layer (15 Å) resulted in a partial attenuation of the photocurrent (46 μA/cm^2). However, complete attenuation of ET (2.7 μA/cm^2, 2% of etched GaP) was observed following addition of the insulating SAM (C_{12} = ~14 Å).[212,213] The introduction of AuNPs in this case rescued the photocurrent approximately fifteen-fold to 44 μA cm^{-2}. Interestingly, similar results were obtained regardless of nanoparticle size, with 5, 10, and 20 nm AuNPs rescuing the observed photocurrent to a similar degree (Figure 82).

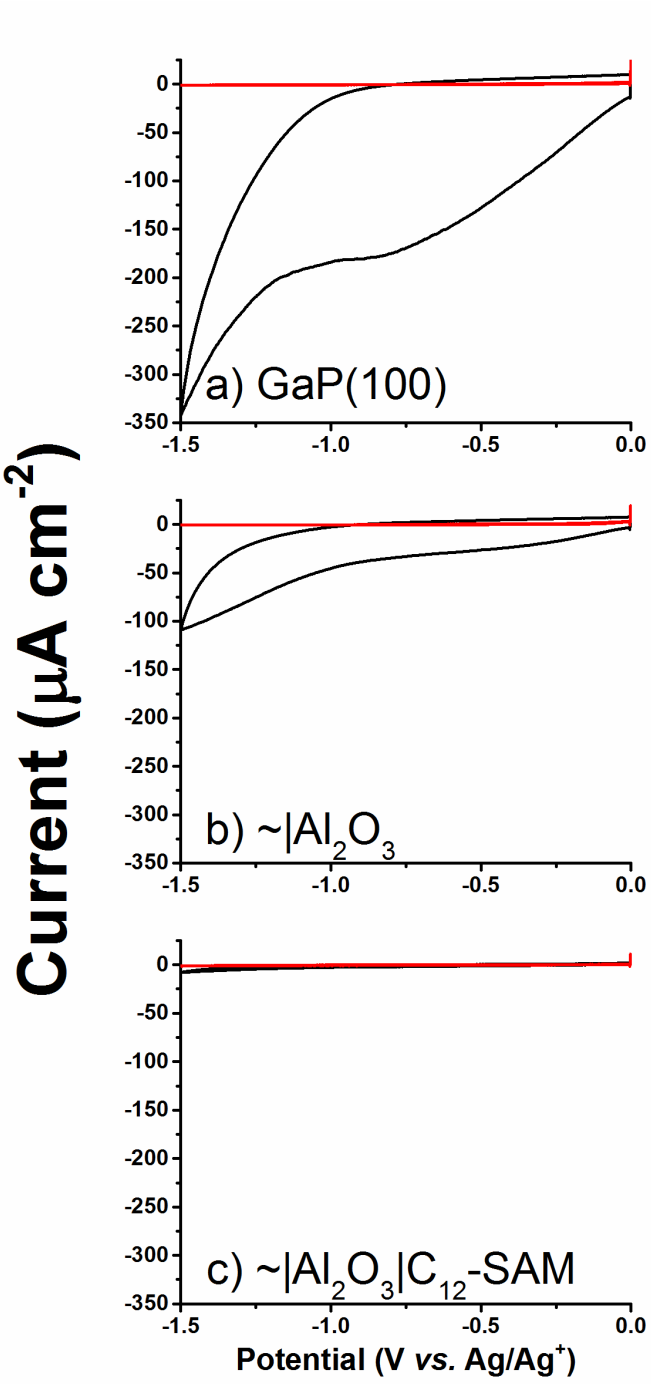

Figure 80. Cyclic voltammograms of the intermediate stages for wafer fabrication showing the reduction in current when going from a fresh etch (top) to the Al_2O_3 deposition (middle), and ultimately with the addition of an alkyl self-assembled monolayer (bottom).

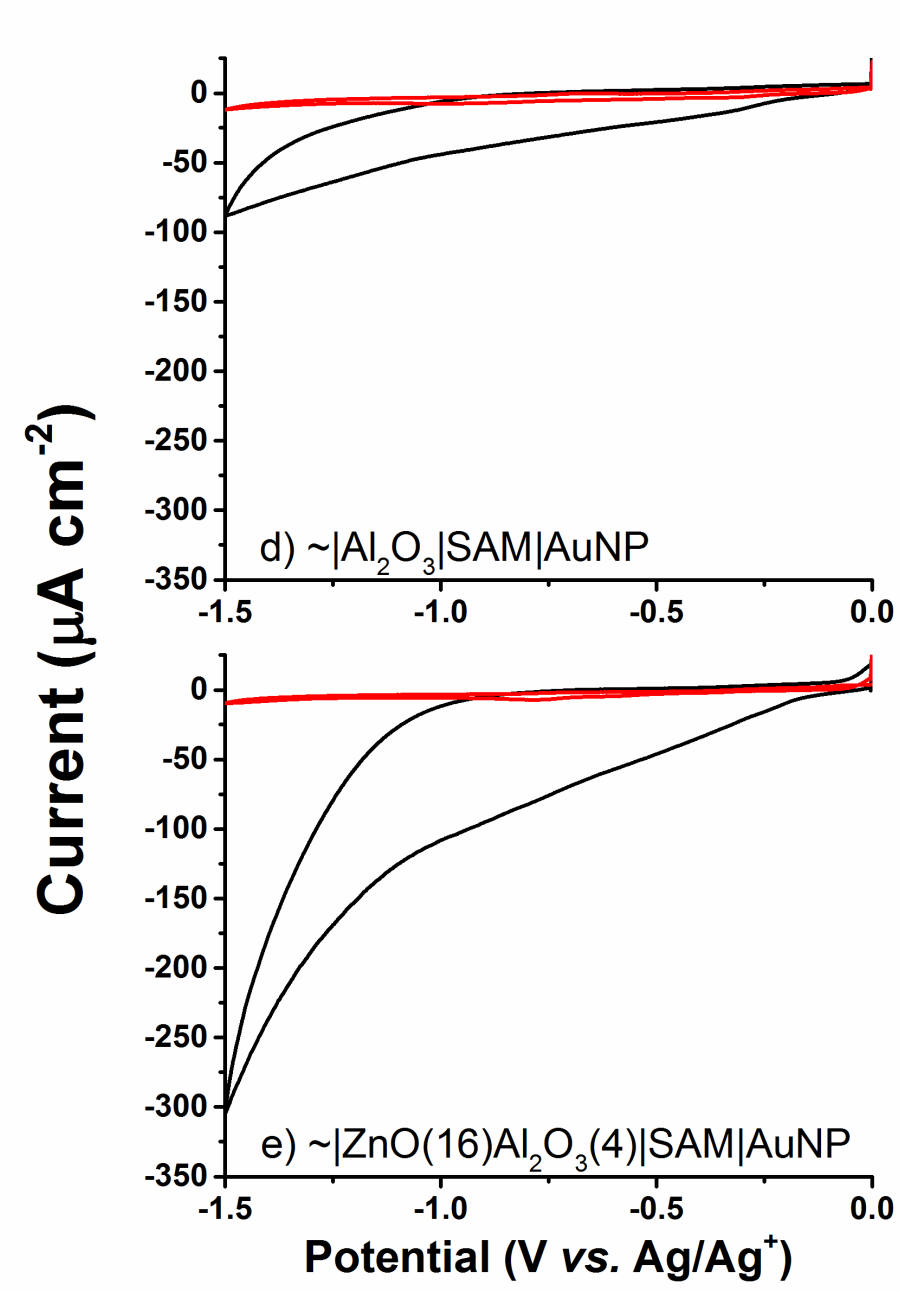

Figure 81. Cyclic voltammograms of fully constructed wafers with Al_2O_3 (top) and $ZnO|Al_2O_3$ metal oxide layers (bottom).

The combined insulating behavior of the Al_2O_3 and alkyl SAM layers limits the accessible photocurrent. We reasoned that while the SAM layer was essential for AuNP binding, the substitution of a metal oxide with a more accessible conduction band (like ZnO)[33,204] would enhance ET. Indeed, the use of ZnO (with 4 cycles of capping Al_2O_3 for aqueous stability) resulted in further rescue of the photocurrent (108 μA/cm^2) to ~60% of the maximum current for freshly etched GaP wafer.

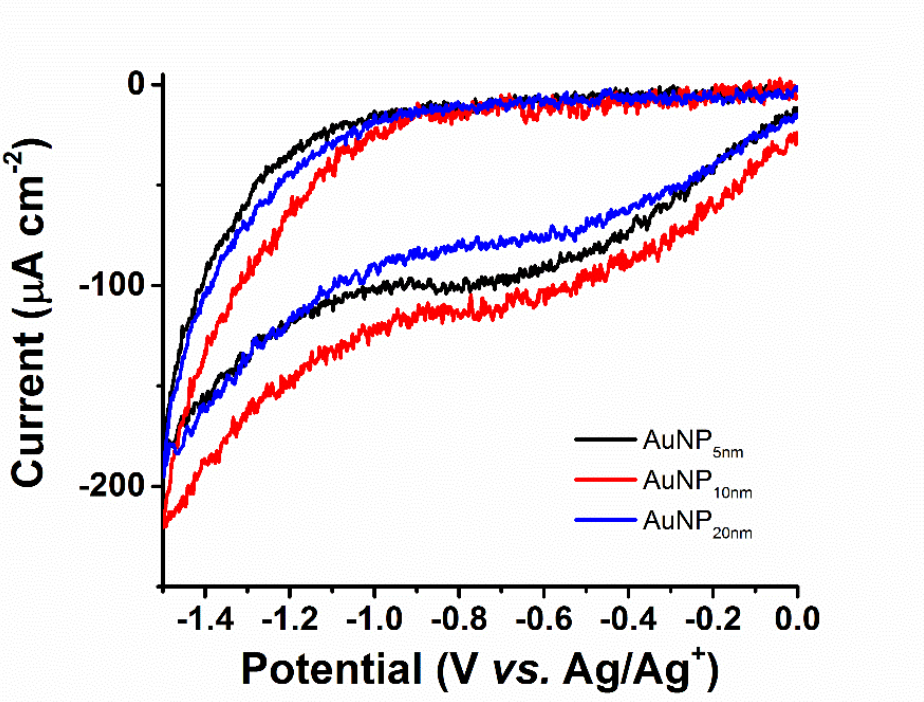

Figure 82. Organic electrochemistry in 5.0 mM EtV^{2+} and 0.1 M $LiClO_4$/MeCN electrolyte for GaP|ZnO(16)Al_2O_3(4)|SAM|AuNP (5, 10, 20 nm) under AM1.5G illumination.

Aqueous Electrochemistry

Having established and optimized the fundamental ET properties of the system under non-aqueous conditions, further experiments were undertaken in aqueous electrolyte (KCl) to ascertain the catalytic properties of composite photocathode. Experiments performed on *p*-GaP(100)|Al_2O_3|SAM|AuNP exhibited significant cathodic current (Figure 83, black line) under one sun illumination (E_{onset} = -0.150 V *vs.* SCE , J_{max} = -825 μA cm^{-2}, E_{Jmax} = -1.125 V *vs.* SCE); this feature is attributed to proton reduction. Saturation of the KCl electrolyte with CO_2 gas resulted in the apperance of a new feature (E = -0.2 → -0.7 V *vs.* SCE), indicating CO_2 reduction (Figure 83, red line). The potential of the $H^+ \rightarrow H_2$ reaction was unchanged (i.e. E_{Jmax} remained the same). In contrast, the *p*-GaP|ZnO(16)Al_2O_3(4)|SAM|AuNP construct (Figure 84) exhibited an anodic shift in E_{Jmax} (-1.15 V under N_2; -0.9 under CO_2). This is likely due to the decrease in pH (from pH 7 to pH 4) upon introduction of CO_2 as a result of the formation of bicarbonate in aqueous media. Furthermore, the CO_2 reduction feature became more pronounced at more anodic potentials (E_{onset} = -0.125 V *vs.* SCE, J_{max} = -212 μA cm^{-2}, $E_{J,CO2}$ = -0.475 V *vs.* SCE).

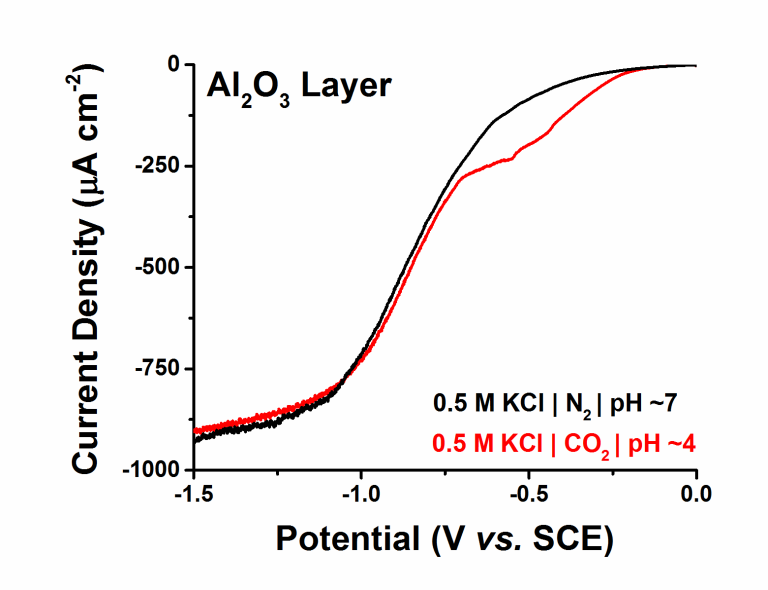

Figure 83. Aqueous electrochemistry performed on a GaP|Al_2O_3|SAM|AuNP device in 0.5 M $NaHCO_3$ at AM1.5G illumination under N_2 (black) and CO_2 (red) saturation.

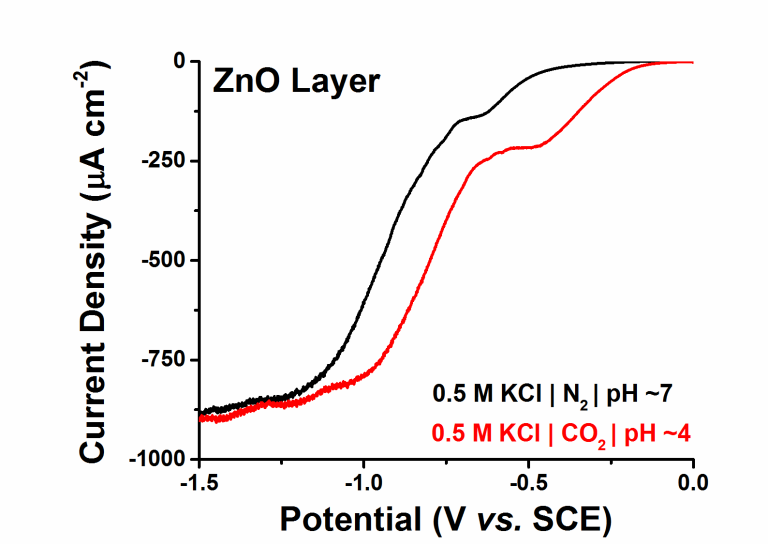

Figure 84. Aqueous electrochemistry performed on a GaP|Al_2O_3|SAM|AuNP device in 0.5 M $NaHCO_3$ at AM1.5G illumination under N_2 (black) and CO_2 (red) saturation.

Table 9. Non-aqueous electrochemistry results of wafers under AM1.5G illumination (100 mW cm^{-2}) showing the loss of current upon ALD and SAM formation, as well as the rescued current upon deposition of AuNPs. (a) Current density determined at -1.0 V vs. Ag/Ag^{+} QRE, i.e. cathodic of the second redox peak of EtV^{2+} and (b) taken as a percentage of the maximum current observed directly after NH_4OH etching treatment.

	J^a	%[b]	E_{onset}	E_{Jmax}
GaP (NH_4OH etch)	-184	-	-	-
GaP|Al_2O_3	-46	25	-	-
GaP|Al_2O_3|PO_3H_2-C_{12}	-2.7	1.5	-	-
GaP|Al_2O_3|PO_3H_2-C_{12}-SH|$AuNP_{10nm}$	-44	24	-0.15	-1.125
GaP|ZnO(16)Al_2O_3(4)|PO_3H_2-C_{12}-SH|$AuNP_{5nm}$	-103	56	-0.05	-1.35(N_2) -1.00(CO_2)
GaP|ZnO(16)Al_2O_3(4)|PO_3H_2-C_{12}-SH|$AuNP_{10nm}$	-121	66	-0.05	-1.1(N_2) -0.90(CO_2)
GaP|ZnO(16)Al_2O_3(4)|PO_3H_2-C_{12}-SH|$AuNP_{20nm}$	-89	48	-	-

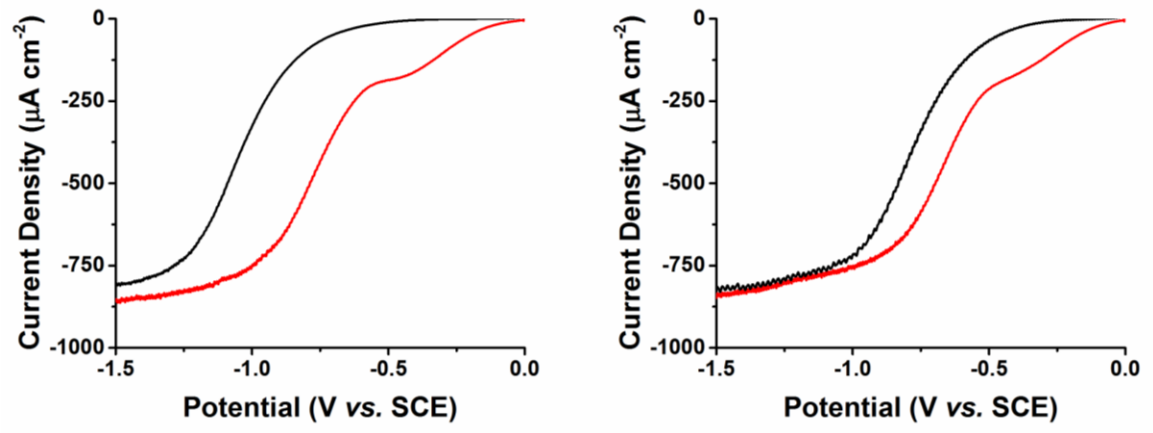

Figure 85. *J-V* curves resulting from the aqueous electrochemistry performed in 0.5 M KCl solution under N_2 (black, pH = 7) and CO_2 (red, pH = 4) saturated conditions. The wafers that were used in these studies consisted of GaP|ZnO(16)Al_2O_3(4)|SAM|AuNP(5nm) (left), and GaP|ZnO(16)Al_2O_3(4)|SAM|AuNP(10nm) (right).

Bulk Electrolysis

Encouraged by these results, we evaluated the bulk electrolysis of the optimized photocathode under 1-sun illumination to determine the product yield of CO and H_2. The electrode was placed in a CO_2 saturated 0.5 M KCl aqueous solution, with an applied

potential of -0.5 V vs. Ag/Ag^+ quasi-reference electrode (CO_2 feature). A gas sample taken after 2 hours (~46.7 mC of charge) showed both hydrogen and carbon monoxide in the headspace by gas chromatography, resulting in FYs of 66% and 1%, respectively. While this does demonstrate the catalytic capability of the system, it also indicates the relatively low selectivity of the AuNPs. A longer (18 hours) bulk electrolysis experiment was also attempted, which resulted in a higher selectivity for $CO_2 \rightarrow CO$ conversion (~6%). Longer times also resulted in degradation of the wafer sample as determined by comparison of LSVs before and after electrolysis.

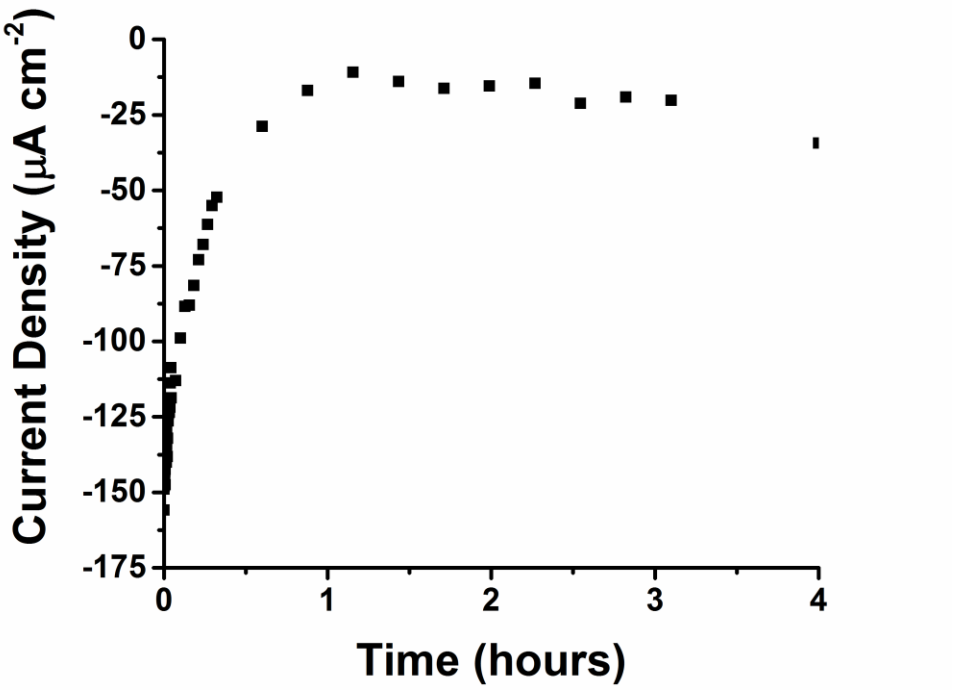

Figure 86. Current was recorded in a chronoamperometric bulk electrolysis that was carried out over a four hour time period. The GC samples confirmed the presence of both H_2 and CO in the headspace.

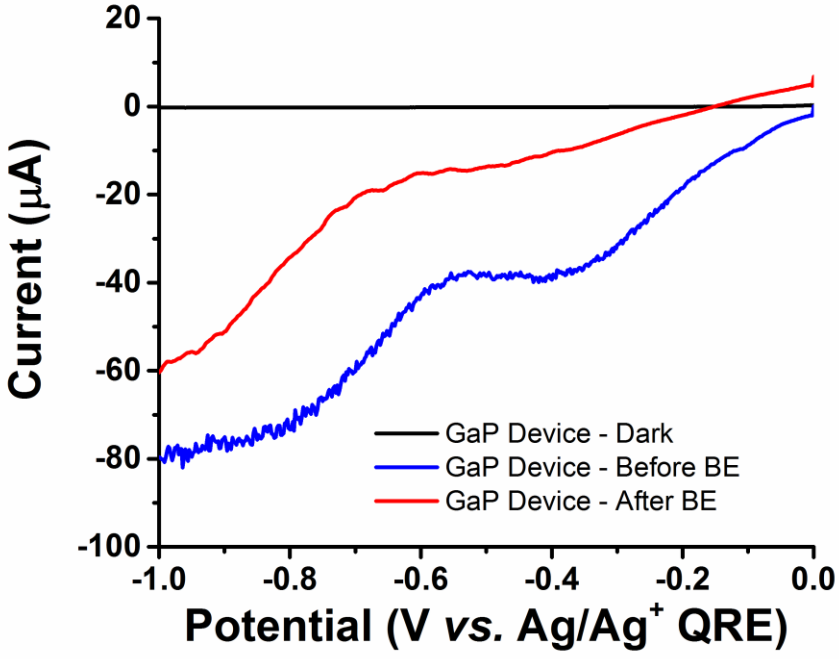

Figure 87. LSV graphs recorded before and after bulk electrolysis revealing the decrease in observable current after electrolysis.

4.3 CONCLUSIONS

In conclusion, we have developed a construct that reliably interfaces a gallium phosphide photoelectrode with gold nanoparticles. The construct exhibited both $H^+ \rightarrow H_2$ and $CO_2 \rightarrow CO$ transformations at reasonable potentials. It is clear that while a self assembled monolayer with phosphonate and thiol functionalities can be utilized to chemically anchor gold nanoparticles to the surface, the stability of this layer presents a problem in aqueous electroreduction conditions. Further studies should focus on modulating the selectivity of the existing AuNP nanoparticles, or on integrating other active catalysts for robust and selective $CO_2 \rightarrow CO$ conversion.

4.4 EXPERIMENTAL

4.4.1 Preparation of Wafers

Wafer Cleaning and Etching Procedures

Zn doped GaP(100) wafers were purchased from ITME with a carrier concentration of 4.7×10^{17} and a resistivity of 2×10^{-1} Ω cm. The wafers were degreased sequentially with acetone, methanol, dichloromethane, methanol, and deionized water under sonication and etched in a 15% aqueous ammonium hydroxide solution, followed by washing with copious amounts of deionized MilliQ water. For ALD procedures, the etched wafers were introduced immediately into the ALD chamber.

Atomic Layer Deposition

Alumina was deposited using trimethylaluminum (TMA) and H_2O as precursors. Zinc oxide was deposited using diethyl zinc (DEZ) and H_2O as precursors. Thirty total cycles were performed at a substrate temperature of 150 ˚C, and precursor pulses of 0.015 seconds, followed by a 5 second purge. To construct the mixed ZnO/Al_2O_3 interface, sixteen total cycles of ZnO deposition were followed by four cycles of alumina deposition, resulting in a nominal layer thickness of ~3.0 nm.

Self-Assembled Monolayer Deposition

Self-assembled monolayers were formed by soaking either the *p*-GaP(100)|Al_2O_3 or *p*-GaP(100)|ZnO(16)Al_2O_3(4) wafers in a 1 mM solution of the corresponding monomer (dodecanethiol, dodecanephosphonic acid, or 12-mercaptododecanephosphonic acid) in

EtOH for 18 hours. The samples were then washed with copious amounts of methanol prior to characterization and further functionalization.

Gold Nanoparticle Deposition

A solution of gold nanoparticles was prepared by diluting a 1 OD Au(citrate) nanoparticles (~10 nm, PDI < 0.2, Sigma Aldrich) in pH 9.3 carbonate/bicarbonate buffer (1:9). The AuNPs were adsorbed to the wafer by immersion in this solution for 18 h. Following Au functionalization, the wafers were washed with copious amounts of water and dried under a nitrogen stream. These as-synthesized samples are stable under ambient light and atmosphere for periods greater than one week.

4.4.3 Electrode Fabrication

The functional GaP electrodes were fabricated by threading a copper wire through a thick walled glass tube. The backside of each sample was scratched with a diamond scribe and GaIn eutectic was applied to the freshly exposed surface of each sample. The samples were further affixed to the copper wire by means of Ag-epoxy (MG Chemicals 8331). The epoxy was allowed to set in a 65 ˚C furnace for 20-30 min. All of the contacts were then encased in blue epoxy paste (Loctite 615 Hysol) that was again set in a 65 ˚C furnace for 30 min. Electrode areas were determined by optical imaging with ImageJ and were typically 0.075 – 0.25 cm^2.

4.4.2 Wafer Characterization

XPS and SEM Measurements

The surface composition and morphology of the wafer pieces were investigated by SEM on a Hitachi S5500 SEM system with a cold probe at a current of 10 mA and voltage of 10 kV. The elemental composition was determined by X-ray photoelectron spectroscopy on a Kratos Axis Ultra with a monochromated Al Kα X-ray source ($h\nu$ = 1486.5 eV). Photoelectron take-off angle was 45° with respect to the X-ray beam, and the analysis chamber pressure remained at *ca.* 2×10^{-9} Torr during measurements. Some non-conductive samples required the use of a charge neutralizer to obtain a suitable signal. Typical region spectra used a pass energy of 20 eV, with the exception of Au 4f scans, for which the pass energy was 40 eV. All signals were standardized to the signal for adventitious carbon fixed at 284.6 eV. The obtained spectra were analyzed using Casa XPS software (version 2.3.15).

Electrochemistry

Electrochemical measurements were performed in a three electrode cell, with a modified semiconductor working electrode (*vide supra*), a platinum wire counter electrode, and either a Ag/Ag^+ (organic) or standard calomel (aqueous) reference electrode. The data were acquired using a Gamry Interface1000 potentiostat. The semiconductor electrodes were illuminated with a 150 W Xenon lamp (Newport, Co.) with an AM1.5G solar filter affixed. Currents are shown as current densities that were determined by the surface area measured for each electrode. All non-aqueous PEC experiments were conducted in 5 mM

ethyl viologen in 0.1 M $LiClO_4$/MeCN electrolyte, while aqueous experiments were conducted in 0.5 M KCl electrolyte. Bulk electrolysis experiments were conducted in an airtight cell with a quartz window and constant stirring.

XPS Spectra of Fully Assembled Wafers

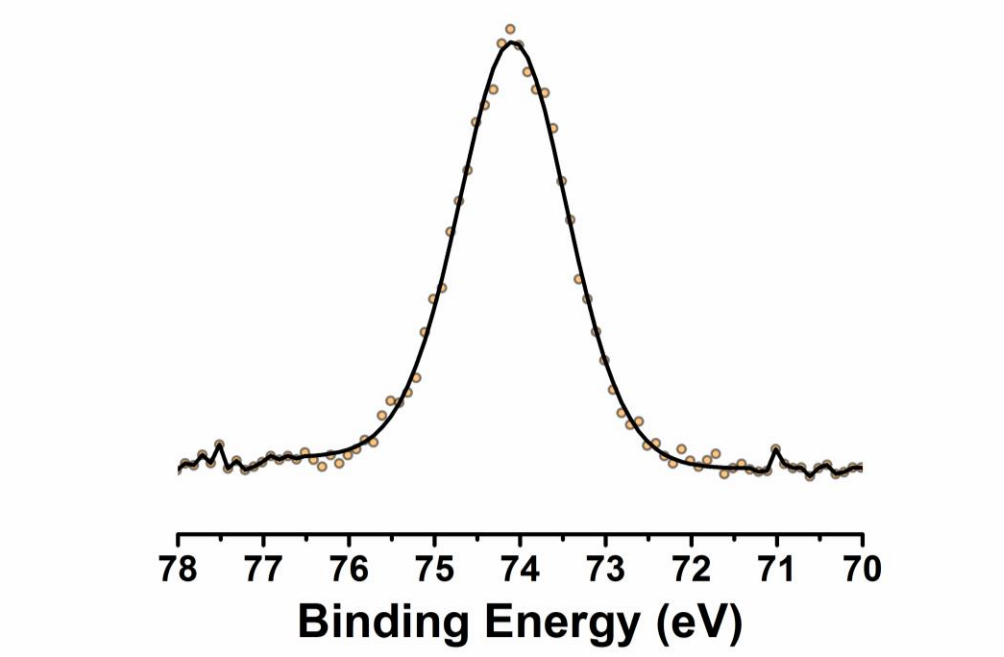

Figure 88. Al 2*p* region spectrum of *p*-GaP(100)|Al_2O_3|SAM|AuNP device.

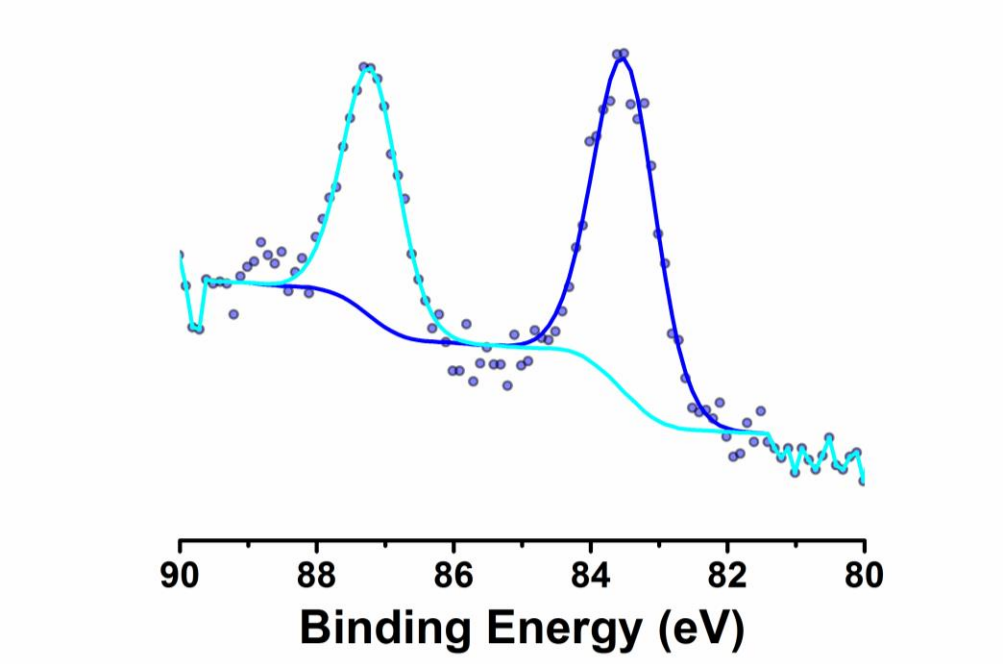

Figure 89. Au 4*f* region spectrum of *p*-GaP(100)|Al_2O_3|SAM|AuNP device.

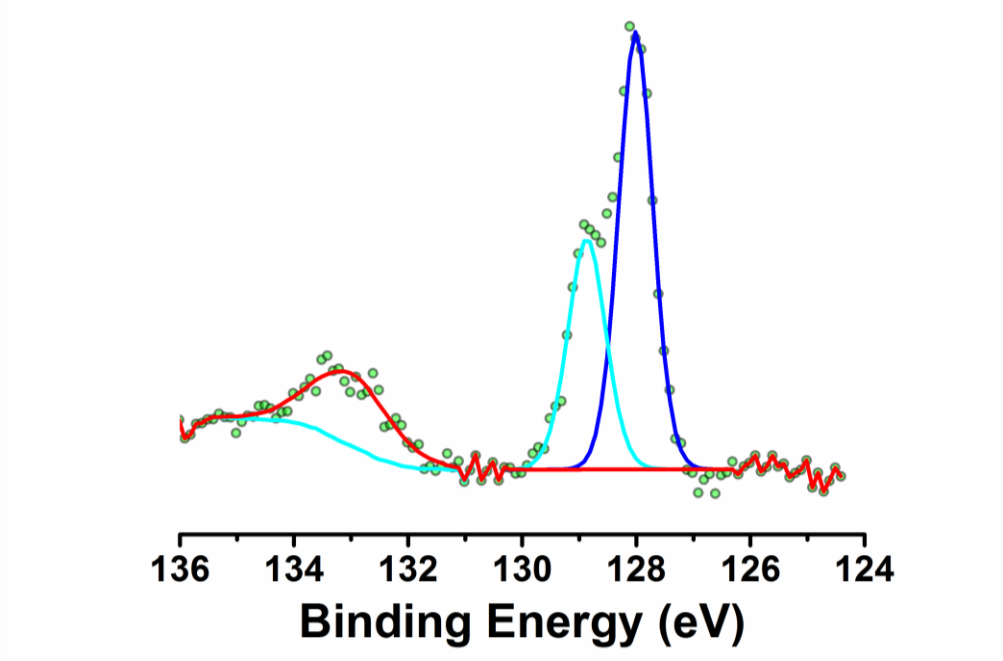

Figure 90. P 2*p* region spectrum of *p*-GaP(100)|Al_2O_3|SAM|AuNP device.

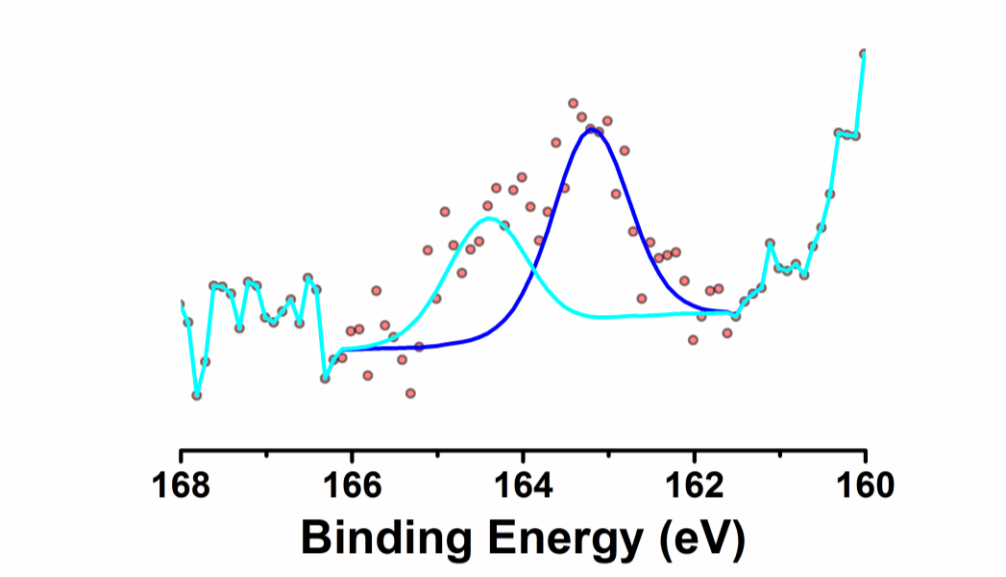

Figure 91. S 2*p* region spectrum of *p*-GaP(100)|Al_2O_3|SAM|AuNP device.

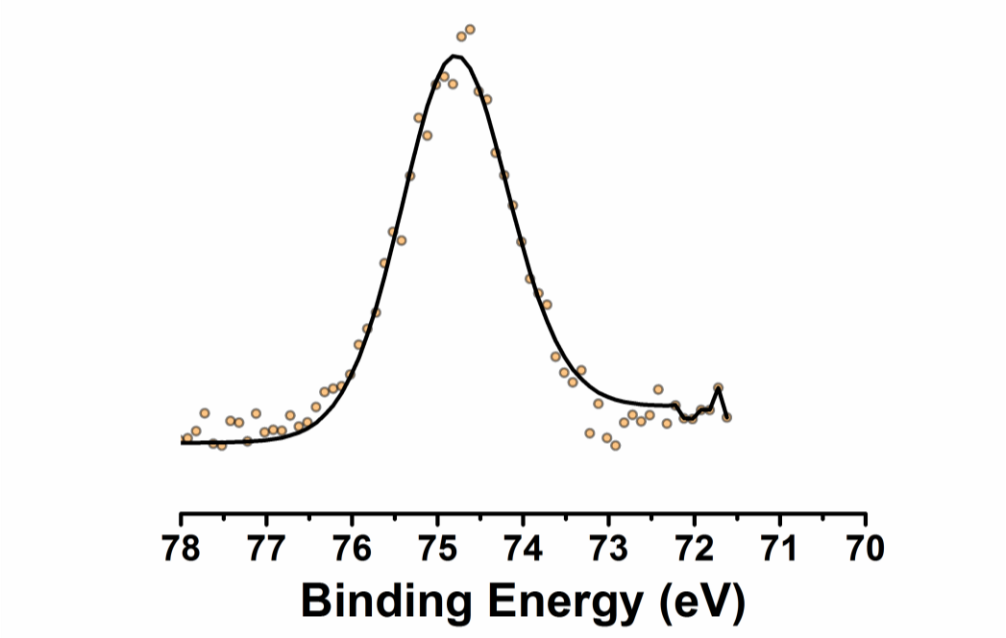

Figure 92. Al 2*p* region spectrum of *p*-GaP(100)|ZnO(16)Al_2O_3(4)|SAM|AuNP device.

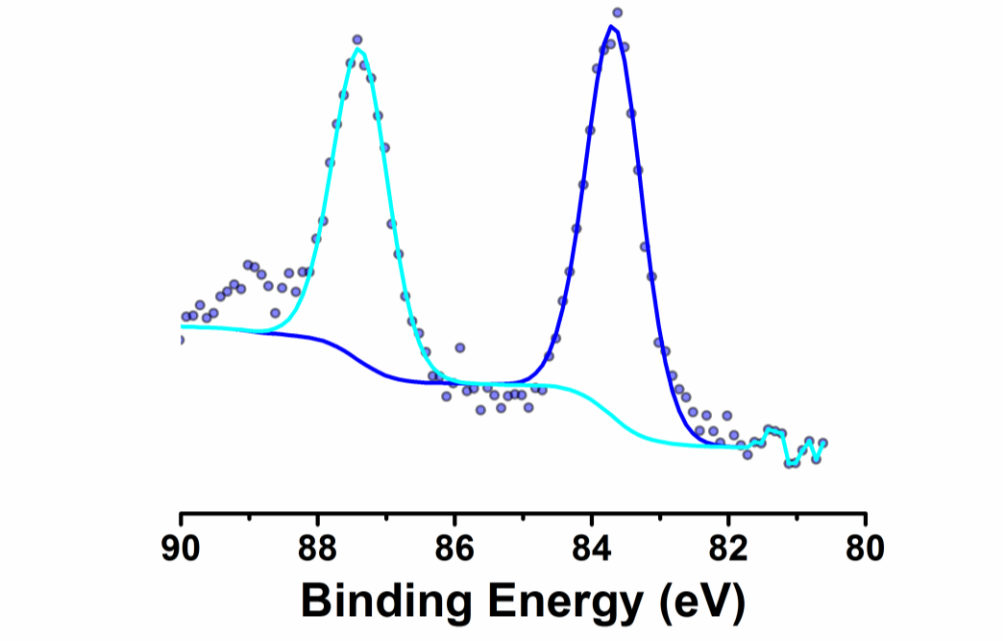

Figure 93. Au 4*f* region spectrum of *p*-GaP(100)|ZnO(16)Al_2O_3(4)|SAM|AuNP device.

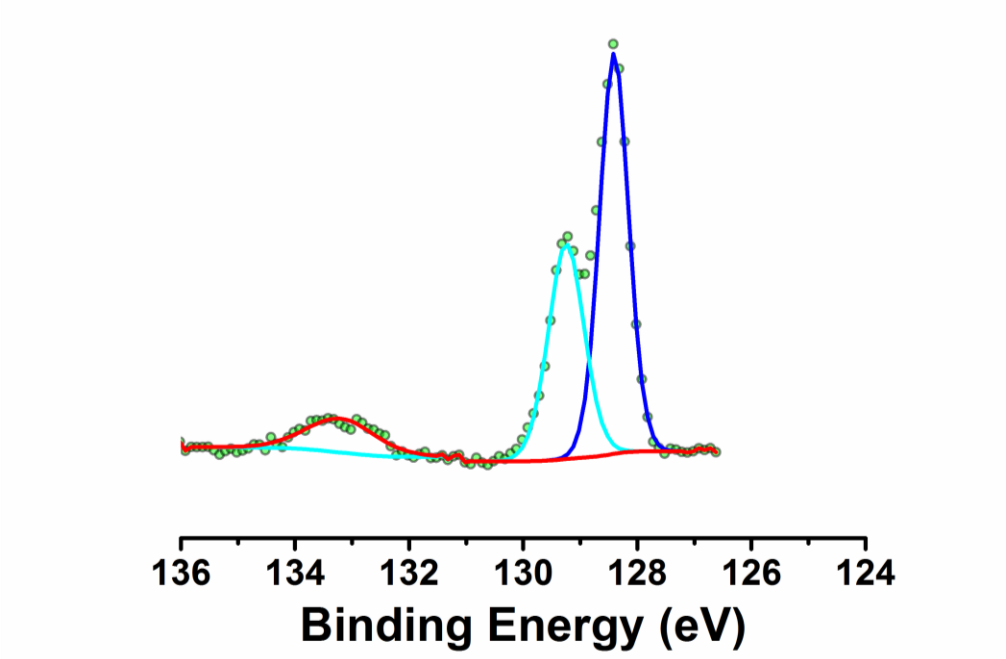

Figure 94. P 2*p* region spectrum of *p*-GaP(100)|ZnO(16)Al_2O_3(4)|SAM|AuNP device.

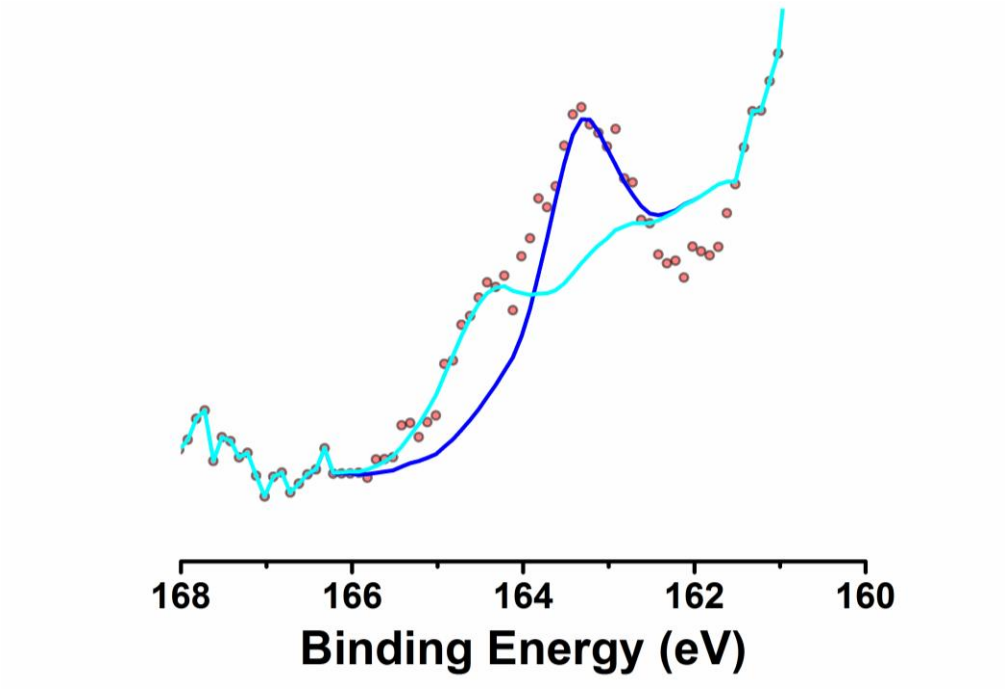

Figure 95. S 2*p* region spectrum of *p*-GaP(100)|ZnO(16)Al_2O_3(4)|SAM|AuNP device.

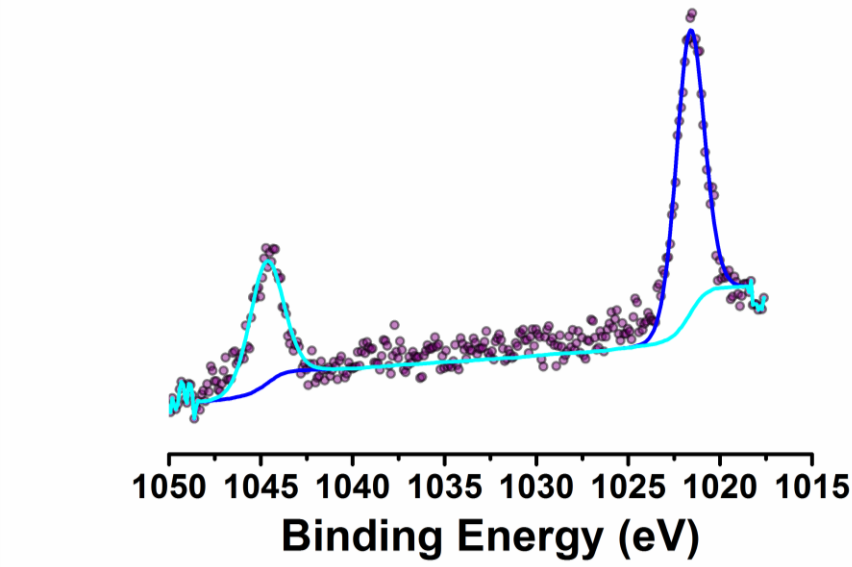

Figure 96. Zn 2*p* region spectrum of *p*-GaP(100)|ZnO(16)Al_2O_3(4)|SAM|AuNP device.

Chapter 5: Thermal Conductivity of Boron Arsenide*

5.1 Introduction

Boron arsenide is a group III-V semiconductor that has been studied far less than other group III-Vs such as GaAs, InP, and GaP. The relative electronegativities of boron (2.04) and arsenic (2.18) suggest a more covalent structure in this binary semiconductor. Similar to other III-V semiconductors, boron arsenide (BAs) predominates in the zinc blende structure. However, the synthesis of boron arsenide has proven much more difficult, with the only published method of true BAs synthesis coming from thermal reaction between the elements.[214–216] Although single source precursor methods have been attempted, the growth of true binary BAs has only been achieved through this method.

*Portions of this chapter have been published elsewhere:
Kim, J.; Evans, D. A.; Sellan, D. P.; Williams, O. M.; Ou, E.; Cowley, A. H.; Shi, L. *Applied Physics Letters* **2016**, *108* (20), 201905.
OMW and DAE synthesized the BAs structures and obtained SEM images. JK, DPS, and EO performed Raman, SEM, and thermal measurements (including construction of a four-point probe). JK, LS, and AHC drafted the manuscript.

In 2012, Swingle *et al.* reported the first experimental data on the semiconducting propterties of BAs.[217] In this study, surficial boron arsenide grown on a boron substrate was shown to have an indirect band gap of 1.46 eV. This material, however, may be useful for properties outside of photovoltaics. Recent first principles calculations have predicted that BAs can possess an unexpectedly high thermal conductivity that surpasses that of diamond.[218] This material may have a large impact in thermal management, particularly in the semiconductor industry. However, the thermal conductivity of this material depends heavily on the purity of the material with respect to defect sites – primarily atomic vacancies. Few experimental results have measured the thermal conductivity properties of BAs and none have successfully corroborated the large values obtained in these calculations.

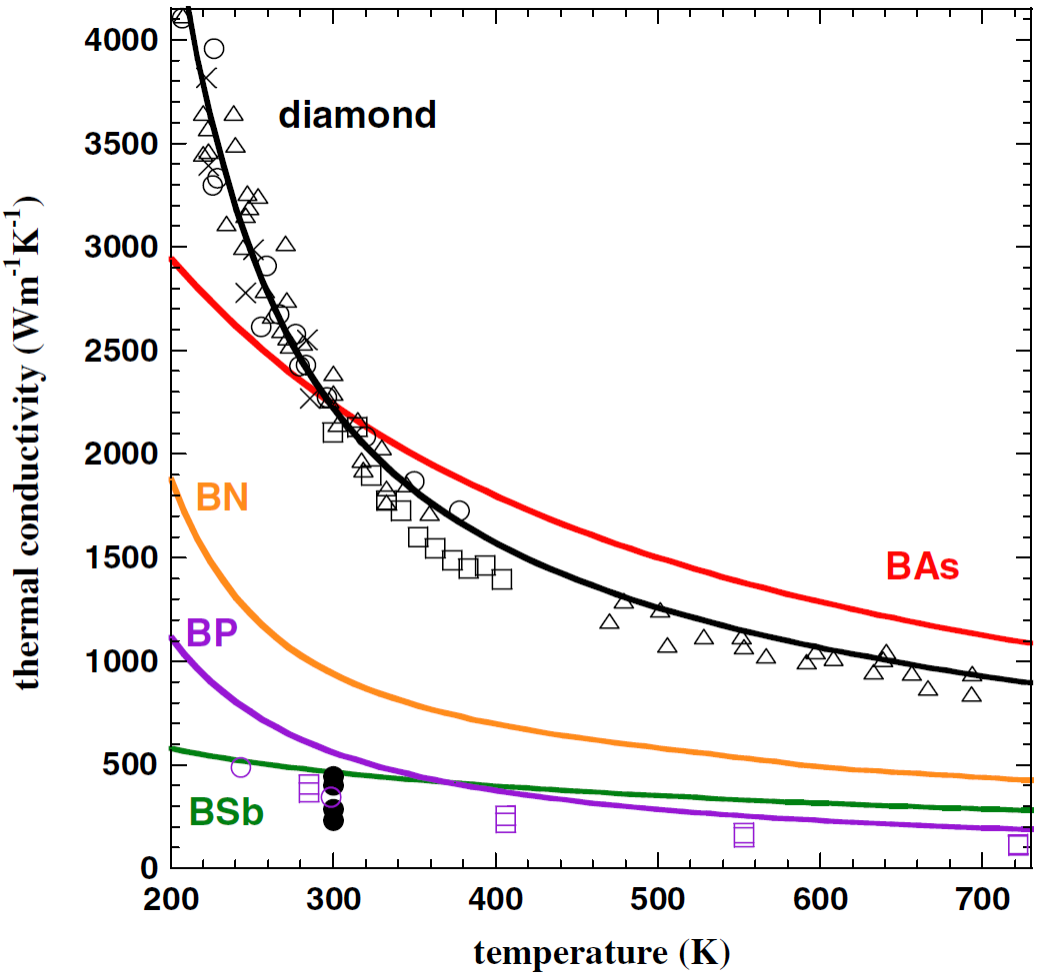

Figure 97. Calculated (solid lines) and experimental (symbols) results for the thermal conductivity of boron pnictides in comparison with that of diamond.[218]

The work of Lindsay *et al.* predicted the thermal conductivity of pure, bulk boron arsenide to be 2240 W m^{-1} K^{-1} at room temperature.[218] Interestingly, while there is a general trend of decreasing thermal conductivity with increasing atomic mass (BN > BP > BSb), BAs was an outlier in this series. Materials that have low average atomic masses, simple crystalline structures, strong bonding, and low anharmonicity are predicted to have high thermal conductivities. The more covalent nature of BAs, in comparison to other boron

pnictogen compounds, may account for part of the increased conductivity. However, calculations suggest that the energy difference between optical (out-of-phase atomic movement) and acoustic (coherent atomic movement) phonons is the driving force behind this high calculated thermal conductivity.

It was proposed that the large atomic mass contrast between boron (B) and arsenic (As), in conjunction with the relatively covalent nature of this bond results in a large energy gap between the optical phonon branches and acoustic phonon branches in BAs, as well as the close bunching of different acoustic branches. This has the effect of reducing the scattering of phonons and increasing the thermal conductivity of the material. Furthermore, most of the short wavelength acoustic phonons are governed by atomic motion of the heavy As atoms, which are isotopically pure. Accordingly, the phonon-isotope impurity scattering is weak in BAs despite the high isotopic impurity concentration in naturally occurring B elements. However, the inclusion of isotopically pure boron into BAs is predicted to raise the thermal conductivity of the material to 3170 W m^{-1} K^{-1}.

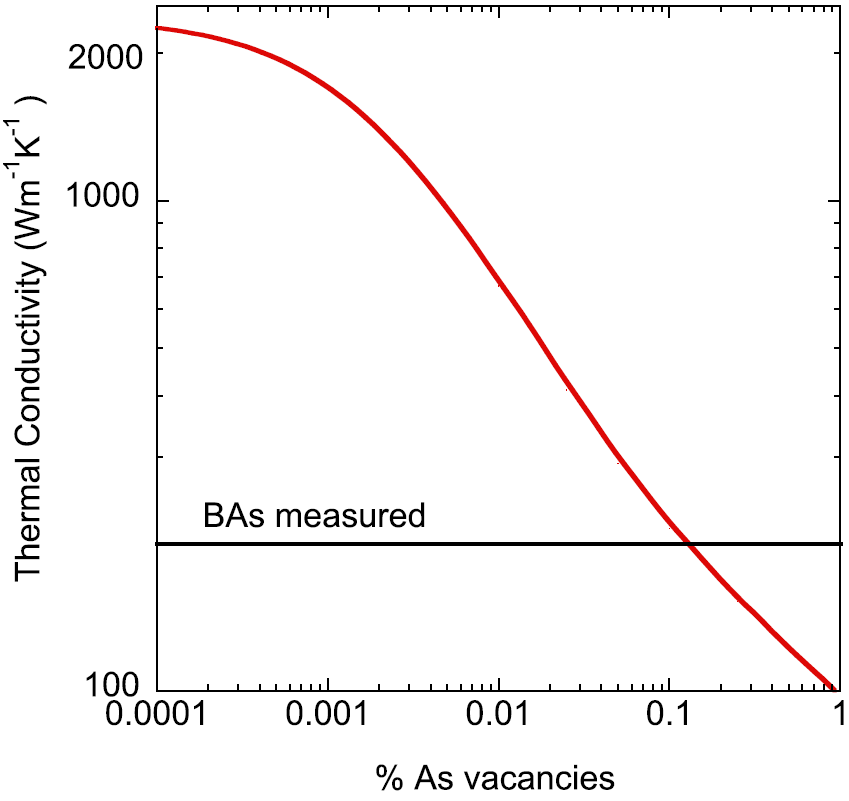

Figure 98. Calculated thermal conductivity (red line) as a function of the percentage of arsenic vacancies. At a vacancy of 0.1% the thermal conductivity decreases by an order of magnitude, thus suggesting that these vacancies may be the reason for the low observed thermal conductivity.[219]

Currently, there is little experimental data available on the thermal transport properties of BAs. However, a recent paper has reported a time domain thermal reflectance (TDTR) measurement of the thermal conductivity of BAs particles with a dimension of a few hundred of microns.[219] The thermal conductivity of BAs at room temperature obtained by this method is 196 W m^{-1} K^{-1}, which is approximately one order of magnitude lower than that of the theoretically calculated value. This discrepancy is attributed to an arsenic deficiency in the BAs sample that was measured. The calculation has predicted that 0.1%

of arsenic vacancies can suppress the thermal conductivity of BAs by one order of magnitude. Furthermore, the structures investigated were twinned crystalline microparticles that may have additional sources of defects other than vacancies. Additional sources of attenuation of the predicted thermal conductivity of BAs were not proposed, though the investigation of these mitigating phenomena could lead to increased device performance.

5.2 Results and Discussion

5.2.1 Synthesis of Boron Arsenide

The synthesis of high-quality bulk BAs crystals has remained a difficult task. Thus far, only small crystals of BAs of various morphologies have been synthesized.[214,216,217,219–221] The BAs microstructure crystals used in the measurement of thermal conductivity were grown by the vapor transport method.[217] Examination of the boron pellets used in the synthesis revealed the presence of a variety of BAs microstructures on the surface that included polycrystalline coatings, micro-rods, dendrites, and platelets, as shown in the scanning electron micrographs (SEMs) of boron arsenide growths (see Figure 100).

While this simple method can be used to synthesize boron arsenide, it has proven difficult to reliably control the growth of the crystalline material. For instance, growths performed on small boron powders (~200-400 mesh) showed growth of longer crystals of BAs, while growths performed on millimeter sized boron rocks predominantly resulted in the growth of spherical crystallites. In many samples, arsenic oxide was found on the surface, suggesting a layer of boron oxide may assist in the growth process on boron

substrates. Additional studies performed with both boron and boron oxide used during thermal growth indicate that boron oxide may be assisting growth by acting as a flux medium for volatile arsenic atoms. At 800 °C, boron oxide would be present as a liquid, supporting this hypothesis. It was observed that BAs growth occurred on the wall of the quartz ampoule as well as over the boron substrate. Furthermore, growths that incorporated boron oxide oftentimes showed holes in crystalline BAs phases, which may indicate the escape of gas during the synthesis. However, growths attempted without the boron substrate resulted in very little BAs growth, although some BAs crystals were found.

$$\text{B (nat. abundance)} + \text{As} \rightarrow {}^{10}\text{B}_{0.2}{}^{11}\text{B}_{0.8}\text{As}$$

$${}^{10/11}\text{B} + \text{As} \rightarrow {}^{10/11}\text{BAs}$$

$${}^{10}\text{B} + {}^{11}\text{B}_2\text{O}_3 + 3\ \text{As} \rightarrow 3\ {}^{10}\text{B}_x{}^{11}\text{B}_{1-x}\text{As} + \frac{3}{2}\,\text{O}_2$$

$${}^{11}\text{B}_2\text{O}_3 + 2\ \text{As} \rightarrow {}^{11}\text{BAs} + \frac{3}{2}\,\text{O}_2\text{*}$$

Scheme 10. Boron arsenide syntheses were attempted in an effort to determine the growth mechanism. *In this synthesis, very minimal BAs growth was observed.

Boron arsenide syntheses were attempted with isotopically pure boron and boron oxide to determine the origin of boron in the resulting BAs microstructures. Growths containing only ^{10}B or ^{11}B boron substrates resulted in the generation of isotopically pure BAs, although there were no observable rod-like structures, precluding the measurement of the thermal conductivities of these materials on a four probe device. Further experiments

attempted with ^{11}B boron substrate and ^{10}B boron oxide indicated that both isotopes had been incorporated into the resultant BAs growths.

5.2.2 Characterization of BAs Microstructures

Spectroscopic characterization of these growths done previously support the assignment of a cubic lattice structure, with a roughly equal molar ratio of boron to arsenic. X-ray photoelectron spectroscopy showed characteristic signals from boron (1s, BE = 191 eV) and arsenic (3d, BE = 41 eV) with a calculated ratio of 1:0.989. Interestingly, in the As 3*d* spectrum, a second peak is observable at 44 eV, which may indicate some degree of oxidation of the material or presence of arsenic oxide. X-ray diffraction spectra show the expected peaks for cubic boron arsenide, as well as the underlying boron substrate (Figure 99).

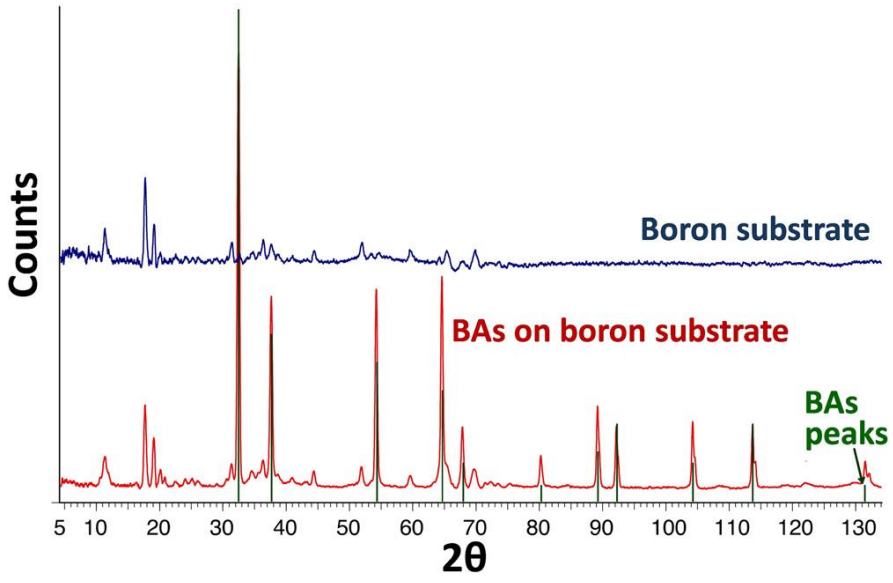

Figure 99. X-ray diffraction pattern of boron arsenide grown on a boron substrate showing the anticipated peaks for cubic boron arsenide.

The primary methods by which microstructures are identified as BAs prior to study of their thermal properties is through scanning electron microscopy (SEM) and Raman spectroscopy. In SEM, there is a clear contrast between the dark boron substrate and light boron arsenide growths. The morphology of these growths typically show a spherical (or hemispherical) polycrystalline growth, although other structures have been observed (Figures 100 and 101). Of particular interest are long, rod-like structures that can be utilized in four probe thermal measurement devices. It was found that utilizing smaller boron powder crystal substrates resulted in a higher density of these types of growths, as well as increased sizes, particularly in one dimension.

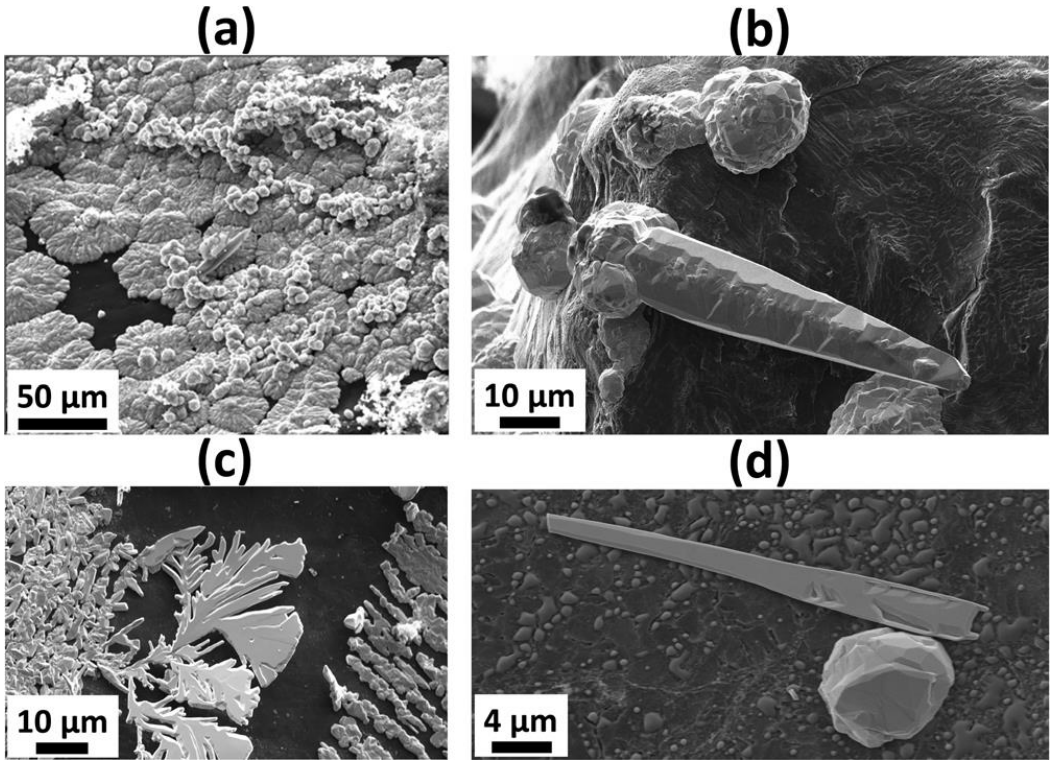

Figure 100. Different growth morphologies for BAs synthesized by the vapor transport method.

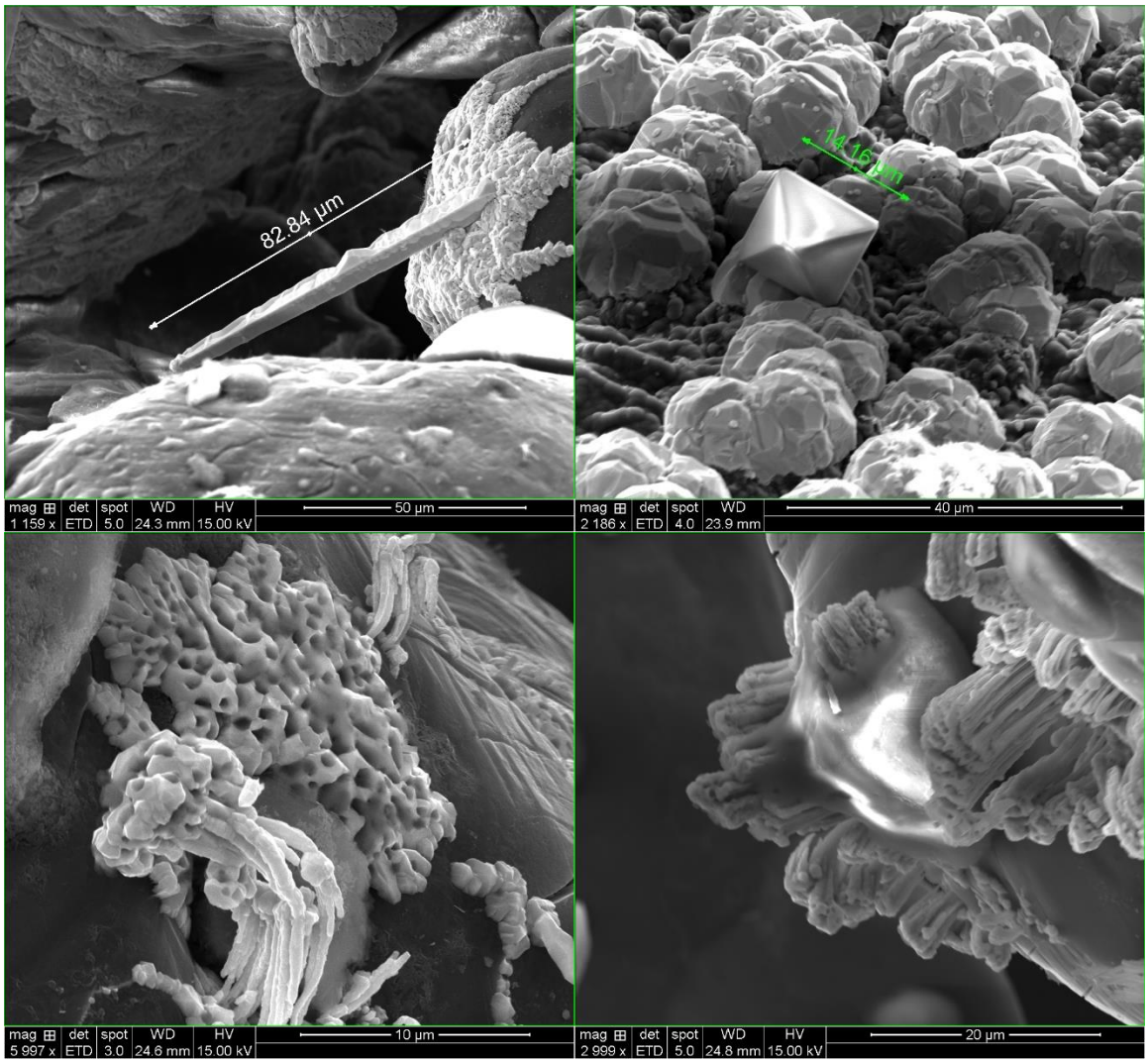

Figure 101. SEM micrographs of a BAs rod synthesized on a small sized particle of boron (top left), observable As_2O_3 in a BAs growth (top right), BAs growth with holes (bottom left) and crystalline BAs growing from a B_2O_3 droplet (bottom right).

Commonly raman measurements are taken on the isolated microstructure in order to confirm its identity by comparison with the known resonance between 690 and 740 wavenumbers. Raman spectra taken with isotopically pure ^{10}B showed a resonance centered at 735 cm^{-1}, while that of ^{11}B shifted this resonance to 702 cm^{-1}. Furthermore,

BAs synthesized with boron precursors containing the natural abundance of boron (20% ^{10}B, 80% ^{11}B) showed distinct peaks for each. A Gaussian fit of these peaks reveal ratios (21% ^{10}B, 79% ^{11}B) that are close to the known natural abundance (20% ^{10}B, 80% ^{11}B). Growths that resulted from a mixed isotope precursor reaction (^{10}B and $^{11}B_2O_3$) showed a similar dual-peak spectrum, with a different isotope ratio (42% ^{10}B, 58% ^{11}B).

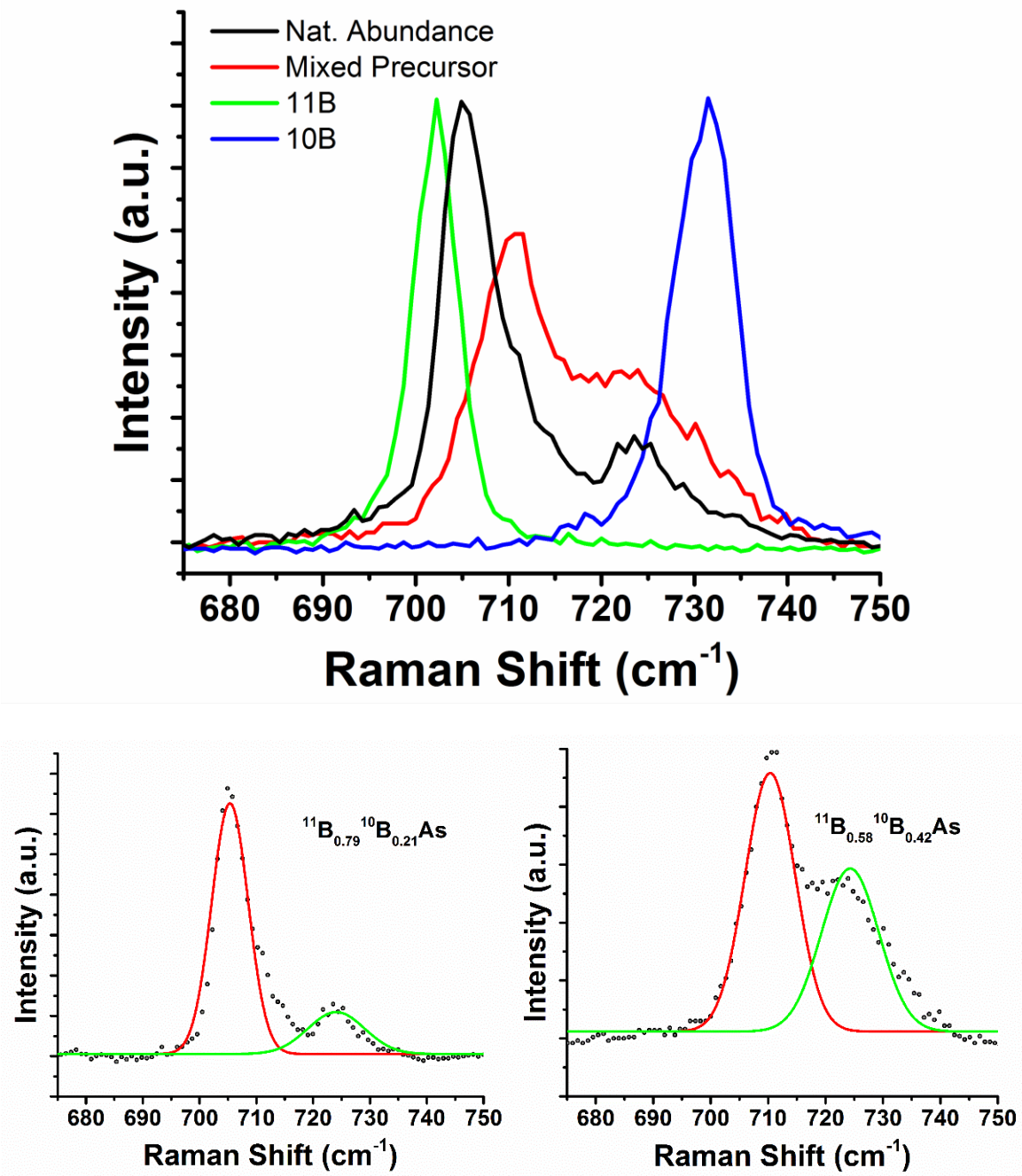

Figure 102. The Raman spectra obtained for the natural abundance, isotopically pure, and mixed isotope BAs growths showing relative abundance of each. The top graph features the experimental data for each growth type. The bottom graphs show the Gaussian fit of each vibrational mode for natural abundance (left) and that for mixed isotope BAs growths (right).

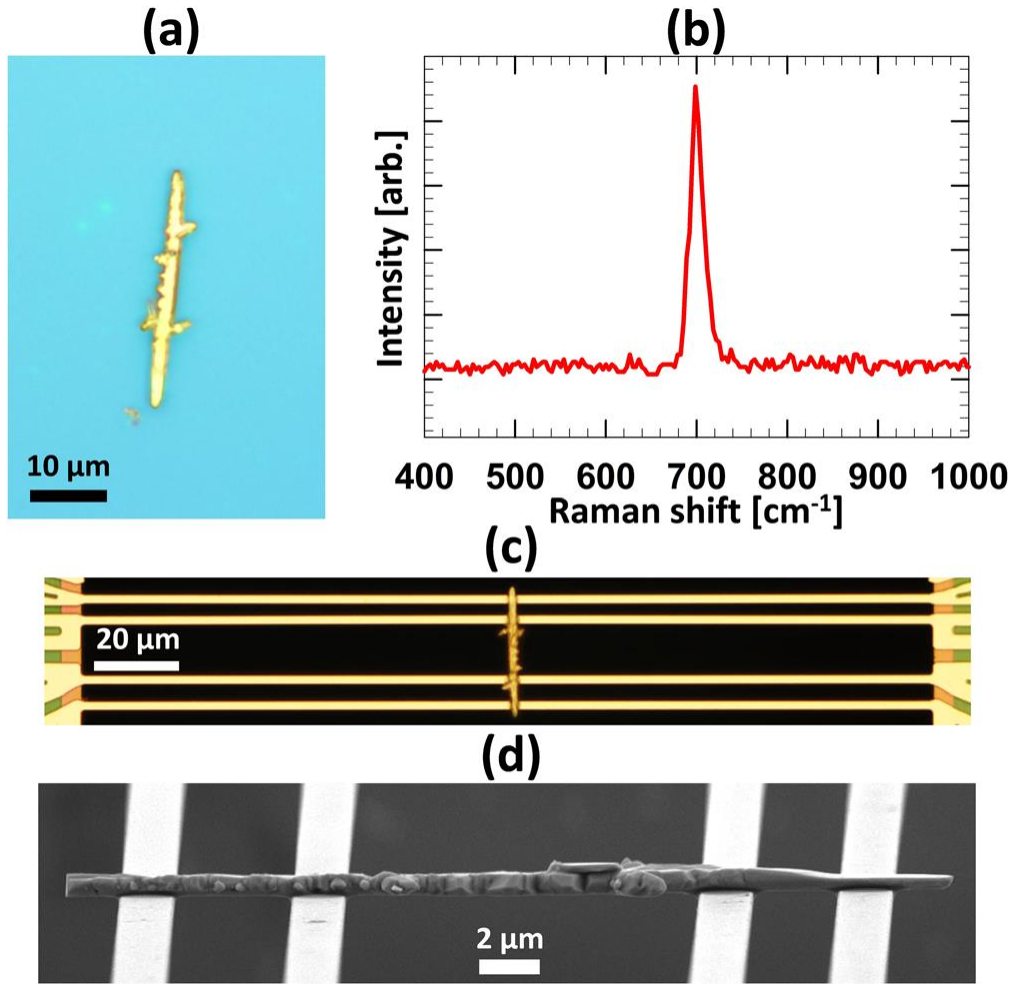

Figure 103. Experimental design for the thermal conductivity measurements: (a) and (c) are optical micrographs for the boron arsenide sample and the assembled device, (b) shows the Raman spectrum used for the identification of BAs and (d) is an SEM showing the points of connection between the sample and the device.

5.2.3 Thermal Conductivity Measurements of BAs

It has been calculated that phonon-boundary scattering can cause a significant reduction in the lattice thermal conductivity of BAs microstructures, which would be more pronounced in structures that have one large lateral dimension.[222] The size-dependent

thermal conductivities contain information on the phonon mean free path distribution.[223] However, measurement of the thermal transport properties of high-thermal conductivity nanostructures and microstructures remains a difficult task. In order to enhance the thermal transport properties of this material, a more robust synthetic method should be developed.

Based on the top-view and the tilted SEM measurement results taken at five different locations, the width (w) and thickness (t) of the BAs microstructure are 1760 ± 210 nm and 591 ± 50 nm, respectively. The BAs microstructure sample was measured using a four probe thermal transport measurement method that has been reported recently.[224] This method is especially useful for high-thermal conductivity micro-rod samples such as the ones obtained in the BAs thermal transport growth.

It was discovered that the BAs microstructure sample made Ohmic electrical contacts to all four thermometer lines. Because of this, a voltage source can be applied to generate a heating current to a single line in the four probe device. The electrical resistance increase in each of the other three thermometer lines was measured individually. In addition to the thermal resistance measurements, the electrical contact allows for four-probe electrical resistance and Seebeck coefficient measurements of the middle suspended segment of the BAs sample.

Figure 104 displays the measurement results of the thermal resistances in the device at three different temperatures, namely 250 K, 300 K, and 350 K. The intrinsic thermal resistance of the middle suspended segment of the BAs sample is approximately a factor of 100 smaller than those of the suspended thermometer lines. Furthermore, the thermal

resistance of the middle segment of the BAs structure decreases slightly with decreasing temperature. When the sample stage temperature decreases to a temperature below 250 K, the difference between the two middle contact point temperatures decreases and approaches the standard error of the measurement, such that values obtained at temperatures below 250 K have a high degree of uncertainty and could not be obtained with precision.

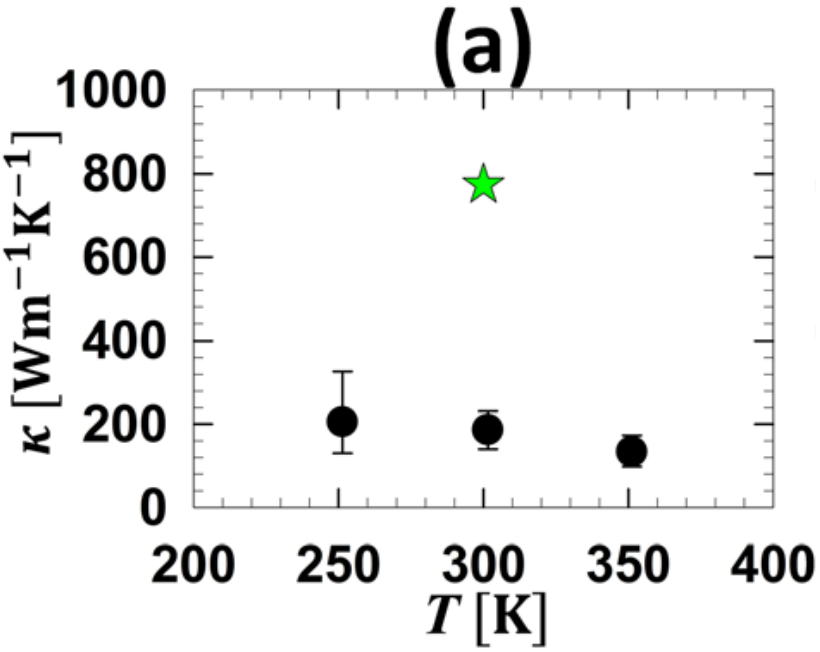

Figure 104. Measured thermal conductivities for boron arsenide (black circles) in comparison with those for the calculated theoretical thermal conductivity (green star).

Figure 104 displays the thermal conductivity of the BAs sample. At a temperature of 300 K, the obtained value is (186 ± 46) W m^{-1} K^{-1}, which is larger than that of bulk silicon. The observed thermal conductivity decreases slightly with increasing temperature. This temperature dependence reveals the effects of umklapp phonon-phonon scattering,

which increases with higher temperatures. However, the temperature dependence is quite weak, suggesting that umklapp phonon scattering is not dominant in comparison with other extrinsic scattering processes such as diffuse phonon-boundary scattering and phonon-defect scattering. At the phonon-boundary scattering mean free path, the room temperature lattice thermal conductivity has been calculated to be about 780 W m^{-1} K^{-1} for natural BAs without isotope purification.[222] The measured value of the BAs microstructure is still considerably lower than this calculation result.

In a recent work, it has been suggested that the presence of As vacancies in BAs can significantly reduce the lattice thermal conductivity of BAs.[219] The measured room-temperature thermal conductivities of single-crystalline BAs particles that are several hundreds of micrometers in size are comparable to the value obtained in the present work for the BAs microstructure. However, the microstructures measured previously had a considerably smaller phonon-boundary scattering mean free path. In the case of silicon, the reported room-temperature thermal conductivity decreases from the bulk value of 156 to 76 W m^{-1} K^{-1} when the thickness is reduced to approximately 1 μm at room temperature.[225,226] This phonon-boundary scattering effect is expected to be more pronounced for materials with higher lattice thermal conductivities. As a consequence, the thermal conductivity of the BAs sample should be significantly higher than that of the measurement value if the boundary scattering effect could be removed by increasing the lateral size at the same defect concentration.

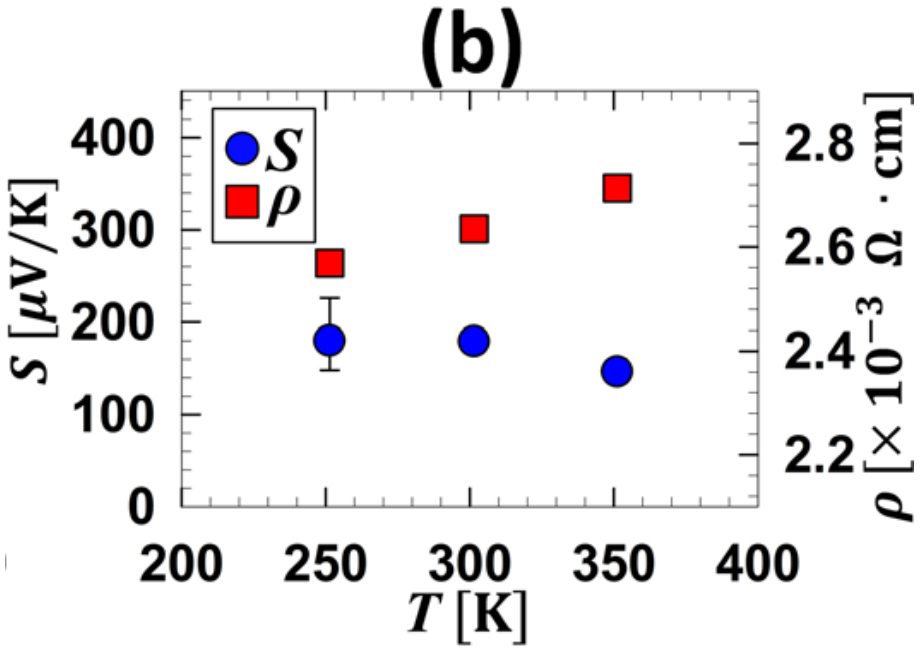

Figure 105. Measured electrical properties of a boron arsenide microstructure: Seebeck coefficient (blue circles, left axis) and resistivity (red squares, right axis).

Additional insights into the thermal transport in the BAs sample can be obtained from the electrical properties of the material. Due to the design of the device, the Seebeck coefficient and electrical resistivity of the BAs sample can be easily measured, the results of which are displayed in Figure 105. The measured Seebeck coefficient is positive, suggesting that the sample is a *p*-type semiconductor. This result corroborates electrochemical results obtained earlier, in which the *p*-type nature of the semiconductor was also observed.[217] Additionally, the electrical resistivity increases linearly with temperatures between 250 K and 350 K. This linear increasing trend is typical for that of a metal, and suggests that the BAs sample is degenerately doped with a high hole concentration. The Seebeck coefficient at room temperature is approximately 180 μV/K at 300 K, which is comparable to that of well-known thermoelectric materials such as bismuth

telluride (Bi_2Te_3).[227] However, the thermal conductivity of the BAs sample is two orders of magnitude higher than that of Bi_2Te_3.

Based on these measurements, the hole concentration was determined to be on the order of 1019 cm^{-3}, which is rather high. The extracted hole mobility is approximately 400 $cm^2 V^{-1} s^{-1}$ at room temperature, and decreases slightly with increasing temperature, due to the effect of electron-phonon scattering. The electronic contribution to the total thermal conductivity was determined to be approximately three orders of magnitude smaller than that of the measured value, which should be dominated by the lattice thermal conductivity.

Despite the negligible electron-phonon conductivity, however, the high hole concentration can play an important role from the standpoint of the lattice thermal conductivity of the sample. A recent calculation has shown that the room-temperature lattice thermal conductivity of bulk silicon can be reduced by as much as 15% and 45%, by electron-phonon scattering when the hole concentration is increased to 1019 and 1021 cm^{-3}, respectively.[228] Since the lattice thermal conductivity of BAs is higher than that of Si, the lattice thermal conductivity is expected to be more sensitive to both boundary scattering and electron scattering in BAs than in Si. As a consequence, the high hole concentration in the BAs sample potentially provides another important cause of the reduced thermal conductivity when compared with the theoretical calculation, which were performed on non-degenerate BAs with low charge carrier concentration.

5.3 CONCLUSION

The four-probe thermal and thermoelectric transport measurements of an individual BAs microstructure that was synthesized via a vapor transport method was determined. It was found that the morphology of BAs growths remains difficult to control, although smaller boron substrates tend to result in larger growths. Raman experiments revealed two distinct vibrational modes for BAs between 705 and 720 cm^{-1} due to the natural abundance of twenty percent boron-10 and eighty percent boron-11. Studies using isotopically pure boron showed a single distinct Raman peak, suggesting an isotopically pure material. Syntheses attempted with boron oxide as a co-reactant was found to help growths. Further isotope studies revealed that boron from both the boron substrate and boron oxide powders were present in the BAs growths.

The foregoing experiments and analyses show that the room-temperature lattice thermal conductivity of the BAs microstructure sample with a critical dimension close to 1 μm is already as high as (186 ± 46) W m^{-1} K^{-1}, which exceeds the bulk thermal conductivity of intrinsic silicon. This value, however, is still a factor of four lower than the expected thermal conductivity of a BAs rod with similar dimensions. The weak temperature dependence of the measured thermal conductivities reveals that umklapp phonon-phonon scattering plays a role but does not dominate other extrinsic scattering mechanisms. The measured Seebeck coefficient and the thermoelectric power factor are as high as those found for bismuth telluride, a commonly used thermoelectric material, and suggests that the BAs microstructure is degenerately *p*-doped with a high hole

concentration (1019 cm^{-3}). In addition to the boundary and defect scattering of phonons, electron-phonon scattering can be another important cause of the lower thermal conductivity found for the BAs microstructure sample than the theoretical calculation of intrinsic BAs crystals. The results indicate that a higher thermal conductivity can potentially be obtained in bulk BAs crystals with a reduced charge carrier and defect concentrations.

5.4 EXPERIMENTAL

5.4.1 Synthesis

For the growth process, elemental boron and arsenic pellets or powders were mixed in a 1:2.1 molar ratio in a quartz tube. This ratio was determined in previous reports to produce the desired molar ratio of boron to arsenic. The quartz tube was subsequently evacuated for one hour by connecting to a Schlenk vacuum line. After sealing the quartz tube by means of an oxy-acetylene torch, the ampoule was placed in a hot box furnace at 800 °C for 72 hours. The ampoule was allowed to cool down to room temperature at the rate of 0.1 °C/min thereby completing the synthesis. Further syntheses incorporated B_2O_3 into the ampoule prior to evacuation. A variety of molar ratios were attempted with no clear difference in the obtained growths.

5.4.2 Characterization

Raman spectra were obtained on a WITec Alpha 300RS confocal Raman imaging and scanning near-field microscope. The instrument was equipped with a 488 nm excitation laser. Powder diffraction data was obtained on a Rigaku R-Axis Spider diffractometer with

an image plate detector. The instrument generated X-rays from a Cu Kα radiation source (λ = 1.51418 Å) in conjunction with a monochromator. Scanning electron microscopy experiments were performed on an FEI Quanta 650 ESEM instrument. X-ray photoelectron spectroscopy was performed on a Kratos Axis Ultra with an Al Kα radiation source (λ = 8.3401 Å) using a pass energy of 80 eV. The spectra were analyzed with CasaXPS software v. 2.3.16 using the Kratos library for relative sensitivity factors.

5.4.3 Thermal Conductivity Measurements

The thermal conductivity device was constructed by an established procedure.[224] A BAs microstructure was picked up with a sharp tungsten probe controlled by a micro-manipulator and transferred onto a silicon substrate coated with a water-soluble polyvinyl alcohol (PVA) layer. The BAs microstructure sample was subsequently transferred to a thermal measurement device by means of a polymethyl methacrylate (PMMA) transfer layer. The PMMA layer was spun onto the PVA coated silicon wafer to which the BAs sample was transferred. After the PVA layer had dissolved in deionized water, the PMMA layer was separated along with the BAs nanostructure sample from the wafer, and was easily picked up with a sharp probe that was controlled by the micro-manipulator. Using an optical microscope, the PMMA layer was then transferred across the four suspended Pd/Cr/SiN_x thermometer lines of the prefabricated thermal measurement device. Following the assembly of the BAs sample on the measurement device, the PMMA layer was removed from the sample by evaporation in a tube furnace that was maintained at a temperature of 350°C and an argon pressure of 1 Torr for two hours.

Appendix A: Structures of Tetrakis(2,6 diisopropylphenyl)imino pyrene and Trinuclear nickel coordination complexes of phenanthrene-9,10-dione dioxime*

A.1 TETRAKIS(2,6 DIISOPROPYLPHENYL)IMINO PYRENE

Imine metal complexes have been widely studied as ligands in organometallic catalysts.[229–232] The Cowley lab has been active in the study of bis-imino acenaphenthene based complexes due to the unique redox characteristics of the ligand.[134,233,234] Below is the structure of a sterically hindered diimine molecule based on the pyrene backbone (tetrakis(2,6-diisopropyl phenyl)imino pyrene, dpp-pyrene). The structure shows a twisted rather than planar backbone, indicating the lack of conjugation across the ring system. The imines adopt an E — *Z*, E — *Z* conformation with relatively large torsion angles across the N – C – C – N fragments.

---

*Portions of this appendix have been published elsewhere:
Williams, O. M.; Cowley, A. H. *Acta Crystallographica Section E Crystallographic Communications* **2016**, *72* (4), 538–542.
Williams, O. M.; Cowley, A. H. *IUCrData* **2016**, *1* (4).
OMW performed the experiments. OMW and AHC prepared the manuscript.

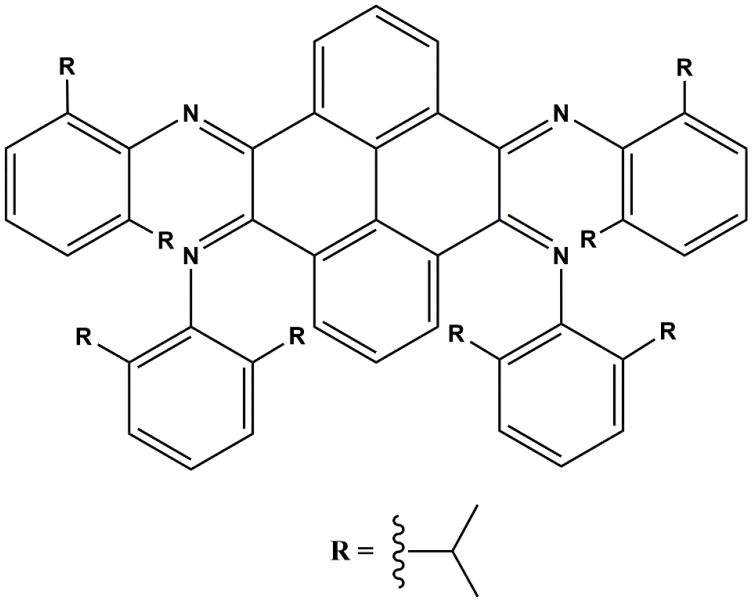

Figure 106. Structure of tetrakis(2,6-diisopropyl phenyl)imino pyrene.

The molecular structure consists of a pyrene backbone with imine moieties located on the 4,5,9, and 10 positions of the ring system. The aryl groups on these imines are sterically bulky 2,6-diisopropylphenyl units. As a consequence, the backbone itself is twisted, with an angle of 15.29 (6) between the mean planes (RMSD/Å = 0.006, 11 0.009) of the phenyl units. The N–C–C–N units are significantly twisted and feature torsion angles of 48.799 for N1–C1– 12 C2–N2 and 46.272 for N3–C8–C9 –N4. The non-planarity of the backbone and short C–N distances (C1—N1 1.283(2), 13 C2—N2 1.281(2), C8—N3 1.283(2), C9—N4 1.285(2) Å) indicate the lack of conjugation in the molecule and double bond nature of the imines. Weak intramolecular and intermolecular C–H●●●π interactions were observed.

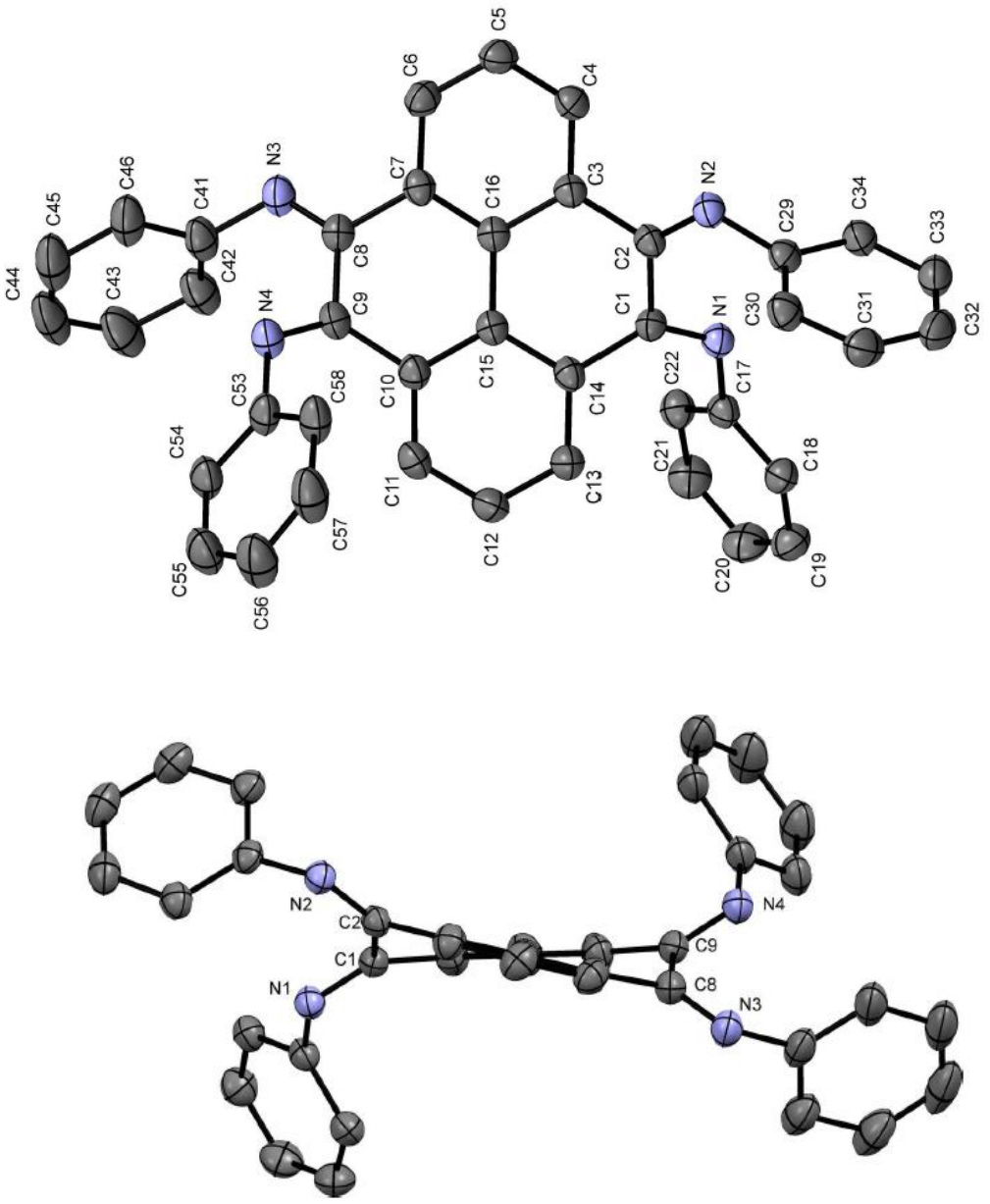

Figure 107. Top down and side on thermal ellipsoid plots (50% probability) of dpp-pyrene. All hydrogen atoms and isopropyl substituents have been removed for clarity.

A.2 TRINUCLEAR NICKEL COORDINATION COMPLEXES OF PHENANTHRENE-9,10-DIONE DIOXIME

Oxime functional groups can coordinate to transition metal ions in a variety of ways, due to the presence of both nitrogen and oxygen donors. On account of the multitude of possible coordinations, these ligands, and particularly α,β dioximes, have the capability of forming bridging multinuclear complexes with many transition metals, including nickel.[235] From the standpoint of single-molecule magnets, these multi-nuclear complexes play an important role due to their ability to facilitate spin-frustration in magnetic transition-metal clusters.[236] Other nickel polynuclear compounds supported by oxime ligands have been reported.[237,238]

Phenanthrenequinone dioxime ($pqdH_2$) is an α,β–dioxime ligand that incorporates a constrained ring system. Similar to other dioximes, however, it exists as three separate stereo-isomers (E – E, E – Z, and Z – Z), as confirmed by liquid chromatography – mass spectrometry. Interestingly, although this compound was synthesized over 100 years ago, no coordination complexes of this ligand have been structurally characterized to date.[239] Reactions of this ligand with nickel(II) acetate produced a trinuclear nickel coordination complex $[Ni_3(pqdH_2)(pqdH)_2(pqd)_2]$, which proved stable enough to undergo a fluoroboration reaction, forming $[Ni_3(pqdH_2)(pqdBF_2)_2(pqd)_2]$

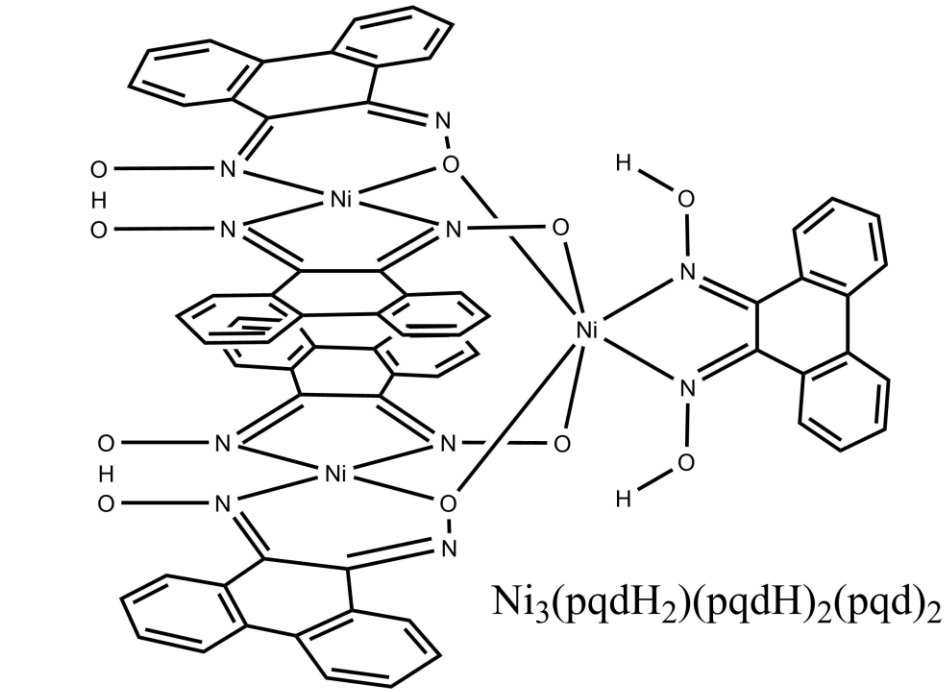

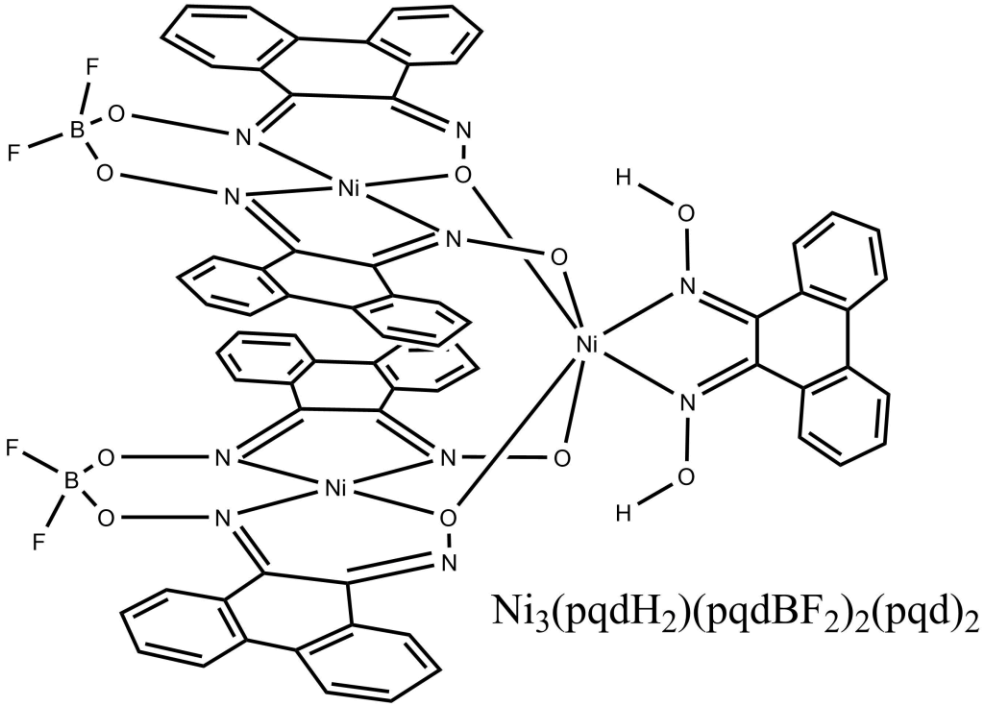

Figure 108. The structures of isolated trinuclear nickel clusters with a phenanthrene – oxime based ligand.

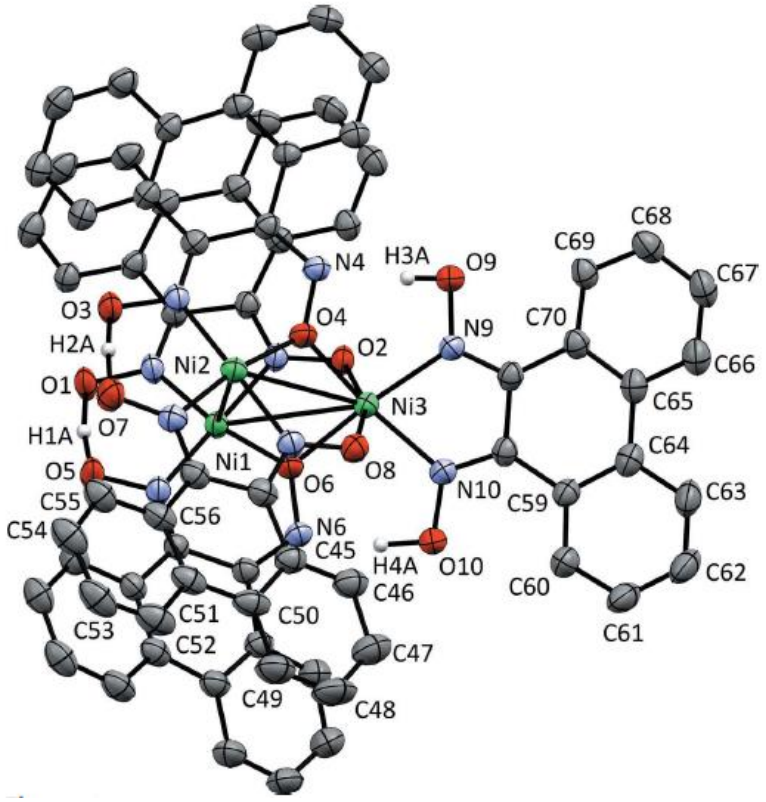

Figure 109. Thermal ellipsoid plot of $[Ni_3(pqdH_2)(pqdH)_2(pqd)_2]$ at the 50% probability level. Non- hydrogen bonded H atoms have been omitted for clarity.

The complex $[Ni_3(pqdH_2)(pqdH)_2(pqd)_2]$ consists of three Ni^{II} atoms in a triangular arrangement, two of which are in a square-planar coordination environment, while the third is in a pseudo-octahedral coordination environment. The square-planar Ni^{II} atoms (Ni1 and Ni2) consist of one N,N-coordinating and one N,O-coordinating ligand. These ligands form bridges with the pseudooctahedral Ni^{II} atom (Ni3) by means of their oxime O atoms. This arrangement permits the formation of Ni—N—O—Ni and Ni—O—Ni bridges between each square-planar Ni^{II} atom and the pseudo-octahedral Ni^{II} atom.

The structural features of the core ligation sphere for the compound warrant special attention. The Ni_{sp}—Ni_{sp} distance is 3.3657 (9) Å a distance that precludes the presence of any metal–metal bonding. However, the distances between each of these nickel moieties and the pseudo-octahedral Ni^{II} atom are nearly identical [Ni_{sp}—Ni_{oct} = 3.2697 (7), 3.2674 (7) Å]. The pseudooctahedral nickel geometry deviates significantly from a perfect octahedral symmetry [O2—Ni3—O8 = 160.00(9), O4—Ni3—N10 = 164.8(1), N9—Ni3—O6 = 165.5(1)].

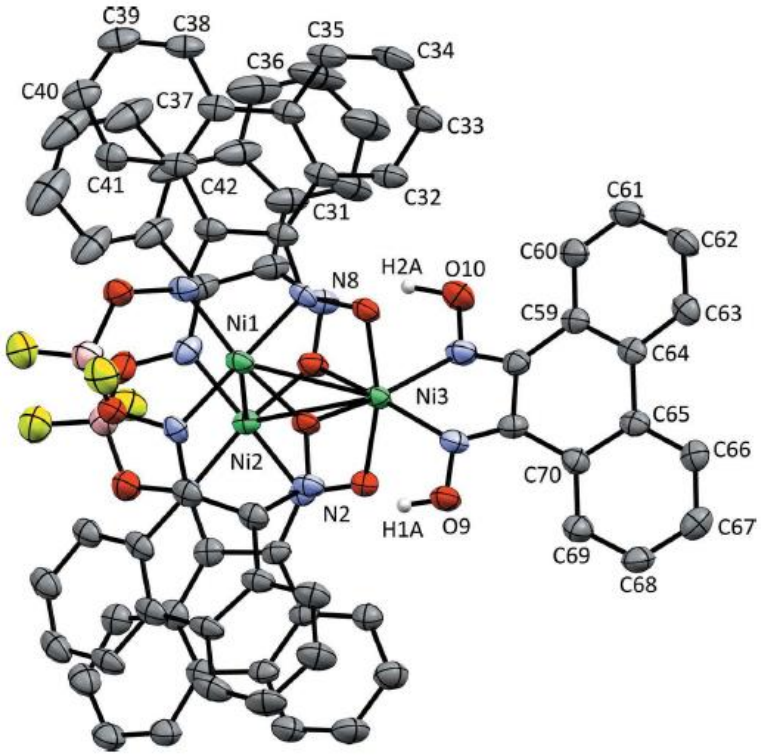

Figure 110. Thermal ellipsoid plot of $[Ni_3(pqdH_2)(pqdBF_2)_2(pqd)_2]$ at the 50% probability level. Non- hydrogen bonded H atoms have been omitted for clarity.

The physical arrangement of the ligation sphere of the fluoroborated compound directly mimics that of the parent complex. In this case, however, the steric bulk of the BF_2 groups forces an expansion of the stacked square-planar nickel units, resulting in an Ni_{sp}—Ni_{sp} distance of 3.592 (1) Å. The distances between these units and the pseudo-octahedral Ni^{II} atom, however, remain similar [Ni_{sp} — Ni_{oct} = 3.274 (1), 3.255 (1) Å]. Overall, the entire structure retains all the other structural features that are present in the proton-bridged compound.

The phenanthrene backbones for both complexes show pronounced twisting between their aromatic rings, which precludes conjugation across this unit. For the proton-bridged complex, the angle between mean planes within a single phenanthrene backbone ranges from 9.24 (19) (between C45–C50 and C51–C56) to 15.44 (13) (between C59–C64 and C65–C70). For the BF_2-bridged complex, there is a wider range of angles, with 5.2 (4) (between C31–C36 and C37–C42) being the smallest, and 17.5 (3) (between C59–C64 and C65–C70) being the largest.

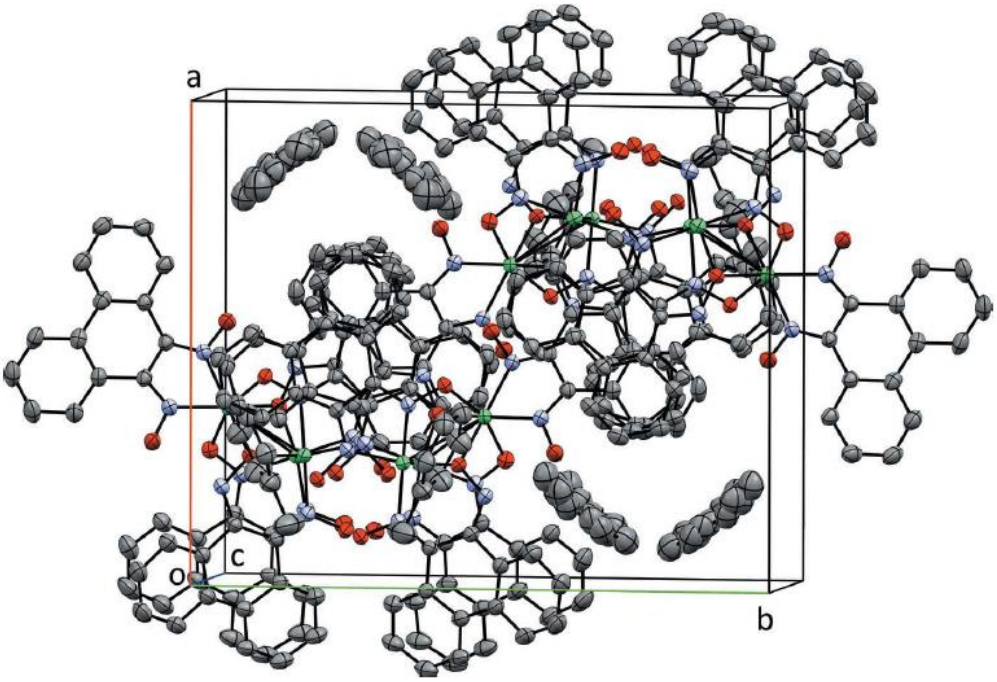

Figure 111. Packing diagram for $[Ni_3(H_2pqd)(Hpqd)_2(pqd)_2]$ viewed approximately down the c-axis direction.

The proton-bridged complex completes the macrocyclic coordination around the square-planar Ni^{II} atoms by means of hydrogen bonds. Furthermore, the ligand that coordinates the pseudo-octahedral Ni^{II} atom features hydrogen-bonding interactions between the oxime hydroxy groups and the ligands of the square-planar Ni^{II} atoms. The nickel units show no direct interaction with their nearest neighbors in the extended lattice. Some π-stacking between adjacent molecules is, however, evident (Fig 111). Two interactions were found, one with a centroid–centroid distance of 3.886 (2) Å and the other with a centroid–centroid distance of 4.256 (3) Å. In the latter case, although not aromatic, the distance to the centroid of the central ring of phenanthrene is shorter, with a distance

of 3.528 (3) Å. Toluene molecules occupy the solvent channels that are oriented along the c axis.

The BF_2-bridged complex completes the macrocyclic coordination around the square-planar Ni^{II} atoms by means of covalent O—B—O bonds. However, the hydrogen-bonding interactions that lock the pseudo-octahedral Ni^{II} atom remain in place. The nickel units show no direct interaction with their nearest neighbors in the extended lattice. A solvent channel oriented along the c axis is also evident (Figure 112). However, the extreme disorder of the solvent does not permit the determination of a suitable model.

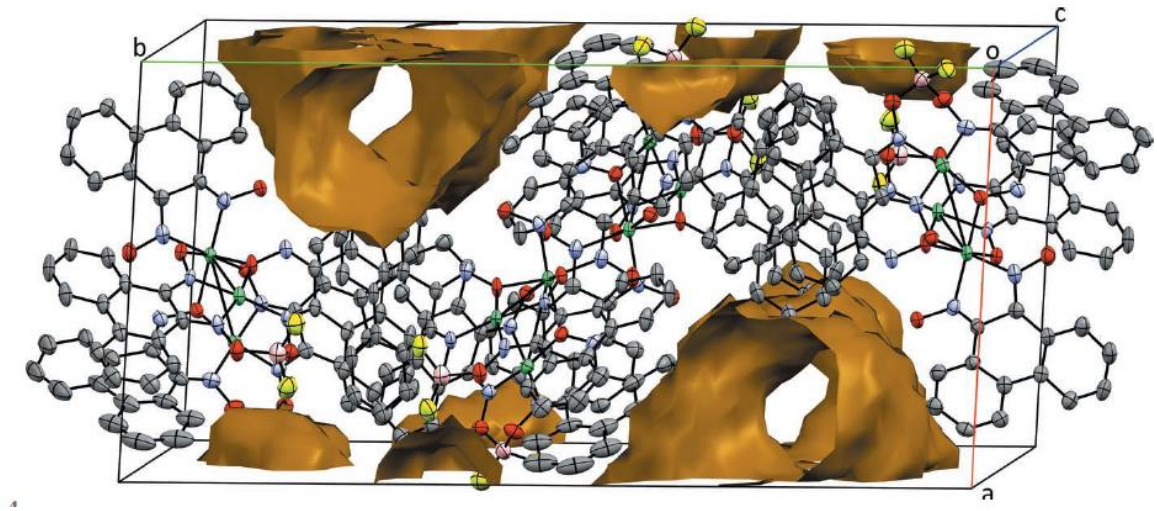

Figure 112. Packing diagram for $Ni_3(H_2pqd)(BF_2pqd)_2(pqd)_2$, viewed approximately down the c-axis direction. Voids for the removed solvent electron density are displayed in yellow.

A.3 EXPERIMENTAL

General Procedures

Pyrene-4,5,9,10-tetraone was synthesized according to literature procedures.[240] 2,6-diisopropylaniline was purchased from Sigma Aldrich and purified by distillation under vacuum. $TiCl_4$ was purchased as a 1 *M* solution in DCM and used as received.

Tetrakis(2,6 diisopropylphenyl)imino pyrene

Pyrene-4,5,9,10-tetraone (52.3 mg; 0.2 mmol) and 2,6-diisopropylaniline (0.4375 g; 2.5 mmol) were added to a Schlenk flask and pumped under vacuum for one hour. To this, 100 ml of dry toluene was added via cannulation. To this, 0.4 ml 28 of 1.0 M $TiCl_4$ was added via syringe. This exothermic reaction was allowed to continue overnight, followed by careful neutralization of excess $TiCl_4$ with 20 ml of deionized water. The solution was washed three times with toluene and aqueous layers discarded. This was further washed with three aliquots (50 ml) of water and dried over magnesium sulfate. The organic solvent was removed *in vacuo*, leaving a crude product with excess aniline oil. The oil was removed by additional washing in acetonitrile (yield: 62.5 mg; 0.07 mmol; 35%) Crystals were afforded by slow evaporation of a saturated solution of the product in DCM.

$[Ni_3(pqdH_2)(pqdH)_2(pqd)_2$

The parent ligand, $pqdH_2$ (0.75 g; 3.1 mmol), was dissolved in 100 ml of ethanol, to which nickel(II) acetate (0.33 g, 1.3 mmol) was added. A red precipitate began to form after approximately 30 min. The solution was then allowed to stir for 1 h, followed by cooling in a freezer and filtration of the crude product (yield: 272 mg, 0.2 mmol, 32%).

The resulting product was dissolved in DMF solution and layered with toluene, resulting in the formation of crystals of $[Ni_3(pqdH_2)(pqdH)_2(pqd)_2]$ after a period of 3 – 4 days. The crystals grew as red blocks with an asymmetric unit consisting of a complete $[Ni_3(H_2pqd)(Hpqd)_2(pqd)_2]$ molecule and two toluene solvent molecules.

$[Ni_3(pqdH_2)(pqdBF_2)_2(pqd)_2]$

The foregoing complex is stable enough to undergo a fluoridoboration reaction with boron trifluoride, thereby affording the compound $[Ni_3(pqdH_2)(pqdBF_2)_2(pqd)_2]$. $[Ni_3(pqdH_2)(pqdH)_2(pqd)_2]$ was diluted in diethyl ether, thereby creating a slurry. One mL of 1.0 molar $BF_3{\bullet}OEt_2$ (in ether) was then added and the mixture was allowed to react overnight. The resulting precipitate was then filtered off and washed thoroughly with EtOH and Et_2O. The resulting precipitate was then dissolved in dichloromethane (DCM) and filtered through Celite (yield: 43 mg, 30 mmol, 79%). Subsequently, a crop of red block-shaped crystals was grown by solvent evaporation over a period of one day.

Data Refinement

Crystal data, data collection and structure refinement details are summarized below. In proton-bridged structure (1), atoms H1A, H2A and H4A were found by assignment of difference map peaks and refined isotropically without geometrical constraints. The proton H3A was initially placed with the SHELXL HFIX 147 command (refinement on rotation) on O9, but was refined freely. Four distinct hydrogen bonding interactions were evident in the trinuclear cluster.

Finally, there were two O—H—O interactions between an oxime and oximato of each [Ni(Hpqd)(pqd)] unit that could not be resolved due to rapid conversion to [Ni(pqd)(Hpqd)] All the restraints that are reported were included for the modelling of the disordered toluene solvent molecules. In the case of BF_2-bridged structure (2), atoms H1A and H2A were affixed to O9 and O10, respectively. They were then refined isotropically without rotational constraints. The SQUEEZE routine as implemented in PLATON was used to remove the electron density of three solvent DCM molecules per unit cell (calculated: 134 e 593 $Å^3$).[147]

Table A1. Crystal data and structure refinement for tetrakis(2,6-diisopropylphenyl)imino pyrene.

Empirical formula	$C_{64}H_{74}N_4$	
Formula weight	899.27	
Temperature	293(2) K	
Wavelength	0.71075 Å	
Crystal system	Monoclinic	
Space group	P $2_1/n$	
Unit cell dimensions	a = 14.527(4) Å	α= 90°.
	b = 10.721(3) Å	β= 97.459(3)°.
	c = 36.004(10) Å	γ = 90°.
Volume	5560(3) $Å^3$	
Z	4	
Density (calculated)	1.074 Mg/m^3	
Absorption coefficient	0.062 mm^{-1}	
F(000)	1944	
Crystal size	0.30 x 0.28 x 0.25 mm^3	
Theta range for data collection	1.454 to 27.500°.	
Index ranges	-18<=h<=18, -13<=k<=13, -46<=l<=46	
Reflections collected	55003	
Independent reflections	12755 [R(int) = 0.0489]	
Completeness to theta = 25.242°	99.9 %	
Absorption correction	Semi-emperical from equivalents	
Max. and min. transmission	1.000 and 0.875	
Refinement method	Full-matrix least-squares on F^2	
Data / restraints / parameters	12755 / 0 / 630	
Goodness-of-fit on F^2	1.063	
Final R indices [I>2sigma(I)]	R1 = 0.0637, wR2 = 0.1556	
R indices (all data)	R1 = 0.0867, wR2 = 0.1745	
Extinction coefficient	0.0022(4)	
Largest diff. peak and hole	0.291 and -0.264 $e.Å^{-3}$	

Table A2. Atomic coordinates (x 10^4) and equivalent isotropic displacement parameters ($Å^2$x 10^3) for tetrakis(2,6-diisopropylphenyl)imino pyrene. U(eq) is defined as one third of the trace of the orthogonalized U^{ij} tensor.

	x	y	z	U(eq)
C(1)	4983(1)	5193(2)	1200(1)	28(1)
C(2)	4807(1)	5005(2)	784(1)	28(1)
C(3)	4179(1)	3939(2)	671(1)	29(1)
C(4)	4267(1)	3255(2)	349(1)	34(1)
C(5)	3691(1)	2231(2)	254(1)	37(1)
C(6)	3015(1)	1906(2)	476(1)	35(1)
C(7)	2902(1)	2598(2)	796(1)	31(1)
C(8)	2165(1)	2278(2)	1031(1)	32(1)
C(9)	1863(1)	3367(2)	1253(1)	31(1)
C(10)	2623(1)	4192(2)	1430(1)	31(1)
C(11)	2573(1)	4853(2)	1761(1)	38(1)
C(12)	3286(1)	5646(2)	1906(1)	40(1)
C(13)	4068(1)	5783(2)	1726(1)	35(1)
C(14)	4147(1)	5117(2)	1399(1)	29(1)
C(15)	3417(1)	4321(2)	1245(1)	28(1)
C(16)	3497(1)	3609(2)	900(1)	28(1)
C(17)	6123(1)	5254(2)	1738(1)	31(1)
C(18)	6526(1)	6343(2)	1905(1)	34(1)
C(19)	6861(1)	6306(2)	2287(1)	41(1)
C(20)	6811(1)	5223(2)	2493(1)	46(1)
C(21)	6423(1)	4153(2)	2321(1)	43(1)
C(22)	6076(1)	4131(2)	1941(1)	35(1)
C(23)	6587(1)	7538(2)	1682(1)	39(1)
C(24)	6036(2)	8601(2)	1834(1)	59(1)
C(25)	7596(2)	7927(2)	1674(1)	52(1)
C(26)	5695(1)	2931(2)	1751(1)	40(1)

C(27)	6419(2)	2308(2)	1542(1)	66(1)
C(28)	5334(2)	1993(3)	2020(1)	75(1)
C(29)	5758(1)	6681(2)	626(1)	31(1)
C(30)	5357(1)	7872(2)	651(1)	38(1)
C(31)	5960(2)	8901(2)	696(1)	44(1)
C(32)	6909(2)	8762(2)	715(1)	46(1)
C(33)	7286(1)	7581(2)	693(1)	44(1)
C(34)	6728(1)	6518(2)	648(1)	36(1)
C(35)	7152(1)	5223(2)	628(1)	45(1)
C(36)	7492(2)	4998(3)	247(1)	85(1)
C(37)	7936(2)	5003(3)	946(1)	62(1)
C(38)	4311(1)	8061(2)	621(1)	50(1)
C(39)	4029(2)	8972(3)	912(1)	75(1)
C(40)	3921(2)	8485(3)	228(1)	81(1)
C(41)	1161(1)	800(2)	1256(1)	43(1)
C(42)	1471(2)	448(2)	1626(1)	51(1)
C(43)	791(2)	67(2)	1848(1)	62(1)
C(44)	-134(2)	19(2)	1705(1)	67(1)
C(45)	-409(2)	303(2)	1334(1)	65(1)
C(46)	225(1)	690(2)	1098(1)	53(1)
C(47)	2498(2)	398(2)	1781(1)	60(1)
C(48)	2740(2)	1124(4)	2136(1)	97(1)
C(49)	2818(3)	-966(3)	1842(1)	108(1)
C(50)	-86(2)	977(3)	689(1)	68(1)
C(51)	-829(2)	1989(3)	642(1)	109(1)
C(52)	-476(3)	-191(3)	472(1)	97(1)
C(53)	631(1)	4667(2)	1384(1)	38(1)
C(54)	133(1)	4563(2)	1692(1)	42(1)
C(55)	-191(2)	5656(2)	1839(1)	58(1)
C(56)	-54(2)	6805(2)	1677(1)	67(1)
C(57)	386(2)	6884(2)	1362(1)	60(1)
C(58)	736(1)	5820(2)	1202(1)	45(1)
C(59)	-37(1)	3312(2)	1868(1)	43(1)

C(60)	433(2)	3211(3)	2271(1)	66(1)
C(61)	-1087(2)	3066(2)	1851(1)	59(1)
C(62)	1164(1)	5925(2)	839(1)	50(1)
C(63)	400(2)	6008(3)	505(1)	80(1)
C(64)	1847(2)	7004(3)	837(1)	72(1)
N(1)	5838(1)	5272(1)	1343(1)	30(1)
N(2)	5165(1)	5628(1)	535(1)	31(1)
N(3)	1836(1)	1167(1)	1019(1)	38(1)
N(4)	984(1)	3549(1)	1235(1)	36(1)

Table A3. Bond lengths [Å] and angles [°] for tetrakis(2,6-diisopropylphenyl)imino pyrene.

C(1)-N(1)	1.283(2)	C(14)-C(15)	1.416(2)
C(1)-C(14)	1.490(2)	C(15)-C(16)	1.476(2)
C(1)-C(2)	1.501(2)	C(17)-C(18)	1.405(2)
C(2)-N(2)	1.281(2)	C(17)-C(22)	1.414(2)
C(2)-C(3)	1.486(2)	C(17)-N(1)	1.428(2)
C(3)-C(4)	1.392(2)	C(18)-C(19)	1.399(3)
C(3)-C(16)	1.414(2)	C(18)-C(23)	1.522(3)
C(4)-C(5)	1.396(2)	C(19)-C(20)	1.384(3)
C(5)-C(6)	1.389(3)	C(20)-C(21)	1.388(3)
C(6)-C(7)	1.398(2)	C(21)-C(22)	1.395(3)
C(7)-C(16)	1.407(2)	C(22)-C(26)	1.526(3)
C(7)-C(8)	1.488(2)	C(23)-C(25)	1.528(3)
C(8)-N(3)	1.283(2)	C(23)-C(24)	1.534(3)
C(8)-C(9)	1.511(2)	C(26)-C(27)	1.525(3)
C(9)-N(4)	1.285(2)	C(26)-C(28)	1.534(3)
C(9)-C(10)	1.492(2)	C(29)-C(30)	1.411(3)
C(10)-C(11)	1.396(2)	C(29)-C(34)	1.412(2)
C(10)-C(15)	1.412(2)	C(29)-N(2)	1.432(2)
C(11)-C(12)	1.388(3)	C(30)-C(31)	1.405(3)
C(12)-C(13)	1.386(2)	C(30)-C(38)	1.523(3)
C(13)-C(14)	1.395(2)	C(31)-C(32)	1.380(3)

C(32)-C(33)	1.386(3)		
C(33)-C(34)	1.395(3)	N(1)-C(1)-C(14)	128.11(15)
C(34)-C(35)	1.525(3)	N(1)-C(1)-C(2)	116.12(14)
C(35)-C(37)	1.524(3)	C(14)-C(1)-C(2)	115.35(14)
C(35)-C(36)	1.533(3)	N(2)-C(2)-C(3)	120.00(15)
C(38)-C(40)	1.524(4)	N(2)-C(2)-C(1)	126.64(15)
C(38)-C(39)	1.526(3)	C(3)-C(2)-C(1)	113.30(13)
C(41)-C(42)	1.401(3)	C(4)-C(3)-C(16)	120.04(15)
C(41)-C(46)	1.409(3)	C(4)-C(3)-C(2)	120.91(15)
C(41)-N(3)	1.434(2)	C(16)-C(3)-C(2)	119.04(15)
C(42)-C(43)	1.409(3)	C(3)-C(4)-C(5)	120.21(16)
C(42)-C(47)	1.525(3)	C(6)-C(5)-C(4)	120.08(17)
C(43)-C(44)	1.377(4)	C(5)-C(6)-C(7)	120.58(16)
C(44)-C(45)	1.376(4)	C(6)-C(7)-C(16)	119.69(15)
C(45)-C(46)	1.393(3)	C(6)-C(7)-C(8)	121.11(15)
C(46)-C(50)	1.516(4)	C(16)-C(7)-C(8)	119.20(15)
C(47)-C(48)	1.497(4)	N(3)-C(8)-C(7)	119.21(16)
C(47)-C(49)	1.541(4)	N(3)-C(8)-C(9)	127.02(15)
C(50)-C(51)	1.524(4)	C(7)-C(8)-C(9)	113.73(14)
C(50)-C(52)	1.544(4)	N(4)-C(9)-C(10)	127.31(16)
C(53)-C(54)	1.404(3)	N(4)-C(9)-C(8)	116.52(15)
C(53)-C(58)	1.416(3)	C(10)-C(9)-C(8)	115.76(14)
C(53)-N(4)	1.434(2)	C(11)-C(10)-C(15)	119.27(15)
C(54)-C(55)	1.393(3)	C(11)-C(10)-C(9)	123.30(15)
C(54)-C(59)	1.517(3)	C(15)-C(10)-C(9)	117.41(15)
C(55)-C(56)	1.387(3)	C(12)-C(11)-C(10)	120.86(16)
C(56)-C(57)	1.376(4)	C(13)-C(12)-C(11)	120.35(17)
C(57)-C(58)	1.403(3)	C(12)-C(13)-C(14)	120.20(16)
C(58)-C(62)	1.523(3)	C(13)-C(14)-C(15)	119.88(15)
C(59)-C(60)	1.524(3)	C(13)-C(14)-C(1)	122.62(15)
C(59)-C(61)	1.542(3)	C(15)-C(14)-C(1)	117.50(15)
C(62)-C(64)	1.525(3)	C(10)-C(15)-C(14)	119.42(15)
C(62)-C(63)	1.529(4)	C(10)-C(15)-C(16)	120.33(15)

C(14)-C(15)-C(16)	120.23(14)	C(29)-C(34)-C(35)	121.10(16)
C(7)-C(16)-C(3)	119.35(15)	C(37)-C(35)-C(34)	111.79(18)
C(7)-C(16)-C(15)	120.71(14)	C(37)-C(35)-C(36)	110.53(19)
C(3)-C(16)-C(15)	119.94(14)	C(34)-C(35)-C(36)	111.44(18)
C(18)-C(17)-C(22)	122.11(16)	C(30)-C(38)-C(40)	110.63(18)
C(18)-C(17)-N(1)	117.78(15)	C(30)-C(38)-C(39)	113.0(2)
C(22)-C(17)-N(1)	119.83(15)	C(40)-C(38)-C(39)	110.2(2)
C(19)-C(18)-C(17)	118.03(17)	C(42)-C(41)-C(46)	122.31(19)
C(19)-C(18)-C(23)	120.47(16)	C(42)-C(41)-N(3)	118.64(18)
C(17)-C(18)-C(23)	121.50(15)	C(46)-C(41)-N(3)	118.8(2)
C(20)-C(19)-C(18)	120.95(18)	C(41)-C(42)-C(43)	117.1(2)
C(19)-C(20)-C(21)	119.98(18)	C(41)-C(42)-C(47)	122.38(18)
C(20)-C(21)-C(22)	121.77(18)	C(43)-C(42)-C(47)	120.4(2)
C(21)-C(22)-C(17)	117.13(17)	C(44)-C(43)-C(42)	121.3(3)
C(21)-C(22)-C(26)	121.07(17)	C(45)-C(44)-C(43)	120.1(2)
C(17)-C(22)-C(26)	121.77(16)	C(44)-C(45)-C(46)	121.7(2)
C(18)-C(23)-C(25)	111.20(16)	C(45)-C(46)-C(41)	117.3(2)
C(18)-C(23)-C(24)	111.62(16)	C(45)-C(46)-C(50)	121.0(2)
C(25)-C(23)-C(24)	110.51(17)	C(41)-C(46)-C(50)	121.68(19)
C(27)-C(26)-C(22)	110.83(16)	C(48)-C(47)-C(42)	113.8(2)
C(27)-C(26)-C(28)	109.8(2)	C(48)-C(47)-C(49)	109.8(3)
C(22)-C(26)-C(28)	113.91(18)	C(42)-C(47)-C(49)	110.3(2)
C(30)-C(29)-C(34)	121.68(16)	C(46)-C(50)-C(51)	111.8(3)
C(30)-C(29)-N(2)	119.16(15)	C(46)-C(50)-C(52)	111.7(2)
C(34)-C(29)-N(2)	118.80(16)	C(51)-C(50)-C(52)	108.2(2)
C(31)-C(30)-C(29)	117.52(17)	C(54)-C(53)-C(58)	122.16(18)
C(31)-C(30)-C(38)	120.37(18)	C(54)-C(53)-N(4)	118.22(16)
C(29)-C(30)-C(38)	122.10(17)	C(58)-C(53)-N(4)	119.47(17)
C(32)-C(31)-C(30)	121.65(19)	C(55)-C(54)-C(53)	117.78(19)
C(31)-C(32)-C(33)	119.72(18)	C(55)-C(54)-C(59)	120.21(18)
C(32)-C(33)-C(34)	121.63(18)	C(53)-C(54)-C(59)	121.99(17)
C(33)-C(34)-C(29)	117.80(18)	C(56)-C(55)-C(54)	121.0(2)
C(33)-C(34)-C(35)	121.10(17)	C(57)-C(56)-C(55)	120.5(2)

C(56)-C(57)-C(58)	121.4(2)	C(58)-C(62)-C(64)	113.4(2)
C(57)-C(58)-C(53)	116.94(19)	C(58)-C(62)-C(63)	110.09(18)
C(57)-C(58)-C(62)	120.17(19)	C(64)-C(62)-C(63)	111.1(2)
C(53)-C(58)-C(62)	122.84(18)	C(1)-N(1)-C(17)	122.66(14)
C(54)-C(59)-C(60)	112.61(19)	C(2)-N(2)-C(29)	122.49(14)
C(54)-C(59)-C(61)	110.40(17)	C(8)-N(3)-C(41)	121.07(16)
C(60)-C(59)-C(61)	110.10(18)	C(9)-N(4)-C(53)	120.64(15)

Table A4. Crystal data and structure refinement for $[Ni_3(pqdH_2)(pqdH)_2(pqd)_2]$.

Empirical formula	$C_{84}H_{60}N_{10}Ni_3O_{10}$	
Formula weight	1545.55	
Temperature	100(2) K	
Wavelength	0.71069 Å	
Crystal system	Monoclinic	
Space group	P $2_1/c$	
Unit cell dimensions	a = 15.973(3) Å	α= 90°.
	b = 18.639(3) Å	β= 101.757(4)°.
	c = 22.785(4) Å	γ = 90°.
Volume	6641.1(19) $Å^3$	
Z	4	
Density (calculated)	1.546 Mg/m^3	
Absorption coefficient	0.918 mm^{-1}	
F(000)	3192	
Crystal size	0.16 x 0.11 x 0.11 mm^3	
Theta range for data collection	1.799 to 27.500°.	
Index ranges	-20<=h<=20, -24<=k<=24, -29<=l<=29	
Reflections collected	79592	
Independent reflections	15260 [R(int) = 0.0541]	
Completeness to theta = 25.240°	99.9 %	
Absorption correction	Semi-emperical from equivalents	
Max. and min. transmission	1.000 and 0.799	
Refinement method	Full-matrix least-squares on F^2	
Data / restraints / parameters	15260 / 291 / 1046	
Goodness-of-fit on F^2	1.211	
Final R indices [I>2sigma(I)]	R1 = 0.0670, wR2 = 0.1467	
R indices (all data)	R1 = 0.0746, wR2 = 0.1507	
Largest diff. peak and hole	0.556 and -0.680 $e.Å^{-3}$	

Table A5. Atomic coordinates (x 104) and equivalent isotropic displacement parameters (Å2x 103) for $[Ni_3(pqdH_2)(pqdH)_2(pqd)_2]$. U(eq) is defined as one third of the trace of the orthogonalized Uij tensor.

	x	y	z	U(eq)
C(1)	3573(2)	2638(2)	7735(2)	30(1)
C(2)	4143(2)	2029(2)	7922(1)	29(1)
C(3)	5058(2)	2146(2)	8144(1)	29(1)
C(4)	5622(2)	1596(2)	8399(2)	34(1)
C(5)	6447(2)	1749(2)	8680(2)	39(1)
C(6)	6738(2)	2450(2)	8712(2)	42(1)
C(7)	6209(2)	2991(2)	8448(2)	41(1)
C(8)	5364(2)	2861(2)	8152(2)	32(1)
C(9)	4809(2)	3450(2)	7863(2)	31(1)
C(10)	5151(2)	4124(2)	7768(2)	37(1)
C(11)	4652(2)	4676(2)	7489(2)	40(1)
C(12)	3783(2)	4571(2)	7278(2)	39(1)
C(13)	3423(2)	3912(2)	7357(2)	33(1)
C(14)	3922(2)	3347(2)	7653(2)	29(1)
C(15)	3654(2)	2458(2)	9361(1)	29(1)
C(16)	4342(2)	1923(2)	9488(1)	28(1)
C(17)	5203(2)	2159(2)	9802(1)	29(1)
C(18)	5819(2)	1651(2)	10055(1)	33(1)
C(19)	6622(2)	1864(2)	10349(2)	36(1)
C(20)	6815(2)	2591(2)	10407(2)	41(1)
C(21)	6211(2)	3092(2)	10169(2)	40(1)
C(22)	5392(2)	2891(2)	9852(1)	32(1)
C(23)	4766(2)	3421(2)	9556(2)	32(1)
C(24)	4995(2)	4137(2)	9493(2)	39(1)
C(25)	4432(3)	4633(2)	9188(2)	43(1)
C(26)	3618(2)	4422(2)	8917(2)	41(1)

C(27)	3360(2)	3721(2)	8974(2)	36(1)
C(28)	3911(2)	3213(2)	9303(2)	31(1)
C(29)	764(2)	1026(2)	7638(1)	29(1)
C(30)	1064(2)	306(2)	7529(2)	31(1)
C(31)	435(2)	-226(2)	7234(2)	35(1)
C(32)	685(2)	-803(2)	6920(2)	43(1)
C(33)	88(3)	-1305(2)	6655(2)	53(1)
C(34)	-749(3)	-1236(2)	6701(2)	54(1)
C(35)	-1009(2)	-668(2)	7002(2)	47(1)
C(36)	-422(2)	-142(2)	7274(2)	37(1)
C(37)	-676(2)	483(2)	7588(2)	36(1)
C(38)	-1479(2)	511(2)	7747(2)	43(1)
C(39)	-1741(2)	1100(2)	8025(2)	46(1)
C(40)	-1214(2)	1683(2)	8152(2)	45(1)
C(41)	-410(2)	1676(2)	8014(2)	39(1)
C(42)	-122(2)	1082(2)	7734(2)	32(1)
C(43)	836(2)	868(2)	9266(2)	35(1)
C(44)	1243(2)	225(2)	9091(2)	35(1)
C(45)	739(2)	-420(2)	8903(2)	38(1)
C(46)	1065(3)	-1008(2)	8641(2)	43(1)
C(47)	542(3)	-1577(2)	8417(2)	56(1)
C(48)	-306(3)	-1576(3)	8468(2)	63(1)
C(49)	-636(3)	-1003(2)	8731(2)	54(1)
C(50)	-134(2)	-412(2)	8958(2)	42(1)
C(51)	-494(2)	194(2)	9233(2)	41(1)
C(52)	-1321(3)	157(2)	9365(2)	51(1)
C(53)	-1662(2)	706(3)	9631(2)	52(1)
C(54)	-1207(2)	1331(3)	9783(2)	51(1)
C(55)	-392(2)	1395(2)	9661(2)	43(1)
C(56)	-28(2)	833(2)	9389(2)	38(1)
C(57)	4778(2)	-960(2)	8798(2)	31(1)
C(58)	4046(2)	-1310(2)	8383(2)	31(1)
C(59)	4055(2)	-2091(2)	8308(1)	32(1)

C(60)	3314(2)	-2495(2)	8088(2)	41(1)
C(61)	3342(3)	-3230(2)	8066(2)	51(1)
C(62)	4101(3)	-3585(2)	8241(2)	53(1)
C(63)	4839(3)	-3203(2)	8458(2)	49(1)
C(64)	4835(2)	-2454(2)	8503(2)	37(1)
C(65)	5628(2)	-2061(2)	8768(2)	37(1)
C(66)	6421(2)	-2409(2)	8859(2)	45(1)
C(67)	7154(3)	-2078(2)	9143(2)	48(1)
C(68)	7123(2)	-1384(2)	9346(2)	44(1)
C(69)	6367(2)	-1005(2)	9251(2)	37(1)
C(70)	5598(2)	-1337(2)	8950(2)	32(1)
C(71)	1134(3)	1368(4)	5502(3)	100(2)
C(72)	2006(3)	1037(3)	5736(2)	60(1)
C(73)	2598(3)	972(2)	5371(2)	51(1)
C(74)	3375(3)	656(2)	5579(2)	50(1)
C(75)	3582(3)	391(2)	6157(2)	50(1)
C(76)	3013(3)	460(3)	6527(2)	63(1)
C(77)	2235(3)	787(3)	6320(2)	72(2)
C(78)	-1860(5)	902(4)	4357(4)	87(2)
C(79)	-1572(3)	1133(3)	4982(3)	73(2)
C(80)	-1792(5)	748(4)	5449(3)	80(2)
C(81)	-1524(6)	964(5)	6039(4)	86(3)
C(82)	-1021(6)	1574(5)	6167(3)	82(3)
C(83)	-800(5)	1963(4)	5703(3)	83(2)
C(84)	-1068(4)	1750(3)	5113(3)	77(2)
C(78A)	-1035(9)	1587(8)	4495(6)	78(4)
C(79A)	-1290(7)	1344(6)	5073(7)	80(3)
C(81A)	-2097(10)	579(9)	5603(8)	82(3)
C(80A)	-1873(8)	791(7)	5038(8)	79(3)
C(82A)	-1790(13)	872(12)	6100(11)	82(3)
C(83A)	-1209(15)	1416(12)	6139(7)	82(3)
C(84A)	-965(12)	1648(9)	5594(6)	81(2)
N(1)	2765(2)	2461(1)	7667(1)	33(1)

N(2)	3714(2)	1422(1)	7917(1)	30(1)
N(3)	2856(2)	2239(1)	9308(1)	31(1)
N(4)	4275(2)	1250(1)	9355(1)	31(1)
N(5)	1304(2)	1565(1)	7651(1)	34(1)
N(6)	1844(2)	73(1)	7664(1)	31(1)
N(7)	1336(2)	1432(2)	9309(1)	35(1)
N(8)	2064(2)	328(2)	9092(1)	33(1)
N(9)	4581(2)	-317(1)	8958(1)	30(1)
N(10)	3456(2)	-857(1)	8145(1)	33(1)
O(1)	2150(2)	2964(1)	7520(1)	42(1)
O(2)	4117(1)	799(1)	8052(1)	33(1)
O(3)	2254(2)	2750(1)	9251(1)	40(1)
O(4)	3492(1)	977(1)	9105(1)	34(1)
O(5)	981(2)	2225(1)	7678(1)	45(1)
O(6)	2477(1)	543(1)	7902(1)	33(1)
O(7)	1062(2)	2078(1)	9454(1)	45(1)
O(8)	2567(2)	-206(1)	8983(1)	36(1)
O(9)	5209(2)	67(1)	9320(1)	40(1)
O(10)	2756(2)	-1128(1)	7745(1)	40(1)
Ni(1)	2513(1)	1499(1)	7762(1)	30(1)
Ni(2)	2461(1)	1280(1)	9220(1)	30(1)
Ni(3)	3468(1)	138(1)	8524(1)	30(1)

Table A6. Bond lengths [Å] and angles [°] for $[Ni_3(pqdH_2)(pqdH)_2(pqd)_2]$.

C(1)-N(1)	1.310(4)	C(6)-C(7)	1.374(5)
C(1)-C(14)	1.461(4)	C(7)-C(8)	1.400(5)
C(1)-C(2)	1.464(4)	C(8)-C(9)	1.479(5)
C(2)-N(2)	1.322(4)	C(9)-C(10)	1.406(4)
C(2)-C(3)	1.462(4)	C(9)-C(14)	1.412(5)
C(3)-C(4)	1.410(5)	C(10)-C(11)	1.373(5)
C(3)-C(8)	1.418(4)	C(11)-C(12)	1.387(5)
C(4)-C(5)	1.373(5)	C(12)-C(13)	1.384(5)
C(5)-C(6)	1.383(5)	C(13)-C(14)	1.408(4)

C(15)-N(3)	1.321(4)	C(39)-C(40)	1.370(6)
C(15)-C(16)	1.468(4)	C(40)-C(41)	1.382(5)
C(15)-C(28)	1.479(4)	C(41)-C(42)	1.401(5)
C(16)-N(4)	1.290(4)	C(43)-N(7)	1.311(4)
C(16)-C(17)	1.481(4)	C(43)-C(44)	1.457(5)
C(17)-C(22)	1.396(4)	C(43)-C(56)	1.465(5)
C(17)-C(18)	1.401(5)	C(44)-N(8)	1.325(4)
C(18)-C(19)	1.380(5)	C(44)-C(45)	1.463(5)
C(19)-C(20)	1.390(5)	C(45)-C(46)	1.399(5)
C(20)-C(21)	1.372(5)	C(45)-C(50)	1.425(5)
C(21)-C(22)	1.410(5)	C(46)-C(47)	1.381(5)
C(22)-C(23)	1.469(5)	C(47)-C(48)	1.383(6)
C(23)-C(24)	1.399(5)	C(48)-C(49)	1.381(7)
C(23)-C(28)	1.424(5)	C(49)-C(50)	1.399(5)
C(24)-C(25)	1.376(5)	C(50)-C(51)	1.465(6)
C(25)-C(26)	1.378(5)	C(51)-C(56)	1.411(5)
C(26)-C(27)	1.384(5)	C(51)-C(52)	1.416(5)
C(27)-C(28)	1.402(5)	C(52)-C(53)	1.359(6)
C(29)-N(5)	1.319(4)	C(53)-C(54)	1.378(6)
C(29)-C(30)	1.465(4)	C(54)-C(55)	1.389(5)
C(29)-C(42)	1.479(4)	C(55)-C(56)	1.402(5)
C(30)-N(6)	1.295(4)	C(57)-N(9)	1.310(4)
C(30)-C(31)	1.472(5)	C(57)-C(70)	1.465(5)
C(31)-C(32)	1.394(5)	C(57)-C(58)	1.495(5)
C(31)-C(36)	1.399(5)	C(58)-N(10)	1.299(4)
C(32)-C(33)	1.384(5)	C(58)-C(59)	1.467(4)
C(33)-C(34)	1.367(6)	C(59)-C(60)	1.406(5)
C(34)-C(35)	1.372(6)	C(59)-C(64)	1.408(5)
C(35)-C(36)	1.410(5)	C(60)-C(61)	1.372(5)
C(36)-C(37)	1.469(5)	C(61)-C(62)	1.368(6)
C(37)-C(38)	1.403(5)	C(62)-C(63)	1.380(6)
C(37)-C(42)	1.420(5)	C(63)-C(64)	1.399(5)
C(38)-C(39)	1.375(6)	C(64)-C(65)	1.481(5)

C(65)-C(66)	1.400(5)	N(4)-O(4)	1.363(3)
C(65)-C(70)	1.416(5)	N(5)-O(5)	1.342(3)
C(66)-C(67)	1.364(6)	N(5)-Ni(1)	1.900(3)
C(67)-C(68)	1.379(6)	N(6)-O(6)	1.364(3)
C(68)-C(69)	1.378(5)	N(7)-O(7)	1.344(4)
C(69)-C(70)	1.420(5)	N(7)-Ni(2)	1.871(3)
C(71)-C(72)	1.517(7)	N(8)-O(8)	1.333(4)
C(72)-C(73)	1.387(6)	N(8)-Ni(2)	1.888(3)
C(72)-C(77)	1.388(7)	N(9)-O(9)	1.365(4)
C(73)-C(74)	1.369(6)	N(9)-Ni(3)	2.035(3)
C(74)-C(75)	1.382(6)	N(10)-O(10)	1.388(4)
C(75)-C(76)	1.365(6)	N(10)-Ni(3)	2.043(3)
C(76)-C(77)	1.377(7)	O(1)-H(1A)	1.29(6)
C(78)-C(79)	1.470(10)	O(2)-Ni(3)	2.050(2)
C(79)-C(80)	1.386(6)	O(3)-H(2A)	1.17(5)
C(79)-C(84)	1.401(6)	O(4)-Ni(2)	1.811(2)
C(80)-C(81)	1.386(7)	O(4)-Ni(3)	2.044(2)
C(81)-C(82)	1.390(7)	O(5)-H(1A)	1.13(6)
C(82)-C(83)	1.386(7)	O(6)-Ni(1)	1.813(2)
C(83)-C(84)	1.384(6)	O(6)-Ni(3)	2.042(2)
C(78A)-C(79A)	1.523(18)	O(7)-H(2A)	1.24(6)
C(79A)-C(84A)	1.32(2)	O(8)-Ni(3)	2.047(2)
C(79A)-C(80A)	1.382(8)	O(9)-H(3A)	0.85(6)
C(81A)-C(82A)	1.26(3)	O(10)-H(4A)	1.04(6)
C(81A)-C(80A)	1.46(2)		
C(82A)-C(83A)	1.36(3)	N(1)-C(1)-C(14)	127.3(3)
C(83A)-C(84A)	1.44(2)	N(1)-C(1)-C(2)	112.3(3)
N(1)-O(1)	1.349(3)	C(14)-C(1)-C(2)	120.4(3)
N(1)-Ni(1)	1.859(3)	N(2)-C(2)-C(3)	127.7(3)
N(2)-O(2)	1.333(3)	N(2)-C(2)-C(1)	111.7(3)
N(2)-Ni(1)	1.884(3)	C(3)-C(2)-C(1)	120.3(3)
N(3)-O(3)	1.341(3)	C(4)-C(3)-C(8)	119.3(3)
N(3)-Ni(2)	1.892(3)	C(4)-C(3)-C(2)	122.9(3)

C(8)-C(3)-C(2)	117.5(3)	C(21)-C(22)-C(23)	122.0(3)
C(5)-C(4)-C(3)	120.8(3)	C(24)-C(23)-C(28)	117.8(3)
C(4)-C(5)-C(6)	120.1(3)	C(24)-C(23)-C(22)	121.4(3)
C(7)-C(6)-C(5)	120.0(3)	C(28)-C(23)-C(22)	120.7(3)
C(6)-C(7)-C(8)	122.1(4)	C(25)-C(24)-C(23)	122.4(3)
C(7)-C(8)-C(3)	117.6(3)	C(24)-C(25)-C(26)	119.6(3)
C(7)-C(8)-C(9)	121.2(3)	C(25)-C(26)-C(27)	119.9(4)
C(3)-C(8)-C(9)	121.2(3)	C(26)-C(27)-C(28)	121.5(3)
C(10)-C(9)-C(14)	117.7(3)	C(27)-C(28)-C(23)	118.6(3)
C(10)-C(9)-C(8)	121.0(3)	C(27)-C(28)-C(15)	122.4(3)
C(14)-C(9)-C(8)	121.3(3)	C(23)-C(28)-C(15)	118.9(3)
C(11)-C(10)-C(9)	122.2(3)	N(5)-C(29)-C(30)	117.8(3)
C(10)-C(11)-C(12)	120.0(3)	N(5)-C(29)-C(42)	125.7(3)
C(13)-C(12)-C(11)	119.5(3)	C(30)-C(29)-C(42)	116.4(3)
C(12)-C(13)-C(14)	121.1(3)	N(6)-C(30)-C(29)	126.8(3)
C(13)-C(14)-C(9)	119.4(3)	N(6)-C(30)-C(31)	114.6(3)
C(13)-C(14)-C(1)	122.9(3)	C(29)-C(30)-C(31)	118.6(3)
C(9)-C(14)-C(1)	117.6(3)	C(32)-C(31)-C(36)	120.4(3)
N(3)-C(15)-C(16)	118.6(3)	C(32)-C(31)-C(30)	120.9(3)
N(3)-C(15)-C(28)	124.4(3)	C(36)-C(31)-C(30)	118.7(3)
C(16)-C(15)-C(28)	117.0(3)	C(33)-C(32)-C(31)	120.1(4)
N(4)-C(16)-C(15)	126.2(3)	C(34)-C(33)-C(32)	120.1(4)
N(4)-C(16)-C(17)	115.3(3)	C(33)-C(34)-C(35)	120.7(4)
C(15)-C(16)-C(17)	118.5(3)	C(34)-C(35)-C(36)	121.0(4)
C(22)-C(17)-C(18)	120.3(3)	C(31)-C(36)-C(35)	117.8(3)
C(22)-C(17)-C(16)	119.6(3)	C(31)-C(36)-C(37)	119.5(3)
C(18)-C(17)-C(16)	120.1(3)	C(35)-C(36)-C(37)	122.8(3)
C(19)-C(18)-C(17)	120.7(3)	C(38)-C(37)-C(42)	118.0(3)
C(18)-C(19)-C(20)	119.5(3)	C(38)-C(37)-C(36)	120.8(3)
C(21)-C(20)-C(19)	120.2(3)	C(42)-C(37)-C(36)	121.1(3)
C(20)-C(21)-C(22)	121.7(3)	C(39)-C(38)-C(37)	121.9(4)
C(17)-C(22)-C(21)	117.7(3)	C(40)-C(39)-C(38)	120.0(4)
C(17)-C(22)-C(23)	120.3(3)	C(39)-C(40)-C(41)	120.2(4)

C(40)-C(41)-C(42)	121.2(4)	N(10)-C(58)-C(59)	128.4(3)
C(41)-C(42)-C(37)	118.7(3)	N(10)-C(58)-C(57)	112.7(3)
C(41)-C(42)-C(29)	122.4(3)	C(59)-C(58)-C(57)	118.8(3)
C(37)-C(42)-C(29)	118.6(3)	C(60)-C(59)-C(64)	118.8(3)
N(7)-C(43)-C(44)	112.4(3)	C(60)-C(59)-C(58)	123.0(3)
N(7)-C(43)-C(56)	127.1(3)	C(64)-C(59)-C(58)	118.0(3)
C(44)-C(43)-C(56)	120.4(3)	C(61)-C(60)-C(59)	121.1(4)
N(8)-C(44)-C(43)	112.2(3)	C(62)-C(61)-C(60)	120.4(4)
N(8)-C(44)-C(45)	127.3(3)	C(61)-C(62)-C(63)	119.8(4)
C(43)-C(44)-C(45)	120.4(3)	C(62)-C(63)-C(64)	121.7(4)
C(46)-C(45)-C(50)	120.2(3)	C(63)-C(64)-C(59)	118.2(3)
C(46)-C(45)-C(44)	122.5(3)	C(63)-C(64)-C(65)	120.5(3)
C(50)-C(45)-C(44)	117.1(3)	C(59)-C(64)-C(65)	121.3(3)
C(47)-C(46)-C(45)	120.6(4)	C(66)-C(65)-C(70)	118.8(3)
C(46)-C(47)-C(48)	119.8(4)	C(66)-C(65)-C(64)	120.2(3)
C(49)-C(48)-C(47)	120.4(4)	C(70)-C(65)-C(64)	120.9(3)
C(48)-C(49)-C(50)	121.9(4)	C(67)-C(66)-C(65)	121.6(4)
C(49)-C(50)-C(45)	117.1(4)	C(66)-C(67)-C(68)	119.8(4)
C(49)-C(50)-C(51)	121.4(4)	C(69)-C(68)-C(67)	121.3(4)
C(45)-C(50)-C(51)	121.5(3)	C(68)-C(69)-C(70)	119.7(3)
C(56)-C(51)-C(52)	117.1(4)	C(65)-C(70)-C(69)	118.7(3)
C(56)-C(51)-C(50)	121.7(3)	C(65)-C(70)-C(57)	118.0(3)
C(52)-C(51)-C(50)	121.2(4)	C(69)-C(70)-C(57)	123.3(3)
C(53)-C(52)-C(51)	122.3(4)	C(73)-C(72)-C(77)	117.9(4)
C(52)-C(53)-C(54)	120.6(4)	C(73)-C(72)-C(71)	121.0(5)
C(53)-C(54)-C(55)	119.4(4)	C(77)-C(72)-C(71)	121.2(5)
C(54)-C(55)-C(56)	120.9(4)	C(74)-C(73)-C(72)	120.7(4)
C(55)-C(56)-C(51)	119.8(3)	C(73)-C(74)-C(75)	120.6(4)
C(55)-C(56)-C(43)	123.0(3)	C(76)-C(75)-C(74)	119.6(4)
C(51)-C(56)-C(43)	117.3(3)	C(75)-C(76)-C(77)	119.9(4)
N(9)-C(57)-C(70)	128.8(3)	C(76)-C(77)-C(72)	121.3(4)
N(9)-C(57)-C(58)	112.0(3)	C(80)-C(79)-C(84)	119.1(5)
C(70)-C(57)-C(58)	119.2(3)	C(80)-C(79)-C(78)	121.0(5)

C(84)-C(79)-C(78)	119.9(5)	O(8)-N(8)-Ni(2)	122.3(2)
C(81)-C(80)-C(79)	121.2(5)	C(57)-N(9)-O(9)	117.4(3)
C(80)-C(81)-C(82)	119.5(5)	C(57)-N(9)-Ni(3)	118.8(2)
C(83)-C(82)-C(81)	119.6(5)	O(9)-N(9)-Ni(3)	122.5(2)
C(84)-C(83)-C(82)	121.0(5)	C(58)-N(10)-O(10)	117.1(3)
C(83)-C(84)-C(79)	119.5(5)	C(58)-N(10)-Ni(3)	118.1(2)
C(84A)-C(79A)-C(80A)	120.4(17)	O(10)-N(10)-Ni(3)	123.1(2)
C(84A)-C(79A)-C(78A)	121.6(11)	N(1)-O(1)-H(1A)	101(3)
C(80A)-C(79A)-C(78A)	117.9(12)	N(2)-O(2)-Ni(3)	111.88(18)
C(82A)-C(81A)-C(80A)	123.7(16)	N(3)-O(3)-H(2A)	103(2)
C(79A)-C(80A)-C(81A)	115.9(14)	N(4)-O(4)-Ni(2)	127.34(19)
C(81A)-C(82A)-C(83A)	121(2)	N(4)-O(4)-Ni(3)	116.88(18)
C(82A)-C(83A)-C(84A)	117.8(17)	Ni(2)-O(4)-Ni(3)	115.78(11)
C(79A)-C(84A)-C(83A)	121.3(18)	N(5)-O(5)-H(1A)	107(3)
C(1)-N(1)-O(1)	120.2(3)	N(6)-O(6)-Ni(1)	127.55(19)
C(1)-N(1)-Ni(1)	117.4(2)	N(6)-O(6)-Ni(3)	116.43(18)
O(1)-N(1)-Ni(1)	122.4(2)	Ni(1)-O(6)-Ni(3)	115.93(11)
C(2)-N(2)-O(2)	121.3(3)	N(7)-O(7)-H(2A)	98(2)
C(2)-N(2)-Ni(1)	116.3(2)	N(8)-O(8)-Ni(3)	111.97(18)
O(2)-N(2)-Ni(1)	122.3(2)	N(9)-O(9)-H(3A)	93(4)
C(15)-N(3)-O(3)	116.8(3)	N(10)-O(10)-H(4A)	102(3)
C(15)-N(3)-Ni(2)	126.6(2)	O(6)-Ni(1)-N(1)	169.58(11)
O(3)-N(3)-Ni(2)	116.3(2)	O(6)-Ni(1)-N(2)	87.73(10)
C(16)-N(4)-O(4)	119.1(3)	N(1)-Ni(1)-N(2)	81.94(11)
C(29)-N(5)-O(5)	116.3(3)	O(6)-Ni(1)-N(5)	91.03(11)
C(29)-N(5)-Ni(1)	126.6(2)	N(1)-Ni(1)-N(5)	99.21(12)
O(5)-N(5)-Ni(1)	116.3(2)	N(2)-Ni(1)-N(5)	176.81(12)
C(30)-N(6)-O(6)	118.6(3)	O(4)-Ni(2)-N(7)	170.22(11)
C(43)-N(7)-O(7)	120.8(3)	O(4)-Ni(2)-N(8)	88.31(11)
C(43)-N(7)-Ni(2)	117.0(2)	N(7)-Ni(2)-N(8)	81.93(12)
O(7)-N(7)-Ni(2)	122.0(2)	O(4)-Ni(2)-N(3)	90.94(11)
C(44)-N(8)-O(8)	121.7(3)	N(7)-Ni(2)-N(3)	98.79(12)
C(44)-N(8)-Ni(2)	115.9(2)	N(8)-Ni(2)-N(3)	177.16(12)

N(9)-Ni(3)-O(6)	165.53(11)	N(10)-Ni(3)-O(8)	89.16(10)
N(9)-Ni(3)-N(10)	76.02(11)	O(4)-Ni(3)-O(8)	80.29(9)
O(6)-Ni(3)-N(10)	95.97(10)	N(9)-Ni(3)-O(2)	91.16(10)
N(9)-Ni(3)-O(4)	96.00(10)	O(6)-Ni(3)-O(2)	79.47(9)
O(6)-Ni(3)-O(4)	94.37(10)	N(10)-Ni(3)-O(2)	106.60(10)
N(10)-Ni(3)-O(4)	164.78(11)	O(4)-Ni(3)-O(2)	86.25(9)
N(9)-Ni(3)-O(8)	104.85(10)	O(8)-Ni(3)-O(2)	159.99(9)
O(6)-Ni(3)-O(8)	86.82(10)		

Table A7. Crystal data and structure refinement for $[Ni_3(pqdH_2)(pqdBF_2)_2(pqd)_2]$.

Empirical formula	$C_{70}H_{42}B_2C_{l0}F_4N_{10}Ni_3O_{10}$	
Formula weight	1456.88	
Temperature	100(2) K	
Wavelength	1.54184 Å	
Crystal system	Monoclinic	
Space group	P $2_1/c$	
Unit cell dimensions	a = 15.6414(8) Å	α= 90°.
	b = 30.8358(11) Å	β= 112.411(6)°.
	c = 14.7380(8) Å	γ = 90°.
Volume	6571.5(6) $Å^3$	
Z	4	
Density (calculated)	1.473 Mg/m^3	
Absorption coefficient	1.671 mm^{-1}	
F(000)	2968	
Crystal size	0.29 x 0.07 x 0.04 mm^3	
Theta range for data collection	3.376 to 74.998°.	
Index ranges	-19<=h<=19, -26<=k<=38, -18<=l<=18	
Reflections collected	25337	
Independent reflections	13041 [R(int) = 0.0595]	
Completeness to theta = 67.684°	99.2 %	
Absorption correction	Semi-emperical from equivalents	
Max. and min. transmission	1.000 and 0.303	
Refinement method	Full-matrix least-squares on F^2	
Data / restraints / parameters	13041 / 0 / 896	
Goodness-of-fit on F^2	1.030	
Final R indices [I>2sigma(I)]	R1 = 0.0771, wR2 = 0.1913	
R indices (all data)	R1 = 0.1112, wR2 = 0.2263	
Largest diff. peak and hole	1.162 and -0.825 e.$Å^{-3}$	

Table A8. Atomic coordinates (x 10^4) and equivalent isotropic displacement parameters ($Å^2$x 10^3) for $[Ni_3(pqdH_2)(pqdBF_2)_2(pqd)_2]$. U(eq) is defined as one third of the trace of the orthogonalized U^{ij} tensor.

	x	y	z	U(eq)
C(1)	3411(3)	3369(2)	7321(4)	32(1)
C(2)	4326(3)	3400(2)	7254(4)	34(1)
C(3)	4765(4)	2995(2)	7127(4)	35(1)
C(4)	5720(4)	2972(2)	7393(4)	42(1)
C(5)	6130(4)	2588(2)	7267(5)	50(1)
C(6)	5574(4)	2227(2)	6875(5)	50(2)
C(7)	4637(4)	2248(2)	6619(4)	46(1)
C(8)	4198(4)	2629(2)	6727(4)	36(1)
C(9)	3201(4)	2664(2)	6448(4)	36(1)
C(10)	2594(4)	2348(2)	5841(4)	39(1)
C(11)	1655(4)	2382(2)	5555(4)	44(1)
C(12)	1264(4)	2731(2)	5831(4)	42(1)
C(13)	1837(4)	3049(2)	6426(4)	36(1)
C(14)	2797(4)	3018(2)	6744(4)	34(1)
C(15)	2126(3)	3650(2)	4672(3)	31(1)
C(16)	3085(3)	3776(2)	4870(3)	30(1)
C(17)	3700(3)	3479(2)	4634(3)	30(1)
C(18)	4630(3)	3577(2)	4827(4)	35(1)
C(19)	5208(4)	3274(2)	4649(4)	44(1)
C(20)	4864(4)	2869(2)	4294(4)	47(1)
C(21)	3950(4)	2770(2)	4081(4)	42(1)
C(22)	3341(3)	3070(2)	4230(4)	33(1)
C(23)	2352(4)	2972(2)	3911(4)	34(1)
C(24)	1973(4)	2591(2)	3381(4)	42(1)
C(25)	1044(4)	2504(2)	3013(4)	46(1)
C(26)	436(4)	2802(2)	3149(4)	45(1)

C(27)	781(4)	3176(2)	3690(4)	38(1)
C(28)	1730(3)	3264(2)	4084(4)	34(1)
C(29)	3296(3)	4767(2)	9399(4)	33(1)
C(30)	3915(3)	5007(2)	9040(3)	32(1)
C(31)	4137(3)	5462(2)	9300(3)	32(1)
C(32)	4728(4)	5705(2)	8987(4)	39(1)
C(33)	4942(4)	6128(2)	9267(4)	45(1)
C(34)	4558(5)	6325(2)	9862(5)	56(2)
C(35)	3969(4)	6097(2)	10163(4)	45(1)
C(36)	3721(4)	5668(2)	9903(3)	34(1)
C(37)	3088(4)	5426(2)	10242(4)	36(1)
C(38)	2666(4)	5639(2)	10798(4)	42(1)
C(39)	2105(4)	5425(2)	11168(4)	50(2)
C(40)	1938(4)	4987(2)	10998(4)	44(1)
C(41)	2339(4)	4766(2)	10439(4)	37(1)
C(42)	2897(4)	4981(2)	10043(3)	36(1)
C(43)	1661(3)	4960(2)	6807(4)	40(1)
C(44)	2317(3)	5296(2)	6755(4)	39(1)
C(45)	2153(4)	5756(2)	6941(4)	51(2)
C(46)	2581(4)	6091(2)	6633(5)	58(2)
C(47)	2434(5)	6522(2)	6804(7)	77(3)
C(48)	1844(5)	6615(3)	7286(7)	94(3)
C(49)	1427(5)	6285(3)	7595(6)	83(3)
C(50)	1571(4)	5845(2)	7429(5)	61(2)
C(51)	1151(4)	5488(3)	7768(4)	62(2)
C(52)	734(5)	5578(3)	8439(5)	73(2)
C(53)	348(5)	5250(4)	8776(5)	88(3)
C(54)	385(4)	4820(4)	8502(5)	77(3)
C(55)	804(4)	4722(3)	7841(4)	60(2)
C(56)	1175(4)	5059(2)	7462(4)	50(2)
C(57)	6326(3)	4847(2)	6652(4)	32(1)
C(58)	5935(3)	5287(2)	6698(3)	32(1)
C(59)	6591(3)	5649(2)	7051(3)	30(1)

C(60)	6390(4)	6013(2)	7479(4)	40(1)
C(61)	7056(4)	6324(2)	7902(5)	46(1)
C(62)	7926(4)	6279(2)	7885(4)	44(1)
C(63)	8141(4)	5919(2)	7452(4)	36(1)
C(64)	7473(3)	5596(2)	7021(3)	30(1)
C(65)	7705(3)	5207(2)	6569(3)	32(1)
C(66)	8480(3)	5197(2)	6315(4)	35(1)
C(67)	8690(3)	4830(2)	5900(4)	39(1)
C(68)	8134(4)	4467(2)	5735(4)	41(1)
C(69)	7366(3)	4467(2)	5982(4)	39(1)
C(70)	7146(3)	4832(2)	6398(4)	33(1)
N(1)	3219(3)	3649(1)	7882(3)	32(1)
N(2)	4789(3)	3750(1)	7289(3)	34(1)
N(3)	1712(3)	3922(1)	5053(3)	32(1)
N(4)	3296(3)	4153(1)	5315(3)	29(1)
N(5)	3158(3)	4367(1)	9063(3)	34(1)
N(6)	4215(3)	4768(1)	8493(3)	29(1)
N(7)	1558(3)	4619(2)	6258(3)	36(1)
N(8)	3047(3)	5233(1)	6565(3)	36(1)
N(9)	5880(3)	4540(1)	6849(3)	35(1)
N(10)	5047(3)	5261(1)	6498(3)	38(1)
O(1)	2406(3)	3586(1)	8007(3)	40(1)
O(2)	4437(2)	4127(1)	7481(3)	33(1)
O(3)	833(2)	3834(1)	4931(3)	44(1)
O(4)	4102(2)	4336(1)	5494(2)	32(1)
O(5)	2580(3)	4111(1)	9310(3)	42(1)
O(6)	4795(2)	4920(1)	8119(3)	32(1)
O(7)	898(3)	4328(1)	6260(3)	45(1)
O(8)	3220(2)	4829(1)	6323(3)	35(1)
O(9)	6191(2)	4123(1)	6839(3)	37(1)
O(10)	4608(3)	5641(1)	6526(3)	46(1)
Ni(1)	3772(1)	4198(1)	8256(1)	31(1)
Ni(2)	2396(1)	4403(1)	5716(1)	30(1)

Ni(3)	4582(1)	4668(1)	6774(1)	28(1)
F(1)	3252(3)	3412(1)	9649(3)	56(1)
F(2)	1678(3)	3513(1)	9084(3)	60(1)
F(3)	-369(2)	3912(1)	5394(3)	61(1)
F(4)	9(2)	4477(1)	4612(3)	51(1)
B(1)	2493(5)	3650(2)	9034(6)	49(2)
B(2)	335(4)	4143(2)	5275(6)	44(2)

Table A9. Bond lengths [Å] and angles [°] for $[Ni_3(pqdH_2)(pqdBF_2)_2(pqd)_2]$.

C(1)-N(1)	1.307(6)	C(17)-C(22)	1.416(7)
C(1)-C(2)	1.475(7)	C(18)-C(19)	1.391(7)
C(1)-C(14)	1.482(7)	C(19)-C(20)	1.384(8)
C(2)-N(2)	1.291(6)	C(20)-C(21)	1.376(8)
C(2)-C(3)	1.470(7)	C(21)-C(22)	1.404(7)
C(3)-C(4)	1.394(7)	C(22)-C(23)	1.465(7)
C(3)-C(8)	1.418(7)	C(23)-C(24)	1.410(7)
C(4)-C(5)	1.394(7)	C(23)-C(28)	1.418(7)
C(5)-C(6)	1.396(9)	C(24)-C(25)	1.370(8)
C(6)-C(7)	1.367(8)	C(25)-C(26)	1.389(8)
C(7)-C(8)	1.400(7)	C(26)-C(27)	1.390(8)
C(8)-C(9)	1.458(8)	C(27)-C(28)	1.399(7)
C(9)-C(14)	1.410(7)	C(29)-N(5)	1.315(6)
C(9)-C(10)	1.417(7)	C(29)-C(30)	1.469(7)
C(10)-C(11)	1.369(8)	C(29)-C(42)	1.476(7)
C(11)-C(12)	1.372(8)	C(30)-N(6)	1.304(6)
C(12)-C(13)	1.391(7)	C(30)-C(31)	1.460(7)
C(13)-C(14)	1.395(7)	C(31)-C(32)	1.398(8)
C(15)-N(3)	1.309(6)	C(31)-C(36)	1.432(7)
C(15)-C(28)	1.464(7)	C(32)-C(33)	1.371(7)
C(15)-C(16)	1.467(7)	C(33)-C(34)	1.379(8)
C(16)-N(4)	1.314(6)	C(34)-C(35)	1.361(9)
C(16)-C(17)	1.464(6)	C(35)-C(36)	1.393(7)
C(17)-C(18)	1.404(7)	C(36)-C(37)	1.470(8)

C(37)-C(38)	1.397(7)	C(62)-C(63)	1.385(8)
C(37)-C(42)	1.411(7)	C(63)-C(64)	1.407(7)
C(38)-C(39)	1.368(9)	C(64)-C(65)	1.483(7)
C(39)-C(40)	1.379(9)	C(65)-C(66)	1.398(7)
C(40)-C(41)	1.390(8)	C(65)-C(70)	1.414(7)
C(41)-C(42)	1.389(8)	C(66)-C(67)	1.384(7)
C(43)-N(7)	1.298(7)	C(67)-C(68)	1.381(8)
C(43)-C(56)	1.471(7)	C(68)-C(69)	1.382(7)
C(43)-C(44)	1.481(8)	C(69)-C(70)	1.385(7)
C(44)-N(8)	1.290(7)	N(1)-O(1)	1.367(5)
C(44)-C(45)	1.485(8)	N(1)-Ni(1)	1.883(4)
C(45)-C(50)	1.385(9)	N(2)-O(2)	1.360(5)
C(45)-C(46)	1.399(10)	N(3)-O(3)	1.346(5)
C(46)-C(47)	1.388(9)	N(3)-Ni(2)	1.872(4)
C(47)-C(48)	1.392(12)	N(4)-O(4)	1.312(5)
C(48)-C(49)	1.375(14)	N(4)-Ni(2)	1.887(4)
C(49)-C(50)	1.413(10)	N(5)-O(5)	1.350(5)
C(50)-C(51)	1.464(11)	N(5)-Ni(1)	1.865(4)
C(51)-C(52)	1.403(9)	N(6)-O(6)	1.314(5)
C(51)-C(56)	1.405(10)	N(6)-Ni(1)	1.875(4)
C(52)-C(53)	1.364(13)	N(7)-O(7)	1.370(6)
C(53)-C(54)	1.395(13)	N(7)-Ni(2)	1.897(4)
C(54)-C(55)	1.399(9)	N(8)-O(8)	1.352(5)
C(55)-C(56)	1.404(10)	N(9)-O(9)	1.378(5)
C(57)-N(9)	1.273(6)	N(9)-Ni(3)	2.029(4)
C(57)-C(70)	1.466(7)	N(10)-O(10)	1.367(5)
C(57)-C(58)	1.502(7)	N(10)-Ni(3)	2.064(4)
C(58)-N(10)	1.308(6)	O(1)-B(1)	1.480(8)
C(58)-C(59)	1.470(7)	O(2)-Ni(1)	1.829(3)
C(59)-C(60)	1.383(7)	O(2)-Ni(3)	2.025(3)
C(59)-C(64)	1.407(7)	O(3)-B(2)	1.440(7)
C(60)-C(61)	1.376(8)	O(4)-Ni(3)	2.022(3)
C(61)-C(62)	1.377(8)	O(5)-B(1)	1.471(8)

O(6)-Ni(3)	2.036(3)	C(12)-C(13)-C(14)	121.1(5)
O(7)-B(2)	1.493(8)	C(13)-C(14)-C(9)	120.0(5)
O(8)-Ni(2)	1.819(3)	C(13)-C(14)-C(1)	121.5(5)
O(8)-Ni(3)	2.036(3)	C(9)-C(14)-C(1)	118.3(5)
O(9)-H(9A)	0.85(7)	N(3)-C(15)-C(28)	127.5(5)
O(10)-H(10A)	1.06(7)	N(3)-C(15)-C(16)	112.3(4)
F(1)-B(1)	1.395(8)	C(28)-C(15)-C(16)	120.1(4)
F(2)-B(1)	1.372(8)	N(4)-C(16)-C(17)	127.5(4)
F(3)-B(2)	1.378(7)	N(4)-C(16)-C(15)	112.2(4)
F(4)-B(2)	1.377(8)	C(17)-C(16)-C(15)	120.2(4)
		C(18)-C(17)-C(22)	119.4(4)
N(1)-C(1)-C(2)	117.6(4)	C(18)-C(17)-C(16)	122.8(5)
N(1)-C(1)-C(14)	126.3(5)	C(22)-C(17)-C(16)	117.7(4)
C(2)-C(1)-C(14)	116.2(4)	C(19)-C(18)-C(17)	121.0(5)
N(2)-C(2)-C(3)	115.7(5)	C(20)-C(19)-C(18)	119.4(5)
N(2)-C(2)-C(1)	126.5(4)	C(21)-C(20)-C(19)	120.4(5)
C(3)-C(2)-C(1)	117.8(4)	C(20)-C(21)-C(22)	121.8(5)
C(4)-C(3)-C(8)	120.7(5)	C(21)-C(22)-C(17)	117.9(5)
C(4)-C(3)-C(2)	120.7(5)	C(21)-C(22)-C(23)	120.6(5)
C(8)-C(3)-C(2)	118.7(5)	C(17)-C(22)-C(23)	121.3(4)
C(3)-C(4)-C(5)	120.3(5)	C(24)-C(23)-C(28)	117.1(5)
C(4)-C(5)-C(6)	119.2(6)	C(24)-C(23)-C(22)	121.3(5)
C(7)-C(6)-C(5)	120.6(5)	C(28)-C(23)-C(22)	121.6(5)
C(6)-C(7)-C(8)	122.0(5)	C(25)-C(24)-C(23)	122.7(5)
C(7)-C(8)-C(3)	117.3(5)	C(24)-C(25)-C(26)	119.7(5)
C(7)-C(8)-C(9)	123.3(5)	C(25)-C(26)-C(27)	119.6(5)
C(3)-C(8)-C(9)	119.4(4)	C(26)-C(27)-C(28)	121.1(5)
C(14)-C(9)-C(10)	117.2(5)	C(27)-C(28)-C(23)	119.7(5)
C(14)-C(9)-C(8)	121.8(4)	C(27)-C(28)-C(15)	123.0(5)
C(10)-C(9)-C(8)	121.0(5)	C(23)-C(28)-C(15)	117.3(4)
C(11)-C(10)-C(9)	121.5(5)	N(5)-C(29)-C(30)	112.0(4)
C(10)-C(11)-C(12)	121.1(5)	N(5)-C(29)-C(42)	127.8(5)
C(11)-C(12)-C(13)	119.0(5)	C(30)-C(29)-C(42)	120.3(4)

N(6)-C(30)-C(31)	126.9(5)	C(46)-C(47)-C(48)	118.5(9)
N(6)-C(30)-C(29)	112.3(4)	C(49)-C(48)-C(47)	120.5(7)
C(31)-C(30)-C(29)	120.9(4)	C(48)-C(49)-C(50)	121.7(8)
C(32)-C(31)-C(36)	118.8(4)	C(45)-C(50)-C(49)	117.4(8)
C(32)-C(31)-C(30)	123.2(5)	C(45)-C(50)-C(51)	119.8(6)
C(36)-C(31)-C(30)	118.0(5)	C(49)-C(50)-C(51)	122.8(7)
C(33)-C(32)-C(31)	121.8(5)	C(52)-C(51)-C(56)	119.2(8)
C(32)-C(33)-C(34)	119.7(6)	C(52)-C(51)-C(50)	118.9(7)
C(35)-C(34)-C(33)	119.5(5)	C(56)-C(51)-C(50)	121.9(6)
C(34)-C(35)-C(36)	123.6(5)	C(53)-C(52)-C(51)	120.0(8)
C(35)-C(36)-C(31)	116.6(5)	C(52)-C(53)-C(54)	121.7(7)
C(35)-C(36)-C(37)	122.7(5)	C(53)-C(54)-C(55)	119.2(9)
C(31)-C(36)-C(37)	120.7(4)	C(54)-C(55)-C(56)	119.5(8)
C(38)-C(37)-C(42)	118.0(5)	C(55)-C(56)-C(51)	120.2(6)
C(38)-C(37)-C(36)	119.4(5)	C(55)-C(56)-C(43)	120.3(6)
C(42)-C(37)-C(36)	122.6(5)	C(51)-C(56)-C(43)	119.3(6)
C(39)-C(38)-C(37)	121.8(5)	N(9)-C(57)-C(70)	130.1(5)
C(38)-C(39)-C(40)	120.3(5)	N(9)-C(57)-C(58)	113.1(4)
C(39)-C(40)-C(41)	119.4(6)	C(70)-C(57)-C(58)	116.8(4)
C(42)-C(41)-C(40)	120.9(5)	N(10)-C(58)-C(59)	131.6(4)
C(41)-C(42)-C(37)	119.6(5)	N(10)-C(58)-C(57)	110.5(4)
C(41)-C(42)-C(29)	123.0(5)	C(59)-C(58)-C(57)	117.4(4)
C(37)-C(42)-C(29)	117.4(5)	C(60)-C(59)-C(64)	120.4(5)
N(7)-C(43)-C(56)	127.1(6)	C(60)-C(59)-C(58)	121.9(4)
N(7)-C(43)-C(44)	117.3(5)	C(64)-C(59)-C(58)	117.5(4)
C(56)-C(43)-C(44)	115.5(5)	C(61)-C(60)-C(59)	120.5(5)
N(8)-C(44)-C(43)	126.5(5)	C(60)-C(61)-C(62)	120.3(5)
N(8)-C(44)-C(45)	114.4(5)	C(61)-C(62)-C(63)	120.3(5)
C(43)-C(44)-C(45)	119.1(5)	C(62)-C(63)-C(64)	120.4(5)
C(50)-C(45)-C(46)	120.8(6)	C(59)-C(64)-C(63)	118.1(5)
C(50)-C(45)-C(44)	118.7(7)	C(59)-C(64)-C(65)	121.3(4)
C(46)-C(45)-C(44)	120.5(6)	C(63)-C(64)-C(65)	120.6(4)
C(47)-C(46)-C(45)	121.0(7)	C(66)-C(65)-C(70)	118.4(5)

C(66)-C(65)-C(64)	121.5(4)	C(58)-N(10)-Ni(3)	115.7(3)
C(70)-C(65)-C(64)	120.0(4)	O(10)-N(10)-Ni(3)	122.3(3)
C(67)-C(66)-C(65)	120.8(5)	N(1)-O(1)-B(1)	113.0(4)
C(68)-C(67)-C(66)	120.1(5)	N(2)-O(2)-Ni(1)	127.1(3)
C(67)-C(68)-C(69)	120.3(5)	N(2)-O(2)-Ni(3)	117.6(3)
C(68)-C(69)-C(70)	120.4(5)	Ni(1)-O(2)-Ni(3)	115.17(16)
C(69)-C(70)-C(65)	120.0(5)	N(3)-O(3)-B(2)	118.8(4)
C(69)-C(70)-C(57)	121.9(4)	N(4)-O(4)-Ni(3)	113.1(3)
C(65)-C(70)-C(57)	118.1(4)	N(5)-O(5)-B(1)	119.5(4)
C(1)-N(1)-O(1)	116.1(4)	N(6)-O(6)-Ni(3)	112.9(3)
C(1)-N(1)-Ni(1)	126.1(3)	N(7)-O(7)-B(2)	114.4(4)
O(1)-N(1)-Ni(1)	115.8(3)	N(8)-O(8)-Ni(2)	128.3(3)
C(2)-N(2)-O(2)	117.3(4)	N(8)-O(8)-Ni(3)	115.4(3)
C(15)-N(3)-O(3)	117.4(4)	Ni(2)-O(8)-Ni(3)	116.21(17)
C(15)-N(3)-Ni(2)	117.0(3)	O(2)-Ni(1)-N(5)	170.30(16)
O(3)-N(3)-Ni(2)	125.6(3)	O(2)-Ni(1)-N(6)	88.27(16)
O(4)-N(4)-C(16)	121.4(4)	N(5)-Ni(1)-N(6)	82.07(18)
O(4)-N(4)-Ni(2)	122.3(3)	O(2)-Ni(1)-N(1)	90.96(16)
C(16)-N(4)-Ni(2)	116.2(3)	N(5)-Ni(1)-N(1)	98.53(18)
C(29)-N(5)-O(5)	118.5(4)	N(6)-Ni(1)-N(1)	173.25(18)
C(29)-N(5)-Ni(1)	116.9(4)	O(8)-Ni(2)-N(3)	170.42(16)
O(5)-N(5)-Ni(1)	124.6(3)	O(8)-Ni(2)-N(4)	88.60(16)
C(30)-N(6)-O(6)	121.7(4)	N(3)-Ni(2)-N(4)	81.88(17)
C(30)-N(6)-Ni(1)	116.8(3)	O(8)-Ni(2)-N(7)	90.78(17)
O(6)-N(6)-Ni(1)	121.5(3)	N(3)-Ni(2)-N(7)	98.56(19)
C(43)-N(7)-O(7)	116.4(4)	N(4)-Ni(2)-N(7)	173.36(18)
C(43)-N(7)-Ni(2)	127.2(4)	O(4)-Ni(3)-O(2)	89.28(14)
O(7)-N(7)-Ni(2)	114.4(3)	O(4)-Ni(3)-N(9)	87.74(15)
C(44)-N(8)-O(8)	118.6(4)	O(2)-Ni(3)-N(9)	96.72(16)
C(57)-N(9)-O(9)	117.6(4)	O(4)-Ni(3)-O(6)	165.12(14)
C(57)-N(9)-Ni(3)	117.9(3)	O(2)-Ni(3)-O(6)	79.77(13)
O(9)-N(9)-Ni(3)	122.1(3)	N(9)-Ni(3)-O(6)	103.43(16)
C(58)-N(10)-O(10)	116.3(4)	O(4)-Ni(3)-O(8)	81.29(14)

O(2)-Ni(3)-O(8)	93.48(15)	F(1)-B(1)-O(5)	111.2(5)
N(9)-Ni(3)-O(8)	164.91(17)	F(2)-B(1)-O(1)	106.8(5)
O(6)-Ni(3)-O(8)	89.28(14)	F(1)-B(1)-O(1)	108.5(5)
O(4)-Ni(3)-N(10)	107.36(16)	O(5)-B(1)-O(1)	112.0(5)
O(2)-Ni(3)-N(10)	161.43(17)	F(4)-B(2)-F(3)	112.3(5)
N(9)-Ni(3)-N(10)	76.28(17)	F(4)-B(2)-O(3)	110.4(5)
O(6)-Ni(3)-N(10)	85.12(16)	F(3)-B(2)-O(3)	105.4(5)
O(8)-Ni(3)-N(10)	97.08(16)	F(4)-B(2)-O(7)	109.1(5)
F(2)-B(1)-F(1)	112.4(5)	F(3)-B(2)-O(7)	106.1(5)
F(2)-B(1)-O(5)	105.9(5)	O(3)-B(2)-O(7)	113.4(5)

Appendix B Crystal Data for Chapter 2 Structures

Table B1. Crystal data and structure refinement for aqdH_2.

Empirical formula	$C_{12}H_8N_2O_2$	
Formula weight	212.20	
Temperature	298(2) K	
Wavelength	0.71073 Å	
Crystal system	Monoclinic	
Space group	P $2_1/c$	
Unit cell dimensions	a = 7.844(3) Å	a= 90°.
	b = 7.8009(29) Å	b= 92.7816(102)°.
	c = 15.3089(59) Å	g = 90°.
Volume	935.68(62) $Å^3$	
Z	4	
Density (calculated)	1.506 Mg/m^3	
Absorption coefficient	0.106 mm^{-1}	
F(000)	440	
Crystal size	0.182 x 0.113 x 0.094 mm^3	
Theta range for data collection	3.632 to 24.997°.	
Index ranges	-9<=h<=9, -9<=k<=9, -16<=l<=18	
Reflections collected	6727	
Independent reflections	1647 [R(int) = 0.0317]	
Completeness to theta = 25.242°	97.1 %	
Absorption correction	Semi-emperical from equivalents	
Max. and min. transmission	1.000 and 0.837	
Refinement method	Full-matrix least-squares on F^2	
Data / restraints / parameters	1647 / 0 / 147	
Goodness-of-fit on F^2	1.105	
Final R indices [I>2sigma(I)]	R1 = 0.0415, wR2 = 0.0905	
R indices (all data)	R1 = 0.0510, wR2 = 0.0956	
Largest diff. peak and hole	0.169 and -0.198 e.$Å^{-3}$	

Table B2. Atomic coordinates (x 10^4) and equivalent isotropic displacement parameters ($Å^2$x 10^3) for aqdH_2. U(eq) is defined as one third of the trace of the orthogonalized U^{ij} tensor.

	x	y	z	U(eq)
C(1)	2029(2)	1322(2)	8944(1)	32(1)
C(2)	1417(2)	-500(2)	8881(1)	31(1)
C(3)	1833(2)	-1315(2)	9735(1)	31(1)
C(4)	1545(2)	-2899(2)	10094(1)	38(1)
C(5)	2126(2)	-3198(2)	10969(1)	43(1)
C(6)	2980(2)	-1982(2)	11464(1)	42(1)
C(7)	3314(2)	-336(2)	11114(1)	36(1)
C(8)	4180(2)	1061(3)	11531(1)	44(1)
C(9)	4374(2)	2592(3)	11104(1)	47(1)
C(10)	3725(2)	2865(2)	10242(1)	41(1)
C(11)	2887(2)	1536(2)	9814(1)	32(1)
C(12)	2708(2)	-48(2)	10251(1)	30(1)
N(1)	1668(2)	2394(2)	8325(1)	40(1)
N(2)	664(2)	-1050(2)	8170(1)	39(1)
O(1)	2276(2)	4052(2)	8527(1)	53(1)
O(2)	193(2)	-2773(2)	8235(1)	47(1)

Table B3. Bond lengths [Å] and angles [°] for aqdH_2.

C(1)-N(1)	1.285(2)	C(5)-C(6)	1.369(3)
C(1)-C(11)	1.472(2)	C(6)-C(7)	1.421(3)
C(1)-C(2)	1.502(2)	C(7)-C(12)	1.400(2)
C(2)-N(2)	1.286(2)	C(7)-C(8)	1.420(3)
C(2)-C(3)	1.476(2)	C(8)-C(9)	1.374(3)
C(3)-C(4)	1.375(2)	C(9)-C(10)	1.407(3)
C(3)-C(12)	1.421(2)	C(10)-C(11)	1.376(2)
C(4)-C(5)	1.413(3)	C(11)-C(12)	1.416(2)

N(1)-O(1)	1.4075(19)	C(12)-C(7)-C(8)	115.75(16)
N(2)-O(2)	1.3990(18)	C(12)-C(7)-C(6)	116.13(16)
		C(8)-C(7)-C(6)	128.13(17)
N(1)-C(1)-C(11)	131.90(16)	C(9)-C(8)-C(7)	120.98(17)
N(1)-C(1)-C(2)	120.65(15)	C(8)-C(9)-C(10)	122.32(17)
C(11)-C(1)-C(2)	107.27(14)	C(11)-C(10)-C(9)	118.39(17)
N(2)-C(2)-C(3)	132.73(16)	C(10)-C(11)-C(12)	119.24(16)
N(2)-C(2)-C(1)	120.17(15)	C(10)-C(11)-C(1)	134.68(16)
C(3)-C(2)-C(1)	107.09(13)	C(12)-C(11)-C(1)	106.08(14)
C(4)-C(3)-C(12)	119.10(16)	C(7)-C(12)-C(11)	123.31(15)
C(4)-C(3)-C(2)	135.02(16)	C(7)-C(12)-C(3)	123.09(16)
C(12)-C(3)-C(2)	105.87(14)	C(11)-C(12)-C(3)	113.59(15)
C(3)-C(4)-C(5)	118.40(17)	C(1)-N(1)-O(1)	112.09(14)
C(6)-C(5)-C(4)	122.49(17)	C(2)-N(2)-O(2)	111.83(14)
C(5)-C(6)-C(7)	120.77(17)		

Table B4. Crystal data and structure refinement for $[Co(aqdBF_2)_2(MeCN)_2]$.

Empirical formula	$C_{32}H_{24}B_2CoF_4N_8O_4$	
Formula weight	741.14	
Temperature	173(2) K	
Wavelength	0.71073 Å	
Crystal system	Monoclinic	
Space group	C2/*m*	
Unit cell dimensions	a = 8.9648(3) Å	a= 90°.
	b = 18.8380(6) Å	b= 99.3490(10)°.
	c = 9.4411(3) Å	g = 90°.
Volume	1573.22(9) $Å^3$	
Z	2	
Density (calculated)	1.565 Mg/m^3	
Absorption coefficient	0.623 mm^{-1}	
F(000)	754	
Crystal size	0.412 x 0.159 x 0.116 mm^3	
Theta range for data collection	2.186 to 28.995°.	
Index ranges	-12<=h<=12, -25<=k<=24, -12<=l<=12	
Reflections collected	17118	
Independent reflections	2136 [R(int) = 0.0319]	
Completeness to theta = 25.242°	99.9 %	
Absorption correction	Semi-emperical from equivalents	
Max. and min. transmission	1.000 and 0.646	
Refinement method	Full-matrix least-squares on F^2	
Data / restraints / parameters	2136 / 2 / 137	
Goodness-of-fit on F^2	1.206	
Final R indices [I>2sigma(I)]	R1 = 0.0274, wR2 = 0.0812	
R indices (all data)	R1 = 0.0338, wR2 = 0.0960	
Largest diff. peak and hole	0.512 and -0.542 $e.Å^{-3}$	

Table B5. Atomic coordinates (x 10^4) and equivalent isotropic displacement parameters ($Å^2$x 10^3) for $[Co(aqdBF_2)_2(MeCN)_2]$. U(eq) is defined as one third of the trace of the orthogonalized U^{ij} tensor.

	x	y	z	U(eq)
C(1)	9346(1)	3631(1)	4404(1)	11(1)
C(1S)	5000	7395(2)	0	43(1)
C(2)	8969(1)	2894(1)	4031(1)	11(1)
C(2S)	5000	6623(2)	0	56(1)
C(3)	7902(1)	2558(1)	3050(1)	15(1)
C(4)	7881(2)	1804(1)	3038(2)	17(1)
C(5)	8890(2)	1402(1)	3972(1)	15(1)
C(6)	10000	1739(1)	5000	12(1)
C(7)	10000	2483(1)	5000	11(1)
C(8)	12044(3)	5000	569(3)	42(1)
C(9)	11593(2)	5000	1985(2)	18(1)
N(1)	8848(1)	4256(1)	4007(1)	10(1)
N(1S)	5000	7998(2)	0	61(1)
N(2)	11265(2)	5000	3101(2)	16(1)
O(1)	7714(1)	4326(1)	2866(1)	12(1)
F(1)	6151(1)	5000	4122(1)	17(1)
F(2)	5793(1)	5000	1659(1)	18(1)
Co(1)	10000	5000	5000	9(1)
B(1)	6820(2)	5000	2911(2)	12(1)

Table B6. Bond lengths [Å] and angles [°] for $[Co(aqdBF_2)_2(MeCN)_2]$.

C(1)-N(1)	1.2932(15)	C(2)-C(3)	1.3721(17)
C(1)-C(2)	1.4588(16)	C(2)-C(7)	1.4199(15)
C(1)-C(1)#1	1.487(2)	C(3)-C(4)	1.4209(18)
C(1S)-N(1S)	1.135(4)	C(4)-C(5)	1.3818(19)
C(1S)-C(2S)	1.455(4)	C(5)-C(6)	1.4220(15)

C(6)-C(7)	1.401(2)	C(5)-C(6)-C(5)#1	126.98(17)
C(6)-C(5)#1	1.4220(15)	C(6)-C(7)-C(2)#1	123.03(8)
C(7)-C(2)#1	1.4199(15)	C(6)-C(7)-C(2)	123.03(8)
C(8)-C(9)	1.459(3)	C(2)#1-C(7)-C(2)	113.93(15)
C(8)-H(1)	0.958(10)	C(9)-C(8)-H(2)	106.7(16)
C(8)-H(2)	0.957(10)	H(1)-C(8)-H(2)	107.8(18)
C(9)-N(2)	1.139(3)	N(2)-C(9)-C(8)	178.9(2)
N(1)-O(1)	1.3628(13)	C(1)-N(1)-O(1)	119.70(10)
N(1)-Co(1)	1.8961(10)	C(1)-N(1)-Co(1)	113.29(8)
N(2)-Co(1)	2.2714(16)	O(1)-N(1)-Co(1)	126.57(8)
O(1)-B(1)	1.5054(13)	C(9)-N(2)-Co(1)	165.23(16)
F(1)-B(1)	1.375(2)	N(1)-O(1)-B(1)	113.04(10)
F(2)-B(1)	1.375(2)	N(1)-Co(1)-N(1)#3	95.34(6)
Co(1)-N(1)#2	1.8961(10)	N(1)#2-Co(1)-N(1)#3	84.66(6)
Co(1)-N(1)#3	1.8961(10)	N(1)-Co(1)-N(1)#1	84.66(6)
Co(1)-N(1)#1	1.8961(10)	N(1)#2-Co(1)-N(1)#1	95.34(6)
Co(1)-N(2)#2	2.2715(16)	N(1)-Co(1)-N(2)	84.92(4)
B(1)-O(1)#3	1.5053(13)	N(1)#2-Co(1)-N(2)	95.08(4)
		N(1)#3-Co(1)-N(2)	84.92(4)
N(1)-C(1)-C(2)	137.85(11)	N(1)#1-Co(1)-N(2)	95.08(4)
N(1)-C(1)-C(1)#1	114.31(7)	N(1)-Co(1)-N(2)#2	95.08(4)
C(2)-C(1)-C(1)#1	107.82(7)	N(1)#2-Co(1)-N(2)#2	84.92(4)
C(3)-C(2)-C(7)	119.57(12)	N(1)#3-Co(1)-N(2)#2	95.08(4)
C(3)-C(2)-C(1)	135.21(11)	N(1)#1-Co(1)-N(2)#2	84.92(4)
C(7)-C(2)-C(1)	105.20(11)	F(1)-B(1)-F(2)	113.11(15)
C(2)-C(3)-C(4)	118.18(12)	F(1)-B(1)-O(1)#3	109.26(10)
C(5)-C(4)-C(3)	122.47(12)	F(2)-B(1)-O(1)#3	105.11(10)
C(4)-C(5)-C(6)	120.24(12)	F(1)-B(1)-O(1)	109.26(10)
C(7)-C(6)-C(5)	116.51(8)	F(2)-B(1)-O(1)	105.11(10)
C(7)-C(6)-C(5)#1	116.51(8)	O(1)#3-B(1)-O(1)	114.99(14)

Symmetry transformations used to generate equivalent atoms:

#1 -x+2,y,-z+1 #2 -x+2,-y+1,-z+1 #3 x,-y+1,z

Table B7. Crystal data and structure refinement for [Na(12-crown-4)$_2$][(Co(aqdBF$_2$)$_2$(MeCN)].

Empirical formula	$C_{46}H_{53}B_2CoF_4N_7NaO_{12}$	
Formula weight	1075.49	
Temperature	150(2) K	
Wavelength	1.54184 Å	
Crystal system	Monoclinic	
Space group	P $2_1/m$	
Unit cell dimensions	a = 12.22900(10) Å	a= 90°.
	b = 15.5856(2) Å	b= 98.8380(10)°.
	c = 13.20690(10) Å	g = 90°.
Volume	2487.30(4) Å^3	
Z	2	
Density (calculated)	1.436 Mg/m^3	
Absorption coefficient	3.509 mm^{-1}	
F(000)	1116	
Crystal size	0.371 x 0.224 x 0.170 mm^3	
Theta range for data collection	3.387 to 75.567°.	
Index ranges	-15<=h<=14, -19<=k<=12, -16<=l<=12	
Reflections collected	15022	
Independent reflections	5252 [R(int) = 0.0197]	
Completeness to theta = 67.684°	100.0 %	
Absorption correction	Semi-empirical from equivalents	
Max. and min. transmission	1.082346 and 0.848342	
Refinement method	Full-matrix least-squares on F^2	
Data / restraints / parameters	5252 / 93 / 468	
Goodness-of-fit on F^2	0.933	
Final R indices [I>2sigma(I)]	R1 = 0.0447, wR2 = 0.1223	
R indices (all data)	R1 = 0.0480, wR2 = 0.1263	
Largest diff. peak and hole	0.601 and -0.642 e.Å^{-3}	

Table B8. Atomic coordinates (x 10^4) and equivalent isotropic displacement parameters ($Å^2$x 10^3) for [Na(12-crown-4)$_2$][(Co(aqdBF$_2$)$_2$(MeCN)]. U(eq) is defined as one third of the trace of the orthogonalized U^{ij} tensor.

	x	y	z	U(eq)
C(1)	2213(1)	2962(1)	3992(1)	27(1)
C(2)	2268(2)	3263(1)	5046(2)	28(1)
C(3)	2333(2)	4044(1)	5533(2)	35(1)
C(4)	2423(2)	4051(2)	6616(2)	42(1)
C(5)	2457(2)	3319(2)	7190(2)	42(1)
C(6)	2391(2)	2500	6708(2)	34(1)
C(7)	2289(2)	2500	5641(2)	28(1)
C(8)	3314(1)	2964(1)	495(1)	25(1)
C(9)	4045(2)	3262(1)	-213(1)	28(1)
C(10)	4399(2)	4045(1)	-514(2)	33(1)
C(11)	5207(2)	4054(2)	-1186(2)	41(1)
C(12)	5631(2)	3319(2)	-1539(2)	41(1)
C(13)	5264(2)	2500	-1257(2)	34(1)
C(14)	4465(2)	2500	-597(2)	28(1)
C(15)	-254(3)	2500	866(3)	48(1)
C(16)	-1366(4)	2500	282(5)	89(2)
B(1)	2156(2)	4543(2)	2013(2)	34(1)
N(1)	2234(1)	3301(1)	3086(1)	27(1)
N(2)	2807(1)	3305(1)	1201(1)	26(1)
N(3)	612(2)	2500	1316(2)	36(1)
O(1)	2364(1)	4177(1)	3061(1)	33(1)
O(2)	2889(1)	4177(1)	1319(1)	32(1)
F(1)	1055(1)	4427(1)	1593(1)	47(1)
F(2)	2433(1)	5397(1)	2114(1)	48(1)
Na(1)	2767(1)	7500	5549(1)	35(1)
Co(1)	2188(1)	2500	2017(1)	24(1)

O(3)	1332(2)	7500	6633(2)	40(1)
O(4)	1587(1)	6212(1)	5202(2)	53(1)
O(5)	1841(2)	7500	3792(2)	65(1)
C(17)	979(8)	6742(5)	3567(6)	58(2)
C(18)	1376(7)	5968(5)	4192(5)	53(2)
C(19)	1019(9)	6132(9)	5958(13)	57(3)
C(20)	478(5)	6920(4)	6308(5)	47(2)
C(17A)	1525(8)	6799(6)	3441(6)	68(2)
C(18A)	901(7)	6318(6)	4140(7)	63(2)
C(19A)	646(8)	6173(9)	5772(11)	51(2)
C(20A)	948(5)	6623(4)	6756(5)	48(2)
O(6)	4153(3)	8669(4)	5167(4)	62(1)
O(7)	3769(3)	8143(4)	7129(5)	60(1)
O(8)	3778(3)	6406(4)	6644(5)	69(1)
O(9)	4137(3)	6848(4)	4734(6)	84(2)
C(21)	4913(4)	7421(12)	4378(5)	78(3)
C(22)	4531(8)	8292(8)	4283(8)	94(2)
C(23)	4888(5)	8821(4)	6028(7)	60(2)
C(24)	4437(9)	8844(7)	6923(9)	101(3)
C(25)	4257(11)	7378(15)	7791(7)	170(6)
C(26)	4154(13)	6694(7)	7618(8)	103(3)
C(27)	4464(8)	5913(7)	6155(11)	97(3)
C(28)	4796(18)	6246(13)	5252(19)	233(10)
C(1B)	9492(10)	6700(9)	1071(7)	83(3)
C(2B)	9200(7)	5827(6)	867(6)	38(2)
N(1B)	8563(12)	5103(8)	1093(10)	63(4)
C(1C)	8101(6)	4589(6)	1280(6)	80(2)
C(2C)	8756(13)	5214(14)	851(10)	100(5)
N(1C)	9260(12)	6058(12)	924(10)	144(5)

Table B9. Bond lengths [Å] and angles [°] for [Na(12-crown-4)$_2$][(Co(aqdBF$_2$)$_2$(MeCN)].

C(1)-N(1)	1.311(2)	C(1)-C(1)#1	1.439(4)

C(1)-C(2)	1.461(3)	Na(1)-O(3)	2.429(2)
C(2)-C(3)	1.374(3)	Na(1)-O(8)	2.445(5)
C(2)-C(7)	1.422(2)	Na(1)-O(7)	2.464(5)
C(3)-C(4)	1.419(3)	Na(1)-O(4)	2.4743(18)
C(4)-C(5)	1.366(4)	Na(1)-O(4)#2	2.4743(18)
C(5)-C(6)	1.423(3)	Na(1)-O(6)	2.590(6)
C(6)-C(7)	1.395(4)	Na(1)-C(19)#2	3.124(12)
C(6)-C(5)#1	1.423(3)	Na(1)-C(19)	3.124(12)
C(7)-C(2)#1	1.423(2)	Co(1)-N(1)#1	1.8791(16)
C(8)-N(2)	1.308(2)	Co(1)-N(2)#1	1.8869(16)
C(8)-C(8)#1	1.445(4)	O(3)-C(20)#2	1.398(5)
C(8)-C(9)	1.465(2)	O(3)-C(20)	1.398(5)
C(9)-C(10)	1.373(3)	O(3)-C(20A)#2	1.462(6)
C(9)-C(14)	1.420(2)	O(3)-C(20A)	1.462(6)
C(10)-C(11)	1.426(3)	O(4)-C(19)	1.307(16)
C(11)-C(12)	1.368(3)	O(4)-C(18)	1.372(6)
C(12)-C(13)	1.421(3)	O(4)-C(19A)	1.470(13)
C(13)-C(14)	1.404(4)	O(4)-C(18A)	1.529(10)
C(13)-C(12)#1	1.421(3)	O(5)-C(17A)#2	1.225(8)
C(14)-C(9)#1	1.420(2)	O(5)-C(17A)	1.225(8)
C(15)-N(3)	1.132(4)	O(5)-C(17)	1.582(9)
C(15)-C(16)	1.456(5)	O(5)-C(17)#2	1.582(9)
B(1)-F(2)	1.375(3)	C(17)-C(18)	1.499(10)
B(1)-F(1)	1.388(3)	C(19)-C(20)	1.500(16)
B(1)-O(1)	1.482(3)	C(20)-C(20)#2	1.809(13)
B(1)-O(2)	1.490(3)	C(17A)-C(18A)	1.488(12)
N(1)-O(1)	1.376(2)	C(19A)-C(20A)	1.473(16)
N(1)-Co(1)	1.8791(16)	O(6)-C(23)	1.357(8)
N(2)-O(2)	1.371(2)	O(6)-C(22)	1.444(11)
N(2)-Co(1)	1.8870(16)	O(7)-C(24)	1.415(12)
N(3)-Co(1)	2.006(2)	O(7)-C(25)	1.54(2)
Na(1)-O(9)	2.357(4)	O(8)-C(27)	1.370(11)
Na(1)-O(5)	2.421(3)	O(8)-C(26)	1.374(12)

O(9)-C(21)	1.434(15)	C(12)-C(11)-C(10)	122.6(2)
O(9)-C(28)	1.353(19)	C(11)-C(12)-C(13)	120.8(2)
C(21)-C(22)	1.43(2)	C(14)-C(13)-C(12)#1	116.10(14)
C(23)-C(24)	1.380(14)	C(14)-C(13)-C(12)	116.10(14)
C(25)-C(26)	1.09(3)	C(12)#1-C(13)-C(12)	127.8(3)
C(27)-C(28)	1.42(2)	C(13)-C(14)-C(9)#1	123.15(12)
C(1B)-C(2B)	1.421(17)	C(13)-C(14)-C(9)	123.15(12)
C(2B)-N(1B)	1.429(12)	C(9)#1-C(14)-C(9)	113.6(2)
C(1C)-C(2C)	1.432(14)	N(3)-C(15)-C(16)	179.7(4)
C(2C)-N(1C)	1.449(14)	F(2)-B(1)-F(1)	111.97(18)
		F(2)-B(1)-O(1)	106.16(18)
N(1)-C(1)-C(1)#1	113.77(11)	F(1)-B(1)-O(1)	109.83(17)
N(1)-C(1)-C(2)	137.34(18)	F(2)-B(1)-O(2)	105.51(17)
C(1)#1-C(1)-C(2)	108.71(11)	F(1)-B(1)-O(2)	110.02(18)
C(3)-C(2)-C(7)	119.21(19)	O(1)-B(1)-O(2)	113.27(16)
C(3)-C(2)-C(1)	136.13(19)	C(1)-N(1)-O(1)	116.16(16)
C(7)-C(2)-C(1)	104.62(17)	C(1)-N(1)-Co(1)	114.53(13)
C(2)-C(3)-C(4)	117.9(2)	O(1)-N(1)-Co(1)	129.13(12)
C(5)-C(4)-C(3)	123.0(2)	C(8)-N(2)-O(2)	116.75(15)
C(4)-C(5)-C(6)	120.4(2)	C(8)-N(2)-Co(1)	114.35(13)
C(7)-C(6)-C(5)	116.23(14)	O(2)-N(2)-Co(1)	128.53(12)
C(7)-C(6)-C(5)#1	116.23(14)	C(15)-N(3)-Co(1)	175.9(3)
C(5)-C(6)-C(5)#1	127.5(3)	N(1)-O(1)-B(1)	113.63(15)
C(6)-C(7)-C(2)	123.28(12)	N(2)-O(2)-B(1)	114.16(15)
C(6)-C(7)-C(2)#1	123.28(12)	O(9)-Na(1)-O(5)	79.79(19)
C(2)-C(7)-C(2)#1	113.3(2)	O(9)-Na(1)-O(3)	153.9(2)
N(2)-C(8)-C(8)#1	113.98(11)	O(5)-Na(1)-O(3)	106.90(9)
N(2)-C(8)-C(9)	136.65(18)	O(9)-Na(1)-O(8)	68.8(3)
C(8)#1-C(8)-C(9)	108.53(11)	O(5)-Na(1)-O(8)	133.34(17)
C(10)-C(9)-C(14)	119.42(18)	O(3)-Na(1)-O(8)	89.83(14)
C(10)-C(9)-C(8)	135.87(18)	O(9)-Na(1)-O(7)	105.44(18)
C(14)-C(9)-C(8)	104.65(17)	O(5)-Na(1)-O(7)	155.52(16)
C(9)-C(10)-C(11)	117.95(19)	O(3)-Na(1)-O(7)	79.14(14)

O(8)-Na(1)-O(7)	69.1(3)	O(4)#2-Na(1)-C(19)	101.0(2)
O(9)-Na(1)-O(4)	90.03(14)	O(6)-Na(1)-C(19)	177.7(2)
O(5)-Na(1)-O(4)	69.41(7)	C(19)#2-Na(1)-C(19)	86.1(5)
O(3)-Na(1)-O(4)	69.87(6)	N(1)-Co(1)-N(1)#1	83.24(10)
O(8)-Na(1)-O(4)	76.77(13)	N(1)-Co(1)-N(2)#1	154.53(7)
O(7)-Na(1)-O(4)	133.41(18)	N(1)#1-Co(1)-N(2)#1	91.13(7)
O(9)-Na(1)-O(4)#2	134.5(2)	N(1)-Co(1)-N(2)	91.14(7)
O(5)-Na(1)-O(4)#2	69.41(7)	N(1)#1-Co(1)-N(2)	154.53(7)
O(3)-Na(1)-O(4)#2	69.87(6)	N(2)#1-Co(1)-N(2)	83.31(10)
O(8)-Na(1)-O(4)#2	154.61(18)	N(1)-Co(1)-N(3)	105.22(7)
O(7)-Na(1)-O(4)#2	91.55(14)	N(1)#1-Co(1)-N(3)	105.22(7)
O(4)-Na(1)-O(4)#2	108.50(9)	N(2)#1-Co(1)-N(3)	100.24(7)
O(9)-Na(1)-O(6)	71.4(2)	N(2)-Co(1)-N(3)	100.24(7)
O(5)-Na(1)-O(6)	92.11(13)	C(20)#2-O(3)-C(20)	80.6(6)
O(3)-Na(1)-O(6)	131.97(12)	C(20A)#2-O(3)-C(20A)	138.4(5)
O(8)-Na(1)-O(6)	108.63(14)	C(20)#2-O(3)-Na(1)	113.1(3)
O(7)-Na(1)-O(6)	67.9(2)	C(20)-O(3)-Na(1)	113.1(2)
O(4)-Na(1)-O(6)	156.19(14)	C(20A)#2-O(3)-Na(1)	109.8(2)
O(4)#2-Na(1)-O(6)	76.91(10)	C(20A)-O(3)-Na(1)	109.8(2)
O(9)-Na(1)-C(19)#2	157.9(4)	C(19)-O(4)-C(18)	132.3(7)
O(5)-Na(1)-C(19)#2	86.2(3)	C(19A)-O(4)-C(18A)	96.4(6)
O(3)-Na(1)-C(19)#2	47.4(3)	C(19)-O(4)-Na(1)	107.3(6)
O(8)-Na(1)-C(19)#2	132.2(4)	C(18)-O(4)-Na(1)	115.0(3)
O(7)-Na(1)-C(19)#2	80.8(3)	C(19A)-O(4)-Na(1)	114.7(5)
O(4)-Na(1)-C(19)#2	101.0(2)	C(18A)-O(4)-Na(1)	107.7(3)
O(4)#2-Na(1)-C(19)#2	23.5(3)	C(17A)#2-O(5)-C(17A)	126.0(9)
O(6)-Na(1)-C(19)#2	92.3(3)	C(17)-O(5)-C(17)#2	96.7(6)
O(9)-Na(1)-C(19)	109.8(3)	C(17A)#2-O(5)-Na(1)	115.9(5)
O(5)-Na(1)-C(19)	86.2(3)	C(17A)-O(5)-Na(1)	115.9(4)
O(3)-Na(1)-C(19)	47.4(3)	C(17)-O(5)-Na(1)	112.4(3)
O(8)-Na(1)-C(19)	73.7(2)	C(17)#2-O(5)-Na(1)	112.4(3)
O(7)-Na(1)-C(19)	113.3(4)	C(18)-C(17)-O(5)	110.3(5)
O(4)-Na(1)-C(19)	23.5(3)	O(4)-C(18)-C(17)	108.1(6)

O(4)-C(19)-C(20)	118.0(9)	C(27)-O(8)-C(26)	118.9(9)
O(4)-C(19)-Na(1)	49.1(4)	C(27)-O(8)-Na(1)	113.8(7)
C(20)-C(19)-Na(1)	80.9(5)	C(26)-O(8)-Na(1)	113.0(7)
O(3)-C(20)-C(19)	106.3(5)	C(21)-O(9)-C(28)	103.1(11)
O(3)-C(20)-C(20)#2	49.7(3)	C(21)-O(9)-Na(1)	115.7(6)
C(19)-C(20)-C(20)#2	144.9(5)	C(28)-O(9)-Na(1)	118.6(9)
O(5)-C(17A)-C(18A)	112.1(6)	O(9)-C(21)-C(22)	113.3(7)
C(17A)-C(18A)-O(4)	111.2(6)	O(6)-C(22)-C(21)	117.0(9)
C(20A)-C(19A)-O(4)	108.8(7)	C(24)-C(23)-O(6)	115.0(7)
O(3)-C(20A)-C(19A)	112.9(7)	C(23)-C(24)-O(7)	117.5(7)
C(23)-O(6)-C(22)	119.7(6)	C(26)-C(25)-O(7)	127.8(10)
C(23)-O(6)-Na(1)	109.2(5)	C(25)-C(26)-O(8)	121.8(11)
C(22)-O(6)-Na(1)	99.9(6)	O(8)-C(27)-C(28)	117.8(10)
C(24)-O(7)-C(25)	121.4(8)	C(27)-C(28)-O(9)	117.0(10)
C(24)-O(7)-Na(1)	112.2(6)	C(1B)-C(2B)-N(1B)	147.8(9)
C(25)-O(7)-Na(1)	105.3(6)	C(1C)-C(2C)-N(1C)	148.1(13)

Symmetry transformations used to generate equivalent atoms:

#1 x,-y+1/2,z #2 x,-y+3/2,z

Table B10. Crystal data and structure refinement for [K(dibenzo-18-crown-6)]$_2$[(Co(aqdBF$_2$)$_2$].

Empirical formula	$C_{72}H_{76}B_2CoF_4K_2N_6O_{17}$	
Formula weight	1532.13	
Temperature	150(2) K	
Wavelength	1.54184 Å	
Crystal system	Monoclinic	
Space group	P $2_1/n$	
Unit cell dimensions	a = 15.568(6) Å	a= 90°.
	b = 20.730(8) Å	b= 95.249(7)°.
	c = 22.817(9) Å	g = 90°.
Volume	7333(5) Å^3	
Z	4	
Density (calculated)	1.388 Mg/m^3	
Absorption coefficient	3.546 mm^{-1}	
F(000)	3188	
Crystal size	? x ? x ? mm^3	
Theta range for data collection	3.301 to 73.804°.	
Index ranges	-17<=h<=19, -25<=k<=25, -28<=l<=18	
Reflections collected	41979	
Independent reflections	14423 [R(int) = 0.0261]	
Completeness to theta = 67.684°	100.0 %	
Absorption correction	Semi-emperical from equivalents	
Max. and min. transmission	1.082 and 0.848	
Refinement method	Full-matrix least-squares on F^2	
Data / restraints / parameters	14423 / 6 / 941	
Goodness-of-fit on F^2	1.045	
Final R indices [I>2sigma(I)]	R1 = 0.0533, wR2 = 0.1422	
R indices (all data)	R1 = 0.0650, wR2 = 0.1519	
Largest diff. peak and hole	0.737 and -0.781 e.Å^{-3}	

Table B11. Atomic coordinates (x 10^4) and equivalent isotropic displacement parameters ($Å^2$x 10^3) for $[K(dibenzo\text{-}18\text{-}crown\text{-}6)]_2[(Co(aqdBF_2)_2]$. U(eq) is defined as one third of the trace of the orthogonalized U^{ij} tensor.

	x	y	z	U(eq)
C(1)	9280(2)	5751(1)	7432(1)	36(1)
C(2)	8552(2)	5338(1)	7232(1)	37(1)
C(3)	8712(2)	5061(1)	6661(1)	41(1)
C(4)	8251(2)	4683(2)	6240(1)	50(1)
C(5)	8666(3)	4508(2)	5727(1)	60(1)
C(6)	9497(3)	4689(2)	5638(1)	61(1)
C(7)	9982(2)	5106(2)	6050(1)	52(1)
C(8)	10828(2)	5362(2)	6016(1)	59(1)
C(9)	11184(2)	5778(2)	6446(1)	56(1)
C(10)	10743(2)	5964(2)	6945(1)	46(1)
C(11)	9933(2)	5707(1)	7004(1)	40(1)
C(12)	9560(2)	5282(1)	6549(1)	42(1)
C(13)	7463(2)	6725(1)	9003(1)	38(1)
C(14)	6752(2)	6303(1)	8796(1)	39(1)
C(15)	5962(2)	6522(2)	9040(1)	43(1)
C(16)	5097(2)	6341(2)	8985(2)	52(1)
C(17)	4511(2)	6712(2)	9300(2)	61(1)
C(18)	4765(2)	7228(2)	9655(2)	60(1)
C(19)	5656(2)	7427(2)	9724(1)	51(1)
C(20)	6026(2)	7953(2)	10069(1)	57(1)
C(21)	6897(2)	8090(2)	10074(1)	54(1)
C(22)	7464(2)	7733(2)	9731(1)	46(1)
C(23)	7133(2)	7210(1)	9401(1)	40(1)
C(24)	6226(2)	7067(2)	9406(1)	44(1)
C(25)	5615(2)	4288(1)	5479(1)	47(1)

C(26)	6090(2)	4868(1)	5423(1)	46(1)
C(27)	6467(2)	4993(2)	4902(2)	53(1)
C(28)	6376(2)	4546(2)	4432(2)	62(1)
C(29)	5904(2)	3987(2)	4483(2)	63(1)
C(30)	5526(2)	3856(2)	5007(2)	57(1)
C(31)	6582(2)	5885(1)	5852(2)	50(1)
C(32)	6669(2)	6220(2)	6437(2)	51(1)
C(33)	5918(3)	6711(2)	7172(2)	61(1)
C(34)	5045(3)	6918(2)	7320(2)	76(1)
C(35)	3766(3)	6433(2)	7634(2)	73(1)
C(36)	3439(3)	7034(3)	7803(2)	96(2)
C(37)	2673(4)	7064(4)	8070(2)	109(2)
C(38)	2229(3)	6518(4)	8175(2)	100(2)
C(39)	2526(3)	5894(3)	8007(2)	102(2)
C(40)	3312(2)	5860(3)	7736(2)	81(1)
C(41)	3181(3)	4694(3)	7577(2)	89(2)
C(42)	3738(3)	4131(2)	7431(2)	78(1)
C(43)	4488(2)	3614(2)	6697(2)	64(1)
C(44)	4724(2)	3648(2)	6070(2)	57(1)
C(45)	9358(2)	3569(2)	7214(1)	47(1)
C(46)	9848(2)	3935(2)	7651(1)	46(1)
C(47)	10705(2)	4084(2)	7573(2)	61(1)
C(48)	11072(3)	3871(2)	7065(2)	77(1)
C(49)	10589(3)	3519(2)	6636(2)	73(1)
C(50)	9732(2)	3365(2)	6711(2)	58(1)
C(51)	9868(2)	4516(1)	8578(1)	48(1)
C(52)	9263(2)	4672(1)	9041(1)	48(1)
C(53)	8453(2)	4197(1)	9775(1)	46(1)
C(54)	8219(2)	3560(2)	10048(1)	47(1)
C(55)	7391(2)	2594(1)	9771(1)	42(1)
C(56)	7585(2)	2309(2)	10322(1)	49(1)
C(57)	7235(2)	1697(2)	10443(2)	55(1)
C(58)	6695(2)	1382(2)	10025(2)	57(1)

C(59)	6506(2)	1660(2)	9463(2)	51(1)
C(60)	6856(2)	2261(1)	9332(1)	42(1)
C(61)	6219(2)	2238(2)	8320(1)	49(1)
C(62)	6199(2)	2661(2)	7779(1)	50(1)
C(63)	7076(2)	3082(2)	7059(1)	48(1)
C(64)	7980(2)	3090(2)	6883(1)	49(1)
C(65)	9971(3)	2830(2)	9312(2)	70(1)
C(66)	10707(3)	3163(2)	9629(2)	80(1)
C(67)	2466(4)	4537(3)	9350(2)	95(2)
C(68)	3020(6)	4393(5)	9822(4)	194(5)
C(69)	2625(8)	2896(7)	8528(4)	245(7)
C(70)	3773(13)	2953(4)	8595(4)	281(8)
C(71)	5051(4)	3717(4)	8946(3)	131(3)
C(72)	5403(8)	4310(5)	9255(4)	200(5)
N(1)	9167(1)	6052(1)	7938(1)	34(1)
N(2)	7934(1)	5330(1)	7600(1)	37(1)
N(3)	8203(1)	6569(1)	8777(1)	35(1)
N(4)	6981(1)	5840(1)	8434(1)	38(1)
N(5)	9374(3)	2580(2)	9074(2)	100(1)
N(6)	2051(4)	4660(5)	8934(3)	196(4)
O(1)	9810(1)	6494(1)	8145(1)	37(1)
O(2)	8919(1)	6976(1)	8911(1)	37(1)
O(3)	7192(1)	4960(1)	7431(1)	43(1)
O(4)	6314(1)	5429(1)	8193(1)	42(1)
O(5)	6139(1)	5271(1)	5911(1)	47(1)
O(6)	5266(1)	4212(1)	6013(1)	49(1)
O(7)	3950(2)	4154(1)	6831(1)	60(1)
O(8)	5836(1)	6350(1)	6633(1)	50(1)
O(9)	3680(2)	5280(2)	7555(1)	74(1)
O(10)	4521(2)	6344(1)	7383(1)	69(1)
O(11)	8517(1)	3440(1)	7328(1)	46(1)
O(12)	9415(1)	4117(1)	8129(1)	45(1)
O(13)	9012(1)	4083(1)	9319(1)	41(1)

O(14)	7053(1)	2716(1)	7597(1)	45(1)
O(15)	6730(1)	2572(1)	8792(1)	44(1)
O(16)	7672(1)	3200(1)	9611(1)	43(1)
O(20)	4175(5)	3586(3)	8868(2)	178(2)
F(1)	10387(1)	7145(1)	8901(1)	43(1)
F(2)	9928(1)	6122(1)	9138(1)	40(1)
F(3)	5933(1)	4494(1)	7684(1)	53(1)
F(4)	7117(1)	4457(1)	8369(1)	48(1)
K(1)	8042(1)	3399(1)	8458(1)	40(1)
K(2)	5093(1)	5206(1)	6851(1)	54(1)
Co(1)	8099(1)	5911(1)	8222(1)	33(1)
B(1)	9751(2)	6667(1)	8776(1)	35(1)
B(2)	6662(2)	4840(2)	7933(2)	42(1)

Table B12. Bond lengths [Å] and angles [°] for [K(dibenzo-18-crown-6)]$_2$[(Co(aqdBF$_2$)$_2$].

C(1)-N(1)	1.339(3)	C(9)-C(10)	1.435(4)
C(1)-C(2)	1.460(4)	C(9)-H(9)	0.9300
C(1)-C(11)	1.475(4)	C(10)-C(11)	1.388(4)
C(2)-N(2)	1.333(4)	C(10)-H(10)	0.9300
C(2)-C(3)	1.467(4)	C(11)-C(12)	1.442(4)
C(3)-C(4)	1.387(4)	C(13)-N(3)	1.344(3)
C(3)-C(12)	1.440(4)	C(13)-C(14)	1.455(4)
C(4)-C(5)	1.434(5)	C(13)-C(23)	1.478(4)
C(4)-H(4)	0.9300	C(14)-N(4)	1.335(4)
C(5)-C(6)	1.380(6)	C(14)-C(15)	1.468(4)
C(5)-H(5)	0.9300	C(15)-C(16)	1.393(4)
C(6)-C(7)	1.441(5)	C(15)-C(24)	1.440(4)
C(6)-H(6)	0.9300	C(16)-C(17)	1.437(5)
C(7)-C(12)	1.414(4)	C(17)-C(18)	1.377(5)
C(7)-C(8)	1.427(5)	C(18)-C(19)	1.442(5)
C(8)-C(9)	1.384(5)	C(19)-C(24)	1.411(4)
C(8)-H(8)	0.9300	C(19)-C(20)	1.433(5)

C(20)-C(21)	1.384(5)	C(43)-C(44)	1.512(5)
C(21)-C(22)	1.437(4)	C(43)-K(2)	3.440(4)
C(22)-C(23)	1.392(4)	C(44)-O(6)	1.454(3)
C(23)-C(24)	1.445(4)	C(45)-O(11)	1.383(4)
C(25)-O(6)	1.389(4)	C(45)-C(50)	1.400(5)
C(25)-C(30)	1.396(5)	C(45)-C(46)	1.420(4)
C(25)-C(26)	1.423(4)	C(46)-O(12)	1.385(4)
C(26)-O(5)	1.389(4)	C(46)-C(47)	1.397(5)
C(26)-C(27)	1.396(5)	C(47)-C(48)	1.409(6)
C(27)-C(28)	1.416(5)	C(48)-C(49)	1.387(6)
C(28)-C(29)	1.382(6)	C(49)-C(50)	1.397(5)
C(29)-C(30)	1.408(5)	C(51)-O(12)	1.449(3)
C(31)-O(5)	1.459(3)	C(51)-C(52)	1.511(5)
C(31)-C(32)	1.502(5)	C(52)-O(13)	1.448(3)
C(32)-O(8)	1.436(4)	C(52)-K(1)	3.447(3)
C(32)-K(2)	3.428(3)	C(53)-O(13)	1.436(4)
C(33)-O(8)	1.435(4)	C(53)-C(54)	1.518(4)
C(33)-C(34)	1.493(6)	C(53)-K(1)	3.437(3)
C(33)-K(2)	3.428(4)	C(54)-O(16)	1.456(3)
C(34)-O(10)	1.457(5)	C(55)-O(16)	1.390(3)
C(35)-O(10)	1.367(5)	C(55)-C(56)	1.397(4)
C(35)-C(40)	1.411(7)	C(55)-C(60)	1.420(4)
C(35)-C(36)	1.412(6)	C(56)-C(57)	1.418(5)
C(36)-C(37)	1.390(7)	C(57)-C(58)	1.377(5)
C(37)-C(38)	1.358(9)	C(58)-C(59)	1.412(5)
C(38)-C(39)	1.437(8)	C(59)-C(60)	1.404(4)
C(39)-C(40)	1.423(6)	C(60)-O(15)	1.389(4)
C(40)-O(9)	1.411(6)	C(61)-O(15)	1.454(3)
C(41)-O(9)	1.444(5)	C(61)-C(62)	1.513(5)
C(41)-C(42)	1.509(7)	C(62)-O(14)	1.432(4)
C(42)-O(7)	1.439(5)	C(62)-K(1)	3.488(3)
C(42)-K(2)	3.417(4)	C(63)-O(14)	1.447(4)
C(43)-O(7)	1.448(5)	C(63)-C(64)	1.499(4)

C(63)-K(1)	3.466(3)	O(15)-K(1)	2.824(2)
C(64)-O(11)	1.450(3)	O(16)-K(1)	2.775(2)
C(65)-N(5)	1.156(6)	F(1)-B(1)	1.412(3)
C(65)-C(66)	1.469(6)	F(2)-B(1)	1.412(3)
C(67)-N(6)	1.129(7)	F(3)-B(2)	1.416(3)
C(67)-C(68)	1.348(8)	F(3)-K(2)	2.655(2)
C(69)-C(70)	1.783(18)	F(4)-B(2)	1.412(4)
C(70)-O(20)	1.560(14)	F(4)-K(1)	2.6208(19)
C(71)-O(20)	1.386(9)	K(2)-B(2)	3.396(3)
C(71)-C(72)	1.495(11)		
N(1)-O(1)	1.406(3)	N(1)-C(1)-C(2)	112.5(2)
N(1)-Co(1)	1.863(2)	N(1)-C(1)-C(11)	138.9(3)
N(2)-O(3)	1.410(3)	C(2)-C(1)-C(11)	108.6(2)
N(2)-Co(1)	1.861(2)	N(2)-C(2)-C(1)	113.3(2)
N(3)-O(2)	1.409(3)	N(2)-C(2)-C(3)	138.2(3)
N(3)-Co(1)	1.859(2)	C(1)-C(2)-C(3)	108.4(2)
N(4)-O(4)	1.416(3)	C(4)-C(3)-C(12)	118.8(3)
N(4)-Co(1)	1.854(2)	C(4)-C(3)-C(2)	135.8(3)
N(5)-K(1)	2.936(4)	C(12)-C(3)-C(2)	105.4(2)
O(1)-B(1)	1.493(3)	C(3)-C(4)-C(5)	117.7(3)
O(2)-B(1)	1.503(3)	C(6)-C(5)-C(4)	123.3(3)
O(3)-B(2)	1.492(4)	C(5)-C(6)-C(7)	120.6(3)
O(4)-B(2)	1.482(4)	C(12)-C(7)-C(8)	116.7(3)
O(5)-K(2)	2.811(2)	C(12)-C(7)-C(6)	115.2(3)
O(6)-K(2)	2.840(2)	C(8)-C(7)-C(6)	128.2(3)
O(7)-K(2)	2.812(2)	C(9)-C(8)-C(7)	120.3(3)
O(8)-K(2)	2.705(2)	C(8)-C(9)-C(10)	122.7(3)
O(9)-K(2)	2.845(3)	C(11)-C(10)-C(9)	118.6(3)
O(10)-K(2)	2.834(3)	C(10)-C(11)-C(12)	118.4(3)
O(11)-K(1)	2.749(2)	C(10)-C(11)-C(1)	136.7(3)
O(12)-K(1)	2.764(2)	C(12)-C(11)-C(1)	104.9(2)
O(13)-K(1)	2.757(2)	C(7)-C(12)-C(3)	124.2(3)
O(14)-K(1)	2.773(2)	C(7)-C(12)-C(11)	123.3(3)

C(3)-C(12)-C(11)	112.5(2)	C(28)-C(29)-C(30)	119.9(3)
N(3)-C(13)-C(14)	112.6(2)	C(25)-C(30)-C(29)	120.8(3)
N(3)-C(13)-C(23)	139.3(3)	O(5)-C(31)-C(32)	109.1(2)
C(14)-C(13)-C(23)	108.1(2)	O(8)-C(32)-C(31)	110.7(2)
N(4)-C(14)-C(13)	113.2(2)	O(8)-C(32)-K(2)	48.69(13)
N(4)-C(14)-C(15)	137.5(3)	C(31)-C(32)-K(2)	87.24(16)
C(13)-C(14)-C(15)	109.3(2)	O(8)-C(33)-C(34)	109.3(3)
C(16)-C(15)-C(24)	119.2(3)	O(8)-C(33)-K(2)	48.70(14)
C(16)-C(15)-C(14)	135.9(3)	C(34)-C(33)-K(2)	88.8(2)
C(24)-C(15)-C(14)	104.9(2)	O(10)-C(34)-C(33)	108.5(3)
C(15)-C(16)-C(17)	117.6(3)	O(10)-C(35)-C(40)	114.7(4)
C(18)-C(17)-C(16)	123.3(3)	O(10)-C(35)-C(36)	125.3(5)
C(17)-C(18)-C(19)	120.6(3)	C(40)-C(35)-C(36)	120.0(4)
C(24)-C(19)-C(20)	116.4(3)	C(37)-C(36)-C(35)	120.2(6)
C(24)-C(19)-C(18)	115.8(3)	C(38)-C(37)-C(36)	120.7(6)
C(20)-C(19)-C(18)	127.8(3)	C(37)-C(38)-C(39)	121.5(5)
C(21)-C(20)-C(19)	120.4(3)	C(40)-C(39)-C(38)	118.1(6)
C(20)-C(21)-C(22)	122.7(3)	O(9)-C(40)-C(35)	116.6(3)
C(23)-C(22)-C(21)	118.7(3)	O(9)-C(40)-C(39)	123.9(5)
C(22)-C(23)-C(24)	118.0(3)	C(35)-C(40)-C(39)	119.5(5)
C(22)-C(23)-C(13)	136.9(3)	O(9)-C(41)-C(42)	108.6(3)
C(24)-C(23)-C(13)	105.1(2)	O(7)-C(42)-C(41)	111.8(4)
C(19)-C(24)-C(15)	123.6(3)	O(7)-C(42)-K(2)	53.58(15)
C(19)-C(24)-C(23)	123.8(3)	C(41)-C(42)-K(2)	88.2(2)
C(15)-C(24)-C(23)	112.6(2)	O(7)-C(43)-C(44)	111.1(3)
O(6)-C(25)-C(30)	125.7(3)	O(7)-C(43)-K(2)	52.81(14)
O(6)-C(25)-C(26)	115.0(3)	C(44)-C(43)-K(2)	87.97(18)
C(30)-C(25)-C(26)	119.3(3)	O(6)-C(44)-C(43)	108.3(3)
O(5)-C(26)-C(27)	125.0(3)	O(11)-C(45)-C(50)	124.6(3)
O(5)-C(26)-C(25)	115.3(3)	O(11)-C(45)-C(46)	115.4(3)
C(27)-C(26)-C(25)	119.7(3)	C(50)-C(45)-C(46)	120.1(3)
C(26)-C(27)-C(28)	120.1(3)	O(12)-C(46)-C(47)	125.5(3)
C(29)-C(28)-C(27)	120.2(4)	O(12)-C(46)-C(45)	115.4(3)

C(47)-C(46)-C(45)	119.1(3)	O(20)-C(70)-C(69)	116.9(9)
C(46)-C(47)-C(48)	120.0(4)	O(20)-C(71)-C(72)	122.4(7)
C(49)-C(48)-C(47)	120.7(4)	C(1)-N(1)-O(1)	116.6(2)
C(48)-C(49)-C(50)	119.8(4)	C(1)-N(1)-Co(1)	114.77(17)
C(49)-C(50)-C(45)	120.3(3)	O(1)-N(1)-Co(1)	128.04(16)
O(12)-C(51)-C(52)	108.8(2)	C(2)-N(2)-O(3)	117.1(2)
O(13)-C(52)-C(51)	109.6(2)	C(2)-N(2)-Co(1)	114.50(18)
O(13)-C(52)-K(1)	50.29(12)	O(3)-N(2)-Co(1)	127.76(16)
C(51)-C(52)-K(1)	85.60(15)	C(13)-N(3)-O(2)	117.5(2)
O(13)-C(53)-C(54)	109.8(2)	C(13)-N(3)-Co(1)	114.42(17)
O(13)-C(53)-K(1)	50.54(12)	O(2)-N(3)-Co(1)	127.29(15)
C(54)-C(53)-K(1)	84.73(16)	C(14)-N(4)-O(4)	116.5(2)
O(16)-C(54)-C(53)	108.2(2)	C(14)-N(4)-Co(1)	114.50(18)
O(16)-C(55)-C(56)	124.8(3)	O(4)-N(4)-Co(1)	128.17(17)
O(16)-C(55)-C(60)	115.6(2)	C(65)-N(5)-K(1)	117.9(3)
C(56)-C(55)-C(60)	119.6(3)	N(1)-O(1)-B(1)	112.05(18)
C(55)-C(56)-C(57)	119.9(3)	N(3)-O(2)-B(1)	112.27(18)
C(58)-C(57)-C(56)	120.7(3)	N(2)-O(3)-B(2)	112.17(19)
C(57)-C(58)-C(59)	120.0(3)	N(4)-O(4)-B(2)	111.75(19)
C(60)-C(59)-C(58)	120.1(3)	C(26)-O(5)-C(31)	116.2(2)
O(15)-C(60)-C(59)	125.0(3)	C(26)-O(5)-K(2)	126.14(16)
O(15)-C(60)-C(55)	115.3(2)	C(31)-O(5)-K(2)	115.11(18)
C(59)-C(60)-C(55)	119.7(3)	C(25)-O(6)-C(44)	116.5(2)
O(15)-C(61)-C(62)	107.3(2)	C(25)-O(6)-K(2)	125.20(16)
O(14)-C(62)-C(61)	109.3(2)	C(44)-O(6)-K(2)	115.6(2)
O(14)-C(62)-K(1)	49.18(12)	C(42)-O(7)-C(43)	111.2(3)
C(61)-C(62)-K(1)	86.33(15)	C(42)-O(7)-K(2)	102.1(2)
O(14)-C(63)-C(64)	109.3(2)	C(43)-O(7)-K(2)	102.98(17)
O(14)-C(63)-K(1)	50.22(11)	C(33)-O(8)-C(32)	110.6(2)
C(64)-C(63)-K(1)	84.58(15)	C(33)-O(8)-K(2)	107.80(18)
O(11)-C(64)-C(63)	108.3(2)	C(32)-O(8)-K(2)	107.82(16)
N(5)-C(65)-C(66)	177.7(5)	C(40)-O(9)-C(41)	118.2(3)
N(6)-C(67)-C(68)	175.2(8)	C(40)-O(9)-K(2)	124.5(3)

C(41)-O(9)-K(2)	114.9(2)	O(13)-K(1)-O(14)	179.46(7)
C(35)-O(10)-C(34)	116.3(3)	O(12)-K(1)-O(14)	118.42(7)
C(35)-O(10)-K(2)	127.5(3)	F(4)-K(1)-O(16)	92.17(6)
C(34)-O(10)-K(2)	115.9(2)	O(11)-K(1)-O(16)	172.40(7)
C(45)-O(11)-C(64)	117.4(2)	O(13)-K(1)-O(16)	63.18(6)
C(45)-O(11)-K(1)	121.50(16)	O(12)-K(1)-O(16)	124.78(6)
C(64)-O(11)-K(1)	116.99(17)	O(14)-K(1)-O(16)	116.47(7)
C(46)-O(12)-C(51)	118.1(2)	F(4)-K(1)-O(15)	97.09(6)
C(46)-O(12)-K(1)	120.80(17)	O(11)-K(1)-O(15)	122.34(6)
C(51)-O(12)-K(1)	116.96(17)	O(13)-K(1)-O(15)	118.85(6)
C(53)-O(13)-C(52)	112.6(2)	O(12)-K(1)-O(15)	175.09(6)
C(53)-O(13)-K(1)	105.76(15)	O(14)-K(1)-O(15)	60.79(6)
C(52)-O(13)-K(1)	105.88(15)	O(16)-K(1)-O(15)	55.68(6)
C(62)-O(14)-C(63)	112.5(2)	F(4)-K(1)-N(5)	151.63(9)
C(62)-O(14)-K(1)	107.80(16)	O(11)-K(1)-N(5)	103.17(11)
C(63)-O(14)-K(1)	106.14(15)	O(13)-K(1)-N(5)	68.86(9)
C(60)-O(15)-C(61)	117.4(2)	O(12)-K(1)-N(5)	84.91(12)
C(60)-O(15)-K(1)	118.27(15)	O(14)-K(1)-N(5)	111.46(9)
C(61)-O(15)-K(1)	116.72(17)	O(16)-K(1)-N(5)	70.09(11)
C(55)-O(16)-C(54)	117.5(2)	O(15)-K(1)-N(5)	90.94(11)
C(55)-O(16)-K(1)	118.73(16)	F(4)-K(1)-C(53)	73.89(7)
C(54)-O(16)-K(1)	114.43(16)	O(11)-K(1)-C(53)	139.50(7)
C(71)-O(20)-C(70)	124.8(9)	O(13)-K(1)-C(53)	23.70(7)
B(2)-F(3)-K(2)	109.21(17)	O(12)-K(1)-C(53)	83.78(7)
B(2)-F(4)-K(1)	139.64(17)	O(14)-K(1)-C(53)	155.79(7)
F(4)-K(1)-O(11)	95.40(6)	O(16)-K(1)-C(53)	44.05(7)
F(4)-K(1)-O(13)	83.51(6)	O(15)-K(1)-C(53)	97.94(7)
O(11)-K(1)-O(13)	118.39(7)	N(5)-K(1)-C(53)	78.07(10)
F(4)-K(1)-O(12)	87.81(7)	F(4)-K(1)-C(52)	70.69(7)
O(11)-K(1)-O(12)	56.44(6)	O(11)-K(1)-C(52)	98.72(7)
O(13)-K(1)-O(12)	61.98(6)	O(13)-K(1)-C(52)	23.82(6)
F(4)-K(1)-O(14)	96.12(6)	O(12)-K(1)-C(52)	43.92(7)
O(11)-K(1)-O(14)	62.01(7)	O(14)-K(1)-C(52)	156.28(7)

O(16)-K(1)-C(52)	84.46(7)	O(5)-K(2)-O(10)	120.90(8)
O(15)-K(1)-C(52)	138.42(7)	O(7)-K(2)-O(10)	115.39(9)
N(5)-K(1)-C(52)	85.28(10)	F(3)-K(2)-O(6)	90.43(7)
C(53)-K(1)-C(52)	40.78(8)	O(8)-K(2)-O(6)	116.39(7)
F(4)-K(1)-C(63)	84.14(7)	O(5)-K(2)-O(6)	54.87(6)
O(11)-K(1)-C(63)	43.36(7)	O(7)-K(2)-O(6)	61.67(7)
O(13)-K(1)-C(63)	156.50(7)	O(10)-K(2)-O(6)	160.96(7)
O(12)-K(1)-C(63)	97.66(7)	F(3)-K(2)-O(9)	88.89(8)
O(14)-K(1)-C(63)	23.64(7)	O(8)-K(2)-O(9)	114.98(8)
O(16)-K(1)-C(63)	137.29(7)	O(5)-K(2)-O(9)	163.74(8)
O(15)-K(1)-C(63)	82.49(7)	O(7)-K(2)-O(9)	61.95(8)
N(5)-K(1)-C(63)	123.99(10)	O(10)-K(2)-O(9)	54.80(9)
C(53)-K(1)-C(63)	157.93(8)	O(6)-K(2)-O(9)	123.02(8)
C(52)-K(1)-C(63)	132.69(7)	F(3)-K(2)-B(2)	23.19(7)
F(4)-K(1)-C(62)	84.75(7)	O(8)-K(2)-B(2)	92.22(7)
O(11)-K(1)-C(62)	82.97(7)	O(5)-K(2)-B(2)	97.88(8)
O(13)-K(1)-C(62)	156.47(7)	O(7)-K(2)-B(2)	104.52(8)
O(12)-K(1)-C(62)	137.78(7)	O(10)-K(2)-B(2)	96.19(8)
O(14)-K(1)-C(62)	23.02(7)	O(6)-K(2)-B(2)	102.75(8)
O(16)-K(1)-C(62)	97.03(7)	O(9)-K(2)-B(2)	98.22(9)
O(15)-K(1)-C(62)	42.91(7)	F(3)-K(2)-C(42)	68.96(9)
N(5)-K(1)-C(62)	118.38(10)	O(8)-K(2)-C(42)	158.79(10)
C(53)-K(1)-C(62)	132.79(8)	O(5)-K(2)-C(42)	138.41(10)
C(52)-K(1)-C(62)	155.44(8)	O(7)-K(2)-C(42)	24.31(9)
C(63)-K(1)-C(62)	40.27(8)	O(10)-K(2)-C(42)	98.46(11)
F(3)-K(2)-O(8)	115.38(6)	O(6)-K(2)-C(42)	83.54(10)
F(3)-K(2)-O(5)	106.93(7)	O(9)-K(2)-C(42)	43.89(11)
O(8)-K(2)-O(5)	62.02(6)	B(2)-K(2)-C(42)	90.05(10)
F(3)-K(2)-O(7)	81.38(7)	F(3)-K(2)-C(33)	101.69(8)
O(8)-K(2)-O(7)	163.21(7)	O(8)-K(2)-C(33)	23.50(8)
O(5)-K(2)-O(7)	115.77(7)	O(5)-K(2)-C(33)	83.55(8)
F(3)-K(2)-O(10)	108.03(8)	O(7)-K(2)-C(33)	158.95(9)
O(8)-K(2)-O(10)	60.33(8)	O(10)-K(2)-C(33)	43.69(9)

O(6)-K(2)-C(33)	138.40(8)	C(32)-K(2)-C(43)	139.15(9)
O(9)-K(2)-C(33)	97.13(9)	N(4)-Co(1)-N(3)	84.59(10)
B(2)-K(2)-C(33)	79.48(8)	N(4)-Co(1)-N(2)	94.66(10)
C(42)-K(2)-C(33)	137.98(11)	N(3)-Co(1)-N(2)	172.73(9)
F(3)-K(2)-C(32)	102.72(7)	N(4)-Co(1)-N(1)	172.93(9)
O(8)-K(2)-C(32)	23.49(7)	N(3)-Co(1)-N(1)	95.50(10)
O(5)-K(2)-C(32)	44.10(7)	N(2)-Co(1)-N(1)	84.36(10)
O(7)-K(2)-C(32)	159.86(8)	F(2)-B(1)-F(1)	110.3(2)
O(10)-K(2)-C(32)	82.43(9)	F(2)-B(1)-O(1)	110.3(2)
O(6)-K(2)-C(32)	98.38(8)	F(1)-B(1)-O(1)	105.1(2)
O(9)-K(2)-C(32)	137.08(9)	F(2)-B(1)-O(2)	110.3(2)
B(2)-K(2)-C(32)	81.49(8)	F(1)-B(1)-O(2)	105.1(2)
C(42)-K(2)-C(32)	171.54(9)	O(1)-B(1)-O(2)	115.5(2)
C(33)-K(2)-C(32)	40.27(9)	F(4)-B(2)-F(3)	109.2(2)
F(3)-K(2)-C(43)	69.63(7)	F(4)-B(2)-O(4)	111.1(2)
O(8)-K(2)-C(43)	160.06(9)	F(3)-B(2)-O(4)	105.6(2)
O(5)-K(2)-C(43)	98.09(8)	F(4)-B(2)-O(3)	111.0(2)
O(7)-K(2)-C(43)	24.21(8)	F(3)-B(2)-O(3)	104.9(2)
O(10)-K(2)-C(43)	138.43(9)	O(4)-B(2)-O(3)	114.7(2)
O(6)-K(2)-C(43)	43.73(8)	F(4)-B(2)-K(2)	156.83(19)
O(9)-K(2)-C(43)	83.71(9)	F(3)-B(2)-K(2)	47.60(13)
B(2)-K(2)-C(43)	91.81(8)	O(4)-B(2)-K(2)	80.91(14)
C(42)-K(2)-C(43)	40.65(11)	O(3)-B(2)-K(2)	79.40(15)
C(33)-K(2)-C(43)	171.28(9)		

Table B13. Crystal data and structure refinement for $[K(18\text{-crown-6})]_2[(Co(aqdBF_2)_2]$.

Empirical formula	$C_{64}H_{92}B_2CoF_4K_2N_4O_{20}$	
Formula weight	1472.16	
Temperature	150(2) K	
Wavelength	1.54184 Å	
Crystal system	Monoclinic	
Space group	P $2_1/c$	
Unit cell dimensions	a = 12.9854(6) Å	a= 90°.
	b = 19.0412(9) Å	b= 93.331(5)°.
	c = 14.1063(8) Å	g = 90°.
Volume	3482.0(3) $Å^3$	
Z	2	
Density (calculated)	1.404 Mg/m^3	
Absorption coefficient	3.725 mm^{-1}	
F(000)	1550	
Crystal size	0.383 x 0.263 x 0.191 mm^3	
Theta range for data collection	3.409 to 74.238°.	
Index ranges	-15<=h<=15, -16<=k<=23, -17<=l<=17	
Reflections collected	13525	
Independent reflections	6892 [R(int) = 0.0262]	
Completeness to theta = 67.684°	100.0 %	
Absorption correction	Semi-emperical from equivalents	
Max. and min. transmission	1.147 and 0.835	
Refinement method	Full-matrix least-squares on F^2	
Data / restraints / parameters	6892 / 0 / 439	
Goodness-of-fit on F^2	1.044	
Final R indices [I>2sigma(I)]	R1 = 0.0544, wR2 = 0.1438	
R indices (all data)	R1 = 0.0694, wR2 = 0.1570	
Largest diff. peak and hole	0.680 and -0.724 e.$Å^{-3}$	

Table B14. Atomic coordinates (x 10^4) and equivalent isotropic displacement parameters ($Å^2$x 10^3) for $[K(18\text{-crown-6})]_2[(Co(aqdBF_2)_2]$. U(eq) is defined as one third of the trace of the orthogonalized U^{ij} tensor.

	x	y	z	U(eq)
Co(1)	5000	5000	0	26(1)
K(1)	6289(1)	4165(1)	-1932(1)	30(1)
F(1)	4039(1)	3419(1)	403(1)	33(1)
F(2)	4603(1)	2723(1)	-787(1)	35(1)
O(1)	5717(1)	3558(1)	-155(1)	29(1)
O(5)	8130(2)	5035(1)	-1559(2)	44(1)
C(2)	3309(2)	4944(2)	-1183(2)	28(1)
O(7)	6954(2)	2738(1)	-2271(2)	51(1)
N(1)	4167(2)	5773(1)	-243(2)	28(1)
C(6)	459(2)	5087(2)	-2777(2)	36(1)
O(2)	4133(2)	3858(1)	-1153(1)	30(1)
C(1)	3350(2)	5655(2)	-832(2)	27(1)
O(6)	8176(2)	3613(1)	-1111(2)	45(1)
N(2)	5909(2)	5447(1)	842(2)	28(1)
O(4)	6341(2)	5608(1)	-2453(2)	58(1)
C(12)	1872(2)	5519(2)	-1781(2)	27(1)
C(10)	2006(2)	6684(2)	-1106(2)	31(1)
C(18)	9055(2)	4065(3)	-950(3)	65(1)
C(11)	2428(2)	6028(2)	-1209(2)	27(1)
O(9)	9032(2)	3586(1)	-4290(2)	50(1)
O(8)	5211(2)	3322(2)	-3233(2)	74(1)
C(5)	944(2)	4448(2)	-2806(2)	35(1)
O(10)	1313(2)	3204(2)	3917(2)	62(1)
O(3)	5097(2)	4756(2)	-3618(2)	71(1)
C(3)	2374(2)	4854(2)	-1790(2)	28(1)
C(9)	1034(2)	6829(2)	-1579(2)	34(1)

C(4)	1913(2)	4312(2)	-2308(2)	32(1)
C(7)	914(2)	5655(2)	-2249(2)	31(1)
B(1)	4606(2)	3390(2)	-407(2)	30(1)
C(16)	7775(4)	5734(2)	-1385(3)	65(1)
C(8)	501(2)	6341(2)	-2134(2)	34(1)
C(20)	7533(4)	2489(2)	-1431(3)	71(2)
C(25)	9111(2)	4044(2)	-5078(2)	39(1)
C(26)	8083(3)	4419(2)	-5218(3)	54(1)
C(19)	8463(4)	2918(2)	-1264(3)	64(1)
C(31)	1649(3)	2073(2)	4527(3)	60(1)
C(17)	8729(3)	4793(3)	-773(3)	60(1)
C(14)	5754(4)	5871(3)	-3250(4)	87(2)
C(15)	7224(4)	6017(2)	-2239(4)	71(1)
C(13)	4804(4)	5449(3)	-3388(4)	91(2)
C(22)	5550(3)	2606(3)	-3381(5)	93(2)
C(29)	1740(4)	3298(2)	4844(4)	69(1)
C(28)	8187(3)	3811(2)	-3764(3)	51(1)
C(21)	6070(4)	2332(2)	-2502(4)	82(2)
C(32)	1583(4)	2514(3)	3649(4)	72(1)
C(23)	4621(3)	3590(4)	-4020(4)	107(3)
C(30)	1678(4)	2589(3)	5325(4)	76(1)
C(24)	4237(3)	4300(4)	-3769(4)	97(2)
C(27)	7550(5)	4248(5)	-4393(5)	165(5)

Table B15. Bond lengths [Å] and angles [°] $[K(18\text{-crown-6})]_2[(Co(aqdBF_2)_2]$.

Co(1)-N(2)	1.835(2)	K(1)-O(6)	2.850(2)
Co(1)-N(2)#1	1.835(2)	K(1)-O(1)	2.896(2)
Co(1)-N(1)	1.847(2)	K(1)-O(7)	2.899(2)
Co(1)-N(1)#1	1.847(2)	K(1)-O(5)	2.931(2)
Co(1)-K(1)	3.6444(6)	K(1)-O(3)	2.981(3)
Co(1)-K(1)#1	3.6444(6)	K(1)-O(2)	3.121(2)
K(1)-O(8)	2.758(3)	K(1)-N(1)#1	3.161(2)
K(1)-O(4)	2.845(3)	K(1)-N(2)#1	3.400(2)

K(1)-B(1)	3.482(3)	O(9)-C(25)	1.421(4)
F(1)-B(1)	1.396(4)	O(9)-C(28)	1.425(4)
F(2)-B(1)	1.379(4)	O(8)-C(23)	1.407(7)
O(1)-N(1)#1	1.397(3)	O(8)-C(22)	1.453(6)
O(1)-B(1)	1.500(3)	C(5)-C(4)	1.429(4)
O(5)-C(17)	1.394(5)	O(10)-C(29)	1.403(5)
O(5)-C(16)	1.434(5)	O(10)-C(32)	1.417(5)
C(2)-N(2)#1	1.326(3)	O(3)-C(13)	1.417(7)
C(2)-C(1)	1.443(4)	O(3)-C(24)	1.420(7)
C(2)-C(3)	1.454(4)	C(3)-C(4)	1.381(4)
O(7)-C(21)	1.408(5)	C(9)-C(8)	1.375(5)
O(7)-C(20)	1.445(5)	C(7)-C(8)	1.424(4)
N(1)-C(1)	1.328(3)	C(16)-C(15)	1.468(7)
N(1)-O(1)#1	1.397(3)	C(20)-C(19)	1.466(7)
N(1)-K(1)#1	3.161(2)	C(25)-C(26)	1.518(5)
C(6)-C(5)	1.372(5)	C(26)-C(27)	1.426(6)
C(6)-C(7)	1.422(4)	C(31)-C(30)	1.493(7)
O(2)-N(2)#1	1.397(3)	C(31)-C(32)	1.495(6)
O(2)-B(1)	1.484(4)	C(14)-C(13)	1.476(8)
C(1)-C(11)	1.464(3)	C(22)-C(21)	1.472(8)
O(6)-C(19)	1.395(5)	C(29)-C(30)	1.514(6)
O(6)-C(18)	1.437(5)	C(28)-C(27)	1.441(6)
N(2)-C(2)#1	1.326(3)	C(23)-C(24)	1.491(9)
N(2)-O(2)#1	1.397(3)		
N(2)-K(1)#1	3.400(2)	N(2)-Co(1)-N(1)	95.65(10)
O(4)-C(15)	1.405(6)	N(2)#1-Co(1)-N(1)	84.35(10)
O(4)-C(14)	1.413(6)	N(2)-Co(1)-N(1)#1	84.35(10)
C(12)-C(7)	1.398(4)	N(2)#1-Co(1)-N(1)#1	95.65(10)
C(12)-C(3)	1.425(4)	N(2)-Co(1)-K(1)	112.36(7)
C(12)-C(11)	1.429(4)	N(2)#1-Co(1)-K(1)	67.64(7)
C(10)-C(11)	1.376(4)	N(1)-Co(1)-K(1)	119.87(7)
C(10)-C(9)	1.419(4)	N(1)#1-Co(1)-K(1)	60.13(7)
C(18)-C(17)	1.474(7)	N(2)-Co(1)-K(1)#1	67.64(7)

N(2)#1-Co(1)-K(1)#1	112.36(7)	O(6)-K(1)-N(1)#1	79.90(6)
N(1)-Co(1)-K(1)#1	60.13(7)	O(1)-K(1)-N(1)#1	26.20(6)
N(1)#1-Co(1)-K(1)#1	119.87(7)	O(7)-K(1)-N(1)#1	105.63(7)
O(8)-K(1)-O(4)	114.11(11)	O(5)-K(1)-N(1)#1	90.09(6)
O(8)-K(1)-O(6)	116.55(9)	O(3)-K(1)-N(1)#1	129.98(7)
O(4)-K(1)-O(6)	115.36(8)	O(2)-K(1)-N(1)#1	56.16(5)
O(8)-K(1)-O(1)	101.42(9)	O(8)-K(1)-N(2)#1	91.17(7)
O(4)-K(1)-O(1)	128.33(7)	O(4)-K(1)-N(2)#1	86.58(7)
O(6)-K(1)-O(1)	76.05(6)	O(6)-K(1)-N(2)#1	128.40(6)
O(8)-K(1)-O(7)	59.31(9)	O(1)-K(1)-N(2)#1	55.34(5)
O(4)-K(1)-O(7)	148.24(7)	O(7)-K(1)-N(2)#1	122.97(6)
O(6)-K(1)-O(7)	57.57(8)	O(5)-K(1)-N(2)#1	119.57(6)
O(1)-K(1)-O(7)	82.10(6)	O(3)-K(1)-N(2)#1	82.43(6)
O(8)-K(1)-O(5)	145.64(8)	O(2)-K(1)-N(2)#1	24.26(5)
O(4)-K(1)-O(5)	57.97(8)	N(1)#1-K(1)-N(2)#1	48.98(6)
O(6)-K(1)-O(5)	57.47(8)	O(8)-K(1)-B(1)	81.48(9)
O(1)-K(1)-O(5)	108.53(6)	O(4)-K(1)-B(1)	126.44(8)
O(7)-K(1)-O(5)	108.13(8)	O(6)-K(1)-B(1)	98.54(7)
O(8)-K(1)-O(3)	57.91(12)	O(1)-K(1)-B(1)	25.12(6)
O(4)-K(1)-O(3)	56.53(10)	O(7)-K(1)-B(1)	84.75(7)
O(6)-K(1)-O(3)	149.03(7)	O(5)-K(1)-B(1)	131.56(7)
O(1)-K(1)-O(3)	133.93(7)	O(3)-K(1)-B(1)	109.71(8)
O(7)-K(1)-O(3)	111.59(9)	O(2)-K(1)-B(1)	25.22(6)
O(5)-K(1)-O(3)	108.07(9)	N(1)#1-K(1)-B(1)	41.98(7)
O(8)-K(1)-O(2)	72.18(7)	N(2)#1-K(1)-B(1)	40.50(7)
O(4)-K(1)-O(2)	107.89(7)	O(8)-K(1)-Co(1)	120.94(6)
O(6)-K(1)-O(2)	123.76(6)	O(4)-K(1)-Co(1)	77.94(5)
O(1)-K(1)-O(2)	48.73(5)	O(6)-K(1)-Co(1)	106.18(5)
O(7)-K(1)-O(2)	99.46(6)	O(1)-K(1)-Co(1)	51.32(4)
O(5)-K(1)-O(2)	141.43(6)	O(7)-K(1)-Co(1)	133.34(5)
O(3)-K(1)-O(2)	85.23(7)	O(5)-K(1)-Co(1)	91.41(5)
O(8)-K(1)-N(1)#1	123.46(8)	O(3)-K(1)-Co(1)	101.09(6)
O(4)-K(1)-N(1)#1	102.92(7)	O(2)-K(1)-Co(1)	50.11(4)

N(1)#1-K(1)-Co(1)	30.45(4)	O(2)#1-N(2)-Co(1)	127.44(16)
N(2)#1-K(1)-Co(1)	29.93(4)	C(2)#1-N(2)-K(1)#1	127.12(18)
B(1)-K(1)-Co(1)	52.50(6)	O(2)#1-N(2)-K(1)#1	66.63(12)
N(1)#1-O(1)-B(1)	111.7(2)	Co(1)-N(2)-K(1)#1	82.43(8)
N(1)#1-O(1)-K(1)	87.53(13)	C(15)-O(4)-C(14)	111.7(4)
B(1)-O(1)-K(1)	99.86(16)	C(15)-O(4)-K(1)	120.8(3)
C(17)-O(5)-C(16)	109.9(3)	C(14)-O(4)-K(1)	121.9(3)
C(17)-O(5)-K(1)	111.5(2)	C(7)-C(12)-C(3)	123.7(3)
C(16)-O(5)-K(1)	106.7(2)	C(7)-C(12)-C(11)	123.2(3)
N(2)#1-C(2)-C(1)	113.0(2)	C(3)-C(12)-C(11)	113.0(2)
N(2)#1-C(2)-C(3)	138.0(3)	C(11)-C(10)-C(9)	118.4(3)
C(1)-C(2)-C(3)	109.0(2)	O(6)-C(18)-C(17)	110.8(3)
C(21)-O(7)-C(20)	112.8(4)	C(10)-C(11)-C(12)	118.9(2)
C(21)-O(7)-K(1)	107.9(3)	C(10)-C(11)-C(1)	136.4(3)
C(20)-O(7)-K(1)	108.6(2)	C(12)-C(11)-C(1)	104.6(2)
C(1)-N(1)-O(1)#1	118.0(2)	C(25)-O(9)-C(28)	108.4(3)
C(1)-N(1)-Co(1)	114.8(2)	C(23)-O(8)-C(22)	112.5(4)
O(1)#1-N(1)-Co(1)	127.14(16)	C(23)-O(8)-K(1)	123.1(3)
C(1)-N(1)-K(1)#1	115.18(16)	C(22)-O(8)-K(1)	119.7(3)
O(1)#1-N(1)-K(1)#1	66.27(12)	C(6)-C(5)-C(4)	122.6(3)
Co(1)-N(1)-K(1)#1	89.42(8)	C(29)-O(10)-C(32)	106.0(3)
C(5)-C(6)-C(7)	120.8(3)	C(13)-O(3)-C(24)	112.6(4)
N(2)#1-O(2)-B(1)	111.6(2)	C(13)-O(3)-K(1)	107.6(3)
N(2)#1-O(2)-K(1)	89.11(13)	C(24)-O(3)-K(1)	104.8(3)
B(1)-O(2)-K(1)	91.12(15)	C(4)-C(3)-C(12)	119.0(3)
N(1)-C(1)-C(2)	112.6(2)	C(4)-C(3)-C(2)	136.1(3)
N(1)-C(1)-C(11)	138.8(3)	C(12)-C(3)-C(2)	104.9(2)
C(2)-C(1)-C(11)	108.5(2)	C(8)-C(9)-C(10)	122.8(3)
C(19)-O(6)-C(18)	112.1(3)	C(3)-C(4)-C(5)	117.9(3)
C(19)-O(6)-K(1)	121.2(2)	C(12)-C(7)-C(6)	116.0(3)
C(18)-O(6)-K(1)	120.0(2)	C(12)-C(7)-C(8)	116.5(3)
C(2)#1-N(2)-O(2)#1	117.4(2)	C(6)-C(7)-C(8)	127.5(3)
C(2)#1-N(2)-Co(1)	115.1(2)	F(2)-B(1)-F(1)	111.4(3)

F(2)-B(1)-O(2)	106.6(2)	C(30)-C(31)-C(32)	104.6(4)
F(1)-B(1)-O(2)	110.0(2)	O(5)-C(17)-C(18)	109.2(3)
F(2)-B(1)-O(1)	105.7(2)	O(4)-C(14)-C(13)	108.7(4)
F(1)-B(1)-O(1)	110.1(2)	O(4)-C(15)-C(16)	109.0(3)
O(2)-B(1)-O(1)	113.1(2)	O(3)-C(13)-C(14)	107.6(3)
F(2)-B(1)-K(1)	97.94(17)	O(8)-C(22)-C(21)	109.9(4)
F(1)-B(1)-K(1)	150.3(2)	O(10)-C(29)-C(30)	106.0(4)
O(2)-B(1)-K(1)	63.66(14)	O(9)-C(28)-C(27)	106.5(3)
O(1)-B(1)-K(1)	55.02(13)	O(7)-C(21)-C(22)	109.1(4)
O(5)-C(16)-C(15)	110.3(3)	O(10)-C(32)-C(31)	107.7(4)
C(9)-C(8)-C(7)	120.2(3)	O(8)-C(23)-C(24)	108.4(4)
O(7)-C(20)-C(19)	109.5(3)	C(31)-C(30)-C(29)	104.4(4)
O(9)-C(25)-C(26)	106.7(3)	O(3)-C(24)-C(23)	108.6(4)
C(27)-C(26)-C(25)	104.5(3)	C(26)-C(27)-C(28)	110.3(4)
O(6)-C(19)-C(20)	109.2(3)		

Symmetry transformations used to generate equivalent atoms:

#1 -x+1,-y+1,-z

References

(1) Monthly Energy Review - Energy Information Administration https://www.eia.gov/totalenergy/data/monthly/index.cfm#consumption (accessed May 9, 2016).

(2) IEA - WEO-2015 http://www.worldenergyoutlook.org/weo2015/ (accessed May 9, 2016).

(3) EIA projects world energy consumption will increase 56% by 2040 - Today in Energy - U.S. Energy Information Administration (EIA) http://www.eia.gov/todayinenergy/detail.cfm?id=12251 (accessed May 9, 2016).

(4) US Department of Commerce, N. ESRL Global Monitoring Division - Global Greenhouse Gas Reference Network http://www.esrl.noaa.gov/gmd/ccgg/trends/global.html#global (accessed May 9, 2016).

(5) Moss, R. H.; Edmonds, J. A.; Hibbard, K. A.; Manning, M. R.; Rose, S. K.; van Vuuren, D. P.; Carter, T. R.; Emori, S.; Kainuma, M.; Kram, T.; Meehl, G. A.; Mitchell, J. F. B.; Nakicenovic, N.; Riahi, K.; Smith, S. J.; Stouffer, R. J.; Thomson, A. M.; Weyant, J. P.; Wilbanks, T. J. *Nature* **2010**, *463* (7282), 747–756.

(6) Zachos, J.; Pagani, M.; Sloan, L.; Thomas, E.; Billups, K. *Science* **2001**, *292* (5517), 686–693.

(7) Farmer, G. T. In *Modern Climate Change Science*; SpringerBriefs in Environmental Science; Springer International Publishing, 2015; pp 1–42.

(8) Farmer, G. T. In *Modern Climate Change Science*; SpringerBriefs in Environmental Science; Springer International Publishing, 2015; pp 43–99.

(9) Schär, C.; Vidale, P. L.; Lüthi, D.; Frei, C.; Häberli, C.; Liniger, M. A.; Appenzeller, C. *Nature* **2004**, *427* (6972), 332–336.

(10) Walther, G.-R.; Post, E.; Convey, P.; Menzel, A.; Parmesan, C.; Beebee, T. J. C.; Fromentin, J.-M.; Hoegh-Guldberg, O.; Bairlein, F. *Nature* **2002**, *416* (6879), 389–395.

(11) Hansen, J.; Sato, M.; Ruedy, R.; Lo, K.; Lea, D. W.; Medina-Elizade, M. *Proc. Natl. Acad. Sci.* **2006**, *103* (39), 14288–14293.

(12) Miller, K. G.; Kominz, M. A.; Browning, J. V.; Wright, J. D.; Mountain, G. S.; Katz, M. E.; Sugarman, P. J.; Cramer, B. S.; Christie-Blick, N.; Pekar, S. F. *Science* **2005**, *310* (5752), 1293–1298.

(13) Lin, N.; Emanuel, K.; Oppenheimer, M.; Vanmarcke, E. *Nat. Clim. Change* **2012**, *2* (6), 462–467.

(14) Mills, E. *Geneva Pap. Risk Insur. - Issues Pract.* **2009**, *34* (3), 323–359.

(15) Bak, T.; Nowotny, J.; Rekas, M.; Sorrell, C. C. *Int. J. Hydrog. Energy* **2002**, *27* (10), 991–1022.

(16) Gust, D.; Moore, T. A.; Moore, A. L. *Acc. Chem. Res.* **2009**, *42* (12), 1890–1898.

(17) Walter, M. G.; Warren, E. L.; McKone, J. R.; Boettcher, S. W.; Mi, Q.; Santori, E. A.; Lewis, N. S. *Chem. Rev.* **2010**, *110* (11), 6446–6473.

(18) Roy, S. C.; Varghese, O. K.; Paulose, M.; Grimes, C. A. *ACS Nano* **2010**, *4* (3), 1259–1278.

(19) Chen, X.; Shen, S.; Guo, L.; Mao, S. S. *Chem. Rev.* **2010**, *110* (11), 6503–6570.

(20) White, J. L.; Baruch, M. F.; Pander III, J. E.; Hu, Y.; Fortmeyer, I. C.; Park, J. E.; Zhang, T.; Liao, K.; Gu, J.; Yan, Y.; Shaw, T. W.; Abelev, E.; Bocarsly, A. B. *Chem. Rev.* **2015**, *115* (23), 12888–12935.

(21) Hochbaum, A. I.; Yang, P. *Chem. Rev.* **2010**, *110* (1), 527–546.

(22) Warren, E. L.; Atwater, H. A.; Lewis, N. S. *J. Phys. Chem. C* **2014**, *118* (2), 747–759.

(23) Grätzel, M. *Nature* **2001**, *414* (6861), 338–344.

(24) Mills, A.; Le Hunte, S. *J. Photochem. Photobiol. Chem.* **1997**, *108* (1), 1–35.

(25) Peng, X.; He, C.; Fan, X.; Liu, Q.; Zhang, J.; Wang, H. *Int. J. Hydrog. Energy* **2014**, *39* (26), 14166–14171.

(26) Kronik, L.; Shapira, Y. *Surf. Sci. Rep.* **1999**, *37* (1–5), 1–206.

(27) Zou, X.; Zhang, Y. *Chem Soc Rev* **2015**, *44* (15), 5148–5180.

(28) Zeng, M.; Li, Y. *J. Mater. Chem. A* **2015**, *3* (29), 14942–14962.

(29) Benson, E. E.; Kubiak, C. P.; Sathrum, A. J.; Smieja, J. M. *Chem. Soc. Rev.* **2008**, *38* (1), 89–99.

(30) Rakowski Dubois, M.; Dubois, D. L. *Acc. Chem. Res.* **2009**, *42* (12), 1974–1982.

(31) McKone, J. R.; Marinescu, S. C.; Brunschwig, B. S.; Winkler, J. R.; Gray, H. B. *Chem. Sci.* **2014**, *5* (3), 865–878.

(32) Solar Spectral Irradiance: Air Mass 1.5 http://rredc.nrel.gov/solar/spectra/am1.5/ (accessed May 9, 2016).

(33) Smith, W. A.; Sharp, I. D.; Strandwitz, N. C.; Bisquert, J. *Energy Environ. Sci.* **2015**, *8* (10), 2851–2862.

(34) Tan, M.; Laibinis, P.; Nguyen, S.; Kesselman, J.; Stanton, C.; Lewis, N. In *Progress In Inorganic Chemistry*; John Wiley & Sons Inc: 605 3rd Ave, New York, NY 10016, **1994**; Vol. 41, pp 21–144.

(35) Hoex, B.; Heil, S. B. S.; Langereis, E.; Sanden, M. C. M. van de; Kessels, W. M. M. *Appl. Phys. Lett.* **2006**, *89* (4), 42112.

(36) Bansal, A.; Li, X.; Lauermann, I.; Lewis, N. S.; Yi, S. I.; Weinberg, W. H. *J. Am. Chem. Soc.* **1996**, *118* (30), 7225–7226.

(37) Bansal, A.; Lewis, N. S. *J. Phys. Chem. B* **1998**, *102* (7), 1067–1070.

(38) Bansal, A.; Lewis, N. S. *J. Phys. Chem. B* **1998**, *102* (21), 4058–4060.

(39) Webb, L. J.; Lewis, N. S. *J. Phys. Chem. B* **2003**, *107* (23), 5404–5412.

(40) Seo, J.; Kim, H. J.; Pekarek, R. T.; Rose, M. J. *J. Am. Chem. Soc.* **2015**, *137* (9), 3173–3176.

(41) Li, F.; Basile, V. M.; Pekarek, R. T.; Rose, M. J. *ACS Appl. Mater. Interfaces* **2014**, *6* (22), 20557–20568.

(42) Yablonovitch, E.; Allara, D. L.; Chang, C. C.; Gmitter, T.; Bright, T. B. *Phys. Rev. Lett.* **1986**, *57* (2), 249–252.

(43) Mukherjee, J.; Peczonczyk, S.; Maldonado, S. *Langmuir* **2010**, *26* (13), 10890–10896.

(44) Peczonczyk, S. L.; Mukherjee, J.; Carim, A. I.; Maldonado, S. *Langmuir* **2012**, *28* (10), 4672–4682.

(45) Spool, A.; Daube, K. A.; Mallouk, T. E.; Belmont, J. A.; Wrighton, M. S. *J. Am. Chem. Soc.* **1986**, *108* (11), 3155–3157.

(46) Sieval, A. B.; Demirel, A. L.; Nissink, J. W. M.; Linford, M. R.; van der Maas, J. H.; de Jeu, W. H.; Zuilhof, H.; Sudhölter, E. J. R. *Langmuir* **1998**, *14* (7), 1759–1768.

(47) Bent, S. F. *Surf. Sci.* **2002**, *500* (1–3), 879–903.

(48) Ciampi, S.; Böcking, T.; Kilian, K. A.; James, M.; Harper, J. B.; Gooding, J. J. *Langmuir* **2007**, *23* (18), 9320–9329.

(49) Richards, D.; Zemlyanov, D.; Ivanisevic, A. *Langmuir* **2010**, *26* (11), 8141–8146.

(50) George, S. M. *Chem. Rev.* **2010**, *110* (1), 111–131.

(51) Puurunen, R. L. *J. Appl. Phys.* **2005**, *97* (12), 121301.

(52) Elam, J. W.; George, S. M. *Chem. Mater.* **2003**, *15* (4), 1020–1028.

(53) Miikkulainen, V.; Leskelä, M.; Ritala, M.; Puurunen, R. L. *J. Appl. Phys.* **2013**, *113* (2), 21301.

(54) Satpati, A. K.; Arroyo-Currás, N.; Ji, L.; Yu, E. T.; Bard, A. J. *Chem. Mater.* **2013**, *25* (21), 4165–4172.

(55) Qiu, J.; Zeng, G.; Pavaskar, P.; Li, Z.; Cronin, S. B. *Phys. Chem. Chem. Phys.* **2014**, *16* (7), 3115–3121.

(56) Fukuzumi, S.; Yamada, Y.; Suenobu, T.; Ohkubo, K.; Kotani, H. *Energy Environ. Sci.* **2011**, *4* (8), 2754–2766.

(57) Kumar, B.; Llorente, M.; Froehlich, J.; Dang, T.; Sathrum, A.; Kubiak, C. P. *Annu. Rev. Phys. Chem.* **2012**, *63* (1), 541–569.

(58) Li, X.; Yu, J.; Low, J.; Fang, Y.; Xiao, J.; Chen, X. *J. Mater. Chem. A* **2015**, *3* (6), 2485–2534.

(59) Yang, J.; Wang, D.; Han, H.; Li, C. *Acc. Chem. Res.* **2013**, *46* (8), 1900–1909.

(60) Fourmond, V.; Jacques, P.-A.; Fontecave, M.; Artero, V. *Inorg. Chem.* **2010**, *49* (22), 10338–10347.

(61) Artero, V.; Saveant, J.-M. *Energy Environ. Sci.* **2014**, *7* (11), 3808–3814.

(62) Anxolabéhère-Mallart, E.; Costentin, C.; Fournier, M.; Robert, M. *J. Phys. Chem. C* **2014**, *118* (25), 13377–13381.

(63) Anxolabéhère-Mallart, E.; Costentin, C.; Fournier, M.; Nowak, S.; Robert, M.; Savéant, J.-M. *J. Am. Chem. Soc.* **2012**, *134* (14), 6104–6107.

(64) Artero, V.; Fontecave, M. *Chem. Soc. Rev.* **2013**, *42* (6), 2338–2356.

(65) Chen, Y.; Sun, K.; Audesirk, H.; Xiang, C.; Lewis, N. S. *Energy Environ. Sci.* **2015**, *8* (6), 1736–1747.

(66) Du, P.; Eisenberg, R. *Energy Environ. Sci.* **2012**, *5* (3), 6012–6021.

(67) Thoi, V. S.; Sun, Y.; Long, J. R.; Chang, C. J. *Chem. Soc. Rev.* **2013**, *42* (6), 2388–2400.

(68) Artero, V.; Berggren, G.; Atta, M.; Caserta, G.; Roy, S.; Pecqueur, L.; Fontecave, M. *Acc. Chem. Res.* **2015**, *48* (8), 2380–2387.

(69) Dey, S.; Das, P. K.; Dey, A. *Coord. Chem. Rev.* **2013**, *257* (1), 42–63.

(70) Rose, M. J.; Gray, H. B.; Winkler, J. R. *J. Am. Chem. Soc.* **2012**, *134* (20), 8310–8313.

(71) Helm, M. L.; Stewart, M. P.; Bullock, R. M.; DuBois, M. R.; DuBois, D. L. *Science* **2011**, *333* (6044), 863–866.

(72) DuBois, M. R.; DuBois, D. L. *Chem. Soc. Rev.* **2008**, *38* (1), 62–72.

(73) Fisher, B. J.; Eisenberg, R. *J. Am. Chem. Soc.* **1980**, *102* (24), 7361–7363.

(74) Hu, X.; Cossairt, B. M.; Brunschwig, B. S.; Lewis, N. S.; Peters, J. C. *Chem. Commun.* **2005**, No. 37, 4723–4725.

(75) Razavet, M.; Artero, V.; Fontecave, M. *Inorg. Chem.* **2005**, *44* (13), 4786–4795.

(76) Hu, X.; Brunschwig, B. S.; Peters, J. C. *J. Am. Chem. Soc.* **2007**, *129* (29), 8988–8998.

(77) Baffert, C.; Artero, V.; Fontecave, M. *Inorg. Chem.* **2007**, *46* (5), 1817–1824.

(78) Solis, B. H.; Hammes-Schiffer, S. *J. Am. Chem. Soc.* **2011**, *133* (47), 19036–19039.

(79) Solis, B. H.; Hammes-Schiffer, S. *Inorg. Chem.* **2011**, *50* (21), 11252–11262.

(80) Solis, B. H.; Yu, Y.; Hammes-Schiffer, S. *Inorg. Chem.* **2013**, *52* (12), 6994–6999.

(81) Niklas, J.; Mardis, K. L.; Rakhimov, R. R.; Mulfort, K. L.; Tiede, D. M.; Poluektov, O. G. *J. Phys. Chem. B* **2012**, *116* (9), 2943–2957.

(82) Dempsey, J. L.; Winkler, J. R.; Gray, H. B. *J. Am. Chem. Soc.* **2010**, *132* (3), 1060–1065.

(83) Dempsey, J. L.; Winkler, J. R.; Gray, H. B. *J. Am. Chem. Soc.* **2010**, *132* (47), 16774–16776.

(84) Schrauzer, G. N.; Windgassen, R. J. *Chem. Ber.* **1966**, *99* (2), 602–610.

(85) Bakac, A.; Espenson, J. H. *J. Am. Chem. Soc.* **1984**, *106* (18), 5197–5202.

(86) Valdez, C. N.; Dempsey, J. L.; Brunschwig, B. S.; Winkler, J. R.; Gray, H. B. *Proc. Natl. Acad. Sci.* **2012**, *109* (39), 15589–15593.

(87) Laga, S. M.; Blakemore, J. D.; Henling, L. M.; Brunschwig, B. S.; Gray, H. B. *Inorg. Chem.* **2014**, *53* (24), 12668–12670.

(88) Berben, L. A.; Peters, J. C. *Chem. Commun.* **2010**, *46* (3), 398–400.

(89) Ji, Z.; He, M.; Huang, Z.; Ozkan, U.; Wu, Y. *J. Am. Chem. Soc.* **2013**, *135* (32), 11696–11699.

(90) Andreiadis, E. S.; Jacques, P.-A.; Tran, P. D.; Leyris, A.; Chavarot-Kerlidou, M.; Jousselme, B.; Matheron, M.; Pécaut, J.; Palacin, S.; Fontecave, M.; Artero, V. *Nat. Chem.* **2013**, *5* (1), 48–53.

(91) Krawicz, A.; Yang, J.; Anzenberg, E.; Yano, J.; Sharp, I. D.; Moore, G. F. *J. Am. Chem. Soc.* **2013**, *135* (32), 11861–11868.

(92) Krawicz, A.; Cedeno, D.; Moore, G. F. *Phys. Chem. Chem. Phys.* **2014**, *16* (30), 15818–15824.

(93) Fihri, A.; Artero, V.; Pereira, A.; Fontecave, M. *Dalton Trans.* **2008**, No. 41, 5567–5569.

(94) Zhang, P.; Wang, M.; Li, C.; Li, X.; Dong, J.; Sun, L. *Chem. Commun.* **2009**, *46* (46), 8806–8808.

(95) McCormick, T. M.; Calitree, B. D.; Orchard, A.; Kraut, N. D.; Bright, F. V.; Detty, M. R.; Eisenberg, R. *J. Am. Chem. Soc.* **2010**, *132* (44), 15480–15483.

(96) Luo, G.-G.; Fang, K.; Wu, J.-H.; Dai, J.-C.; Zhao, Q.-H. *Phys. Chem. Chem. Phys.* **2014**, *16* (43), 23884–23894.

(97) Stubbert, B. D.; Peters, J. C.; Gray, H. B. *J. Am. Chem. Soc.* **2011**, *133* (45), 18070–18073.

(98) McCrory, C. C. L.; Uyeda, C.; Peters, J. C. *J. Am. Chem. Soc.* **2012**, *134* (6), 3164–3170.

(99) Yin, X.; Liu, C.; Zhuo, S.; Xu, Y.; Zhang, B. *Dalton Trans.* **2014**, *44* (4), 1526–1529.

(100) Troppmann, S.; König, B. *Chem. – Eur. J.* **2014**, *20* (45), 14570–14574.

(101) Bacchi, M.; Berggren, G.; Niklas, J.; Veinberg, E.; Mara, M. W.; Shelby, M. L.; Poluektov, O. G.; Chen, L. X.; Tiede, D. M.; Cavazza, C.; Field, M. J.; Fontecave, M.; Artero, V. *Inorg. Chem.* **2014**, *53* (15), 8071–8082.

(102) Kelley, P.; Day, M. W.; Agapie, T. *Eur. J. Inorg. Chem.* **2013**, *2013* (22–23), 3840–3845.

(103) Jacques, P.-A.; Artero, V.; Pécaut, J.; Fontecave, M. *Proc. Natl. Acad. Sci.* **2009**, *106* (49), 20627–20632.

(104) Barton Cole, E.; Lakkaraju, P. S.; Rampulla, D. M.; Morris, A. J.; Abelev, E.; Bocarsly, A. B. *J. Am. Chem. Soc.* **2010**, *132* (33), 11539–11551.

(105) Beley, M.; Collin, J.-P.; Ruppert, R.; Sauvage, J.-P. *J. Chem. Soc. Chem. Commun.* **1984**, No. 19, 1315–1316.

(106) Beley, M.; Collin, J. P.; Ruppert, R.; Sauvage, J. P. *J. Am. Chem. Soc.* **1986**, *108* (24), 7461–7467.

(107) Froehlich, J. D.; Kubiak, C. P. *Inorg. Chem.* **2012**, *51* (7), 3932–3934.

(108) Bhugun, I.; Lexa, D.; Savéant, J.-M. *J. Phys. Chem.* **1996**, *100* (51), 19981–19985.

(109) Bhugun, I.; Lexa, D.; Savéant, J.-M. *J. Am. Chem. Soc.* **1996**, *118* (7), 1769–1776.

(110) Hawecker, J.; Lehn, J.-M.; Ziessel, R. *J. Chem. Soc. Chem. Commun.* **1984**, No. 6, 328–330.

(111) Ishida, H.; Tanaka, K.; Tanaka, T. *Organometallics* **1987**, *6* (1), 181–186.

(112) Bourrez, M.; Molton, F.; Chardon-Noblat, S.; Deronzier, A. *Angew. Chem. Int. Ed.* **2011**, *50* (42), 9903–9906.

(113) DuBois, D. L.; Miedaner, A.; Haltiwanger, R. C. *J. Am. Chem. Soc.* **1991**, *113* (23), 8753–8764.

(114) Dubois, D. L. *Comments Inorg. Chem.* **1997**, *19* (5), 307–325.

(115) Haines, R. J.; Wittrig, R. E.; Kubiak, C. P. *Inorg. Chem.* **1994**, *33* (21), 4723–4728.

(116) Hammouche, M.; Lexa, D.; Savéant, J. M.; Momenteau, M. *J. Electroanal. Chem. Interfacial Electrochem.* **1988**, *249* (1–2), 347–351.

(117) Hawecker, J.; Lehn, J.-M.; Ziessel, R. *J. Chem. Soc. Chem. Commun.* **1983**, No. 9, 536–538.

(118) Benson, E. E.; Sampson, M. D.; Grice, K. A.; Smieja, J. M.; Froehlich, J. D.; Friebel, D.; Keith, J. A.; Carter, E. A.; Nilsson, A.; Kubiak, C. P. *Angew. Chem. Int. Ed.* **2013**, *52* (18), 4841–4844.

(119) Keith, J. A.; Grice, K. A.; Kubiak, C. P.; Carter, E. A. *J. Am. Chem. Soc.* **2013**, *135* (42), 15823–15829.

(120) Fujita, E.; Szalda, D. J.; Creutz, C.; Sutin, N. *J. Am. Chem. Soc.* **1988**, *110* (14), 4870–4871.

(121) Creutz, C.; Schwarz, H. A.; Wishart, J. F.; Fujita, E.; Sutin, N. *J. Am. Chem. Soc.* **1991**, *113* (9), 3361–3371.

(122) Fujita, E.; Creutz, C.; Sutin, N.; Brunschwig, B. S. *Inorg. Chem.* **1993**, *32* (12), 2657–2662.

(123) Fujita, E.; Furenlid, L. R.; Renner, M. W. *J. Am. Chem. Soc.* **1997**, *119* (19), 4549–4550.

(124) Fujita, E.; van Eldik, R. *Inorg. Chem.* **1998**, *37* (2), 360–362.

(125) Gangi, D. A.; Durand, R. R. *J. Chem. Soc. Chem. Commun.* **1986**, No. 9, 697–699.

(126) Schmidt, M. H.; Miskelly, G. M.; Lewis, N. S. *J. Am. Chem. Soc.* **1990**, *112* (9), 3420–3426.

(127) Amatore, C.; Saveant, J. M. *J. Am. Chem. Soc.* **1981**, *103* (17), 5021–5023.

(128) Gennaro, A.; Isse, A. A.; Severin, M.-G.; Vianello, E.; Bhugun, I.; Savéant, J.-M. *J Chem Soc Faraday Trans* **1996**, *92* (20), 3963–3968.

(129) Gambarotta, S.; Arena, F.; Floriani, C.; Zanazzi, P. F. *J. Am. Chem. Soc.* **1982**, *104* (19), 5082–5092.

(130) Chan, S. L.-F.; Lam, T. L.; Yang, C.; Yan, S.-C.; Cheng, N. M. *Chem. Commun.* **2015**, *51* (37), 7799–7801.

(131) Lacy, D. C.; McCrory, C. C. L.; Peters, J. C. *Inorg. Chem.* **2014**, *53* (10), 4980–4988.

(132) Shaffer, D. W.; Johnson, S. I.; Rheingold, A. L.; Ziller, J. W.; Goddard, W. A.; Nielsen, R. J.; Yang, J. Y. *Inorg. Chem.* **2014**, *53* (24), 13031–13041.

(133) van Asselt, R.; Elsevier, C. J. *Tetrahedron* **1994**, *50* (2), 323–334.

(134) Hill, N. J.; Vargas-Baca, I.; Cowley, A. H. *Dalton Trans.* **2008**, No. 2, 240–253.

(135) Fedushkin, I. L.; Maslova, O. V.; Morozov, A. G.; Dechert, S.; Demeshko, S.; Meyer, F. *Angew. Chem. Int. Ed.* **2012**, *51* (42), 10584–10587.

(136) Mondal, P.; Agarwala, H.; Jana, R. D.; Plebst, S.; Grupp, A.; Ehret, F.; Mobin, S. M.; Kaim, W.; Lahiri, G. K. *Inorg. Chem.* **2014**, *53* (14), 7389–7403.

(137) Hu, X.; Cossairt, B. M.; Brunschwig, B. S.; Lewis, N. S.; Peters, J. C. *Chem. Commun.* **2005**, No. 37, 4723–4725.

(138) Connelly, N. G.; Geiger, W. E. *Chem. Rev.* **1996**, *96* (2), 877–910.

(139) Fedushkin, I. L.; Skatova, A. A.; Chudakova, V. A.; Fukin, G. K. *Angew. Chem. Int. Ed.* **2003**, *42* (28), 3294–3298.

(140) Fourmond, V.; Jacques, P.-A.; Fontecave, M.; Artero, V. *Inorg. Chem.* **2010**, *49* (22), 10338–10347.

(141) Jödecke, M.; Pérez-Salado Kamps, Á.; Maurer, G. *J. Chem. Eng. Data* **2012**, *57* (4), 1249–1266.

(142) McCarthy, B. D.; Martin, D. J.; Rountree, E. S.; Ullman, A. C.; Dempsey, J. L. *Inorg. Chem.* **2014**, *53* (16), 8350–8361.

(143) Anxolabéhère-Mallart, E.; Costentin, C.; Fournier, M.; Robert, M. *J. Phys. Chem. C* **2014**, *118* (25), 13377–13381.

(144) Satake, M.; Miura, J. 'ichiro; Usami, S.; Puri, B. K. *Analyst* **1989**, *114* (7), 813–818.

(145) Burla, M. C.; Caliandro, R.; Camalli, M.; Carrozzini, B.; Cascarano, G. L.; De Caro, L.; Giacovazzo, C.; Polidori, G.; Spagna, R. *J. Appl. Crystallogr.* **2005**, *38* (2), 381–388.

(146) Sheldrick, G. M. *Acta Crystallogr. A* **2008**, *64* (1), 112–122.

(147) Spek, A. L. *Acta Crystallogr. Sect. C Struct. Chem.* **2015**, *71* (1), 9–18.

(148) Farrugia, L. J. *J. Appl. Crystallogr.* **2012**, *45* (4), 849–854.

(149) Wilson, A. J. C. *International Tables for X-ray Crystallography*; Kluwer Academic Press: Boston, **1992**; Vol. C.

(150) Macrae, C. F.; Bruno, I. J.; Chisholm, J. A.; Edgington, P. R.; McCabe, P.; Pidcock, E.; Rodriguez-Monge, L.; Taylor, R.; van de Streek, J.; Wood, P. A. *J. Appl. Crystallogr.* **2008**, *41* (2), 466–470.

(151) Granovsky, A. *Firefly*.

(152) Wachters, A. J. H. *J. Chem. Phys.* **1970**, *52* (3), 1033–1036.

(153) Barbieri, P. L.; Fantin, P. A.; Jorge, F. E. *Mol. Phys.* **2006**, *104* (18), 2945–2954.

(154) Andrienko, G. *Chemcraft*.

(155) Greeley, J.; Jaramillo, T. F.; Bonde, J.; Chorkendorff, I.; Nørskov, J. K. *Nat. Mater.* **2006**, *5* (11), 909–913.

(156) Laursen, A. B.; Kegnæs, S.; Dahl, S.; Chorkendorff, I. *Energy Environ. Sci.* **2012**, *5* (2), 5577–5591.

(157) Jaramillo, T. F.; Jørgensen, K. P.; Bonde, J.; Nielsen, J. H.; Horch, S.; Chorkendorff, I. *Science* **2007**, *317* (5834), 100–102.

(158) Dau, H.; Limberg, C.; Reier, T.; Risch, M.; Roggan, S.; Strasser, P. *ChemCatChem* **2010**, *2* (7), 724–761.

(159) McCrory, C. C. L.; Jung, S.; Peters, J. C.; Jaramillo, T. F. *J. Am. Chem. Soc.* **2013**, *135* (45), 16977–16987.

(160) Li, Y.; Chan, S. H.; Sun, Q. *Nanoscale* **2015**, *7* (19), 8663–8683.

(161) Kortlever, R.; Shen, J.; Schouten, K. J. P.; Calle-Vallejo, F.; Koper, M. T. M. *J. Phys. Chem. Lett.* **2015**, *6* (20), 4073–4082.

(162) Back, S.; Kim, H.; Jung, Y. *ACS Catal.* **2015**, *5* (2), 965–971.

(163) Habisreutinger, S. N.; Schmidt-Mende, L.; Stolarczyk, J. K. *Angew. Chem. Int. Ed.* **2013**, *52* (29), 7372–7408.

(164) Highfield, J. *Molecules* **2015**, *20* (4), 6739–6793.

(165) Hori, Y. In *Modern Aspects of Electrochemistry*; Vayenas, C. G., White, R. E., Gamboa-Aldeco, M. E., Eds.; Modern Aspects of Electrochemistry; Springer New York, **2008**; pp 89–189.

(166) Kuhl, K. P.; Cave, E. R.; Abram, D. N.; Jaramillo, T. F. *Energy Environ. Sci.* **2012**, *5* (5), 7050–7059.

(167) Zhai, Q.; Xie, S.; Fan, W.; Zhang, Q.; Wang, Y.; Deng, W.; Wang, Y. *Angew. Chem. Int. Ed.* **2013**, *52* (22), 5776–5779.

(168) Kauffman, D. R.; Alfonso, D.; Matranga, C.; Qian, H.; Jin, R. *J. Am. Chem. Soc.* **2012**, *134* (24), 10237–10243.

(169) Chen, Y.; Li, C. W.; Kanan, M. W. *J. Am. Chem. Soc.* **2012**, *134* (49), 19969–19972.

(170) Zhu, W.; Michalsky, R.; Metin, Ö.; Lv, H.; Guo, S.; Wright, C. J.; Sun, X.; Peterson, A. A.; Sun, S. *J. Am. Chem. Soc.* **2013**, *135* (45), 16833–16836.

(171) Lates, V.; Falch, A.; Jordaan, A.; Peach, R.; Kriek, R. J. *Electrochimica Acta* **2014**, *128*, 75–84.

(172) Manthiram, K.; Surendranath, Y.; Alivisatos, A. P. *J. Am. Chem. Soc.* **2014**, *136* (20), 7237–7240.

(173) Kim, D.; Resasco, J.; Yu, Y.; Asiri, A. M.; Yang, P. *Nat. Commun.* **2014**, *5*, 4948.

(174) Zhu, W.; Zhang, Y.-J.; Zhang, H.; Lv, H.; Li, Q.; Michalsky, R.; Peterson, A. A.; Sun, S. *J. Am. Chem. Soc.* **2014**, *136* (46), 16132–16135.

(175) Feng, X.; Jiang, K.; Fan, S.; Kanan, M. W. *J. Am. Chem. Soc.* **2015**, *137* (14), 4606–4609.

(176) Back, S.; Yeom, M. S.; Jung, Y. *ACS Catal.* **2015**, *5* (9), 5089–5096.

(177) Dick, J. E.; Renault, C.; Bard, A. J. *J. Am. Chem. Soc.* **2015**, *137* (26), 8376–8379.

(178) Dick, J. E.; Hilterbrand, A. T.; Boika, A.; Upton, J. W.; Bard, A. J. *Proc. Natl. Acad. Sci. U. S. A.* **2015**, *112* (17), 5303–5308.

(179) Kim, B.-K.; Boika, A.; Kim, J.; Dick, J. E.; Bard, A. J. *J. Am. Chem. Soc.* **2014**, *136* (13), 4849–4852.

(180) Li, Y.; Deng, H.; Dick, J. E.; Bard, A. J. *Anal. Chem. Wash. DC U. S.* **2015**, *87* (21), 11013–11021.

(181) Zhou, H.; Park, J. H.; Fan, F.-R. F.; Bard, A. J. *J. Am. Chem. Soc.* **2012**, *134* (32), 13212–13215.

(182) Xiao, X.; Bard, A. J. *J. Am. Chem. Soc.* **2007**, *129* (31), 9610–9612.

(183) Lebegue, E.; Anderson, C. M.; Dick, J. E.; Webb, L. J.; Bard, A. J. *Langmuir* **2015**, *31* (42), 11734–11739.

(184) Zeng, G.; Qiu, J.; Li, Z.; Pavaskar, P.; Cronin, S. B. *ACS Catal.* **2014**, *4* (10), 3512–3516.

(185) Price, M. J.; Maldonado, S. *J. Phys. Chem. C* **2009**, *113* (28), 11988–11994.

(186) Brown, E. S.; Peczonczyk, S. L.; Wang, Z.; Maldonado, S. *J. Phys. Chem. C* **2014**, *118* (22), 11593–11600.

(187) Peczonczyk, S. L.; Brown, E. S.; Maldonado, S. *Langmuir* **2014**, *30* (1), 156–164.

(188) Brown, E. S.; Peczonczyk, S. L.; Maldonado, S. *J. Phys. Chem. C* **2015**, *119* (3), 1338–1345.

(189) Dumas, P.; Chabal, Y. J. *Chem. Phys. Lett.* **1991**, *181* (6), 537–543.

(190) Webb, L. J.; Lewis, N. S. *J. Phys. Chem. B* **2003**, *107* (23), 5404–5412.

(191) Mukherjee, J.; Peczonczyk, S.; Maldonado, S. *Langmuir* **2010**, *26* (13), 10890–10896.

(192) Zeng, G.; Qiu, J.; Li, Z.; Pavaskar, P.; Cronin, S. B. *ACS Catal.* **2014**, *4* (10), 3512–3516.

(193) Hu, S.; Shaner, M. R.; Beardslee, J. A.; Lichterman, M.; Brunschwig, B. S.; Lewis, N. S. *Science* **2014**, *344* (6187), 1005–1009.

(194) Standing, A.; Assali, S.; Gao, L.; Verheijen, M. A.; van Dam, D.; Cui, Y.; Notten, P. H. L.; Haverkort, J. E. M.; Bakkers, E. P. A. M. *Nat. Commun.* **2015**, *6*, 7824.

(195) Sun, J.; Liu, C.; Yang, P. *J. Am. Chem. Soc.* **2011**, *133* (48), 19306–19309.

(196) Liu, C.; Sun, J.; Tang, J.; Yang, P. *Nano Lett.* **2012**, *12* (10), 5407–5411.

(197) Halmann, M. *Nature* **1978**, *275* (5676), 115–116.

(198) Barton, E. E.; Rampulla, D. M.; Bocarsly, A. B. *J. Am. Chem. Soc.* **2008**, *130* (20), 6342–6344.

(199) Halmann, M. *Nature* **1978**, *275* (5676), 115–116.

(200) Inoue, T.; Fujishima, A.; Konishi, S.; Honda, K. *Nature* **1979**, *277* (5698), 637–638.

(201) Barton, E. E.; Rampulla, D. M.; Bocarsly, A. B. *J. Am. Chem. Soc.* **2008**, *130* (20), 6342–6344.

(202) Beiler, A. M.; Khusnutdinova, D.; Jacob, S. I.; Moore, G. F. *ACS Appl. Mater. Interfaces* **2016**, *8* (15), 10038–10047.

(203) Hagedorn, K.; Collins, S.; Maldonado, S. *J. Electrochem. Soc.* **2010**, *157* (11), D588–D592.

(204) Kim, H. J.; Kearney, K. L.; Le, L. H.; Pekarek, R. T.; Rose, M. J. *ACS Appl. Mater. Interfaces* **2015**.

(205) Morota, H.; Adachi, S. *J. Appl. Phys.* **2007**, *101* (11), 113518.

(206) Rokugawa, H.; Adachi, S. *J. Electrochem. Soc.* **2009**, *156* (2), H92–H97.

(207) Morota, H.; Adachi, S. *J. Appl. Phys.* **2006**, *100* (5), 54904.

(208) Liakos, I. L.; Newman, R. C.; McAlpine, E.; Alexander, M. R. *Langmuir* **2007**, *23* (3), 995–999.

(209) Debrassi, A.; Ribbera, A.; de Vos, W. M.; Wennekes, T.; Zuilhof, H. *Langmuir* **2014**, *30* (5), 1311–1320.

(210) Branch, B.; Dubey, M.; Anderson, A. S.; Artyushkova, K.; Baldwin, J. K.; Petsev, D.; Dattelbaum, A. M. *Appl. Surf. Sci.* **2014**, *288*, 98–108.

(211) Groner, M. D.; Elam, J. W.; Fabreguette, F. H.; George, S. M. *Thin Solid Films* **2002**, *413* (1–2), 186–197.

(212) Spori, D. M.; Venkataraman, N. V.; Tosatti, S. G. P.; Durmaz, F.; Spencer, N. D.; Zürcher, S. *Langmuir* **2007**, *23* (15), 8053–8060.

(213) Yildirim, O.; Yilmaz, M. D.; Reinhoudt, D. N.; Blank, D. H. A.; Rijnders, G.; Huskens, J. *Langmuir* **2011**, *27* (16), 9890–9894.

(214) Perri, J. A.; La Placa, S.; Post, B. *Acta Crystallogr.* **1958**, *11* (4), 310–310.

(215) Williams, F. V.; Ruehrwein, R. A. *J. Am. Chem. Soc.* **1960**, *82* (6), 1330–1332.

(216) Ku, S. M. *J. Electrochem. Soc.* **1966**, *113* (8), 813–816.

(217) Wang, S.; Swingle, S. F.; Ye, H.; Fan, F.-R. F.; Cowley, A. H.; Bard, A. J. *J. Am. Chem. Soc.* **2012**, *134* (27), 11056–11059.

(218) Lindsay, L.; Broido, D. A.; Reinecke, T. L. *Phys. Rev. Lett.* **2013**, *111* (2), 25901.

(219) Lv, B.; Lan, Y.; Wang, X.; Zhang, Q.; Hu, Y.; Jacobson, A. J.; Broido, D.; Chen, G.; Ren, Z.; Chu, C.-W. *Appl. Phys. Lett.* **2015**, *106* (7), 74105.

(220) Chu, T. L.; Hyslop, A. E. *J. Electrochem. Soc.* **1974**, *121* (3), 412–415.

(221) Greene, R. G.; Luo, H.; Ruoff, A. L.; Trail, S. S.; DiSalvo, F. J. *Phys. Rev. Lett.* **1994**, *73* (18), 2476–2479.

(222) Broido, D. A.; Lindsay, L.; Reinecke, T. L. *Phys. Rev. B* **2013**, *88* (21), 214303.

(223) Yang, F.; Dames, C. *Phys. Rev. B* **2013**, *87* (3), 35437.

(224) Kim, J.; Ou, E.; Sellan, D. P.; Shi, L. *Rev. Sci. Instrum.* **2015**, *86* (4), 44901.

(225) Yu, C.; Saha, S.; Zhou, J.; Shi, L.; Cassell, A. M.; Cruden, B. A.; Ngo, Q.; Li, J. *J. Heat Transf.* **2005**, *128* (3), 234–239.

(226) Glassbrenner, C. J.; Slack, G. A. *Phys. Rev.* **1964**, *134* (4A), A1058–A1069.

(227) Wang, Z.; Mingo, N. *Appl. Phys. Lett.* **2010**, *97* (10), 101903.

(228) Liao, B.; Qiu, B.; Zhou, J.; Huberman, S.; Esfarjani, K.; Chen, G. *Phys. Rev. Lett.* **2015**, *114* (11), 115901.

(229) Xing, Q.; Song, K.; Liang, T.; Liu, Q.; Sun, W.-H.; Redshaw, C. *Dalton Trans.* **2014**, *43* (21), 7830–7837.

(230) Song, K.; Yang, W.; Li, B.; Liu, Q.; Redshaw, C.; Li, Y.; Sun, W.-H. *Dalton Trans.* **2013**, *42* (25), 9166–9175.

(231) Zhao, T.; Xing, Q.; Song, K.; Ban, Q.; Liang, T.; Liu, Q.; Sun, W.-H. *RSC Adv.* **2015**, *5* (19), 14228–14234.

(232) Gao, B.; Luo, X.; Gao, W.; Huang, L.; Gao, S.; Liu, X.; Wu, Q.; Mu, Y. *Dalton Trans.* **2012**, *41* (9), 2755–2763.

(233) Vasudevan, K.; Cowley, A. H. *Chem. Commun.* **2007**, No. 33, 3464–3466.

(234) Vasudevan, K. V.; Findlater, M.; Vargas-Baca, I.; Cowley, A. H. *J. Am. Chem. Soc.* **2012**, *134* (1), 176–178.

(235) Chaudhuri, P. *Coord. Chem. Rev.* **2003**, *243* (1–2), 143–190.

(236) Aromí, G.; Brechin, E. K. In *Single-Molecule Magnets and Related Phenomena*; Winpenny, R., Ed.; Structure and Bonding; Springer Berlin Heidelberg, **2006**; pp 1–67.

(237) Jiang, Y.-B.; Kou, H.-Z.; Wang, R.-J.; Cui, A.-L.; Ribas, J. *Inorg. Chem.* **2005**, *44* (3), 709–715.

(238) Biswas, B.; Pieper, U.; Weyhermüller, T.; Chaudhuri, P. *Inorg. Chem.* **2009**, *48* (14), 6781–6793.

(239) Schmidt, J.; Söll, J. *Berichte Dtsch. Chem. Ges.* **1907**, *40* (2), 2454–2460.

(240) Hu, J.; Zhang, D.; Harris, F. W. *J. Org. Chem.* **2005**, *70* (2), 707–708.

Vita

Owen Williams was born in Syracuse, NY and raised in Las Vegas, NV. Upon matriculating from Rancho High School, he attended Tulane University. During his time there, he was afforded the opportunity to study abroad in Cork, Ireland at the University College Cork and work under the guidance of Professor Scott Grayson and Mark Fink. Ultimately, he graduated Cum Laude with a B.S. in Chemistry in 2010. After his undergraduate studies, Owen worked as a Research Assistant for Nanoprobes Inc. in Yaphank, NY focusing on biodistribution studies. In August of 2011 he joined the incoming graduate class in the Chemistry Department at the University of Texas at Austin, joining the Cowley Group. In February of 2013, he joined the group of Professor Rose, focusing on research of photoelectrochemical cell constructs.

Permanent email: owenm.williams@gmail.com

This dissertation was typed by Owen Williams.